MICROSOURCE INTERFACE FOR A MICROGRID

A thesis submitted to The University of Manchester for the degree of

Doctor of Philosophy

in the Faculty of Engineering and Physical Sciences

2010

PRABATH JANAKA BINDUHEWA

SCHOOL OF ELECTRICAL AND ELECTRONIC ENGINEERING

LIST OF CONTENTS

Word count = 53667

LIST OF FIGURES

LIST OF TABLES

LIST OF SYMBOLS AND ABBREVIATIONS

Abbreviation	Description
CHP	Combined Heat and Power
DPLL	Digital Phase Locked Loop
MPP	Maximum Power Point
MPPT	Maximum Power Point Tracker
PV	Photovoltaic
PEC	Power Electronic Converter
PLL	Phase Locked Loop
PV	Photovoltaic
PWM	Pulse Width Modulation
STC	Standard Test Condition
VCO	Voltage Controlled Oscillator

Symbol	Description	Unit
Photovoltaic panel		
A	Ideality factor	
E_{OUT}	Output voltage of the natural logarithmic amplifier	V
E_{IN}	Input voltage of the natural logarithmic amplifier	V
G_a	Irradiance	W/m^2
G_a	Irradiance at STC	W/m^2
I_{pv}	Output current of a photovoltaic panel/cell	A
I_{ph}	Photocurrent	A
I_{sc}	Short circuit current	A
I_{scs}	Short circuit current at STC	A
I_{sat}	Diode saturation current of the PV panel model	A
I_{MPP}	Output current at MPP	A
I_d	Current through the diode of the PV cell model	A
I_{ADJ}	Current flowing through the ADJ terminal of the linear voltage regulator	A
k	Boltzmann's constant	m^{2}kgs^{-2}K^{-1}

L	Series inductance in the simulation model	H
N	Number of cells in series	
q	Charge of an electron	C
R	Load resistance	Ω
R_1	Resistor connected in between OUT and ADJ terminal of linear voltage regulator	Ω
R_2	Resistor connected in between ADJ terminal of linear voltage regulator and 0V	Ω
R_s	Series resistance of the PV model	Ω
R_{sh}	Shunt resistance of the PV model	Ω
R_{load}	Load resistor connected to the PV hardware emulator	Ω
T	Temperature	K
V_{CT}	Output voltage of the current transducer	V
V_{in}	Input voltage of the linear voltage regulator	V
V_{MPP}	Voltage at Maximum Power Point	V
V_{pv}	Output voltage of a PV panel/cell	V
V_{ref}	Controller output of the PV hardware emulator	V
V_t	Thermal voltage	V
V_{oc}	Open circuit voltage of a panel/cell	V
V_{ocs}	Open circuit voltage of a panel/cell at STC	V
ΔI_{sc}	Temperature coefficient of short-circuit current	A
ΔV_{oc}	Temperature coefficient of open-circuit voltage	V

Unidirectional dc-dc converter

C_{p1}	Input capacitance	F
C_{p2}	Output capacitance	F
D	Duty ratio	
D_1 to D_4	Diodes	
G	Gate signals	
I_{in}	Input current	A
I_{load}	Output current	A
I_{pr}	Primary current of the transformer	A
I_{se}	Secondary current of the transformer	A
L_p	Output filter inductance	H

N	Turns-ratio	
Q_1, Q_2	Switches	
T_s	Switching period	s
V_{in}	Input voltage	V
V_{dc}	Output voltage	V
V_{pr}	Voltage across the primary of the transformer	V
V_{se}	Voltage across the secondary of the transformer	V
ΔQ_1	Charge stored in input capacitor	C
ΔI_{ind}	Inductor current ripple	A
ΔV_{in}	Input voltage ripple	V
ΔV_{dc}	Output voltage ripple	V

Bi-directional dc-dc converter

C_{ph}	High-voltage side capacitance	F
D	Duty ratio	
D_1 to D_6	Diodes	
I_L	Battery current	A
I_H	High-voltage side current	A
I_{ind}	Inductor current	A
I_{trh}	High-voltage side transformer current	A
I_{trl1}, I_{trl2}	Currents of low-voltage side transformer winding	A
L_p	Low-votlage side filter inductance	H
N	Turns-ratio	
Q_1 to Q_6	Switches	
t_{on}	On-state period	s
V_L	Battery voltage	V
V_{dc}	High-voltage end voltage	V
V_{ind}	Voltage across the inductor	V
V_{trh}	Voltage across high-voltage side winding	V
V_{trc}	Voltage at the centre of low-voltage end windings	V
V_{trl1}, V_{trl2}	Voltage at across Q_5 and Q_6	A
ΔI_{ind}	Inductor current ripple	A
ΔV_{dc}	Output voltage ripple	V
ΔQ	Charge stored in high-voltage side capacitor	C

Grid connected single-phase inverter

C_{in}	Input capacitance	F
D_1 to D_4	Diodes of the inverter	
E_{INV}, e_{INV}	Inverter output voltage before the filter	V
$E_{INV,f}$	Fundamental of the inverter output voltage before the filter	V
f	Grid frequency	Hz
G_1 to G_4	Gate signals to the inverter switches	
I_{grid}	Grid current	A
I_{load}	Load current	A
I_{INV}, i_{INV}	Inverter ac output current	A
I_{INVrms}	RMS of the inverter output current	A
i_{in}	Input current of the inverter	A
I_{dc}	Average input current of the inverter	A
I_{mag}	Magnitude of the inverter current reference	A
I_{phase}	Phase of the inverter current reference	rad
$I_{INV,ref}$	Current reference to inverter current controller	A
I_{INVP}	Inverter output current at the primary side of the transformer	A
I_{INVS}	Inverter output current at the secondary side of the transformer	A
K_d	Gain of the phase detector	
K_o	Gain of the VCO	
K_α	Gain of the filter of the DPLL	
L_p	Inductance of the coupling inductor	H
m_a	Modulation index	
p_{ac}	Instantaneous active inverter output power	W
P_{ac}	Average active inverter output power	W
p_{dc}	Instantaneous inverter intput power	W
P_{dc}	Average inverter input power	W
P_{ref}	Active power reference	W
P_{max}	Maximum output power of the inverter	W
Q_{ref}	Reactive power reference	VAr

R_{load}	Load resistance	Ω
R_p	Internal resistance of the coupling inductor	Ω
S_1 to S_4	Switches of the inverter	
t	Time	s
V_{dc}	Input voltage	V
V_c	Input signal to the pulse width modulator	
V_{grid}	Grid voltage	V
V_{load}	Load voltage	V
V_{INV}, v_{INV}	Inverter output voltage	V
V_{INVrms}	RMS voltage of the inverter output voltage	V
τ_1, τ_2	Time constants of the filter in the DPLL	s
ω_o	Centre frequency of the VCO	rad/s
ω_{sync}	Ouptut frequency of the VCO	rad/s
θ_e	Phase difference between grid voltage and PLL output signal	rad
θ_{grid}	Phase of grid voltage	rad
θ_{sync}	Phase of voltage controlled oscillator	rad
ΔQ	Excess charge supplied by the capacitor	C
δ	Phase difference between voltages at the ends of the coupling inductor	

ABSTRACT

A MicroGrid is typically a small power system, which consists of several microsources and energy storage units, providing heat and electricity to local loads. The MicroGrid has the capability to island and operate autonomously from the main utility network. MicroGrids potentially enable a greater integration of small-scale renewable energy sources. The objective of this thesis is to develop a single-phase microsource interface with energy storage unit embedded into the interface. An integrated energy storage unit avoids the necessity of a separate stand-alone energy storage unit in the MicroGrid. Thus the 'plug-and-play' functionality of the MicroGrid can be improved. A collection of power electronic converter based microsources with storage units connected to form a MicroGrid is a complex system. Development of such simple controllers, which decouple the effect of sub-unit while achieving the desired 'plug-and-play' capabilities, is a complex but important challenge.

A photovoltaic panel was considered as the microsource and a battery bank was used as the energy storage unit. The proposed microsource interface consists of three power electronic converters. A photovoltaic panel is connected to a unidirectional dc-dc converter and its output is connected to the input of the single-phase inverter which can be connected to the MicroGrid. Energy storage is connected to the dc-link,which is the input of the single-phase inverter, through a bi-directional dc-dc converter.

A simulation model of a photovoltaic panel was developed in the EMTDC/PSCAD software. The limitations of the model and a method to reduce these limitations are discussed. For the experimental validation of the proposed system, an adjustable-voltage-regulator hardware photovoltaic emulator was designed. The characteristic curves of the hardware emulator are compared with those obtained from the simulation model.

A controller was designed for the unidirectional dc-dc converter to keep the output voltage of the photovoltaic panel at a given reference. Similarly the controller of the bi-directional dc-dc converter was designed to keep the dc-link voltage approximately constant. The behaviour of the dc-dc converters, which are connected to microsource and energy storage unit, around the steady state and worst-case scenarios was analysed, simulated and experimentally validated. Simulation and experimental results are compared.

A current controller, based on instantaneous measured current, was implemented. This was designed to achieve good dynamic stiffness and command tracking properties. Furthermore a smooth grid connection method with the aid of the current controller is presented. The ability of the inverter to control the active and reactive power output was also analysed and verified with the aid of the simulation model and experimental set-up. Results corresponding to current controller, grid connection and power control are presented.

The integrated system was simulated in EMTDC/PSCAD. The system response to the variations in the microsource and inverter output power variations was analysed. A smooth start-up method is shown which reduces the inrush current. Simulation results corresponding to different case studies and start-up transient are also included.

DECLARATION

That no portion of the work referred to in the thesis has been submitted in support of an application for another degree or qualification of this or any other university or other institute of learning.

COPYRIGHT STATEMENT

DEDICATION

To my father, mother and sister

ACKNOWLEDGEMENTS

First of all, I would like to express my gratitude to Dr. Mike Barnes for giving me the opportunity to pursue my degree of Doctor of Philosophy at the University of Manchester. In addition, my gratitude goes to the University of Manchester for accepting me as a student and providing me with funding to continue my studies. The IET also funded my studies for a year; I am thankful to the IET as well.

Supervision of my supervisor, Dr. Mike Barnes was excellent. The continuous guidance and encouragement was highly beneficial and appreciated. Dr. Alasdair Renfrew, who was my co-supervisor in the first half of my research, was also very helpful and provided excellent guidance. Dr. Barnes and Dr. Renfrew are among the best gentlemen I've ever met and it was a pleasure to be with them. I am highly indebted to both my supervisors and thank you very much.

From the first day I joined the Power Conversion Group, Dr. (Mrs.) Nilanga Jayawarna has been very helpful to me in providing necessary information, guidance, encouragement and correcting reports. I was able to settle in the UK quickly due to the kind help of Mr. Jayawan Wijekoon and he continues to provide his support and guidance to date. My friend, Upendra Dayaratne provided me continuous encouragement and support. I would like to extend my gratitude to these three friends for their support over the years.

I would like to acknowledge all the lecturers and colleagues in the Power Conversion Group of the University of Manchester for their support through out. Furthermore I thank all the staff members of workshops, stores and Financial Division.

I sincerely pass my sincere acknowledgement to all the lecturers and teachers who taught me throughout my life. Without them I would not be in this position. Especially I would like to thank Prof. J.B. Ekanayake and Dr. A. Atputharajah for their continuous support. Finally I would like to show appreciation my parents and sister for their continuous support and encouragement given in my entire life.

CHAPTER 1

INTRODUCTION

1.1 INTRODUCTION

Electricity is an essential component in modern society, and the demand for electricity is increasing rapidly. At the same time traditional energy resources used for electricity generation, such as fossil fuels, are reducing. Further, environmental effects caused by the conventional power stations are causing global debate.

The investigation of alternative energy sources, which are more environmental friendly, or developing methods to use existing energy resources more effectively are a top priority of leading engineers in the world. A number of renewable energy sources such as photovoltaics, wind, hydro and tidal exist as (relatively) environmentally benign methods to generate electricity. The challenges surrounding renewable energy sources however are their cost competitiveness, dependency on environmental conditions and technical barriers.

In conventional power plants, overall energy conversion efficiency is poor due to waste heat. Recently it has been suggested to operate generators with smaller capacity from fossil fuels and to use the heat generated for local heating purposes. Such systems are known as Combined Heat and Power (CHP) plants.

Integration of renewable energy sources and CHP plants into a utility network introduces a new set of challenges. Demand-supply matching is a problem when the output power of renewable sources depends on the environmental conditions. These sources typically would be connected to a weak distribution network which in turn introduces power quality issues within the network. Additionally the direction of power flow may be in the opposite direction to conventional power flow, thus new protection schemes may be required.

The MicroGrid concept is a solution which has been suggested to use alternative energy sources effectively while enabling increased amounts of renewables to connect to the utility network. A typical MicroGrid contains several generation units which are known as microsources. Further a MicroGrid could be connected to the utility network to export or to import power. It makes use of two concepts. Firstly net power flow to or from the main utility network is controlled, improving the apparent behaviour of local microsources. Secondly the MicroGrid may island from the main network, continuing to supply power to loads during network disturbances. Both these concepts should 'add value'. Figure 1-1 presents the structure of a typical MicroGrid.
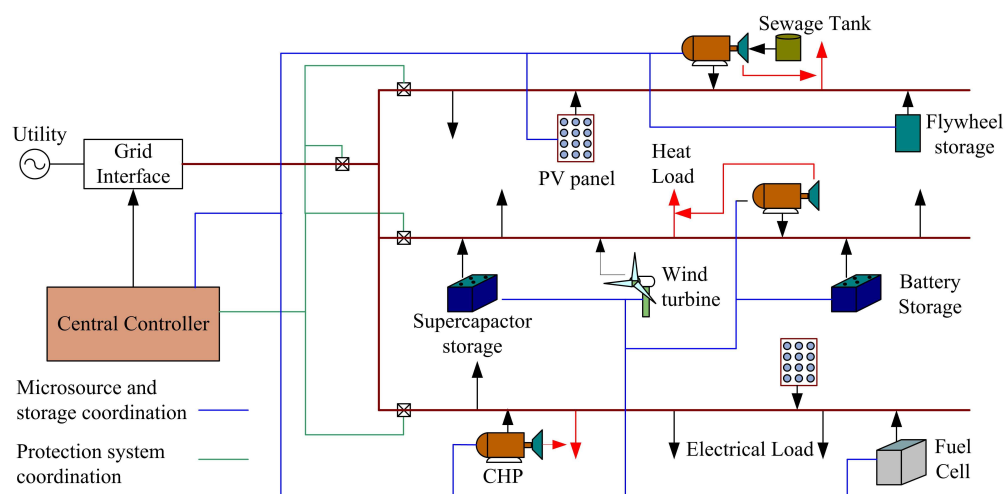
Figure 1-1: Structure of a typical MicroGrid

The advantages provided by a MicroGrid thus include use of renewable energy sources, use of waste heat during generation, and improved reliability of power. However the implementation of MicroGrid introduces many challenges such as lack of proven technology and cost.

1.2 AIM OF THE THESIS

Even though the capacity of most of the microsources connected to real-world MicroGrids are several tens of kilowatts or more, microsources with smaller capacity also could be integrated. The microsource interface would be single-phase when the capacity is less than several kilowatts. Such units would be typical for home-based micro-generation.

In June 2008 the review of micro-generation for the UK government's Department of Business Enterprise and Regulator Reform (DBERR) concluded that the UK has the potential for: "micro-generation technologies [to] contribute up to 30 MtCO2 reduction by 2030, equivalent to a 5% cut in total 2006 UK CO2 emissions." [1]. This is "equivalent to removing the emissions from all Heavy Goods Vehicles and Buses from UK roads" [1]. The majority of this micro-generation would be variable frequency generators or DC sources. Thus power electronic converters are required to integrate them to the utility network. Furthermore considering the power rating of these generators and their location, these micro-generation units would be connected as single-phase ac Voltage Source Inverters (VSIs).

Therefore there is a very high probability of a necessity for integration of single-phase microsources into a MicroGrid. However, there is very little research being undertaken in the development of single-phase microsource interfaces for MicroGrids.

Further some form of energy storage unit is essential for the stable operation of a MicroGrid. In most of the real-world MicroGrids the energy storage unit is a separate unit. The capacity of this storage unit needs to be progressively increased as more and more microsources are connected to the MicroGrid. When an energy storage unit is a separate unit, upgrading it would be expensive and this cost would have to be carried by the utility (or Microgrid operator) who in turn would pass it on to all generators and/or customers. If the microsource is integrated with the storage unit itself, a separate energy storage unit would not be necessary. This would make the upgrade process easier and financially beneficial. This is an underlying concept of the CERTS MicroGrid [2].

This thesis describes the development of a single-phase power electronic based microsource interface with embedded energy storage for a MicroGrid. Figure 1-2 presents the proposed microsource interface. The integrated energy storage provides two benefits. Dynamics incorporated with microsource could be decoupled from the utility network by providing power from the storage unit. As a result, high power quality could be realised. Also integrated storage would remove the necessity of separate energy storage units in a MicroGrid. MicroGrid management would be easier and cheaper.
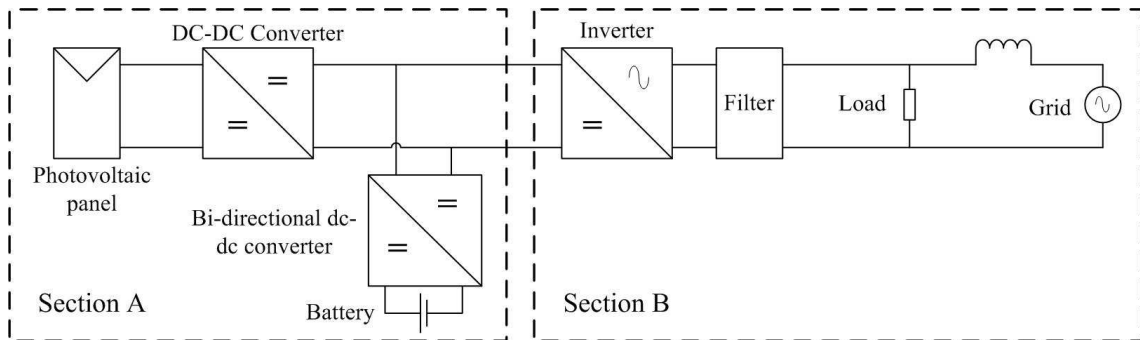
Figure 1-2: Proposed microsource interface

The controllers associated with the power electronic converters in this thesis are designed based on dynamic stiffness properties and command tracking properties allowing straight-forward controllers to be used to achieve superior performance. Thus power electronic converters will withstand disturbances better. Further simple controllers can be used in the system thus the implementation can be realised easily. The goal is to achieve a grid connection technique that is simple but allows microsources to be integrated smoothly into the network.

1.3 OVERVIEW OF THE THESIS

The thesis consists of ten chapters. Initial chapters review the literature to obtain the state of art of individual components required for the proposed microsource interface. Later chapters present the design, implementation and results of the proposed system. Finally the conclusions are presented in last chapter.

Chapter 2 includes a review of MicroGrids. The definition and structure of a typical MicroGrid are presented. The benefits, features and issues of MicroGrids are discussed. The state of real-world MicroGrids across the globe is summarised. Finally microsource control techniques are discussed.

Photovotlaics is selected as the microsource to verify the proposed system and a review of photovoltaic panel modelling is included in **Chapter 3**. The basics of photovoltaic panels are introduced briefly. Widely used electrical models of photovoltaic cells are presented. A method to extract parameters in the electrical model from manufacturer datasheets is presented. A review of maximum power point tracking methods and grid

connected photovoltaic system configurations are also discussed briefly at the end of the chapter.

Three power electronic converters are used in the proposed model: a unidirectional dc-dc converter, a bi-directional dc-dc converter and a single-phase inverter. The principles of operation of the selected converter topologies are presented in **Chapter 4**. State feedback block diagrams of the converters are derived.

Chapter 5 presents the development of a simulation model and a hardware emulator of a photovoltaic panel. A well-behaved simulation model of a photovoltaic panel with known limitations is developed in EMTDC/PSCAD software. A simple and inexpensive photovoltaic panel emulator is designed and implemented which is used for the experimental validation of the proposed system.

Three converters are designed, simulated, developed and implemented. The open loop simulation and experimental results of the converters are presented in **Chapter 6**.

The controller of the unidirectional dc-dc converter connected to the photovoltaic panel ensures the photovoltaic panel is operating at the maximum power point. The input voltage to the single-phase inverter, which is represented as dc-link voltage, is kept constant by the controller of the bi-directional dc-dc converter. **Chapter 7** presents the design and implementation of closed loop controllers for dc-dc converters. Furthermore the behaviour of the dc-dc converters and their controllers when operated together under different conditions are analysed. Simulation and experimental results are presented for all case studies.

The single-phase inverter uses two control loops. An inner loop controls the output current of the inverter and the outer loop synchronises the inverter with the MicroGrid. **Chapter 8** presents the simulation and experimental results of the inverter current controller and grid connection when inverter is supplied by a laboratory power supply.

The behaviour of the proposed Microsource interface is presented in **Chapter 9**. All three converters are connected together. The proposed microsource interface behaviour under load variations and microsource output power variations is discussed. A starting

method for the system is also presented. Simulation results of the proposed microsource interface are presented.

Chapter 10 contains a detailed discussion of the system behaviour and conclusions are made comparing the simulation and experimental results with the theoretical analysis. Finally potential future work is discussed.

A Literature review on lead acid batteries is included in Appendix A. Appendix B contains the MATLAB code used to find the ideality factor of the photovoltaic panel. Screen captures of the simulation model of the photovoltaic panel is also included. Appendix C contains the detailed open loop test results of the simulation model and the prototypes of the power electronic converters. Controllers for the dc-dc converters are developed individually before testing dc-dc converter operation together. Simulation and experimental results obtained when developing controllers individually are presented in Appendix D.

The key challenge within this research is the systems integration – taking a series of relatively well-known systems but getting them to work together using appropriate control and suitable analysis to ensure that good overall performance is achieved.

CHAPTER 2

LITERATURE REVIEW ON MICROGRIDS

2.1 INTRODUCTION

In this chapter the definition of a MicroGrid and the structure of a typical MicroGrid are explained. Further a brief introduction to the components of a MicroGrid is given. The benefits, features and issues are also discussed. Prototypes and real world MicroGrids around the world are summarised. Further some of the proposed microsource control techniques are presented.

2.2 DEFINITION OF A MICROGRID

The definition and typical composition of a MicroGrid are both not standardised and still evolving. According to R.H. Lasseter "The MicroGrid concept assumes a cluster of loads and microsources operating as a single controllable system that provides both power and heat to its local area" [3]. Alternatively a "Microgrid is a small grid in which distributed generators and electric loads are placed together and controlled efficiently in an integrated manner" according to Toshihisa Funabashi and Ryuichi Yokoyama [4]. Chris Marnay and Ryan Firestone define it as "A controller grouping of energy (including electricity) sources and sinks that is connected to the macrogrid but can function independent of it" [5]. Alternatively "A MicroGrid (MG) can be defined as an LV network (e.g., a small urban area, a shopping center, or and industrial park) plus its loads and several small modular generation systems connected to it, providing both power and heat to local loads [combined heat and power (CHP)]" according to J.A.Lopes, C.L. Moreira and A.G. Madureira [6].

A MicroGrid is thus a power network which is comparatively lower in total generation capacity compared with a conventional power system. It typically consists of loads, several small generation units and possibly storage and some degree of intelligent

control. Critically, a MicroGrid is designed to be capable of operating either in grid-connected mode or islanded mode. In addition to electrical loads, heat loads are also often connected to this small power system. A MicroGrid typically only consists of part of a distribution network, and the distance between loads and generation units are close.

2.3 COMPONENTS OF A TYPICAL MICROGRID

The structure of a typical MicroGrid is presented in Figure 2-1. The main components of a MicroGrid are generation units, loads, energy storage, the actual distribution network, the protection system, the control system and the grid interface unit.
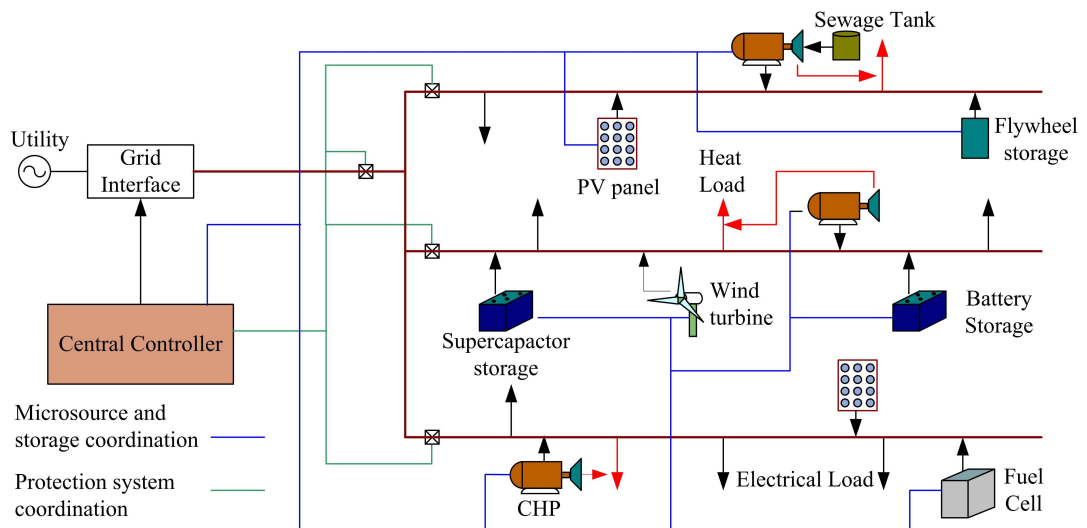
Figure 2-1: Structure of a typical MicroGrid

2.3.1 Generation units

The capacity of generation units connected to a MicroGrid is relatively small in capacity compared with conventional power stations, and thus they are known as microsources [3]. In most cases, the upper limit of the capacity of a microsource is below 500kW. Renewable energy sources such as photovoltaics (PV), wind turbines and hydro power plants are proposed and used in various pilot MicroGrids [3,6-9]. The output power of renewable sources is subjected to environmental conditions, and this introduces availability constraints which creates problems in matching demand to supply when the MicroGrid is not connected to the remaining utility network. Dispatchable microsources which have been proposed for use in a MicroGrid are fuel cells, microturbines and diesel generators [10-12]. These are 'dispatchable' because in theory the fuel source is

readily available without significant supply constraints. However if heat generated from the microsources such as microturbines and fossil fuel generators are used for heating purposes (i.e. in Combined Heat and Power (CHP) plants) then a constraint is imposed requiring reasonable economic use of such heat.

2.3.2 Loads

In some prototypes the loads are classified as critical and non-critical loads [3]. Continuous power to the critical loads is ensured. Generation-demand mismatch during islanded operation mode may results in disconnection of non-critical loads. Authors in [3,13] have proposed to use separate feeders for critical and non-critical loads which makes the disconnection process easier. Loads connected to a typical MicroGrid are not only electrical loads but also heating loads. As mentioned above, heating loads are linked to the MicroGrid both by direct heat loads and by CHP plants. The potential interactions between loads and generation source are thus relatively complex.

2.3.3 Distribution network

The typical MicroGrids implemented so far are operated at low voltages. Operating votlage of CERTS, Tokyo Gas, CESI and Kythnos MicroGrid are 480V, 200V, 400V and 400V respectively [3,14-18]. High voltage transmission lines are avoided due to the fact that the distance between loads and microsources is typically short. The MicroGrid is interfaced to the utility network at a higher voltage, in the UK this may be through a 11kV/400V distribution transformer or similar.

2.3.4 Energy storage

Most microsources are connected to the MicroGrid through power electronic converters and the generators connected are small in capacity. Thus the inertia of generation units and the energy stored in generation elements are either very small or zero [3,6,19-20]. Significantly the energy stored in the boiler of a conventional central generating station, is eliminated in most microsources. As a result MicroGrid would be able to withstand substantial power fluctuation transients only with difficulty. Stability during such transients is realised through the energy storage units connected to a MicroGrid. Most of the real-world MicroGrids have used batteries as the storage method while some have

used flywheels and ultracapacitors along with the batteries [11-13,17-18,21-22]. Authors in [23] have studied the possibility of operation of a MicroGrid with a flywheel as the only storage method. Energy storage could be either centralised where the total storage capacity is in a single unit or distributed where the total capacity is distributed across the MicroGrid in several units. With distributed energy storage, incremental expansion of storage is less costly.

2.3.5 Controllers in a MicroGrid

The control system of a MicroGrid typically consists of two layers. At the top layer, the controller is responsible for the stable operation of the MicroGrid and coordinates with the individual units such as microsources, loads and protection system. Local controllers are then used at the lower layer in microsources, loads and the grid connection interface. Optical fibre lines, power line communication and local area networks can be used as the communication methods to realise the control requirements of the MicroGrid.

2.3.6 Protection system

The protection system should ensure the stable operation of both MicroGrid and utility network. Any fault within the MicroGrid should be dealt with internally and the utility should not view the fault [2-3,10,20,24-26]. In case of a fault in the utility network, the MicroGrid may be disconnected from the utility to ensure stable operation within the MicroGrid [2-3,10,20,24-26].

2.3.7 Grid interface

The grid interface is responsible for the connection and disconnection of the MicroGrid from the utility network. The utility voltage and MicroGrid voltage need to be synchronised before connecting the MicroGrid to the utility and this synchronisation process is realised by the grid interface unit. The MicroGrid also has to isolate from the utility in case of a fault or any maintenance requirement. The grid interface thus has to coordinate with the protection system to identify those faults which result in disconnection of MicroGrid from the utility, and must be capable of instigating a forced disconnection to achieve maintenance. Mechanical and semiconductor based switches have been proposed for use as the grid interface switch [27]. A mechanical switch

would be relatively cheaper however the operation delay is higher. Asynchronous interconnection switch based on back to back converter is also proposed [28].

2.4 BENEFITS, FEATURES AND ISSUES RELATED TO A TYPICAL MICROGRID

In principal, a MicroGrid structure is beneficial for both utilities and customers. In grid connected mode, power could be imported from the utility to meet the demand if required. At least the critical loads could be powered from local microsources when operating autonomously. Thus from consumer point of view, reliability of power supply is improved in a MicroGrid [16,20]. Further, excess generation could be exported to the utility network. There is however a cost premium for this.

It has also been argued that energy resources can be more effectively used in a MicroGrid. As mentioned earlier, CHP based microsources provide heat to the heat loads which improve the system energy efficiency significantly [16,29-30]. Another benefit of the MicroGrid system is the possibility of connecting smaller generation plants especially renewable energy sources into the network. In the Aichi MicroGrid, methane gas required for the operation of a fuel cell and microturbine is generated from garbage, wood and plastic waste [11]. The key issue is that by allowing local voltage management as a by-product of the control needed to create a MicroGrid, more and more 'difficult' microgeneration can be connected than would otherwise be possible. Overall resource management is thus potentially 'better' with a MicroGrid. A comparatively smaller distance between loads and generation units also reduces the transmission losses.

The 'plug-and-play' functionality of a MicroGrid should in principal enable it to be possible to connect any microsource at any point of the MicroGrid without altering the system configuration significantly [3,16,19]. Thus generation units could be added in or removed quickly with minimal maintenance or installation costs.

Another key feature of a typical MicroGrid is the peer-to-peer control technique. With this technique, microsources are controlled from terminal quantities which remove the necessity of communication between microsources [16]. However, there are MicroGrid

prototypes based on master-slave based control techniques with advanced communication methods.

Even though the MicroGrid can be an attractive solution, the implementation of real MicroGrids is hampered by the technological barriers and cost involved. The energy storage units are essential for the stable operation of a MicroGrid. The capital required for the energy storage and associated power electronic converters is significant, and this is not required in a conventional system. In pilot MicroGrids, energy storage is often realised from new methods such as flywheels and ultracapacitors. These methods are not only expensive but also introduce health and safety issues. Advanced technology is used to forecast generation, predict demand and communicate between the central controller and microsources. Whether it is possible to realise these features in real MicroGrids at a reasonable price is questionable at the moment. However much of this is dependent on the low cost and ready availability of alternatives such as fossil fuel for large conventional power generation stations.

2.5 MICROGRID STRUCTURES ACROSS THE WORLD

Research projects and pilot MicroGrids have been implemented around the world to test different configurations and to identify practical difficulties. America, Japan and Europe are leading in the evaluation and development of MicroGrids. The following sub-sections present details of major real world and laboratory based MicroGrids.

2.5.1 MicroGrids in America

Figure 2-2(a) presents the structure of the CERTS MicroGrid in America [3,31]. In this structure separate feeders are used for critical and non-critical loads. Non-critical loads are disconnected when generation is less than demand and the MicroGrid is operating isolated from the utility network. The central controller is known as the energy manager which coordinates the protection units, microsources and utility interconnection of the MicroGrid. The total generation capacity of the MicroGrid is 120 kW, all CHP plant [11]. The generation units are connected to the MicroGrid through power electronic converters. All the microsources adopt the droop-line control method which controls the active and reactive power based on the frequency and voltage respectively. A battery

bank is connected to the dc-link of the inverter of each microsource. The MicroGrid is interfaced to the utilities at 13.2kV [31].

The Mad River Park MicroGrid was developed by Northern Power Systems in 2004 and its structure is presented in Figure 2-2(b) [31-33]. The microsources used in this system are wind turbines, microturbines, photovoltaic system and fossil fuel based generators. The total generation is more than 350kW [31-32]. This MicroGrid provides electricity for residential houses, industries and companies.

A hydro power plant based MicroGrid is presented in Figure 2-2(c). This system does not contain any external energy storage units [34-35]. Figure 2-2(d) presents the MicroGrid proposed by General Electric Company [31,36-37]. The microsources connected to the grid are wind turbines, photovoltaic, fuel cells and a conventional generator in this case. Heat generated from the conventional generator is used in a water treatment plant and residential heating loads. The central manager communicates with all the units within the MicroGrid which optimises the system performance in terms of cost, environmental benefits, etc. Dispatch control and pricing are also another responsibility of the central controller. Each element connected to the MicroGrid has a local controller which controls the frequency and voltage of the system.
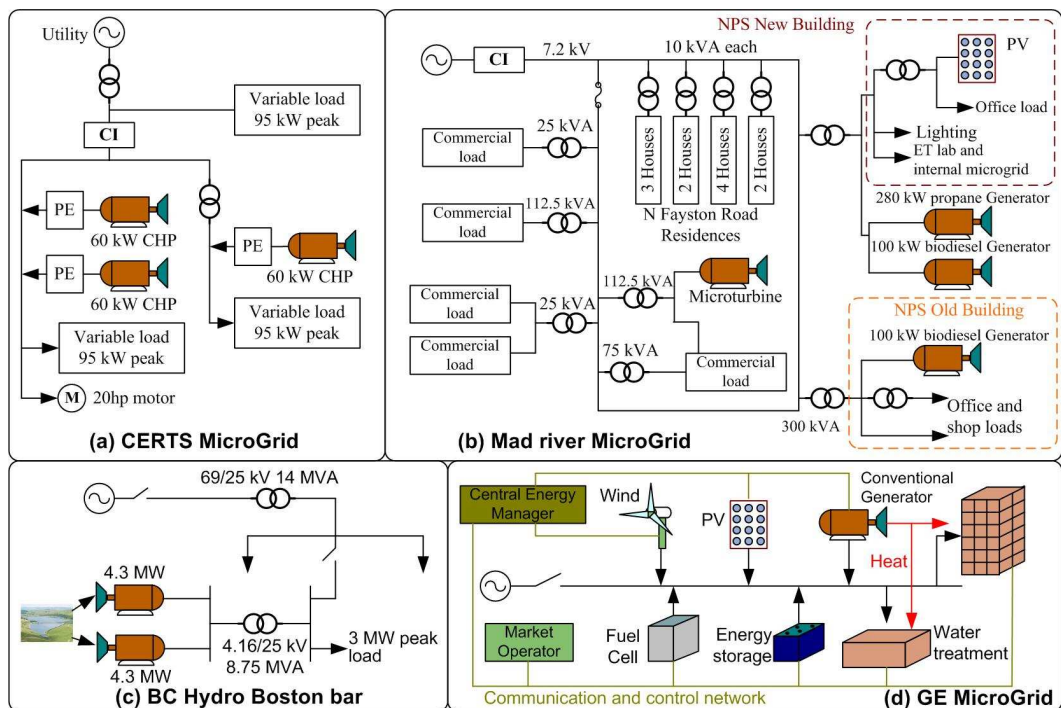
Figure 2-2: Structures of some selected MicroGrids in America

2.5.2 MicroGrids in Japan

The Aichi project, the Kyoto project and the Hachinohe project (in Aomori) are some MicroGrid demonstration projects in Japan [4,12-13,31,38]. Japanese MicroGrids are mainly focused on generation costs, environmental affects, diversified generation methods and rural electrification [21]. Figure 2-3 shows the system block diagram of four MicroGrids implemented in Japan [10-14,22,31].

All MicroGrids use some form of renewable energy source; either photovoltaics or wind. The capacity of photovoltaics in the Aichi MicroGrid is 330 kW [4,11]. Further, in the Aichi MicroGrid, different types of fuel cells are used as microsources. Gas engines are used in all four MicroGrids. In the Hachinohe MicroGrid, gas released from a digestion chamber is used to operate the gas engines [12]. Heat generated from the gas engine and a separate steam boiler are used to operate the digestion chamber which minimises the energy wastage. In order to operate the microturbine and Molten Carbonate fuel cell (MCFC), methane is produced using garbage, wood and plastic waste in the Aichi MicroGrid [11]. Heat generated from the gas engines is used for water heating and cooling water and air-conditioning in the Shimizu, Tokyo gas and Aichi MicroGrids [11,13,22].

Batteries are used as the primary energy storage method in all four MicroGrids in Figure 2-3, however in Shimizu's MicroGrid ultracapacitors are also used [4,13,22,31]. In the Tokyo Gas MicroGrid, loads are classified as shed-able, sensitive and very sensitive [13,18]. Separate feeders are allocated for each type of load. Energy to the very sensitive loads is guaranteed through the connection of two battery banks.

The controller of these MicroGrids monitors the weather forecast to estimate the daily generation and is updated in shorter periods as well [4,12]. Load demand is also estimated. Optimisation methods are used in the operation planning by considering all the cost involved and environmental effects. In the islanded mode of operation, battery storage is used to control the frequency during the transients as the inertia of the generators is small.
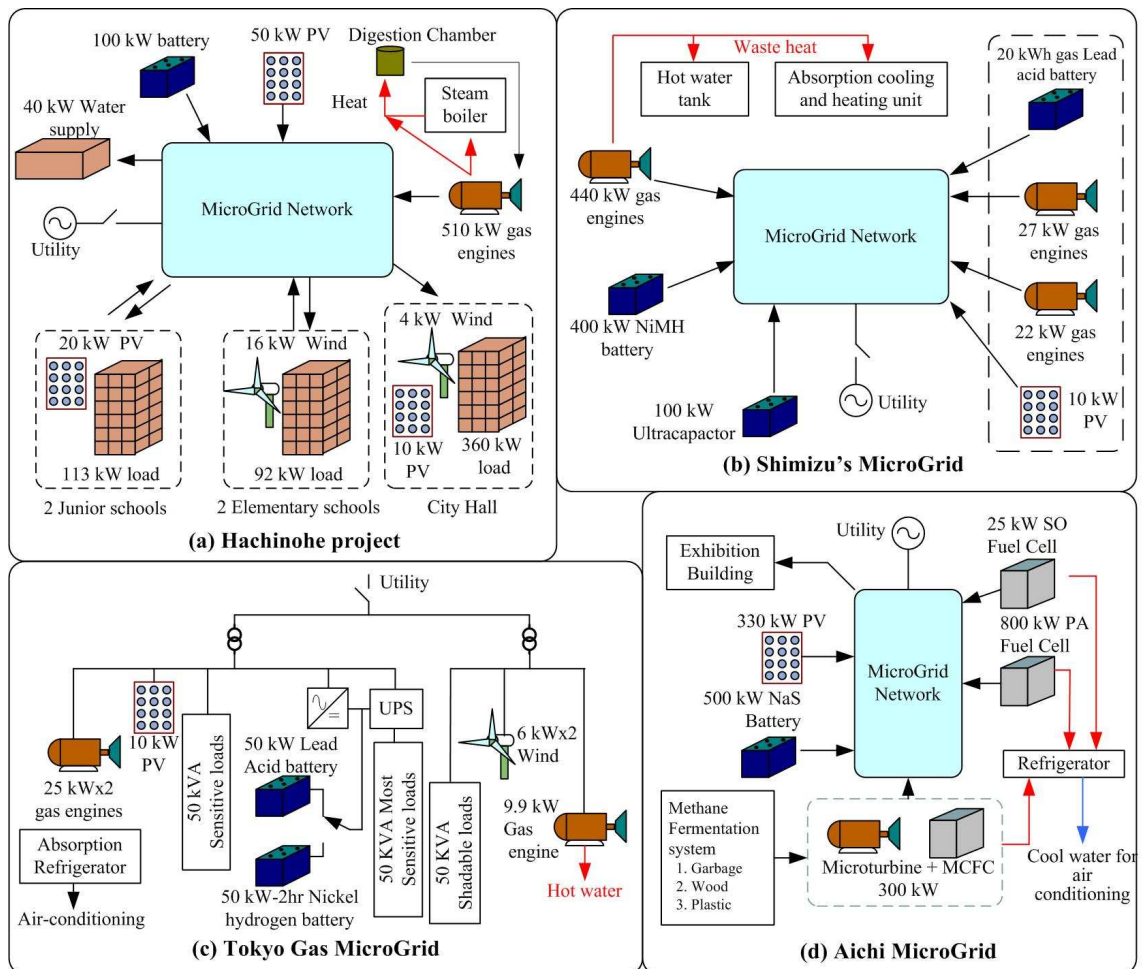
Figure 2-3: Structures of some selected MicroGrids in Japan

2.5.3 MicroGrids in Europe

The European Union has funded several projects across Europe, linked to the research studies carried out under various 'Framework' research portfolios. Pilot MicroGrid systems have been implemented in Greece, Spain, Portugal, Denmark and Germany [7,10,23,39-41]. Figure 2-4 presents some of these.

In Milan, the CESI MicroGrid has been implemented, Figure 2-4(a) [17,31]. Renewable energy sources such as photovoltaics and wind are used, while fuel cells and microturbines are also connected. Energy storage is comprised of batteries and a fast acting flywheel. Controllable loads are connected to the system. The CESI MicroGrid voltage rating is 400V and it is connected to the utility at 23kV through a transformer. An optical fibre network, Wi-Fi and power-line communication are used as the communication methods.

The structure of the MicroGrid test set-up developed in Germany, which is known as Demotec, is presented in Figure 2-4(b) [7,31,42]. Diesel generator sets and renewable energy sources in the form of wind and photovoltaics are connected to the MicroGrid. The energy storage method is batteries. Battery, wind turbine and load simulators are also connected to the system. Most of the microsources and loads are monitored and controlled through a Local Area Network.

The MicroGrid developed by the Labein Research Institute in Spain has total generation capacity of 170kW and is based on PV arrays, wind turbines, microturbines and diesel generators [31,43]. As shown in Figure 2-4(c), three types of energy storage namely batteries, ultracapacitors and a flywheel are used in this MicroGrid. The MicroGrid is connected to the utility via 1250kVA transformers [31].

The Kythnos MicroGrid in Greece is a 'real-world' MicroGrid project. This system is powered by a 11 kW photovoltaic panel and a 5kVA diesel generator. Battery energy storage is used and storage is centralised. Figure 2-4(d) shows the structure of the Kythnos MicroGrid [15,31,44,45]. The operating voltage of the system is 400V.
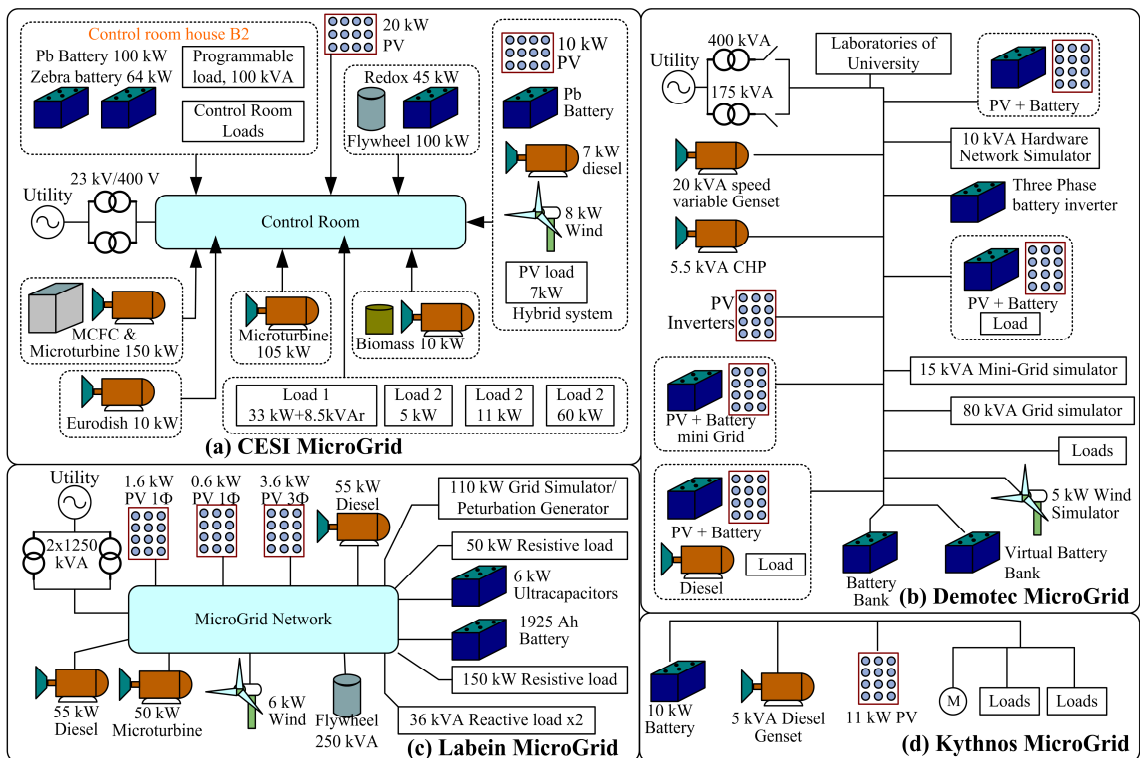
Figure 2-4: Structures of some selected MicroGrids in Europe

2.6 MICROSOURCE INTEGRATION TO A MICROGRID

2.6.1 Microsource interface

Many microsources (such as fuel cells and PV panels) produce dc voltage. Further, the remainder (wind turbines and microturbines) mostly operate at variable frequency. Thus power electronic converters (PEC) must be used to interconnect the microsources to the MicroGrid. Figure 2-5 presents the generalised block diagram for a microsource [3,6,46-48]. Power electronic converter topologies in Section-A depend on the microsource. When considering a photovoltaic array, the power electronic converter may be a dc-dc converter while it could be a controllable rectifier for a wind turbine. However Section-B is common to every microsource. Typically microsources are connected to a MicroGrid using an inverter through a filter which removes the high frequency harmonics. Inverters could be either single-phase or three-phase. However when considering the real-world and research based MicroGrids, three-phase microsource interfaces have so far been favoured.
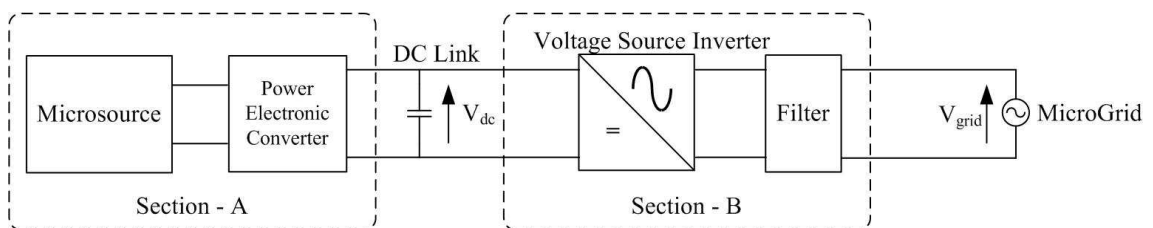
Figure 2-5: Simplified model of a microsource interface

A microsource interface embedded with energy storage is also proposed [46]. This method would probably help to realise the plug-and-play functionality of a MicroGrid as the total capacity of energy storage would also increase with additional microsources. The CERTS MicroGrid in America adopts this method in Figure 2-6(a) [46]. Alternatively energy storage could be integrated to the dc-link through a power electronic converter, typically a bi-directional converter, in the method shown in Figure 2-6(b). This method would be expensive (in terms of hardware) when compared with method in Figure 2-6(a). However, integration of energy storage through a power electronic converter increases the degree of controllability in the system, allowing longer term savings in terms of overall system efficiency.

(a) Direct connection of energy storage

(b) Connection of energy storage through a power electronic converter
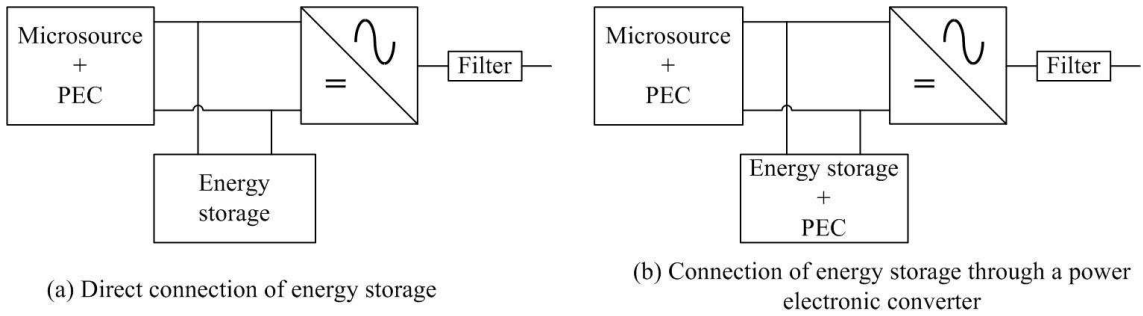
Figure 2-6: Microsource interface with energy storage unit integrated

2.6.2 Microsource controller

Inverters connected to the MicroGrid could be controlled in two methods. In the first method, the microsources could operate at a particular set of active and reactive power references [6,49]. This method arguably works reasonably well in the grid connected mode since any short fall or excess could be taken from the utility network. However, local voltage control is not achieved. More importantly, the MicroGrid would not operate to control frequency and voltage when the system is isolated from the utility due to generation-demand mismatch. Thus a set reference active and reactive power method is not suitable for use as the only control method of microsources in a MicroGrid.

Droop line control is the presently favoured control technique, which can be used to control each inverter independently [3,6,49-50]. In this method, frequency and voltage are given as references. The frequency is varied with output active power and the voltage is varied with reactive power. This method works well with both utility connected and islanded operating modes. Figure 2-7 presents a typical droop line characteristic used for the inverters' control.

(a) Active power – frequency control

(b) Reactive power – voltage control
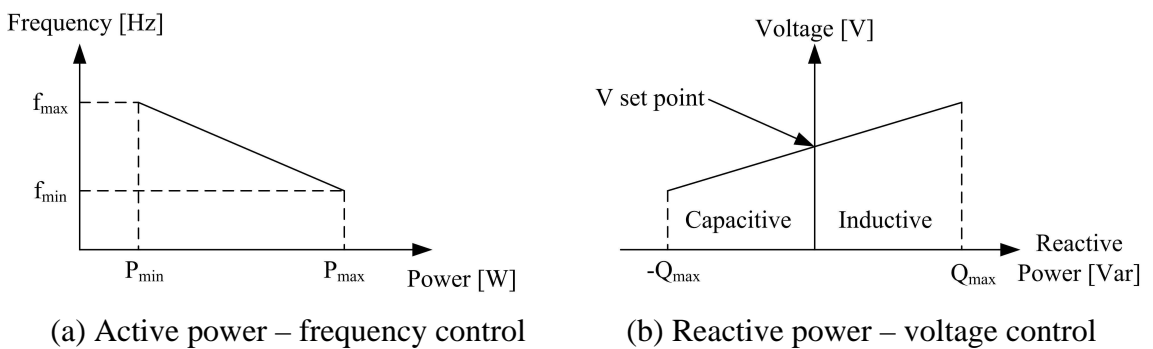
Figure 2-7: Active and reactive power control of a microsource

Figure 2-8 shows the use of above mentioned two control techniques to control microsources in a MicroGrid with a master-slave control technique [6,49]. A microsource with a droop line controller acts as the 'master' while microsources operating with power references act as the slaves. As shown in Figure 2-8 one or more microsources may operate with droop line control technique. In [7,23], a flywheel energy storage unit is used as the Master controller which controls the frequency and voltage of the MicroGrid. A communication network within the MicroGrid is essential to realise the master-slave control technique since it is required to provide the active and reactive power references.

(a) Single-master operation   (b) Multi-master operation
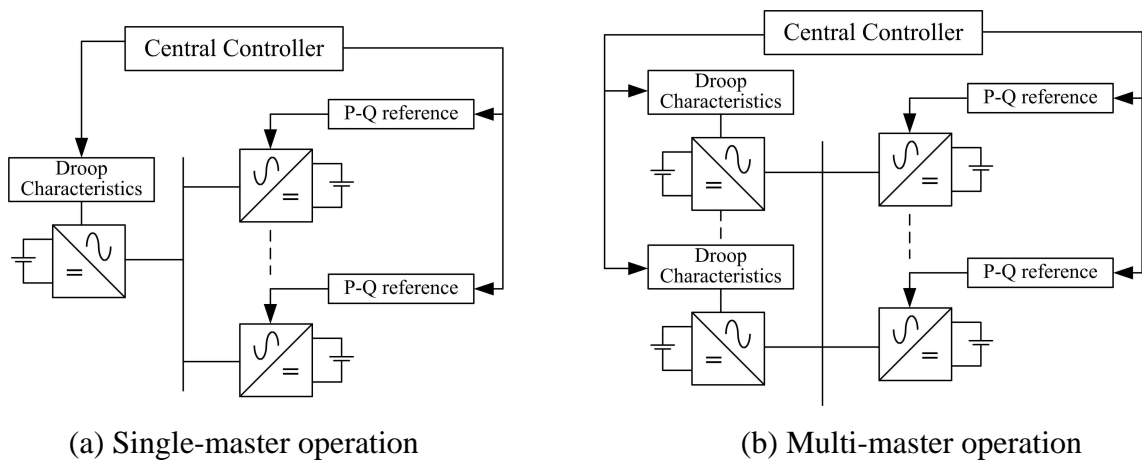
Figure 2-8: Microsource control with Master-slave control

The CERTS MicroGrid uses a droop-line control technique for all the microsources thus no separate communication technique is required between the microsources [3,30]. In order to make sure the microsources can respond fast enough, i.e. in order to decouple the slow response of the actual energy sources from the inverter response, energy storage units are connected to the dc-link of the inverter. Plug-and-play functionality is easily achievable with this method. Figure 2-9 presents the controller of the microsources used in CERTS MicroGrid [3,30].

2.7 SUMMARY

A typical MicroGrid structure has been presented and details of the components of a MicroGrid have been discussed. A MicroGrid is potentially attractive from the customer and utility point of view due to improved power quality and potentially an increase in the potential for the integration of low-carbon generation. Further, there is increased

scope to use resources effectively to improve the overall system efficiency. Implementation of real world MicroGrids is held back by the need of advanced technology and costs involved. Pilot projects have been implemented across the globe to evaluate different microsources, energy storage methods and control techniques. A droop-line control technique is mainly used to control the microsources. Microsources in some pilot MicroGrids have adopted both droop-line control and power reference control.
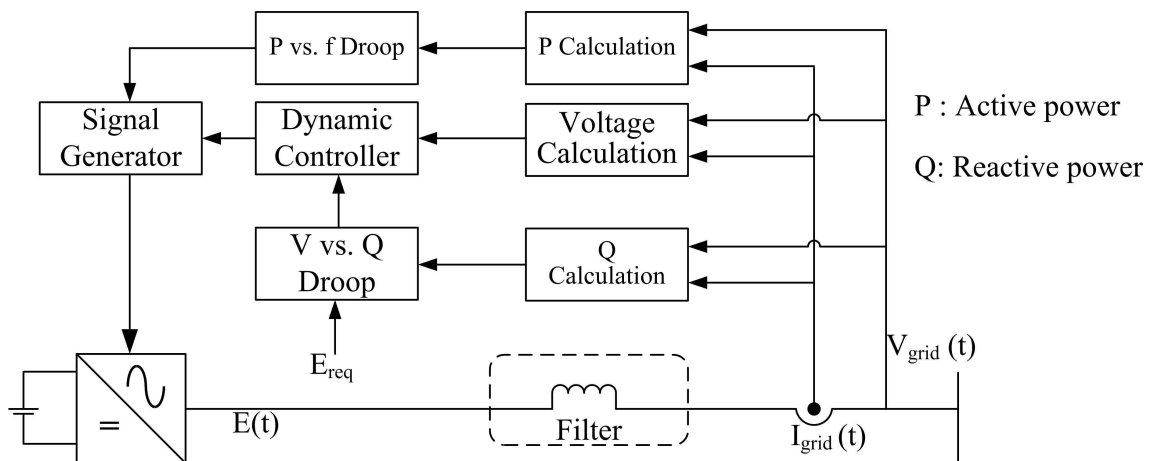
Figure 2-9: Microsource controller used in CERTS MicroGrid without master-slave control

A single-phase microsource interface is proposed in this thesis. Since microsources with energy storage units enable them to realise plug-and-play functionality, energy storage is integrated to the microsource interface. Further in the proposed microsource interface would integrate the energy storage through a power electronic converter.

CHAPTER 3

REVIEW OF PHOTOVOLTAIC PANEL MODELLING

3.1 INTRODUCTION

This chapter presents a detailed review of photovoltaic (PV) panel modelling which includes the basic physics, modelling and governing equations of a photovoltaic panel. Maximum power point tracking methods are also discussed and different photovoltaic systems are reviewed.

Photovoltaics is a renewable energy source with huge prospects. According to the Solar Generation IV 2007 report, the total electricity demand in Europe could be realised if photovoltaic panels are placed on 0.71% of the area of Europe [51]. Reduction of manufacturing costs as well as government grants, incentives and legislation are driving the photovoltaic market [52-53]. The cumulative capacity of photovoltaics around the globe reached 9162 MW peak at the end of 2006 [54]. The benefits of photovoltaic systems include a reduction of green house gas emission at the point of use, rural electrification and employment opportunities [51,54-55]. For decades, cost competiveness was the major factor which overshadowed these benefits. However at present most off-grid photovoltaic systems are cost competitive with the alternatives [51]. The price margin between distributed grid connected photovoltaic electricity and conventional electricity generation are reducing fast [51].

3.2 BASICS OF PHOTOVOLTAICS

A photovoltaic cell converts sunlight into electricity and each generates a few watts of electricity [51]. A photovoltaic panel or module is a collection of cells and typically cells are connected in series to increases the output voltage and the output power [51]. The output power of a panel varies from 40 W to 300 W [56,57]. In most applications, a number of panels are connected in series or parallel to increase the output power. Such a

system is known as a photovoltaic array [56-57]. The performance of a photovoltaic panel is presented under special conditions known as Standard Test Conditions (STC). A panel is said to be tested under standard test conditions, if a) the panel is tested at 25°C, b) the incident irradiance is 1000W/m^2 and c) the air mass (AM) is 1.5 [58]. Air Mass represents the angle between the sun light and zenith as shown in Figure 3-1 [59]. On the earth's surface the air mass varies but it is typically around 1.5 thus this value is selected for the standard test conditions [59].
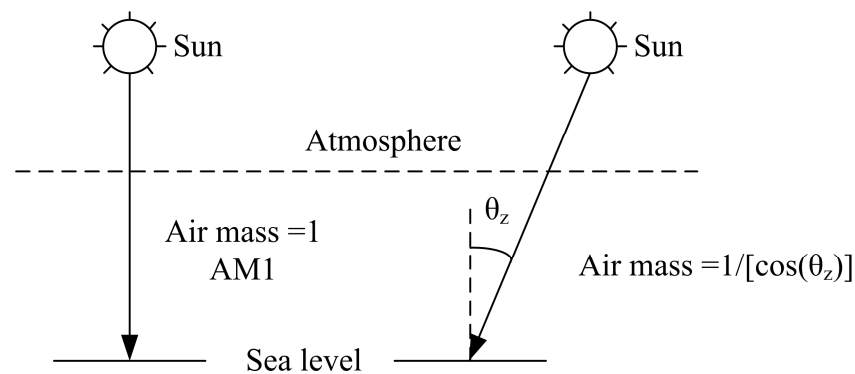
Figure 3-1: Air mass depending on the sunlight path

3.2.1 Types of cell

The major cell types are crystalline silicon and thin film cells. At present the highest market share belongs to crystalline silicon cells which are manufactured from very small slices of silicon wafers [51]. These are further divided into two categories: mono and multi crystalline cells. The efficiency of a crystalline cell is around 14-17% while the efficiency of a module is around 12-15% [51,55]. The commercial thin film cells are based on amorphous silicon (a-Si), copper indium diselenide (CIS, CIGS) and cadmium telluride (CdTe) [51]. These photosensitive materials are coated on a low cost material such as glass or plastic. Efficiency of thin film based cells varies between 6 and 11% [51,56-57]. Thin film panels are cheaper than crystalline silicon panels. However to generate the same output power, more thin film panels are required when compared with crystalline silicon panels.

The efficiency of concentrator cells is about 30% [51]. This cell type generates more electrical power from fewer cells. A disadvantage of this method is that electricity is only produced from direct sunlight. Heat generation and expensive concentrating optics

are challenges for concentrator cells. Bifacial photovoltaic cells generate electricity from the back side as well as the front side of the cell [60]. Typically the front side is oriented directly to the light and the back side generates power from the light reflected from surroundings. Efficiency of a bifacial cell is increased by 5 to 20% comparing with conventional cell, without increasing the cost significantly [60-61].

3.2.2 Characteristic curves of a photovoltaic cell

The characteristic curves of a photovoltaic cell are shown in Figure 3-2 [62-64]. The voltage-current relationship is highly non-linear and as a result the voltage-power relationship is also non-linear. The maximum power is delivered at a particular voltage and the corresponding operating point on the characteristic curve is known as the Maximum Power Point (MPP).
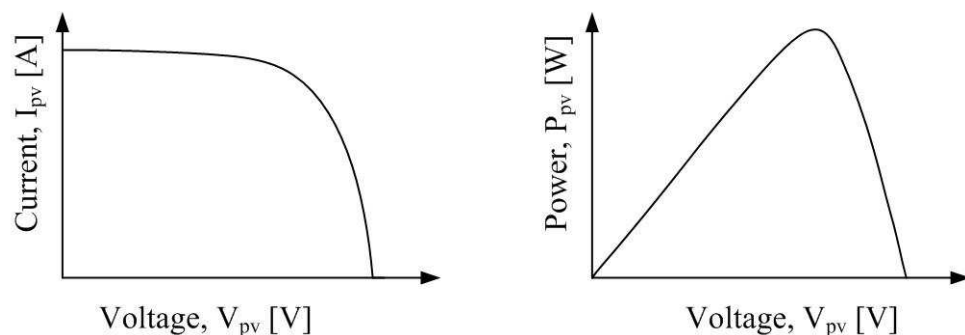
Figure 3-2: Characteristic curves of a photovoltaic cell

3.2.3 Electrical models of a photovoltaic cell

Figure 3-3 presents some of the electrical models of a photovoltaic cell which could be found in literature [58,62,65-77]. The simplest model contains a current source and a diode which is connected anti-parallel to the current source. The model presented in Figure 3-3(b) contains a resistor in series at the output which represents the electrical losses of the cell [58,65-68]. A more complex model contains a resistor in parallel to the current source and a resistor in series with the output as shown in Figure 3-3(c) [58,62,66,69-75]. The model shown in Figure 3-3(d) consists of two anti-parallel diodes [58]. Characteristics of each diode are slightly different, thus better curve fitting could be achieved with this model.
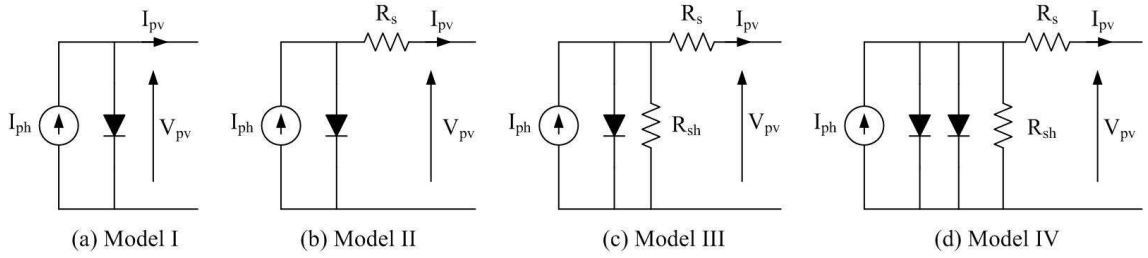
Figure 3-3: Electrical models of a photovoltaic cell

Equation 3-1 gives the characteristic equation of a photovoltaic cell for the model shown in Figure 3-3 (b) where I_{pv}, I_{ph}, I_{sat}, V_{pv}, R_s and V_t represent the PV panel current, the photocurrent, the diode saturation current, the PV panel voltage, the series resistance and the thermal voltage respectively [58,66-68]. The thermal voltage is related to the ideality factor (A), the Boltzmann constant (k), the temperature (T) and the charge of an electron (q) as given in Equation 3-2 [58,66]. The ideality factor is a constant which depends on the material of the cell and typically it varies between one and two [58-59].

$$I_{pv} = I_{ph} - I_{sat}\left[\exp\left(\frac{V_{pv} + I_{pv}R_s}{V_t}\right) - 1\right]$$
<div align="right">Equation 3-1</div>

$$V_t = \frac{AkT}{q}$$
<div align="right">Equation 3-2</div>

Most of the parameters required for models presented in Figure 3-3(a) and Figure 3-3(b) can be found from datasheets while remaining parameters can found by performing mathematical calculations. As the complexity of the model increases, extracting parameters for the model becomes difficult.

3.2.4 Dependent parameters of a photovoltaic panel

The output power of a photovoltaic panel depends on the environmental temperature and the irradiance incident on the panel [62-64,78]. Figure 3-4 highlights the affect of temperature and irradiance on the characteristic curves of SM110-24P photovoltaic panel [79]. Irradiance affects the short circuit current as well as the open circuit voltage. However, the effect on the short circuit current is more significant than that on the open circuit voltage. The output power at the maximum power point increases as the

irradiance increases. Temperature affects the open circuit voltage of the panel and the open circuit voltage decreases due to an increase in temperature.

Equation 3-3 and Equation 3-4 present the relationship of temperature and irradiance with the short circuit current and the open circuit voltage [58,80] . G_a, I_{sc}, T, V_{oc}, ΔI_{sc} and ΔV_{oc} represent the irradiance, the short circuit current, the temperature, the open circuit voltage, the temperature coefficient of the short circuit current and the temperature coefficient of the open circuit voltage respectively. Constants with an additional letter 's' correspond to the values at standard test conditions.

(a) Irradiance   (b) Temperature
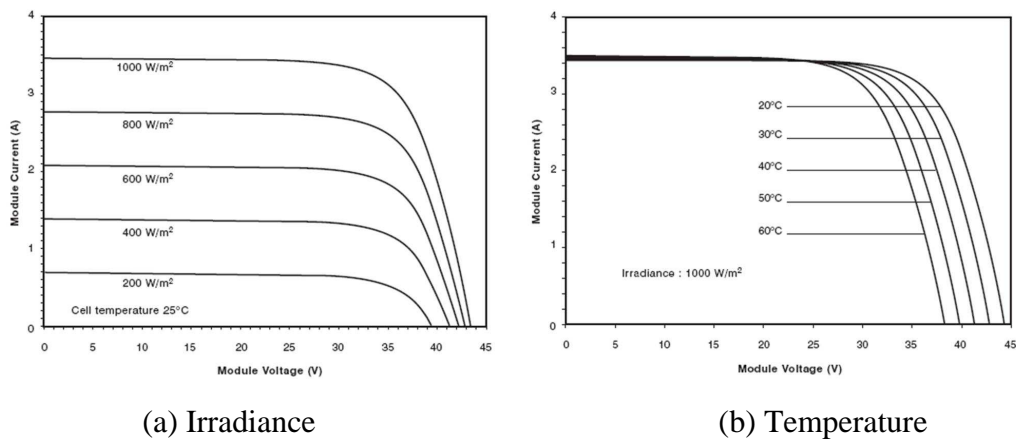
Figure 3-4: Effect of environmental conditions on characteristic curves

$$I_{sc} = \frac{G_a}{G_{as}}\left[I_{scs} + \Delta I_{sc}\left(T - T_s\right)\right]$$
<div align="right">Equation 3-3</div>

$$V_{oc} = V_{ocs} + \Delta V_{oc}\left(T - T_s\right) + V_t \ln\left(\frac{I_{sc}}{I_{scs}}\right)$$
<div align="right">Equation 3-4</div>

3.2.5 Extracting values for unknown parameters of the characteristic equation from the datasheet of a panel

The photocurrent, the diode saturation current, the series resistance and the ideality factor in the characteristic equation (Equation 3-1) are unknown quantities. They vary from panel to panel and according to environmental conditions. These parameters could be extracted by considering the open circuit condition, the short circuit condition and properties at maximum power point.

The panel under short circuit and open circuit conditions are presented in Figure 3-5 [58]. Under the short circuit condition, current flowing through the diode could be neglected when compared with the output current. Therefore the photocurrent could be approximated to the short circuit current as given in Equation 3-5. The output current of the panel is zero during the open circuit condition, thus the photocurrent flows through the diode. Therefore the diode saturation current could be obtained as given in Equation 3-6 which is derived from Equation 3-1.

$$I_{ph} \approx I_{sc}$$

Equation 3-5

$$I_{sat} = \frac{I_{ph}}{\exp\left(\dfrac{V_{oc}}{V_t}\right) - 1}$$

Equation 3-6

(a) Short circuit   (b) Open circuit
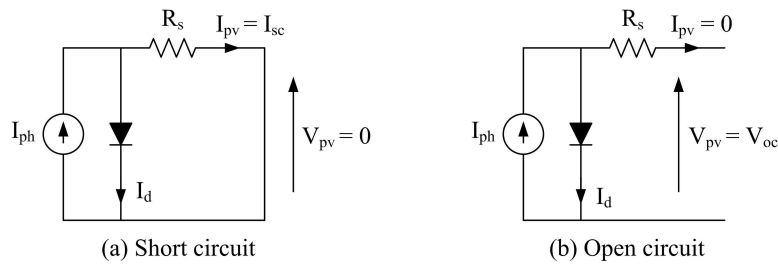
Figure 3-5: Photovoltaic cell under open circuit and short circuit test condition

The ideality factor and the series resistance of a cell could be calculated considering the properties at MPP [58,72]. At the MPP, the derivative of the power with respect to voltage should be equal to zero as in Equation 3-7. Equation 3-8 could be obtained from Equation 3-7. PV panel voltage and current at MPP is represented by V_{MPP} and I_{MPP}.

$$\left.\frac{dP_{pv}}{dV_{pv}}\right|_{MPP} = \left.\frac{d(V_{pv}I_{pv})}{dV_{pv}}\right|_{MPP} = V_{MPP}\left.\frac{dI_{pv}}{dV_{pv}}\right|_{MPP} + I_{MPP} = 0$$

Equation 3-7

$$\left.\frac{dI_{pv}}{dV_{pv}}\right|_{MPP} + \frac{I_{MPP}}{V_{MPP}} = 0$$

Equation 3-8

The series resistance of the panel could be written in terms of maximum power point quantities as in Equation 3-9 which is derived from the characteristic equation. Equation

3-10 gives the derivative of current with respect to voltage at the maximum power point.

$$R_s = \frac{V_t}{I_{MPP}} \ln \left\{ \left(1 - \frac{I_{MPP}}{I_{ph}} \right) \left[\exp \left(\frac{V_{oc}}{V_t} \right) - 1 \right] \right\} - \frac{V_{MPP}}{I_{MPP}}$$

Equation 3-9

$$\left. \frac{dI_{pv}}{dV_{pv}} \right|_{MPP} = - \frac{I_{sat} \exp \left(\dfrac{V_{MPP} + I_{MPP} R_s}{V_t} \right)}{V_t \left[1 + \dfrac{R_s I_{sat}}{V_t} \exp \left(\dfrac{V_{MPP} + I_{MPP} R_s}{V_t} \right) \right]}$$

Equation 3-10

Figure 3-6 presents the algorithm which could be used to obtain the ideality factor and the series resistance based on Equation 3-8, Equation 3-9 and Equation 3-10 [58,72]. In this method, the ideality factor is swept across a range of values and the correct ideality factor corresponds to the minimum of $\left| \left(\dfrac{dI_{pv}}{dV_{pv}} \right) \right|_{@\ MPP} + \dfrac{I_{MPP}}{V_{MPP}} \right|$. Then the series resistance is calculated based on Equation 3-9.
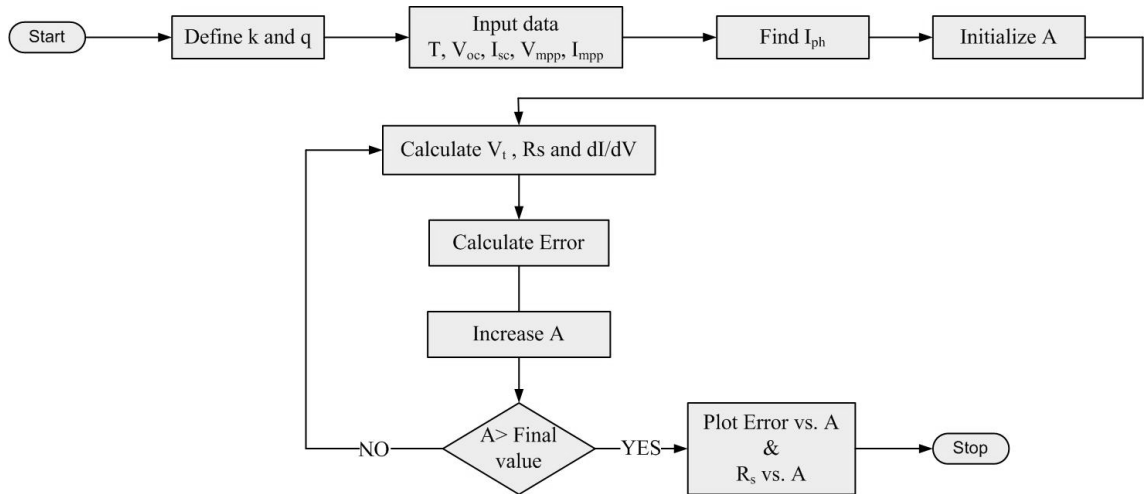
Figure 3-6: Algorithm used to find ideality factor and the series resistance

3.3 MAXIMUM POWER POINT TRACKING METHODS

The characteristic curve of a photovoltaic panel shows that the panel should operate at the MPP to extract the maximum available power. Maximum Power Point Tracker

(MPPT) is the device used to track the maximum power point. Different MPPT methods can be found in the literature with distinct features as well as inherent disadvantages.

Almost all the PV panels are connected through power electronic converters. A converter is associated with a controller and the controller makes sure that the converter is operating at a given reference voltage. In a photovoltaic system, MPPT generates the reference voltage applied to the controller of the converter.

The simplest MPPT generates a predefined voltage reference which is the voltage at maximum power point corresponding to a particular environmental condition [81]. This would be the cheapest MPPT as it neither requires any sensor nor needs to perform complex calculations. The voltage reference does not change dynamically. Thus the panel would not operate at the MPP all the time, which is the main drawback of this method.

The voltage at the maximum power point is approximately equal to 70-80% of the open circuit voltage while the current at the maximum power point is approximately equal to 90% of the short circuit current [81-86]. There are MPPTs built based on these two factors and such a MPPT requires either a current sensor or a voltage sensor. A voltage sensor is typically cheaper than a current sensor therefore a MPPT based on the open circuit voltage would be cheaper than a MPPT based on the short circuit current. The open circuit voltage and the short circuit current are measured periodically in respective MPPT methods. This process disrupts the continuous power flow. Authors in [82] have indicated that some systems proposed a pilot cell to measure the open circuit voltage for MPPTs based on open circuit voltage. Both of these MPPTs are better than the previous method as dynamic tracking is available.

The perturbation and observation method based trackers vary the reference voltage signal applied to the controller of the converter by a small fraction and observe the variation in the output power of the panel [62,81-83,87-89]. Depending on the output power change, the controller perturbs the reference voltage signal positively or negatively at the next sampling time as given in Table 3-1 [82].

Table 3-1: Voltage reference step change in the perturbation and observation method

Perturbation	Output power	Next perturbation
Positive	Increase	Positive
Positive	Decrease	Negative
Negative	Increase	Negative
Negative	Decrease	Positive

The incremental conductance method is another widely used MPPT technique. In this method the incremental conductance is compared with the conductance value at each sampling instance and then perturbs the reference voltage applied to the controller [81-84,87,90-91]. Figure 3-7 presents the algorithm used in incremental conductance method [82].
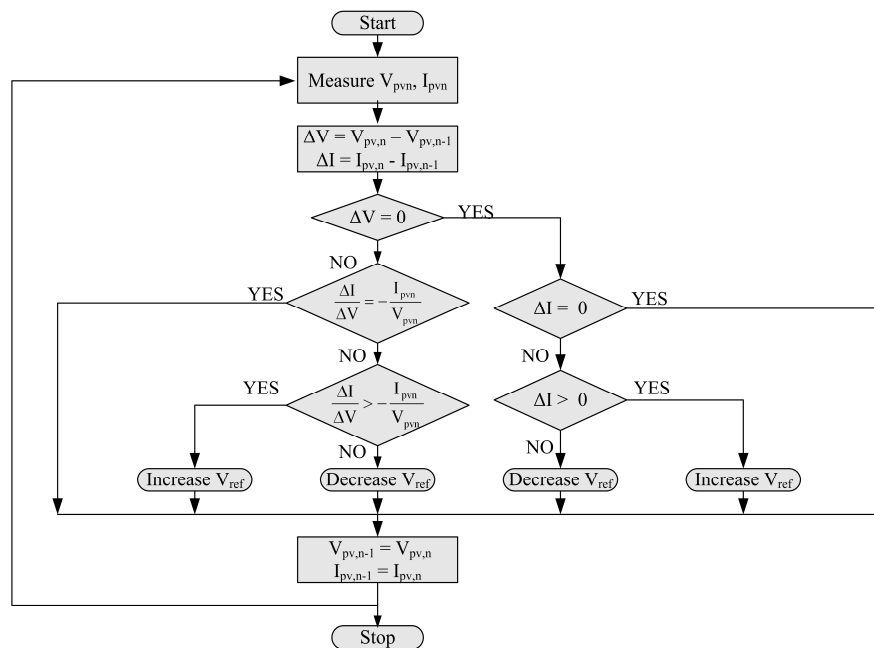
Figure 3-7: Algorithm used in MPPTs based on Incremental conductance method

The accuracy of these two MPPT methods ('perturbation and observation' and Incremental conductance) increases as step change in the reference decreases. However the speed of convergence of the MPPTs decreases at the same time. Furthermore these MPPT methods need to perform complex calculations, thus the controller requires relatively sophisticated (and costly) hardware. A current sensor and a voltage sensor are required for these MPPTs. Thus the cost of the MPPT is increased further.

A current sweep technique which sweeps the characteristic curve periodically and calculates the maximum power point from measured current is also discussed in [82]. MPPTs are also designed based on the fuzzy logic control technique and neural networks [82,92].

The selection of a suitable MPPT method depends on several factors. MPPTs used in space applications are focused on generating as much as electricity as possible and implementation cost is neglected [82]. However in most other cases, implementation cost is very important. Electrical vehicles powered by photovoltaic panels tend to use MPPTs with a higher rate of convergence [82].

3.4 POWER ELECTRONIC INTERFACES FOR GRID CONNECTED PHOTOVOLTAIC SYSTEMS

Photovoltaic panels generate a dc output voltage, thus connection to the utility network is not straight-forward. Power electronic converters are used to convert dc voltage into ac voltage. Different power electronic interface methods are available in the literature. However the suitability of a method depends on the application, the capacity of the system and available capital. The power electronic interface may contain either a single converter or multiple converters.

The systems presented in Figure 3-8 contain a single power electronic converter. A PV panel is connected to an inverter in the system shown in Figure 3-8(a) and the isolation transformer is used for step up purposes [70,89,93]. A number of panels are connected in series and parallel in the systems presented in Figure 3-8(b) and Figure 3-8(c) [70,90,93-100]. Such systems could be connected to the grid with or without a transformer. The controller of a PV system with a single converter is responsible for grid connection and maximum power point tracking [89-90,94]. Implementation and maintenance cost is less due to less number of components in the system.
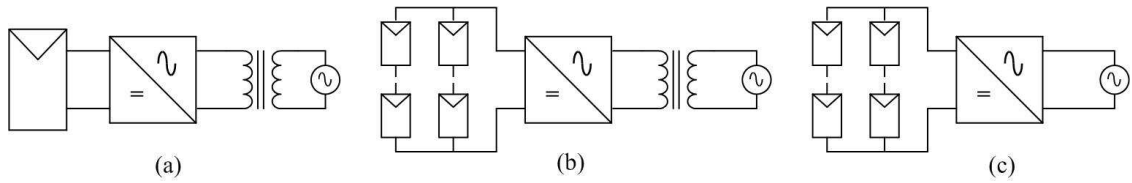
Figure 3-8: Grid connected PV systems with a single power electronic converter

Multiple power electronic converter based PV systems are shown in Figure 3-9 and these interfaces comprise dc-dc converters and inverters [86,93-94,96-97,100-105]. These systems could be integrated to the grid either with or without a transformer. Further panels could be connected in series or parallel. Typically the controller of the inverter is responsible for grid connection and power control [76,86,94,102,105]. A DC-DC converter connected to the panel steps up the voltage and the controller of the converter makes sure that the panel is operating at the MPP [76,86,94,102-103,105]. The system shown in Figure 3-9(e) has a dc-dc converter per panel. Each dc-dc converter may contain a separate controller and MPPT, therefore such a system ensures that each panel is operating at the maximum power point [97,103]. Energy loss due to partial shading of panels could be reduced by this arrangement [103]. These systems are complex and require higher capital costs.
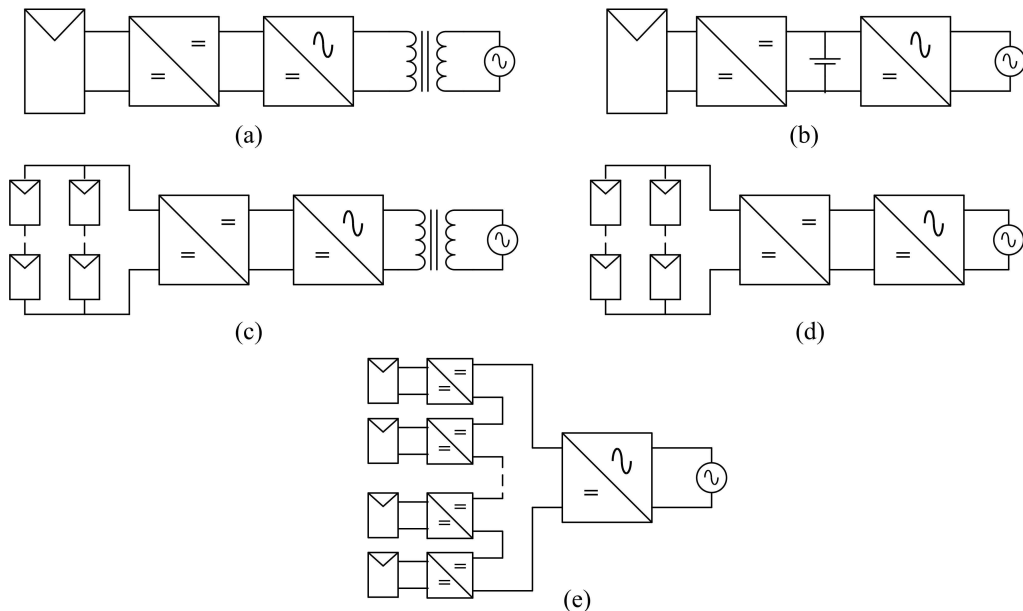
Figure 3-9: Grid connected PV systems with multiple power electronic converters

3.5 SUMMARY

As a renewable energy source photovoltaics has great prospects. However the output power of a photovoltaic cell depends on the irradiance and the temperature. The electrical model consisting of a series resistor is selected for the development of the simulation model as the required parameters could be extracted from the data available in the datasheet. With the aid of the equations relating irradiance and temperature to the parameters in the electrical model, output power of the simulation model could be varied appropriately.

The proposed microsource interface unit should be capable of integrating an energy storage unit. Thus a single stage power electronic interface is not suitable for this application. Therefore a two stage power electronic converter is selected. A dc-dc converter is connected to the output of the photovoltaic panel which steps-up the voltage. The associated controller would ensure the panel is operating at the maximum power point. The single-phase inverter would convert the dc voltage into ac voltage. The controller of the inverter is responsible for grid connection and output power control.

CHAPTER 4

REVIEW OF POWER ELECTRONIC CONVERTERS

4.1 INTRODUCTION

The block diagram of the proposed microsource interface is shown in Figure 4-1. The system consists of three power electronic converters namely a unidirectional dc-dc converter, a bi-directional dc-dc converter and a single-phase inverter. The principles of operation and modelling of these converters are explained in the chapter.
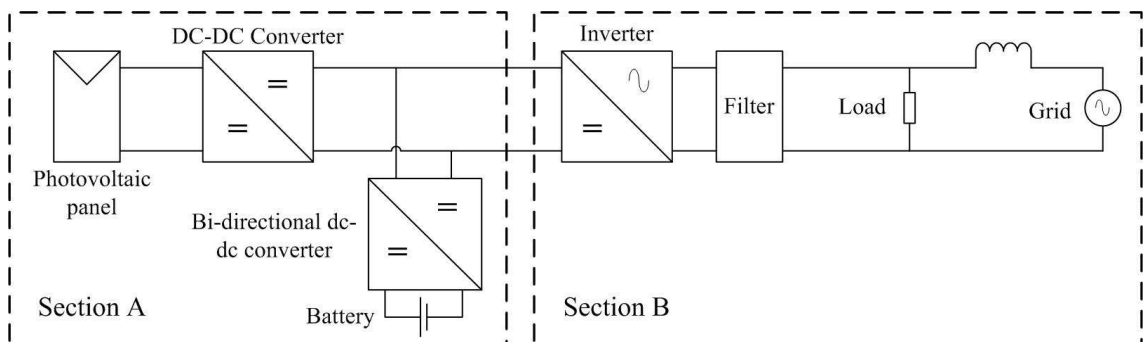
Figure 4-1: Proposed microsource interface

4.2 DC-DC CONVERTER

The dc-dc converter is connected to the photovoltaic panel and the converter steps up the output voltage of the photovoltaic panel. The controller associated with the converter ensures that the photovoltaic panel is operating at the maximum power point.

4.2.1 Principle of operation of the modified forward dc-dc converter

The schematic diagram of the modified forward dc-dc converter is presented in Figure 4-2 [106-107]. Fewer components results in reduced losses. The high frequency transformer provides the voltage step-up and isolation. Thus this topology was selected as the unidirectional dc-dc converter. The converter comprises two switches S_1 and S_2

which are operated simultaneously. Energy is transferred to the right hand side of the transformer when the switches are turned on. Energy is stored in the inductor and the current flowing through the inductor increases approximately linearly. Diode D_4 acts as a freewheeling path during the off-state of the switches. Energy stored in the inductor is released and the current flowing through the inductor linearly decreases. The output current of the converter is equal to the average current flowing through the inductor. Figure 4-3 shows voltages at different nodes and currents flowing through different paths of the converter. The diodes D_1 and D_2 provide a path for the magnetising current to flow during the off-state of the switches. Equation 4-1 presents the relationship between the input and the output voltage of the converter in the steady state where N and D are the turns-ratio of the transformer and the duty ratio respectively.

$$\frac{V_{dc}}{V_{in}} = ND \qquad\qquad\qquad\qquad \text{Equation 4-1}$$
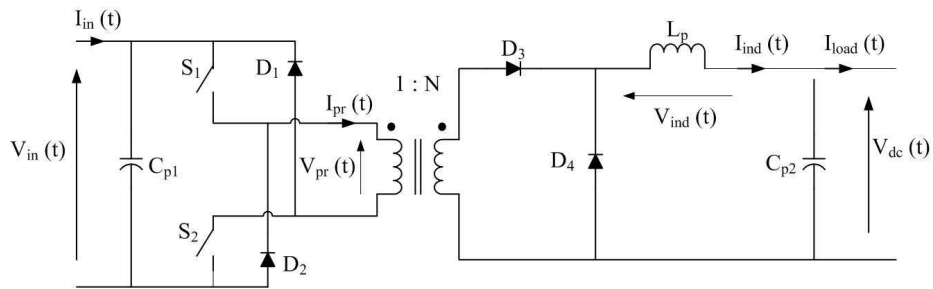
Figure 4-2: Schematic diagram of the modified forward dc-dc converter
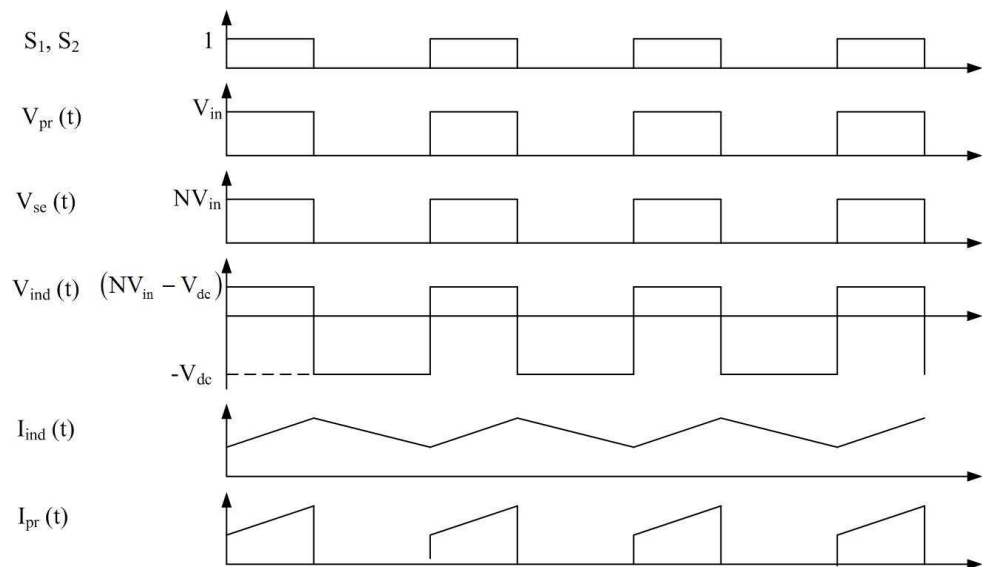
Figure 4-3: Principle of operation of the modified forward dc-dc converter

4.2.2 Modelling of modified forward dc-dc converter

An electrical model of the converter is required for the design of a controller. The converter has two equivalent circuits for the on-state and off-state of the switches. Thus an averaged model is obtained which would be non-linear. A linear system can be obtained by developing an operating point model. This section illustrates the averaged and operating point model of the converter [108].

Figure 4-4 presents equivalent circuits of the converter during on-state and off-state of the switches. R_p is the internal resistance of the inductor. Equation 4-2 to Equation 4-4 are obtained by applying Kirchhoff's voltage and current laws to on-state equivalent circuit. Similarly Equation 4-5 to Equation 4-7 are obtained by considering the off-state equivalent circuit.

(a) On state   (b) Off state
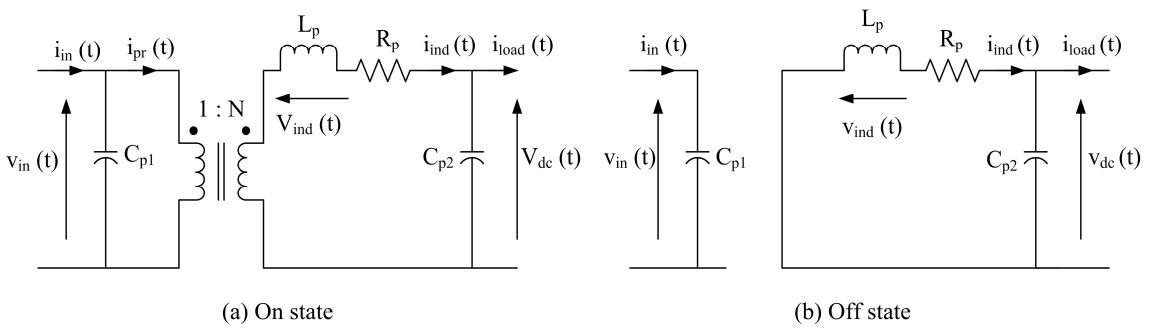
Figure 4-4: Equivalent circuit of the modified forward dc-dc converter

$$C_{p1} \frac{dv_{in}(t)}{dt} = i_{in}(t) - Ni_{ind}(t) \qquad \text{Equation 4-2}$$

$$L_p \frac{di_{ind}(t)}{dt} = Nv_{in}(t) - R_p i_{ind}(t) - v_{dc}(t) \qquad \text{Equation 4-3}$$

$$C_{p2} \frac{dv_{dc}(t)}{dt} = i_{ind}(t) - i_{load}(t) \qquad \text{Equation 4-4}$$

$$C_{p1} \frac{dv_{in}(t)}{dt} = i_{in}(t) \qquad \text{Equation 4-5}$$

$$L_p \frac{di_{ind}(t)}{dt} = -R_p i_{ind}(t) - v_{dc}(t) \qquad \text{Equation 4-6}$$

$$C_{p2} \frac{dv_{dc}(t)}{dt} = i_{ind}(t) - i_{load}(t) \qquad \text{Equation 4-7}$$

Equation 4-8 is obtained by averaging Equation 4-2 and Equation 4-5 over a switching cycle. Averaged values of the variables are represented in brackets. Similarly by averaging over a switching cycle for Equation 4-3 and Equation 4-6, Equation 4-9 is obtained. Finally Equation 4-10 is obtained by averaging Equation 4-4 and Equation 4-7 over a switching cycle. A state feedback block diagram of the converter based on the averaged state equations is shown in Figure 4-5. The averaged dc-dc converter model is non-linear.

$$C_{p1} \frac{d\langle v_{in}(t)\rangle}{dt} = \langle i_{in}(t)\rangle - Nd(t)\langle i_{ind}(t)\rangle \qquad \text{Equation 4-8}$$

$$L_p \frac{d\langle i_{ind}(t)\rangle}{dt} = Nd(t)\langle v_{in}(t)\rangle - R_p\langle i_{ind}(t)\rangle - \langle v_{dc}(t)\rangle \qquad \text{Equation 4-9}$$

$$C_{p2} \frac{d\langle v_{dc}(t)\rangle}{dt} = \langle i_{ind}(t)\rangle - \langle i_{load}(t)\rangle \qquad \text{Equation 4-10}$$
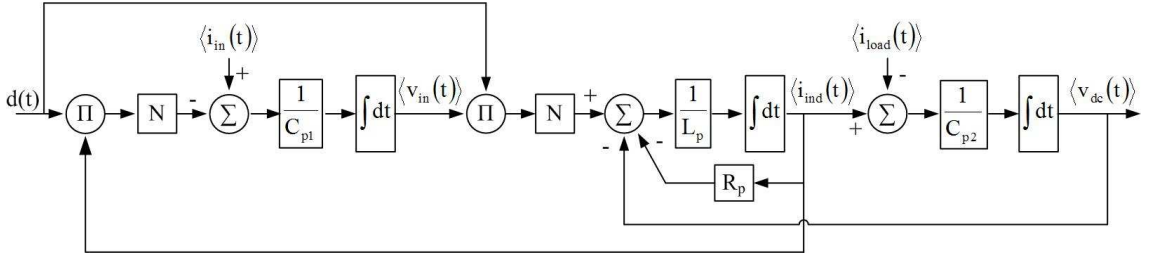
Figure 4-5: State feedback block diagram of the modified forward dc-dc converter based on averaged state equations

A Taylor series expansion was applied to the averaged state equations. By neglecting the higher order terms, above 1st order, a linear set of equations were derived as given in Equation 4-11 to Equation 4-13.

$$C_{p1} \frac{d\langle v_{in}(t)\rangle}{dt} = \langle i_{in}(t)\rangle - Nd(t)\langle i_{ind}(t)\rangle = f\{\langle i_{in}(t)\rangle, d(t), \langle i_{ind}(t)\rangle\}$$

$$\left.\frac{\partial f}{\partial\langle i_{in}(t)\rangle}\right|_{op} = 1 \qquad\qquad \left.\frac{\partial f}{\partial\langle d(t)\rangle}\right|_{op} = -NI_{indo} \qquad\qquad \left.\frac{\partial f}{\partial\langle i_{ind}(t)\rangle}\right|_{op} = -ND_o$$

$$C_{p1}\Delta\langle \overset{\circ}{v}_{in}(t)\rangle = \Delta\langle i_{in}(t)\rangle - NI_{indo}\Delta d(t) - ND_o\Delta\langle i_{ind}(t)\rangle \qquad \text{Equation 4-11}$$

$$L_p \frac{d\langle i_{ind}(t)\rangle}{dt} = Nd(t)\langle v_{in}(t)\rangle - R_p\langle i_{ind}(t)\rangle - \langle v_{dc}(t)\rangle = g\{d(t), \langle v_{in}(t)\rangle, \langle i_{ind}(t)\rangle, \langle v_{dc}(t)\rangle\}$$

$$\left.\frac{\partial f}{\partial\langle d(t)\rangle}\right|_{op} = NV_{in} \qquad \left.\frac{\partial f}{\partial\langle v_{in}(t)\rangle}\right|_{op} = ND_o \qquad \left.\frac{\partial f}{\partial\langle i_{ind}(t)\rangle}\right|_{op} = -R_p \qquad \left.\frac{\partial f}{\partial\langle v_{dc}(t)\rangle}\right|_{op} = -1$$

$$L_p\Delta\langle \overset{\circ}{i}_{ind}(t)\rangle = NV_{ino}\Delta d(t) + ND_o\Delta\langle v_{in}(t)\rangle - R_p\Delta\langle i_{ind}(t)\rangle - \Delta\langle v_{dc}(t)\rangle$$

<div align="right">Equation 4-12</div>

$$C_{p2}\frac{d\langle v_{dc}(t)\rangle}{dt} = \langle i_{ind}(t)\rangle - \langle i_{load}(t)\rangle = h\{\langle i_{ind}(t)\rangle, \langle i_{load}(t)\rangle\}$$

$$\left.\frac{\partial h}{\partial\langle i_{ind}(t)\rangle}\right|_{op} = 1 \qquad\qquad \left.\frac{\partial h}{\partial\langle i_{load}(t)\rangle}\right|_{op} = -1$$

$$C_{p2}\Delta\langle \overset{\circ}{v}_{in}(t)\rangle = \Delta\langle i_{ind}(t)\rangle - \Delta\langle i_{load}(t)\rangle \qquad\qquad \text{Equation 4-13}$$

By applying the Laplace transformation to the operating point time domain equations, Equation 4-14 to Equation 4-16 are obtained. The state feedback block diagram of the converter based on operating point equations is presented in Figure 4-6.

$$C_{p1}s\Delta V_{in}(s) = \Delta I_{in}(s) - NI_{indo}\Delta D(s) - ND_o\Delta I_{ind}(s) \qquad\qquad \text{Equation 4-14}$$

$$L_ps\Delta I_{ind}(s) = NV_{ino}\Delta D(s) + ND_o\Delta V_{in}(s) - R_p\Delta I_{ind}(s) - \Delta V_{dc}(s) \qquad \text{Equation 4-15}$$

$$C_{p2}s\Delta V_{dc}(s) = \Delta I_{ind}(s) - \Delta I_{load}(s) \qquad\qquad \text{Equation 4-16}$$
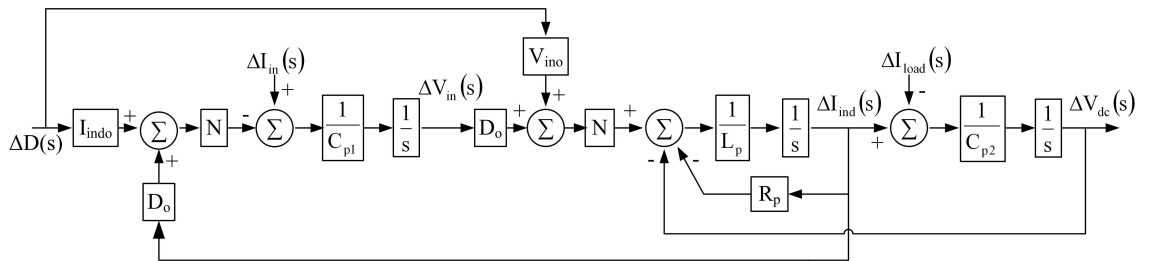
Figure 4-6: State feedback block diagram of the modified forward dc-dc converter based on the operating point state equations

4.3 BI-DIRECTIONAL DC-DC CONVERTER

Energy transfer in both directions in dc systems are realised through bi-directional dc-dc converter topologies. Bi-directional dc-dc converters consist of two operating modes and each operating mode contains set of switches.

4.3.1 Principle of operation

The schematic diagram of the bi-directional dc-dc converter selected for this system is presented in Figure 4-7 [109-110]. This topology was selected because a) it has fewer components on the low-voltage side, b) the full-bridge on the high voltage side removes the necessity of voltage dividing capacitors. $V_{dc}(t)$ corresponds to the high voltage end while $V_L(t)$ correspond to the low voltage end. Step-up and step-down are the two operating modes of the converter. The converter is comprised of six diodes and switches. The high frequency transformer provides the necessary voltage step-up or step-down depending on the operating mode. Figure 4-8 summarises the principle of operation of the converter in each mode.
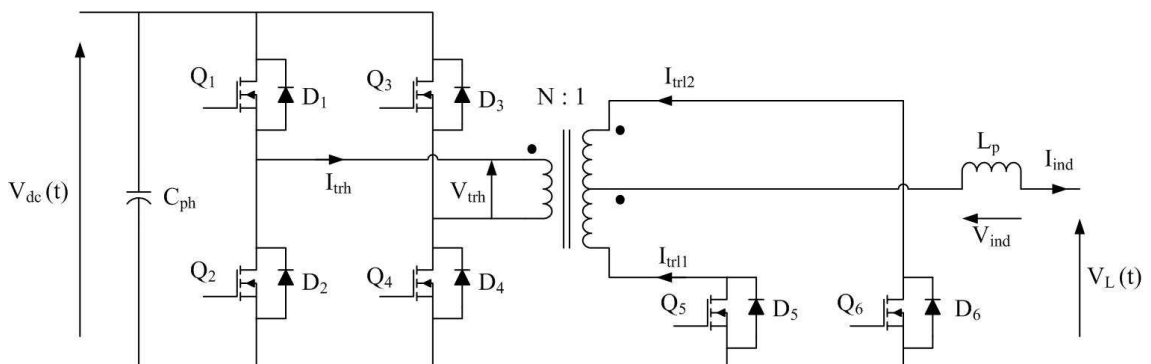
Figure 4-7: Schematic diagram of the bi-directional dc-dc converter

Energy is transferred to the low voltage side when the converter is operating in step-down mode. In this mode switches Q_5 and Q_6 are completely turned off. Switches Q_1 to Q_4 are operated by a PWM signal. As shown in Figure 4-8(a), the switches are operated in pairs: Q_1 and Q_4 being one pair, Q_2 and Q_3 the other. When a switch pair is turned on, energy is transferred to the low voltage side of the converter thus the current flowing through the secondary auxiliary inductor L_p is linearly increased. The direction of the current flowing through the high-voltage side winding of the transformer alternates while the current flowing through low-voltage side windings conducts alternatively.

During the off-state of the switches, current flowing through the inductor linearly decreases and diodes in the low-voltage side windings share the current flowing through the inductor.

In the step-up mode, energy is transferred to the high voltage side from the low voltage side. In this mode, switches Q_1 to Q_4 are completely turned off. The switches Q_5 and Q_6 are operated as shown in Figure 4-8(b). Energy is stored in the inductor when both Q_5 and Q_6 are turned on. Therefore the current flowing though the inductor increases and the low voltage side windings share the current flowing through the inductor. Energy is transferred to the high voltage side when either Q_5 or Q_6 is turned off. Current flowing though the high voltage side winding is transferred to the load through either diode pairs D_1 and D_4 or D_2 and D_3.

(a) Step-down mode　　　　　　　(b) Step-up mode
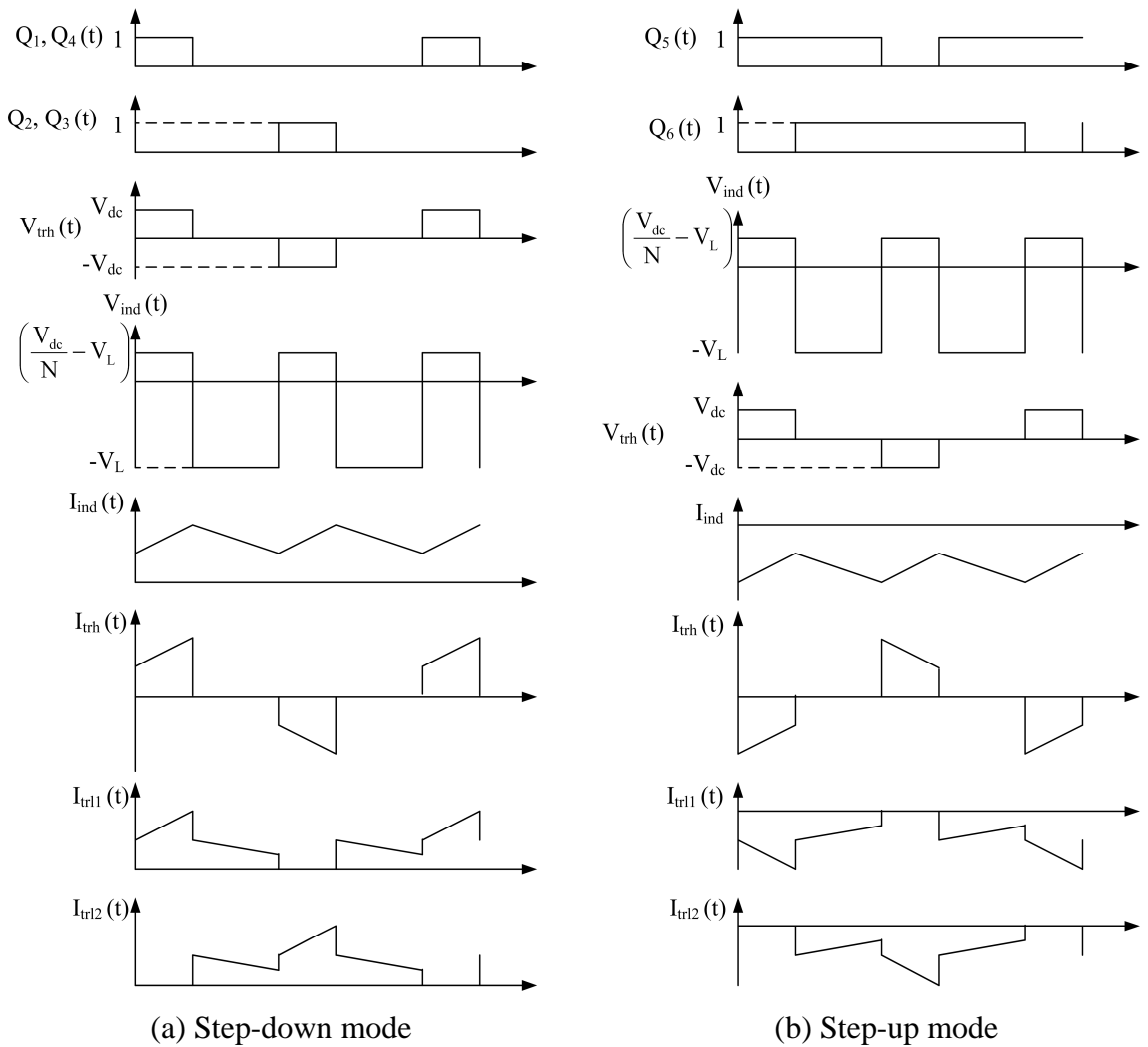
Figure 4-8: Principle of operation of the bi-directional dc-dc converter

Equation 4-17 and Equation 4-18 represent the relationship between the voltage at the high-voltage side and voltage at low-voltage side in steady state during the step-down and step-up modes respectively. The duty ratio should be less than 0.5 for the step-down mode while it should be greater than 0.5 for step-up mode. N and D are the turns-ratio of the transformer and the duty ratio respectively.

$$\frac{V_L}{V_{dc}} = \frac{2D}{N} \text{ Step-down mode} \qquad\qquad \text{Equation 4-17}$$

$$\frac{V_{dc}}{V_L} = \frac{N}{2(1-D)} \text{ Step-up mode} \qquad\qquad \text{Equation 4-18}$$

4.3.2 Modelling of bi-directional dc-dc converter

In the same way as for the dc-dc converter, an electrical model for the bi-directional dc-dc converter must be developed in order to design the controller. Electrical models should be developed for both operating modes. Again an averaged model was developed from two equivalent circuits and an operating point model was derived from the non-linear averaged model.

4.3.2.1 Step-up mode

Figure 4-9 shows the equivalent circuits of the converter during on and off states for the step-up mode. Equation 4-19 and Equation 4-20 are obtained by applying Kirchhoff's voltage and current laws to on-state equivalent circuit. Similarly Equation 4-21 and Equation 4-22 are obtained for the off-state.

(a) On-state   (b) Off-state
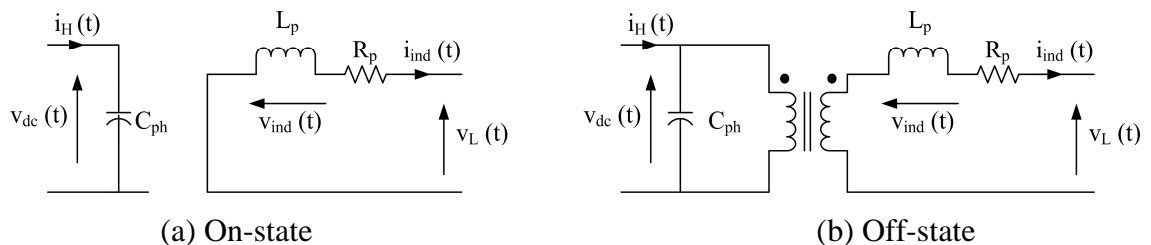
Figure 4-9: Equivalent circuits of the bi-directional dc-dc converter in step-up mode

$$L_p \frac{di_{ind}(t)}{dt} = -R_p i_{ind}(t) - v_L(t) \qquad\qquad \text{Equation 4-19}$$

$$C_{ph} \frac{dv_{dc}(t)}{dt} = i_H(t)$$ Equation 4-20

$$L_p \frac{di_{ind}(t)}{dt} = -R_p i_{ind}(t) - v_L(t) + \frac{v_{dc}(t)}{N}$$ Equation 4-21

$$C_{ph} \frac{dv_{dc}(t)}{dt} = -\frac{i_L(t)}{N} + i_H(t)$$ Equation 4-22

Equation 4-23 can be obtained by averaging Equation 4-19 and Equation 4-21 over a switching cycle. Similarly Equation 4-24 can be obtained by averaging Equation 4-20 and Equation 4-22. Based on Equation 4-23 and Equation 4-24, the averaged state feedback block diagram of the converter for the step-up mode is shown in Figure 4-10.

$$L_p \frac{d\langle i_{ind}(t)\rangle}{dt} = -\langle v_L(t)\rangle - R_p \langle i_{ind}(t)\rangle + \frac{d'(t)\langle v_{dc}(t)\rangle}{N}$$ Equation 4-23

$$C_{ph} \frac{d\langle v_{dc}(t)\rangle}{dt} = -\frac{d'(t)\langle i_{ind}(t)\rangle}{N} + \langle i_H(t)\rangle$$ Equation 4-24
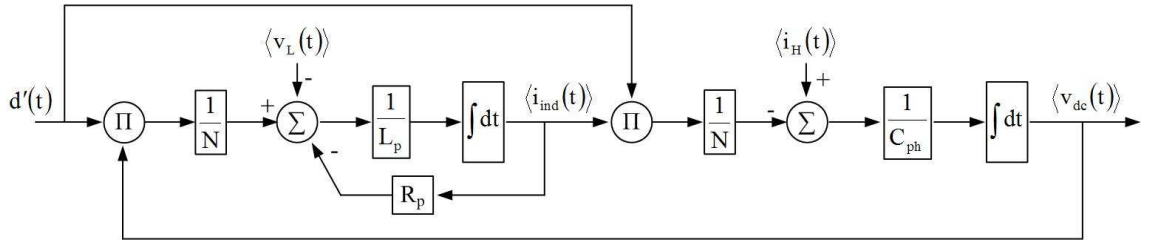
Figure 4-10: State feedback block diagram of the bi-directional dc-dc converter in step-up mode based on the averaged state equations

The operating point state equations were obtained using the Taylor series and neglecting higher order terms. Operating point state equations in the time domain are given in Equation 4-25 and Equation 4-26 while Equation 4-27 and Equation 4-28 represent the operating point state equations which were obtained by applying the Laplace transformation. Figure 4-11 shows the operating point state feedback block diagram of the converter during step-up mode.

$$L_p \frac{d\langle i_{ind}(t)\rangle}{dt} = -\langle v_L(t)\rangle - R_p \langle i_{ind}(t)\rangle + \frac{d'(t)\langle v_{dc}(t)\rangle}{N} = f\{\langle i_L(t)\rangle, \langle v_{ind}(t)\rangle, \langle v_{dc}(t)\rangle, d'(t)\}$$

$$\frac{\partial f}{\partial \langle i_{ind}(t)\rangle}\bigg|_{op} = -R_p \qquad \frac{\partial f}{\partial \langle v_L(t)\rangle}\bigg|_{op} = -1 \qquad \frac{\partial f}{\partial \langle v_{dc}(t)\rangle}\bigg|_{op} = \frac{D'_o}{N} \qquad \frac{\partial f}{\partial d'(t)}\bigg|_{op} = \frac{V_{dco}}{N}$$

$$L_p \Delta \langle \overset{\circ}{i}_{ind}(t)\rangle = -\Delta\langle v_L(t)\rangle - R_p \Delta\langle i_{ind}(t)\rangle + \frac{D'_o}{N}\Delta\langle v_{dc}(t)\rangle$$
$$+ \frac{V_{dco}}{N}\Delta d'(t)$$

<div align="right">Equation 4-25</div>

$$C_{ph}\frac{d\langle v_{dc}(t)\rangle}{dt} = -\frac{d'(t)\langle i_{ind}(t)\rangle}{N} + \langle i_H(t)\rangle = g\{\langle i_{ind}(t)\rangle, d'(t), \langle i_H(t)\rangle\}$$

$$\frac{\partial g}{\partial \langle i_{ind}(t)\rangle}\bigg|_{op} = -\frac{D'_o}{N} \qquad\qquad \frac{\partial g}{\partial d'(t)}\bigg|_{op} = -\frac{I_{indo}}{N} \qquad\qquad \frac{\partial g}{\partial \langle i_H(t)\rangle}\bigg|_{op} = 1$$

$$C_{ph}\Delta\langle \overset{\circ}{v}_{dc}(t)\rangle = -\frac{D'_o}{N}\Delta\langle i_{ind}(t)\rangle - \frac{I_{indo}}{N}\Delta d'(t) + \Delta\langle i_H(t)\rangle$$

<div align="right">Equation 4-26</div>

$$L_p s\Delta I_{ind}(s) = -\Delta V_L(s) - R_p \Delta I_{ind}(s) + \frac{D'_o}{N}\Delta V_{dc}(s) + \frac{V_{dco}}{N}\Delta D'(s)$$

<div align="right">Equation 4-27</div>

$$C_{ph}s\Delta V_{dc}(s) = -\frac{D'_o}{N}\Delta I_{ind}(s) - \frac{I_{indo}}{N}\Delta D'(s) + \Delta I_H(s)$$

<div align="right">Equation 4-28</div>
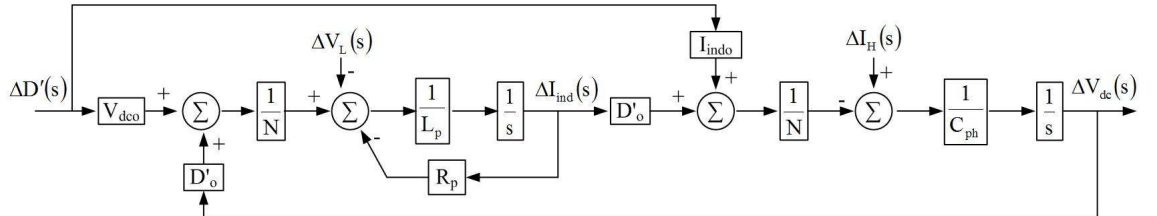
Figure 4-11: State feedback block diagram of the bi-directional dc-dc converter in step-up mode based on operating point state equations

4.3.2.2 Step-down mode

Figure 4-12 presents on-state and off-state equivalent circuits of the converter during the step-down mode. Equation 4-29 and Equation 4-30 are obtained by applying Kirchhoff's voltage and current laws to the on-state equivalent circuit and similarly Equation 4-31 and Equation 4-32 are obtained considering the off-state. The corresponding equations are averaged over a switching cycle to obtain the averaged state equations which are given in Equation 4-33 and Equation 4-34. The non-linear

state feedback block diagram of the converter for the step-down mode is presented in Figure 4-13.

(a) On state   (b) Off state
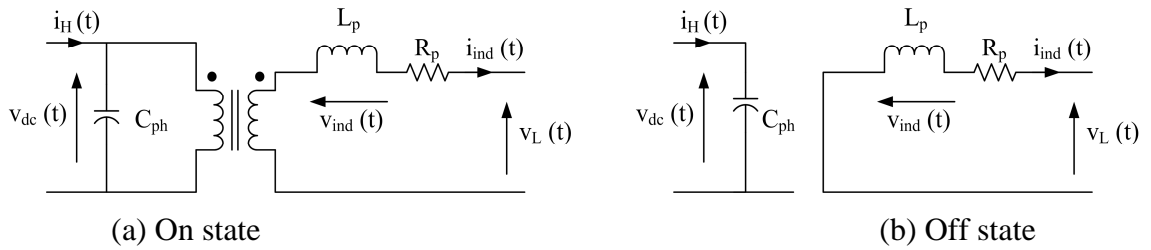
Figure 4-12: Equivalent circuits of the bi-directional dc-dc converter in step-down mode

$$L_p \frac{di_{ind}(t)}{dt} = \frac{v_{dc}(t)}{N} - R_p i_{ind}(t) - v_L(t) \qquad \text{Equation 4-29}$$

$$C_{ph} \frac{dv_{dc}(t)}{dt} = i_H(t) - \frac{i_{ind}(t)}{N} \qquad \text{Equation 4-30}$$

$$L_p \frac{di_{ind}(t)}{dt} = -R_p i_{ind}(t) - v_L(t) \qquad \text{Equation 4-31}$$

$$C_{ph} \frac{dv_{dc}(t)}{dt} = i_H(t) \qquad \text{Equation 4-32}$$

$$L_p \frac{d\langle i_{ind}(t)\rangle}{dt} = \frac{d(t)\langle v_{dc}(t)\rangle}{N} - R_p \langle i_{ind}(t)\rangle - \langle v_L(t)\rangle \qquad \text{Equation 4-33}$$

$$C_{ph} \frac{d\langle v_{dc}(t)\rangle}{dt} = \langle i_H(t)\rangle - \frac{d(t)\langle i_{ind}(t)\rangle}{N} \qquad \text{Equation 4-34}$$
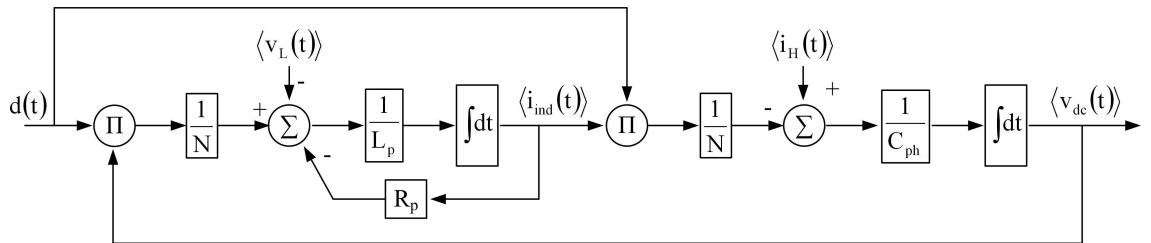
Figure 4-13: State feedback block diagram of the bi-directional dc-dc converter in step-down mode based on averaged state equations

As before operating point state equations were obtained by applying Taylor series and neglecting higher order terms to the averaged state equations. Equation 4-35 and Equation 4-36 are the operating point time domain equations while Equation 4-37 and Equation 4-38 are obtained by applying Laplace transformation. Figure 4-14 presents the operating point state feedback block diagram of the converter during the step-down mode.

$$L_p \frac{d\langle i_{ind}(t)\rangle}{dt} = \frac{d(t)\langle v_{dc}(t)\rangle}{N} - R_p \langle i_{ind}(t)\rangle - \langle v_L(t)\rangle = f\{d(t), \langle v_{dc}(t)\rangle, \langle i_{ind}(t)\rangle, \langle v_L(t)\rangle\}$$

$$\left.\frac{\partial f}{\partial d(t)}\right|_{op} = \frac{V_{dco}}{N} \qquad \left.\frac{\partial f}{\partial\langle v_{dc}(t)\rangle}\right|_{op} = \frac{D_o}{N} \qquad \left.\frac{\partial f}{\partial\langle i_{ind}(t)\rangle}\right|_{op} = -R_p \qquad \left.\frac{\partial f}{\partial\langle v_L(t)\rangle}\right|_{op} = -1$$

$$L_p \Delta\langle \overset{\circ}{i}_{ind}(t)\rangle = \frac{V_{dco}}{N}\Delta d(t) + \frac{D_o}{N}\Delta\langle v_{dc}(t)\rangle - R_p\Delta\langle i_{ind}(t)\rangle - \Delta\langle v_L(t)\rangle \quad \text{Equation 4-35}$$

$$C_{ph} \frac{d\langle v_{dc}(t)\rangle}{dt} = \langle i_H(t)\rangle - \frac{d(t)\langle i_{ind}(t)\rangle}{N} = g\{\langle i_H(t)\rangle, d(t), \langle i_{ind}(t)\rangle\}$$

$$\left.\frac{\partial g}{\partial\langle i_H(t)\rangle}\right|_{op} = 1 \qquad \left.\frac{\partial g}{\partial d(t)}\right|_{op} = -\frac{I_{indo}}{N} \qquad \left.\frac{\partial g}{\partial\langle i_{ind}(t)\rangle}\right|_{op} = -\frac{D_o}{N}$$

$$C_{ph}\Delta\langle \overset{\circ}{v}_{dc}(t)\rangle = \Delta\langle i_H(t)\rangle - \frac{I_{indo}}{N}\Delta d(t) - \frac{D_o}{N}\Delta\langle i_{ind}(t)\rangle \qquad \text{Equation 4-36}$$

$$L_p s\Delta I_{ind}(s) = \frac{V_{dco}}{N}\Delta D(s) + \frac{D_o}{N}\Delta V_{dc}(s) - R_p\Delta I_{ind}(s) - \Delta V_L(s) \qquad \text{Equation 4-37}$$

$$C_{ph}s\Delta V_{dc}(s) = \Delta I_H(s) - \frac{I_{indo}}{N}\Delta D(s) - \frac{D_o}{N}\Delta I_{ind}(s) \qquad \text{Equation 4-38}$$
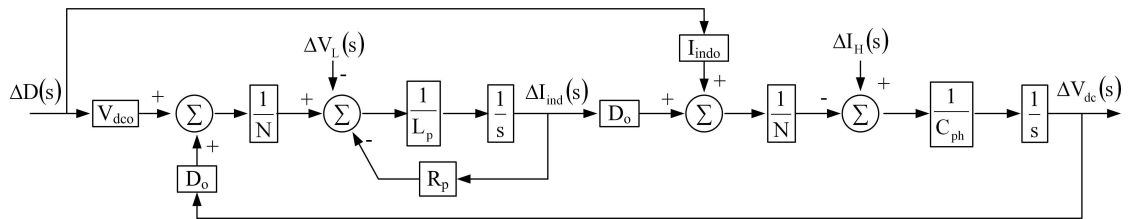
Figure 4-14: State feedback block diagram of the bi-directional converter in step-down mode based on the operating point state equations

4.4 SINGLE-PHASE INVERTER

The full-bridge single-phase inverter is used to integrate renewable energy sources widely in literature. Since typical input dc voltage is considered to be stiff, the inverter is also known as a voltage source inverter. Sinusoidal pulse width modulation (PWM) can be used as the switching technique. PWM with unipolar voltage switching was selected ahead of bipolar voltage switching due to the reduction in harmonics achieved [108].

The relationship between the fundamental component of the instantaneous output voltage (e_{INV},f) of the single-phase inverter with the modulation index (m_a) and the input dc voltage (V_{dc}) is presented in Equation 4-39 [108]. The maximum modulation index is unity. Thus the maximum peak output voltage is equal to dc voltage source. In UK, the distribution voltage is subjected to a 10% variation [111]. Thus the input dc voltage should be capable of producing a smooth waveform even at 110% of the nominal voltage. This is the criterion used to select the input voltage of the single-phase inverter.

$$e_{INV,f}(t) = m_a V_{dc} \sin(2\pi ft) \qquad\qquad\text{Equation 4-39}$$

4.4.1 Single-phase inverter grid interface methods

The output voltage of an inverter is square wave with varying duty ratio. Therefore the output of the inverter needs to couple through a filter to the grid. This coupling method also helps to control the output power flow from the inverter. Figure 4-15 presents several coupling methods used to connect an inverter to the grid. The simplest method is to use an inductor, which filters the output current from the inverter [3,23]. By controlling the magnitude and phase difference between the voltages at the ends of the inductor, reactive power and active power from the inverter can be controlled. An LC filter could also be used in Figure 4-15(c), which helps to shape the output voltage [47]. Figure 4-15 (d) shows an LCL filter as the coupling method [30,112]. The coupling method shapes the voltage better than coupling with only an inductor. Active and reactive power flow could be controlled in this method as well. This method is more expensive than other methods due to higher number of components.
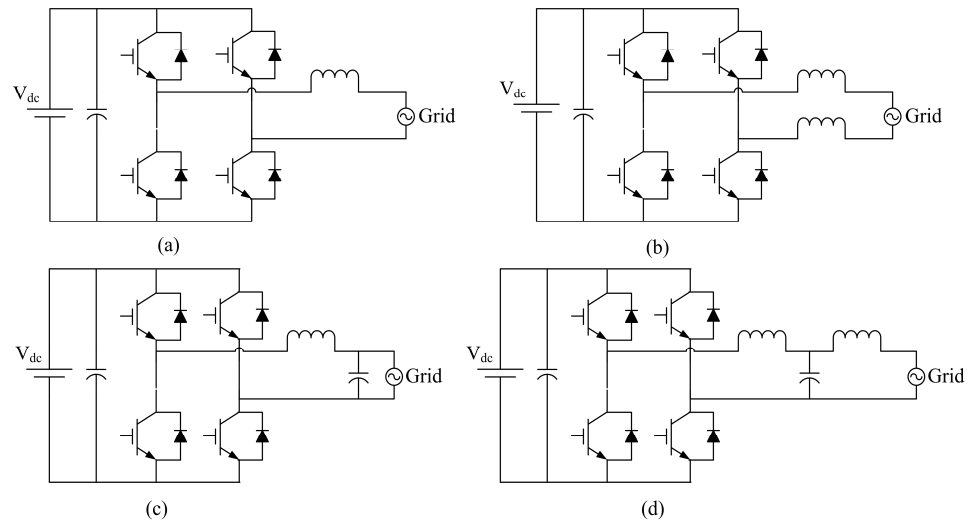
Figure 4-15: Coupling methods used to connect an inverter to a grid

4.4.2 Sizing the coupling inductor and modelling of single-phase inverter with coupling inductor

A single-phase inverter coupled through an inductor is selected in this application due to its simplicity and low cost. The phase angle of the voltages between the ends of the inductor was set to 10° at full power. The inductance was calculated to ensure this criterion [30]. Equation 4-40 presents the approximated inductance of the inductor where L_P, E_{INVrms}, V_{INVrms}, f, P_{max}, and δ correspond to inductance, magnitude of voltages at the ends of the inductor, frequency, maximum active power and phase angle between the voltages at the ends of the inductor.

$$L_p \approx \frac{E_{INVrms} V_{INVrms} \sin \delta}{2\pi f P_{max}}$$ Equation 4-40

A single-phase inverter connected to a grid through a coupling inductor is presented in Figure 4-16. Equation 4-41 can be obtained by applying Kirchhoff's voltage law and by applying the Laplace transformation Equation 4-42 is obtained. The single phase inverter output voltage and the input dc voltage are related as in Equation 4-43 where m_a is the amplitude modulation ratio. Equation 4-44 is again derived by applying the Laplace transformation. The state feedback block diagram of the inverter connected to the grid through a coupling inductor is presented in Figure 4-17 based on Equation 4-42 and Equation 4-44.
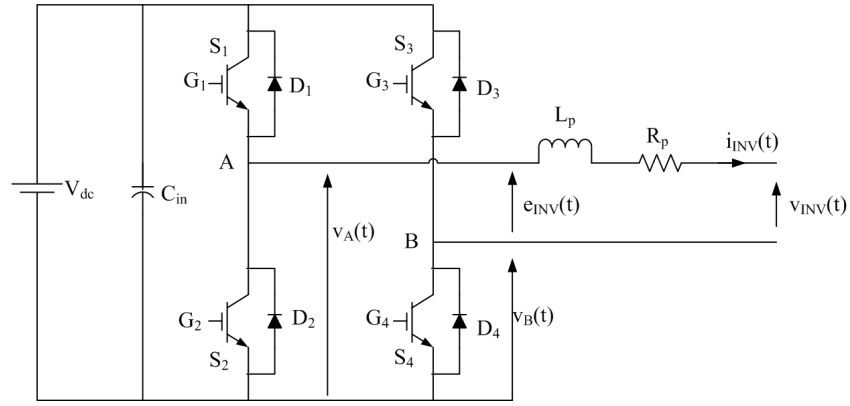
Figure 4-16: Single-phase inverter connected to grid through a coupling inductor showing definition of variables

$$L_p \frac{di_{INV}(t)}{dt} = e_{INV}(t) - R_p i_{INV}(t) - v_{INV}(t) \qquad \text{Equation 4-41}$$

$$L_p s I_{INV}(s) = E_{INV}(s) - R_p I_{INV}(s) - V_{INV}(s) \qquad \text{Equation 4-42}$$

$$e_{INV}(t) = m_a V_{dc} \sin(\omega t) = V_{dc} V_c(t) \qquad \text{Equation 4-43}$$

$$E_{INV}(s) = V_{dc} V_c(s) \qquad \text{Equation 4-44}$$
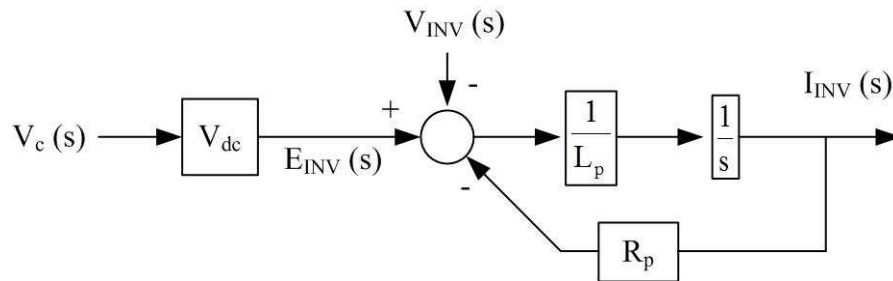
Figure 4-17: State feedback block diagram of the system

4.4.3 Sizing the input capacitance of the single-phase inverter

The dc-link capacitance should be selected in such a way that the voltage ripple at the dc-link is small. Figure 4-18(a) shows the block diagram of the single-phase inverter. The variation of inverter input current, inverter output current and inverter output voltage with time are plotted and shown in Figure 4-18(b) assuming the output voltage and current are in-phase. The average intput current (I_{dc}) is also shown in Figure 4-18(b). The excess charge, ΔQ, should be supplied by the capacitor.

Equation 4-45 gives the instantaneous output power of the inverter while Equation 4-46 gives instantaneous input power to the inverter. Assuming a lossless inverter, the inverter input current can be written as in Equation 4-47 with the aid of Equation 4-45 and Equation 4-46.
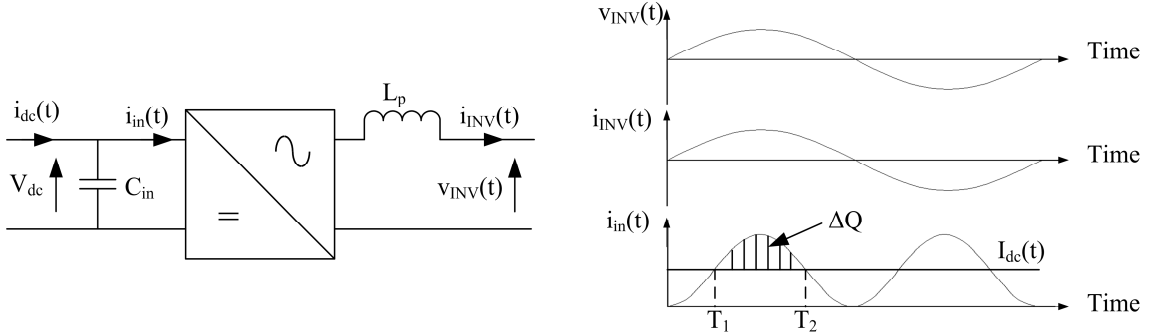
Figure 4-18: Inverter output current and principle input current

$$p_{ac} = V_{INVrms}\sqrt{2}\sin(2\pi ft)I_{INVrms}\sqrt{2}\sin(2\pi ft)$$

Equation 4-45

$$p_{dc} = V_{dc}i_{in}(t)$$

Equation 4-46

$$i_{in}(t) = \frac{2V_{INVrms}I_{INVrms}\sin^2(2\pi ft)}{V_{dc}}$$

Equation 4-47

Average input current (I_{dc}) and the instantaneous intput current [$i_{in}(t)$] cross-over point can be calculated by making the input current equal to I_{dc} (see Equation 4-48). The average output and input power of the inverter can be written as in Equation 4-49 and Equation 4-50 respectively. Then Equation 4-48 can be reduced to Equation 4-51 assuming the inverter is lossless. T_1 and T_2 can be calculated from Equation 4-51.

$$I_{dc}(t) = \frac{2V_{INVrms}I_{INVrms}\sin^2(2\pi ft)}{V_{dc}}$$

Equation 4-48

$$P_{ac} = V_{INVrms}I_{INVrms}$$

Equation 4-49

$$P_{in} = V_{dc}I_{dc}$$

Equation 4-50

$$2\sin^2(2\pi ft) = 1$$

Equation 4-51

The excess charge (ΔQ) can be calculated from Equation 4-52. Finally the size of the capacitor could be calculated from Equation 4-53 based on the required voltage ripple and amount of excess charge.

$$\Delta Q = \frac{2V_{INVrms}I_{INVrms}}{V_{dc}} \int_{T_1}^{T_2} \sin^2(2\pi ft)dt - I_{dc}(T_2 - T_1) \qquad \text{Equation 4-52}$$

$$C_{in} = \frac{\Delta Q}{V_{dc}\left(\dfrac{\Delta V_{dc}}{V_{dc}}\right)} \qquad \text{Equation 4-53}$$

4.4.4 Phase Locked Loop for synchronization of grid voltage

In order to connect the inverter to the grid, the output voltage of the inverter must be synchronised with the grid voltage. A Phase Locked Loop (PLL) is typically the device which is used to generate a signal in-phase with grid voltage.

Figure 4-19 shows the block diagram of a Digital Phase Locked Loop (DPLL) which consists of three main blocks [113-114]. The phase detector is used to extract the phase difference between the measured signal (θ_{grid}) and PLL generated signal (θ_{sync}). In this application, an EXOR logic gate based phase detector is used. The average output of the phase detector ($\overline{U}_d$) is proportional to the phase error (θ_e) between the grid signal and Voltage Controlled Oscillator (VCO) output signal (see Equation 4-54). The constant K_d depends on the output limits of the EXOR output as given in Equation 4-55 where U_{sat+} and U_{sat-} are the supply voltage levels of the EXOR gate. The output of the phase detector is a square signal with variable duty ratio, thus a low pass filter is used to extract the average of the phase error. A transfer function of first order low pass filter [F(s)] is presented in Equation 4-56. K_α is the gain of the filter. The time constants of the filter are τ_1 and τ_2. The VCO produces a signal whose frequency varies linearly based on the output of the low pass filter. ω_o is the centre frequency and K_o is the gain of the VCO. The governing equation of the VCO is given in Equation 4-57, and Equation 4-58 is obtained by applying the Laplace transformation. θ_{sync} is the phase of the VCO output.
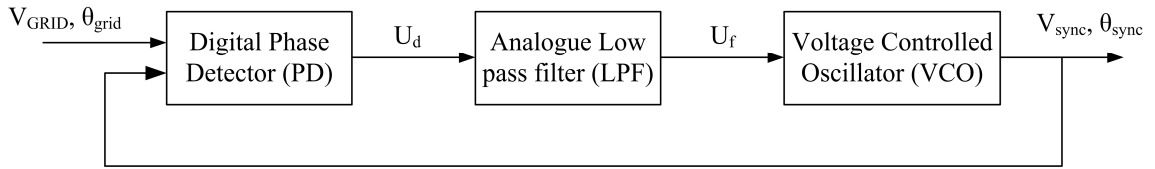
Figure 4-19: Block diagram of the Digital Phase Locked Loop

$$\overline{U}_d(t) = K_d \theta_e(t) \qquad\qquad \text{Equation 4-54}$$

$$K_d = \frac{U_{sat+} - U_{sat}}{\pi} \qquad\qquad \text{Equation 4-55}$$

$$F(s) = K_\alpha \left(\frac{1+s\tau_2}{1+s\tau_1}\right) \qquad\qquad \text{Equation 4-56}$$

$$\omega_{sync}(t) = \omega_o + K_o u_f(t) \qquad\qquad \text{Equation 4-57}$$

$$\theta_{sync}(s) = \frac{K_0}{s} U_f(s) \qquad\qquad \text{Equation 4-58}$$

The block diagram of the DPLL in s-domain is presented in Figure 4-20 based on Equation 4-54, Equation 4-56 and Equation 4-58. The relationship between the phase of the grid signal and VCO output is given in Equation 4-59. The natural frequency and damping ratio is governed by the Equation 4-60 and Equation 4-61. ξ and ω_n are the damping ratio and natural frequency of the system.
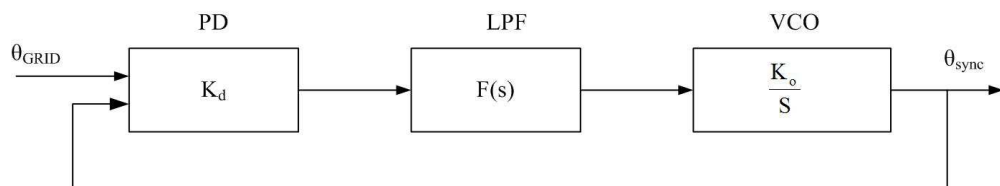
Figure 4-20: Mathematical model of the Digital Phase Locked Loop

$$\frac{\theta_{sync}(s)}{\theta_{GRID}(s)} = \frac{K_o K_d K_\alpha \left(\dfrac{1+s\tau_2}{1+s\tau_1}\right)}{s^2 + \left(\dfrac{1+K_o K_d \tau_2}{\tau_1 + \tau_2}\right)s + \dfrac{K_o K_d}{\tau_1 + \tau_2}} \qquad\qquad \text{Equation 4-59}$$

$$\omega_n = \sqrt{\frac{K_o K_d}{\tau_1 + \tau_2}} \qquad\qquad \text{Equation 4-60}$$

$$\xi = \omega_n \left(\tau_2 + \frac{1}{K_o K_d} \right)$$

Equation 4-61

Lock range ($\Delta\omega_L$), pull-in range ($\Delta\omega_p$) and hold range ($\Delta\omega_H$) are important parameters of a PLL. The PLL would lock to reference signal if the frequency is within lock range [114-115]. The definition of the hold range, is the frequency range in which the PLL would be able to complete phase tracking [113]. When the reference frequency is above lock range and below pull-in range, the PLL would 'lock to' after a slow process. The relationship of these parameters with the natural frequency and damping ratio of the control loop are given in Equation 4-62, Equation 4-63 and Equation 4-64.

$$\Delta\omega_H = \frac{K_d K_o \pi}{2}$$

Equation 4-62

$$\Delta\omega_L = \pi\xi\omega_n$$

Equation 4-63

$$\Delta\omega_p = \frac{\pi}{\sqrt{2}} \sqrt{\xi\omega_n K_o K_d}$$

Equation 4-64

4.5 SUMMARY

The principle of operation of switch mode dc-dc converter topologies is presented. The averaged and operating point model of the modified dc-dc converter is developed. In the case of the bi-directional dc-dc converter; averaged and operating point models for both step-up and step-down mode were developed. Based on the models, state feedback block diagrams for the converters were created.

A full-bridge single-phase inverter model was used and a sinusoidal pulse width modulation technique was adopted. PWM with unipolar voltage switching produces lower harmonics compared with bipolar voltage switching thus the former was used. In the literature, several inverter grid connection techniques are proposed. For this application, the inverter is coupled to the grid through an inductor. A state feedback block diagram for the instantaneous current control can be developed. Synchronisation is essential for the grid connection of an inverter. A digital Phase Locked Loop is used for this.

CHAPTER 5

SIMULATION MODEL OF PHOTOVOLTAIC PANEL AND DESIGN OF HARDWARE PHOTOVOLTAIC EMULATOR

5.1 INTRODUCTION

In this analysis, a photovoltaic panel is considered as the microsource in order to demonstrate the behaviour of the proposed microsource interface. The development of the microsource interface consists of three stages: analytical, simulation and experimental. This chapter presents the development of a well behaved simulation model and hardware emulator of a photovoltaic panel. A simulation model was developed with known limits and reasonable accuracy. For the experimental work, neither a real photovoltaic panel nor commercial photovoltaic emulator was available. Therefore a photovoltaic emulator was designed.

5.2 MODELLING OF PHOTOVOLTAIC PANEL IN PSCAD/EMTDC SOFTWARE

A photovoltaic cell model presented in Figure 5-1 was used for the simulation purposes. This model comprises a current source, an anti-parallel diode and a series resistor. Equation 5-1 gives the characteristic equation of this photovoltaic cell model where I_{pv}, I_{ph}, I_{sat}, V_{pv}, R_s and V_t correspond to PV cell current, photocurrent, diode saturation current, PV cell voltage, series resistance and thermal voltage respectively. The thermal voltage is related to the ideality factor (A), Boltzmann's constant (k), temperature (T) and charge of an electron (q) as given in Equation 5-2.

$$I_{pv} = I_{ph} - I_{sat}\left[\exp\left(\frac{V_{pv} + I_{pv}R_s}{V_t}\right) - 1\right] \qquad \text{Equation 5-1}$$
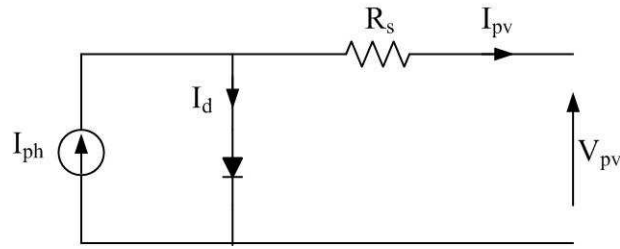
Figure 5-1: Photovoltaic cell model used to develop simulation model

$$V_t = \frac{AkT}{q}$$ Equation 5-2

5.2.1 Obtaining the parameters for the model

An SM110-24P photovoltaic panel was selected for this study and Table 5-1 presents the summary of the panel data [79].

Table 5-1: Summary of data of the SM110-24P photovoltaic panel

Parameter	Value
Peak power (power at MPP at STC, P_{MPP})	110 W
Voltage at MPP at STC (V_{MPP})	35.0 V
Current at MPP at STC (I_{MPP})	3.15 V
Open circuit voltage at STC (V_{oc})	43.5 V
Short circuit current at STC (I_{sc})	3.45 V
Temperature coefficient for short-circuit current (ΔI_{sc})	1.4 mA/°C
Temperature coefficient for open-circuit voltage (ΔI_{sc})	-152 mV/°C
Number of cells in series	72

The photocurrent is related to the irradiance and temperature as given in Equation 5-3 and by rearranging the terms it can be written as Equation 5-4. The relationship between temperature and open circuit voltage is given by Equation 5-5, and Equation 5-6 is obtained by rearranging the terms. Thermal voltage, which is given in Equation 5-2, can be rewritten as in Equation 5-7. Table 5-2 presents the constants in Equation 5-4, Equation 5-6 and Equation 5-7 corresponding to the SM110-24P panel. Diode saturation current is a function of photocurrent, open circuit voltage and thermal voltage as given in Equation 5-8.

$$I_{ph} = \frac{G_a}{G_{as}}\left[I_{scs} + \Delta I_{sc}\left(T - T_s\right)\right]$$

Equation 5-3

$$I_{ph} = G_a\left[\frac{\left(I_{scs} - \Delta I_{sc}T_s\right)}{G_{as}} + \frac{\Delta I_{sc}}{G_{as}}T\right] = G_a\left[K_1 + K_2 T\right]$$

Equation 5-4

$$V_{oc} = V_{ocs} + \Delta V_{oc}\left(T - T_s\right) + V_t \ln\left(\frac{I_{sc}}{I_{scs}}\right)$$

Equation 5-5

$$V_{oc} = \left(V_{ocs} - \Delta V_{oc}T_s\right) + \Delta V_{oc}T + V_t \ln\left(\frac{I_{sc}}{I_{scs}}\right)$$

$$V_{oc} = K_3 + K_4 T + V_t \ln\left(\frac{I_{sc}}{I_{scs}}\right)$$

Equation 5-6

$$V_t = \frac{AkT}{q} = K_5 T$$

Equation 5-7

$$I_{sat} = \frac{I_{ph}}{\exp\left(\frac{V_{oc}}{V_t}\right) - 1}$$

Equation 5-8

Table 5-2: Values of the constants required for the photovoltaic panel model

Parameter	Value
K_1 [A/Wm^{-2}]	3.42×10^{-3}
K_2 [A/°CWm^{-2}]	1.40×10^{-6}
K_3 [V]	47.3
K_4 [V/°C]	-0.152
K_5 [V/°C]	1.53×10^{-4}

The ideality factor of the photovoltaic panel was calculated based on the algorithm presented in Figure 5-2 and the corresponding MATLAB code is presented in Appendix B. Typically the ideality factor lies between one and two therefore the value of the ideality factor was swept from 0.5 to 2.5. The value of $\left|\left(\frac{dI_{pv}}{dV_{pv}}\right)\right|_{@ MPP} + \frac{I_{MPP}}{V_{MPP}}\Big|$ and the series resistance of the cell was plotted with respect to ideality factor and is shown in

Figure 5-3. The minimum of $\left| \left(\dfrac{dI_{pv}}{dV_{pv}} \right)\Big|_{@\,MPP} + \dfrac{I_{MPP}}{V_{MPP}} \right|$ occurs when the ideality factor is

equal to 1.775 which corresponds to the ideality factor of the SM110-24P panel. The

corresponding series resistance is 0.0021 Ω.
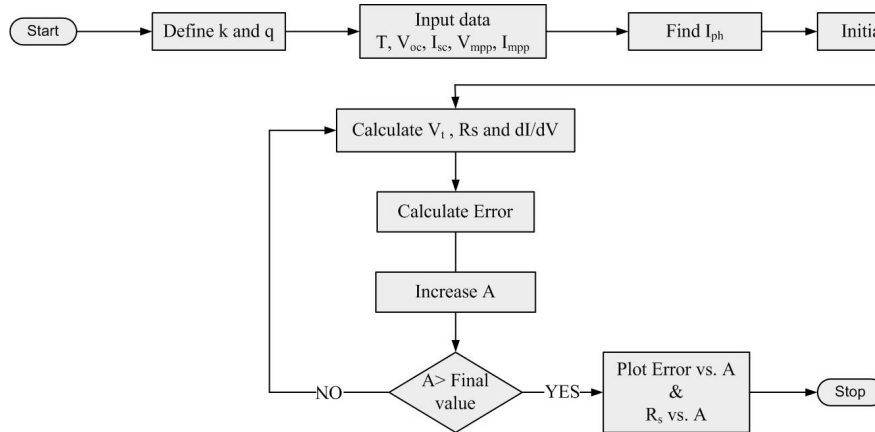
Figure 5-2: Flow chart used to calculate the ideality factor

(a) Whole swept range   (b) Close up of operating point
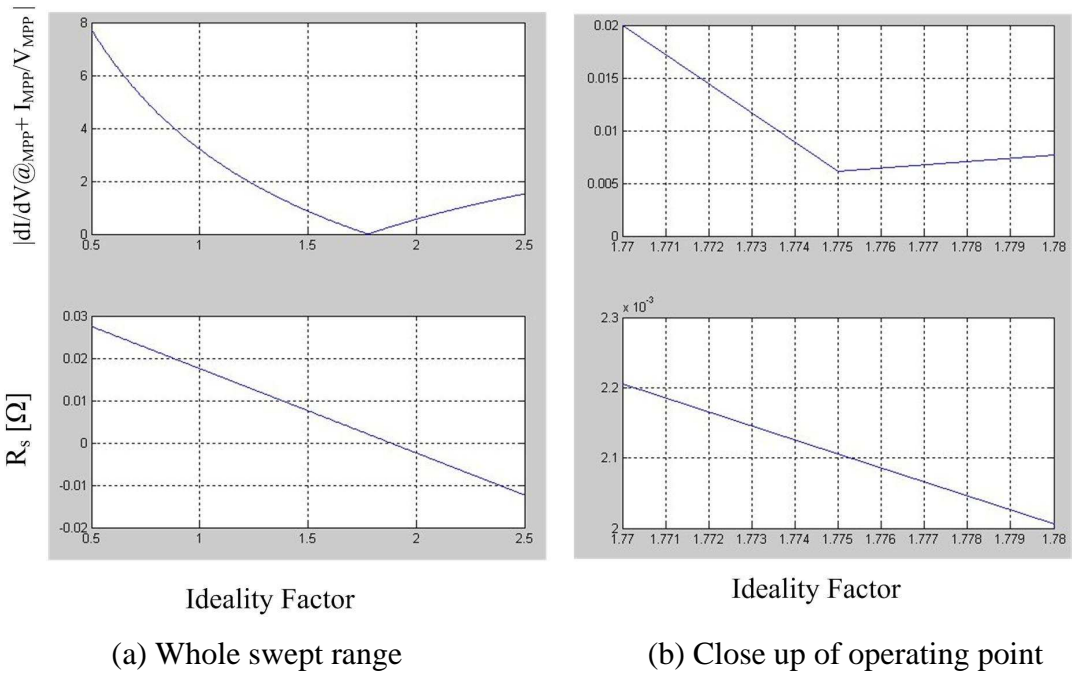
Figure 5-3: Variations of absolute difference and series resistance with ideality factor

5.2.2 PSCAD/EMTDC simulation model

Figure 5-4 shows the block diagram of the simulation model which was developed

using the PSCAD/EMTDC software. The photovoltaic panel is represented by a

controllable voltage source. The heart of the controller is the characteristic equation given in Equation 5-1 which commands the voltage of the source based on the output current.

Temperature (T) and irradiance (G_a) are the inputs to the panel model which are used to calculate the photocurrent, open circuit voltage and thermal voltage based on Equation 5-4, Equation 5-6 and Equation 5-7 respectively. Then the diode saturation current is calculated from Equation 5-8. Thermal voltage and diode saturation current are also fed to the characteristic equation block. Appendix B presents the screen captures of the simulation model of the photovoltaic panel.
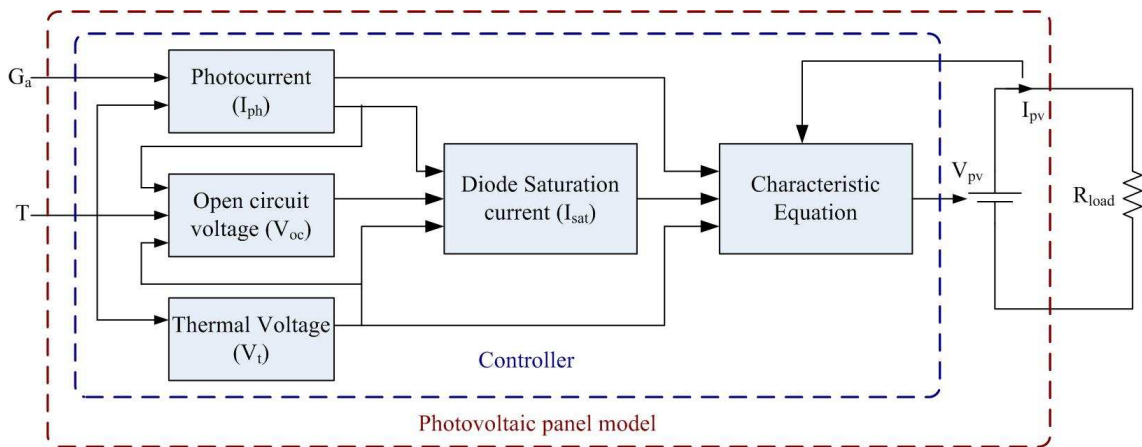
Figure 5-4: Block diagram of the simulation model of the photovoltaic panel

5.2.3 Simulation results and limits of the photovoltaic panel model

The photovoltaic panel simulation model was connected to a variable resistive load as shown in Figure 5-5. The load resistance was decreased linearly from 75Ω to 1Ω in steps of 0.1Ω. The duration, solution time step and channel plot step of the simulation were set to 10s, 0.5μs and 27μs respectively.
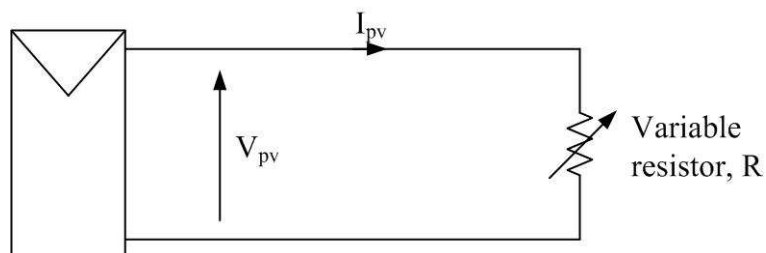
Figure 5-5: Test set-up used to test the simulation of the photovoltaic panel

Variation of photovoltaic voltage against photovoltaic current is presented in Figure 5-6(a). Load resistance, PV current and PV voltage near the failure point against time is plotted and shown in Figure 5-6(b). It is clear that the photovoltaic panel model fails at a certain voltage and the corresponding load resistance is 11.1Ω.
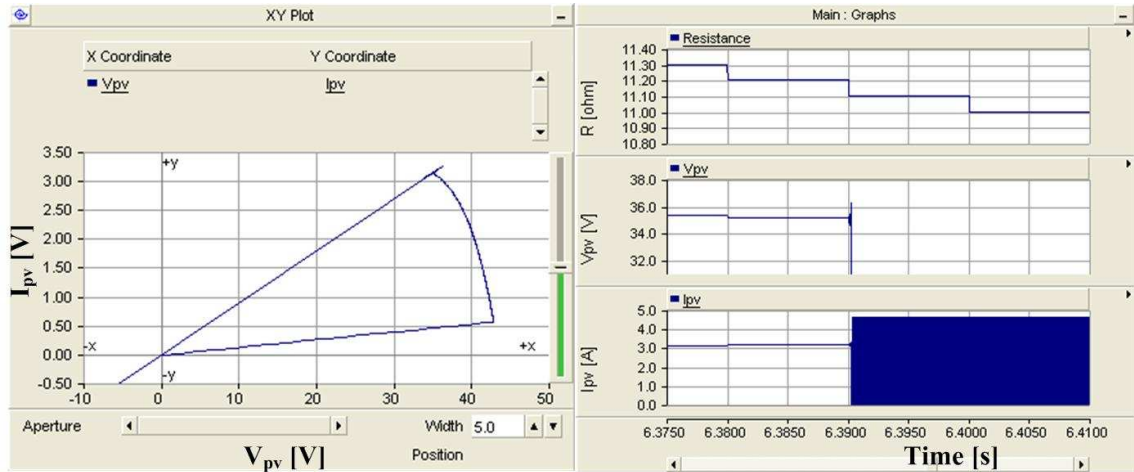
(a) I_{pv} vs. V_{pv} (b) R, I_{pv} and V_{pv} near the failure point

Figure 5-6: Simulation results of the photovoltaic panel model

By rearranging the characteristic equation of the photovoltaic panel, Equation 5-1 and considering the number of cells in series (N), we can obtain Equation 5-9. If the irradiance and the temperature are kept constant, then photovoltaic current, open circuit voltage, thermal voltage and diode saturation current are constants. Thus the model of the photovoltaic panel could be reduced to block diagram shown in Figure 5-7.
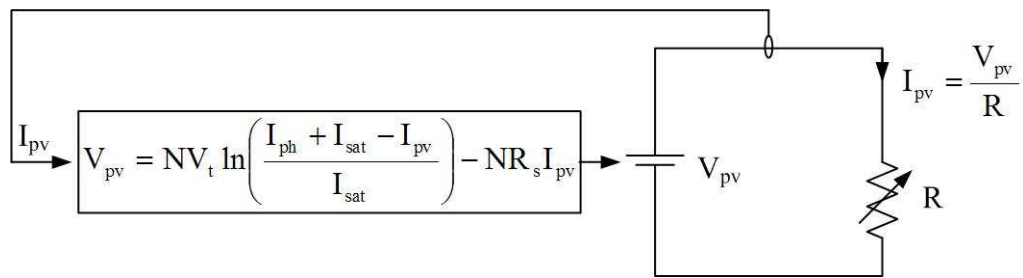
Figure 5-7: Simplified simulation model at constant irradiance and temperature

$$V_{pv} = NV_t \ln\left(\frac{I_{ph} + I_{sat}}{I_{sat}} - \frac{I_{pv}}{I_{sat}}\right) - NI_{pv}R_s \qquad \text{Equation 5-9}$$

$$I_{pv} = \frac{V_{pv}}{R}$$ Equation 5-10

Combining Equation 5-9 and Equation 5-10,

$$V_{pv} = NV_t \ln\left(\frac{I_{ph} + I_{sat}}{I_{sat}} - \frac{V_{pv}}{I_{sat}R}\right) - \frac{NV_{pv}R_s}{R}$$ Equation 5-11

In simulations, the new voltage is calculated based on the value of the earlier time step. Therefore Equation 5-11 could be represented as an iteration as given in Equation 5-12.

$$V_{pv,n+1} = NV_t \ln\left(\frac{I_{ph} + I_{sat}}{I_{sat}} - \frac{V_{pv,n}}{RI_{sat}}\right) - \frac{NR_s V_{pv,n}}{R}$$ Equation 5-12

$$\left.\begin{array}{l} V_{pv,n+1} = G(V_{pv,n}) \text{ where} \\[2mm] G(V_{pv,n}) = NV_t \ln\left(\frac{I_{ph} + I_{sat}}{I_{sat}} - \frac{V_{pv,n}}{RI_{sat}}\right) - \frac{NR_s V_{pv,n}}{R} \end{array}\right\}$$ Equation 5-13

$$G'(V_{pv}) = -\frac{NV_t}{R(I_{ph} + I_{sat}) - V_{pv}} - \frac{NR_s}{R}$$ Equation 5-14

If $\left|G'(V_{pv})\right| < 1$, then the iteration would converge to root V_{pv} [116]. Therefore from Equation 5-14, it is possible to find the inequality given in Equation 5-15.

$$V_{pv} < R(I_{ph} + I_{sat}) - \frac{RNV_t}{(R - NR_s)}$$ Equation 5-15

The convergence limit and the output voltage of a photovoltaic panel with respect to the load resistance are presented in Figure 5-8. It is clear that the convergence voltage limit is less than the actual voltage of the photovoltaic panel when the load resistance goes below approximately 11 Ω. The cross-over point load resistance coincides with the failure point load resistance of the simulation model.
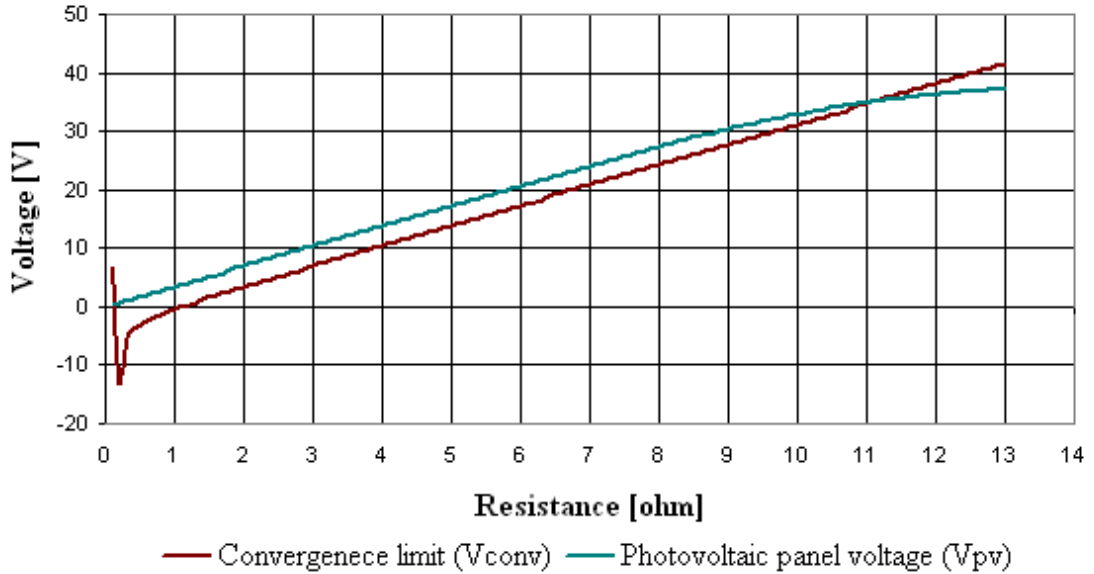
Figure 5-8: Variation of convergence limit (V_{conv}) and photovoltaic panel voltage (V_{pv}) with load resistance (R)

5.2.4 Extending the limits of the simulation model

The simulation model fails close to the maximum power point. Therefore it is desirable to extend the stable region of the PV cell model. If the convergence limit could be increased at low voltages, the model would be stable. It is possible to reduce the limitations by adding an inductor in series with the voltage source. The simplified photovoltaic panel model with the inclusion of inductor is shown in Figure 5-9.
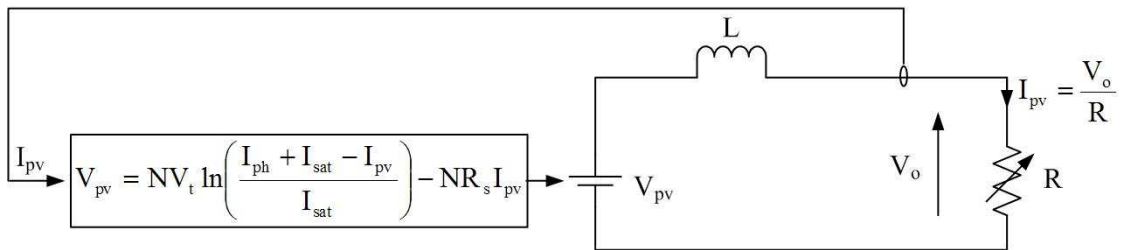
Figure 5-9: Simplified model with the inductor in series with the voltage source

5.2.4.1 Modelling of the inductor

The current flowing through the inductor which is governed by Equation 5-16 has to be represented in iterative format. Figure 5-10 shows the simplified circuit diagram and voltage across the inductor.

91
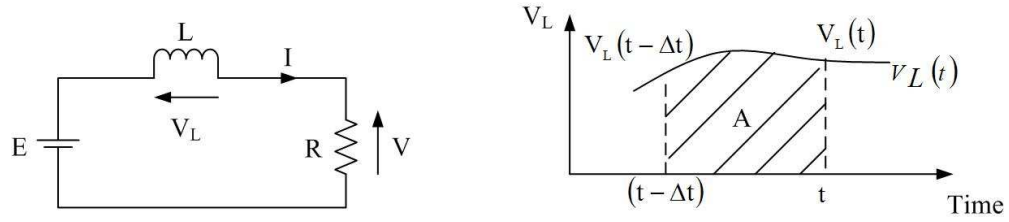
Figure 5-10: Simplified circuit diagram and the voltage across the inductor

The voltage across the inductor can be described as in Equation 5-16 and can be approximated to Equation 5-18.

$$V_L = L\frac{dI}{dt} \qquad\qquad \text{Equation 5-16}$$

$$\int dI = \int \frac{V_L}{L} dt$$

$$I(t) - I(t - \Delta t) = \int_{t-\Delta t}^{t} \frac{V_L}{L} d(t)$$

Consider the waveform of voltage across the inductor: If Δt is small, then A can be approximated as

$$A = \int_{t-\Delta t}^{t} V_L dt \approx V_L (t - \Delta t)\Delta t$$

Therefore,

$$I(t) - I(t - \Delta t) \approx \frac{V_L (t - \Delta t)\Delta t}{L} \qquad\qquad \text{Equation 5-17}$$

It is possible to write

$$V_L (t - \Delta t) = E(t - \Delta t) - V_o (t - \Delta t)$$

$$V_L (t - \Delta t) = E(t - \Delta t) - RI(t - \Delta t) \qquad\qquad \text{Equation 5-18}$$

Merging Equation 5-17 and Equation 5-18, Equation 5-19 was obtained. It is possible to represent as an iteration as given in Equation 5-20.

$$I(t) \approx I(t - \Delta t) + \frac{\Delta t}{L}[E(t - \Delta t) - RI(t - \Delta t)] \qquad\qquad \text{Equation 5-19}$$

$$I_n \approx I_{n-1} + \frac{\Delta t}{L}\left(E_{n-1} - RI_{n-1}\right)$$

Equation 5-20

Now iterative equation for the current could be applied to the Equation 5-9 and Equation 5-21 is obtained.

$$V_{pv,n+1} = NV_t \ln\left\{\frac{I_{ph} - I_{sat}}{I_{sat}} - \frac{1}{I_{sat}}\left[I_{pv,n} + \frac{\Delta t}{L}\left(V_{pv,n} - RI_{pv,n}\right)\right]\right\} - NR_s\left[I_{pv,n} + \frac{\Delta t}{L}\left(V_{pv,n} - RI_{pv,n}\right)\right]$$

Equation 5-21

It is possible to express Equation 5-21 in the form of $V_{pv,n+1} = G\left(V_{pv,n}\right)$ as given in Equation 5-22. Applying the condition for iteration, it is possible to find an inequality given in Equation 5-23,

$$G\left(V_{pv,n}\right) = NV_t \ln\left\{\frac{I_{ph} - I_{sat}}{I_{sat}} - \frac{1}{I_{sat}}\left[I_{pv,n} + \frac{\Delta t}{L}\left(V_{pv,n} - RI_{pv,n}\right)\right]\right\} - NR_s\left[I_{pv,n} + \frac{\Delta t}{L}\left(V_{pv,n} - RI_{pv,n}\right)\right]$$

Equation 5-22

$$V_{pv} < \frac{L}{\Delta t}\left(I_{ph} + I_{sat} - I_{pv}\right) + RI_{pv} - \frac{LNV_t}{\left(L - NR_s \Delta t\right)}$$

Equation 5-23

Figure 5-11 shows the analytical results with an inductor in series at different inductances. The blue curve represents variation of the PV cell output voltage with the load resistance while the other three curves represent the convergence limits for different values of inductance. Figure 5-12 shows the voltage and current of PV panel near the failure point.

According to the theoretical analysis, the convergence limits for 10mH, 1mH, 100μH and 10μH are 3.5 Ω, 5.7 Ω, 8 Ω and 11.2 Ω respectively. Comparing with results shown in Figure 5-12, the simulation model fails at 2.9 Ω, 5.1 Ω, 7.3 Ω and 9.5 Ω for inductances of 10mH, 1mH, 100μH and 10μH. Thus the simulation model fails near the points predicted by the theoretical analysis.

Figure 5-11: Variation of convergence limit with load resistance for different inductor values and output voltage of the photovoltaic panel (V_{pv}) with load resistance

(a) L = 0.00001 H

(b) L = 0.0001 H

(c) L = 0.001 H

(d) L = 0.01 H
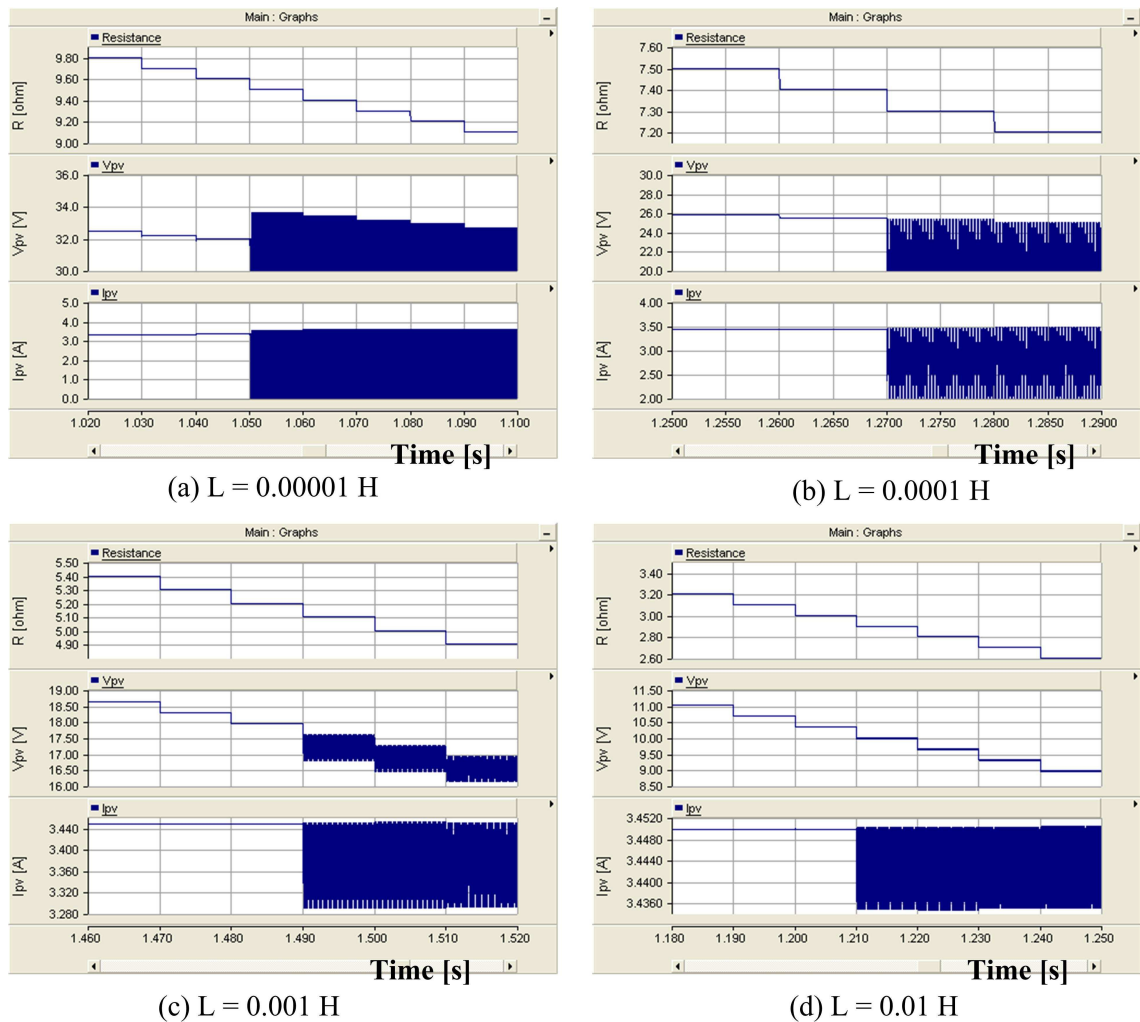
Figure 5-12: Failure point of the simulation model of the photovoltaic panel for different inductance values

5.2.5 Comparison of characteristic curves

The characteristic curves of the SM110-24P were determined from the manufacturer's datasheet. Figure 5-13 compares the mapped characteristic curve from the datasheet (in green) and characteristic curve obtained from the simulation model (in blue) for different irradiance values. At 400W/m^2, characteristic curve data points obtained from the datasheet is not very accurate. Thus simulation model characteristic curve is slightly different from the characteristic curve mapped from the datasheet but can be considered reasonable.
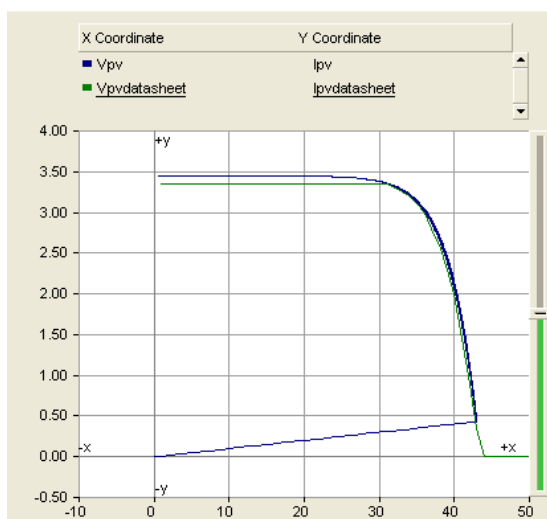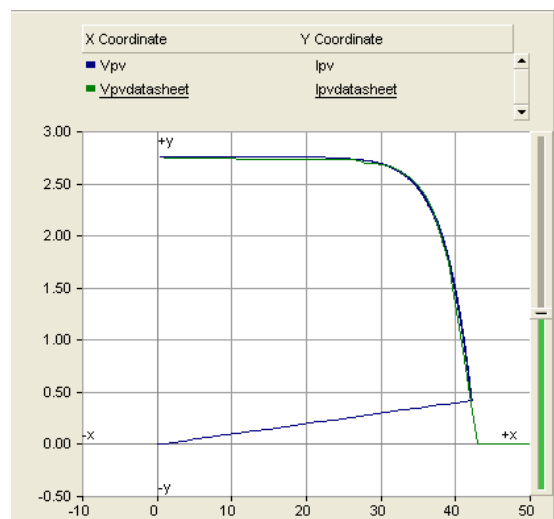
(a) 1000 W/m^2 (b) 800 W/m^2
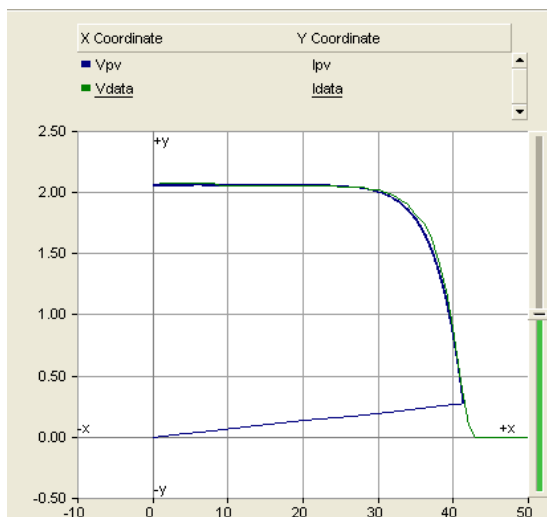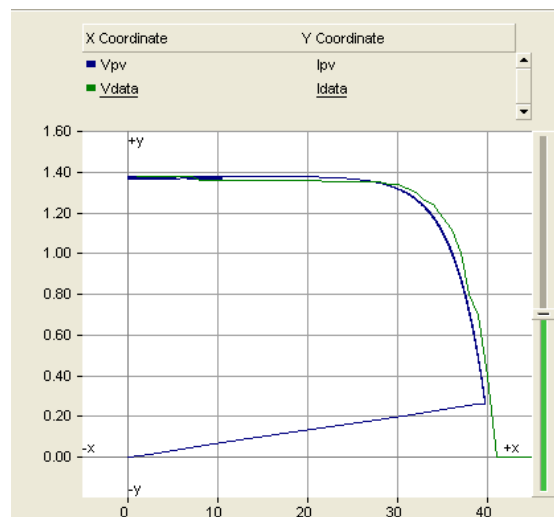
(c) 600 W/m^2 (d) 400 W/m^2

Y-axis: Current [A], X-axis: Voltage [V]; Blue: Simulation model, Green: Datasheet

Figure 5-13: Comparison of characteristic curves at 25°C for different irradiance conditions

5.3 DESIGN OF PHOTOVOLTAIC (PV) EMULATOR

In order to complete research on the photovoltaic system, a photovoltaic panel or module is necessary. The cost of a photovoltaic panel is significant compared with the rest of the components required for the system. Even if it were possible to spend money to buy the required photovoltaic panel, another drawback will be producing the necessary environmental conditions especially considering the weather in Manchester. Some researchers have used artificial lamps as an alternative to the sun-light [78]. Different environmental conditions could be achieved by varying the intensity of the lamps. This is a feasible solution; however it wastes a lot of energy due to the poor efficiency of a photovoltaic panel.

For research purposes the most attractive solution would be to have a photovoltaic emulator with reasonable accuracy. There are several advantages associated with a PV emulator. It is comparatively cheaper than a similarly rated real PV panel. Variable environmental conditions could be replicated easily with comparatively lower energy loss. Finally the PV emulator could be tuned to replicate characteristics of different PV panels in a short time. Therefore the PV emulator could be used for different research activities. This section presents the developments of a photovoltaic emulator which is based on linear voltage regulators.

The typical application diagram of TL783 variable voltage regulator is presented in Figure 5-14 [117]. The voltage across the resistor R_1 is kept typically around 1.25 V. The value of the output voltage is determined by the resistance of resistor R_2 as given in Equation 5-24. Current flowing through the common terminal (I_{ADJ}) is negligible compared with the current flowing through resistors R_1 and R_2, therefore the output voltage of the adjustable voltage regulator could be approximated to Equation 5-25.

$$V_{out} = 1.25\left(1+\frac{R_2}{R_1}\right) + I_{ADJ}R_2 \qquad\qquad \text{Equation 5-24}$$

$$V_{out} \approx 1.25\left(1+\frac{R_2}{R_1}\right) \qquad\qquad \text{Equation 5-25}$$
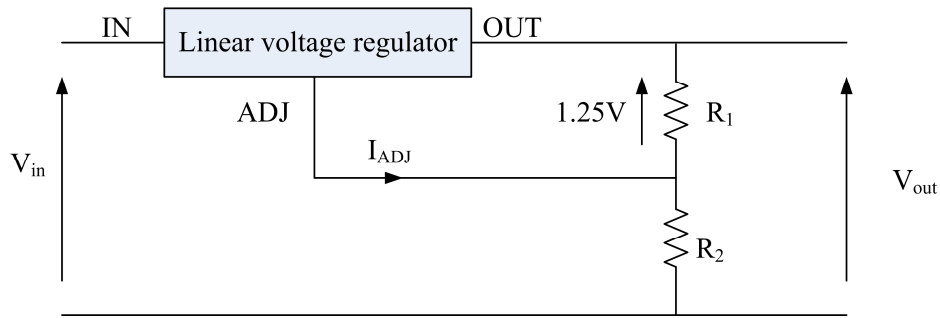
Figure 5-14: Typical application diagram of an adjustable linear voltage regulator

The idea behind the design of this PV emulator is to replace the variable resistor, R_2, with external circuitry. The external circuitry would sense the output current of the regulator. This current is fed to a controller which represents the characteristic equation of a photovoltaic panel. The output of the controller gives the necessary voltage of the panel corresponding to the output current.

Table 5-3 presents the main data of the commonly used adjustable voltage regulator [117-119]. The rated current and the maximum input voltage are the main parameters to be considered in selection. It is possible to increase the current carrying capability by connecting number of regulators in parallel. The maximum output voltage should be more than the open circuit voltage of the photovoltaic panel. A typical voltage regulator produces about 2 V drop across the output and input terminals. Therefore the maximum input voltage of the voltage regulator should be maximum output voltage plus the voltage drop across the input and output terminals.

Table 5-3: Important parameters of typical adjustable voltage regulators

Parameter	Value		
	LM317	LM338	TL783
Output voltage range [V]	1.2 to 37	1.2 to 32	1.25 to 125
Continuous current [A]	1.5	5	0.7
Reference voltage [V]	1.25	1.24	1.27
Maximum input voltage [V]	40	40	125

The feasibility of the method of controlling adjustable voltage regulator via an external circuit was tested with the aid of the simple electronic circuit presented in Figure 5-15.

The sinusoidal signal was generated from a laboratory signal generator and is fed to a non-inverting summing amplifier. Figure 5-16 shows the output voltage and the voltage at the ADJ terminal for 100 Hz and 10 kHz sinusoidal signal. According to the results, it is possible to use an adjustable voltage regulator with external control circuit.
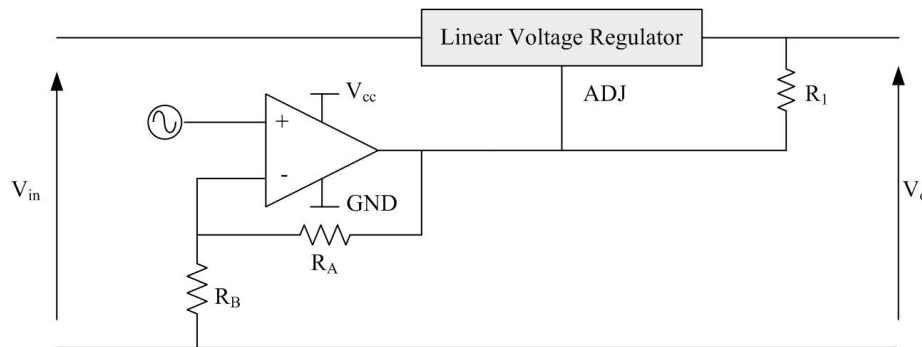
Figure 5-15: Feasibility testing of adjustable voltage regulator for the application of PV Emulator

Time (2ms/div)   Time (20µs/div)

Y-axix [Top: Regulator output voltage (2V/div), Bottom: Voltage at ADJ terminal]

(a) Frequency = 100Hz   (b) Frequency = 10kHz
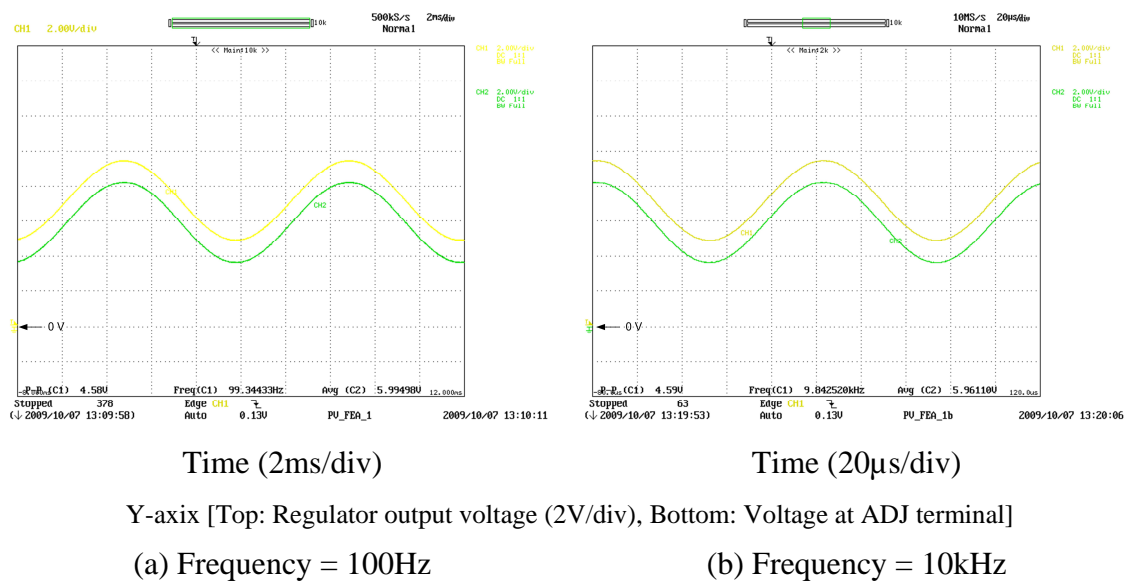
Figure 5-16: Response of the adjustable voltage regulator to the signals applied from the signal generator

5.3.1 Design of Photovoltaic Emulator with TL783 Adjustable Linear Voltage Regulator

Figure 5-17 presents the block diagram of the adjustable voltage regulator based photovoltaic emulator. A hall-effect current transducer is used to measure the current. The control circuit replicates the characteristic equation of a photovoltaic panel. The

control signal applied to the ADJ terminal of the adjustable voltage regulator ensures that the correct voltage is applied for corresponding current.
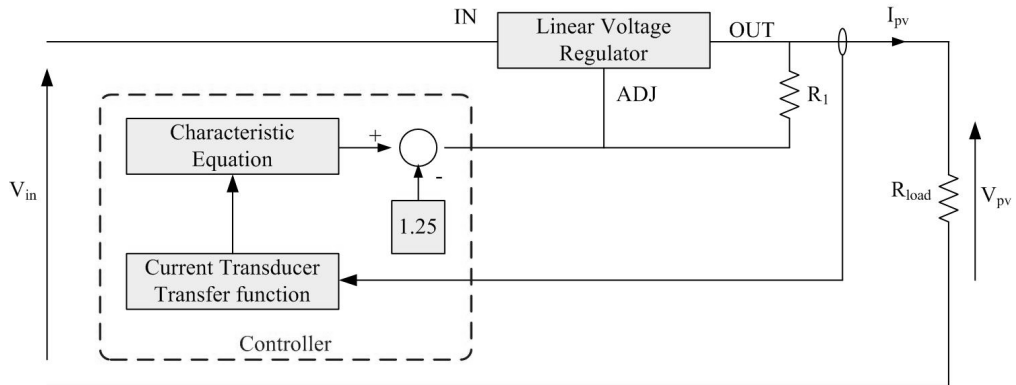
Figure 5-17: Block diagram of the PV Emulator

Equation 5-1 is the characteristic equation of a photovoltaic panel taking output current of the panel as the dependent variable. By swapping the variables, the output voltage of a PV panel is made to be the dependent variable and assuming zero series resistance, Equation 5-26 results.

$$V_{PV} = NV_t \ln\left(\frac{I_{ph} - I_{PV} + I_{sat}}{I_{sat}}\right)$$ Equation 5-26

Since $I_{sat} << (I_{ph} - I_{pv})$, it is possible to approximate further with $I_{ph} - I_{pv} + I_{sat} \approx I_{ph} - I_{pv}$

Then from Equation 5-26,

$$V_{PV} \approx NV_t \ln\left(\frac{I_{ph} - I_{PV}}{I_{sat}}\right)$$

$$V_{PV} \approx NV_t \left\{\ln(I_{ph} - I_{PV}) - \ln(I_{sat})\right\}$$

$$V_{PV} \approx NV_t \ln(I_{ph} - I_{PV}) - NV_t \ln(I_{sat})$$ Equation 5-27

The approximated output voltage of the photovoltaic panel is given in Equation 5-27. However, the voltage drop across the resistor (R_1) should be compensated in the

controller. Therefore the output of the controller could be written as in Equation 5-28. Figure 5-18 presents the block diagram of the PV emulator based on Equation 5-28.

$$V_{ref} \approx NV_t \times \ln(I_{ph} - I_{PV}) - NV_t \times \ln(I_{sat}) - 1.25 \qquad \text{Equation 5-28}$$
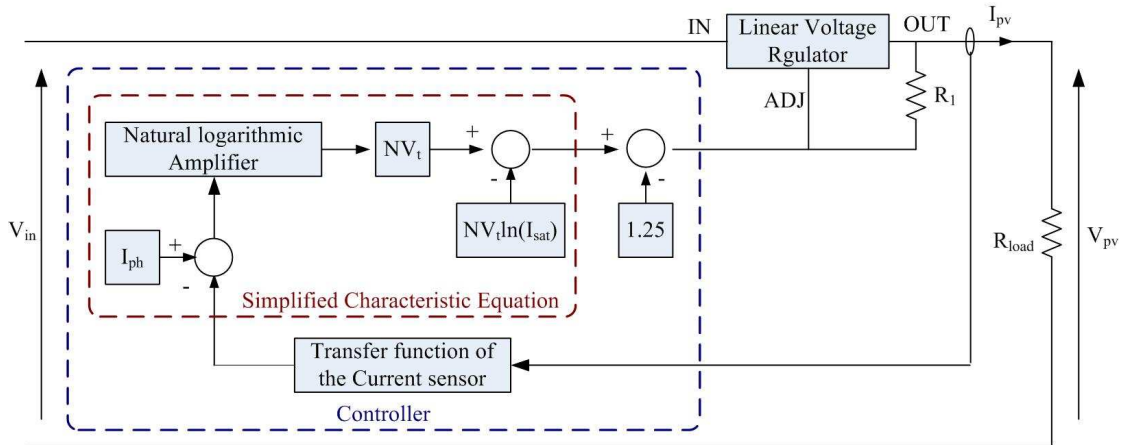
Figure 5-18: Block diagram of the photovoltaic emulator with simplified characteristic equation of the photovoltaic panel

5.3.1.1 Transfer function of the current transducer

Figure 5-19 presents the characteristic curve of the current transducer HY20 and the relationship is mathematically given according to Equation 5-29 [120]. The maximum current (I_{PN}) of the current transducer is 20A. The inverse of the transfer function of the current transducer is implemented in the controller; therefore output current of the linear voltage regulator is available.
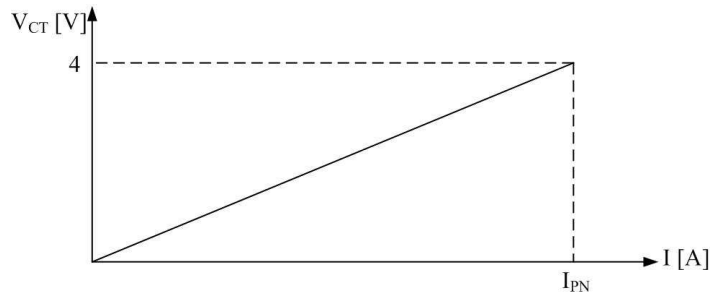
Figure 5-19: Characteristic curve of the current transducer

$$V_{CT} = \frac{4}{I_{PN}} \times I \qquad \text{Equation 5-29}$$

5.3.1.2 Natural logarithmic amplifier

Equation 5-28 is comprised of logarithmic terms; therefore an analogue logarithmic amplifier is necessary. The schematic diagram of a logarithmic amplifier is shown in Figure 5-20 [121]. The relationship between the input and the output of the amplifier is given by Equation 5-30 and it could be approximated to Equation 5-31 assuming $\frac{7}{6.9}$ is equal to one.
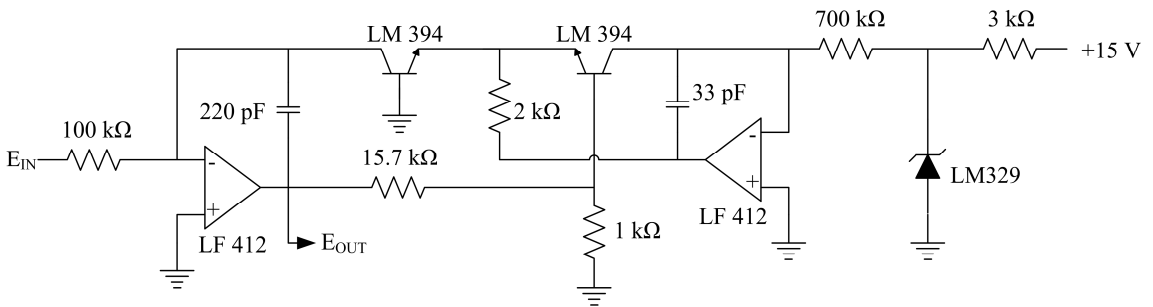
Figure 5-20: Schematic diagram of a logarithmic amplifier

$$E_{OUT} = -\frac{kT}{q} \times 16.7 \times \ln\left(\frac{7}{6.9} E_{IN}\right)$$ Equation 5-30

$$E_{OUT} \approx -\frac{kT}{q} \times 16.7 \times \ln\left(E_{IN}\right)$$ Equation 5-31

If $\left(I_{ph} - I_{pv}\right) = E_{IN}$, then Equation 5-28 can be written as in Equation 5-32 with the aid of Equation 5-2. Then Equation 5-31 and Equation 5-32 can be merged, which is shown in Equation 5-33. The block diagram of the photovoltaic emulator based on Equation 5-33 and current transducer transfer function is shown in Figure 5-21.

$$V_{ref} = -\frac{AN}{16.7}\left[-\frac{kT}{q} \times 16.7 \times \ln\left(E_{IN}\right)\right] - NV_t \ln\left(I_{sat}\right) - 1.25$$ Equation 5-32

$$V_{ref} = -\frac{AN}{16.7} E_{OUT} - NV_t \ln\left(I_{sat}\right) - 1.25$$ Equation 5-33
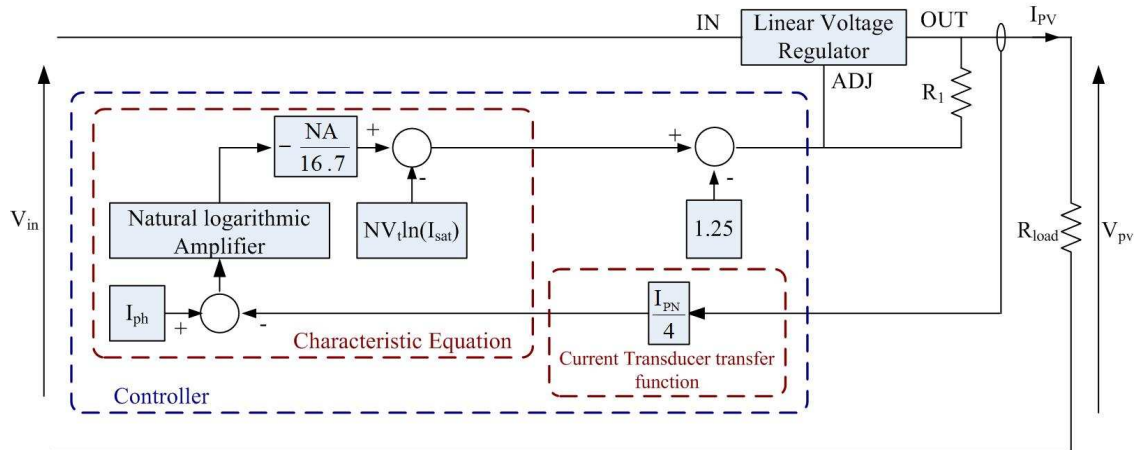
Figure 5-21: Block diagram of the photovoltaic emulator based on Equation 5-33 and current transducer transfer function

The thermal voltage (V_t) and diode saturation current (I_{sat}) depend on temperature and irradiance. In this design, the effect of temperature is neglected and as a result the thermal voltage can be treated as a constant. However the diode saturation current should be adjusted accordingly to the irradiance change. Equation 5-33 can be simplified to Equation 5-35 when V_a is defined as in Equation 5-34. Then V_a can be changed manually according to irradiance variations.

$$V_a = NV_t \ln(I_{sat}) + 1.25 \qquad\qquad\qquad \text{Equation 5-34}$$

$$V_{ref} = -\frac{AN}{16.7}E_{OUT} - V_a \qquad\qquad\qquad \text{Equation 5-35}$$

Analysing the characteristic curve of the photovoltaic panel, it is clear that the variation of the output current at low voltages is effectively insignificant and close to the photovoltaic current (I_{ph}). The current transducer is not accurate enough to measure the variations at low voltages. Further at low voltages the input to the natural logarithmic amplifier is very small and consists of a considerable amount of noise. Therefore the emulator does not behave properly at low voltage. An additional block is added to the PV emulator to overcome this problem as shown in Figure 5-22. In this improved model, the characteristic curve is divided into two regions. At high voltages the emulator follows the characteristic equation while at low voltages emulator behaves as a constant current controller. The change-over voltage is selected such a way that the characteristic curve controller is not disturbed.
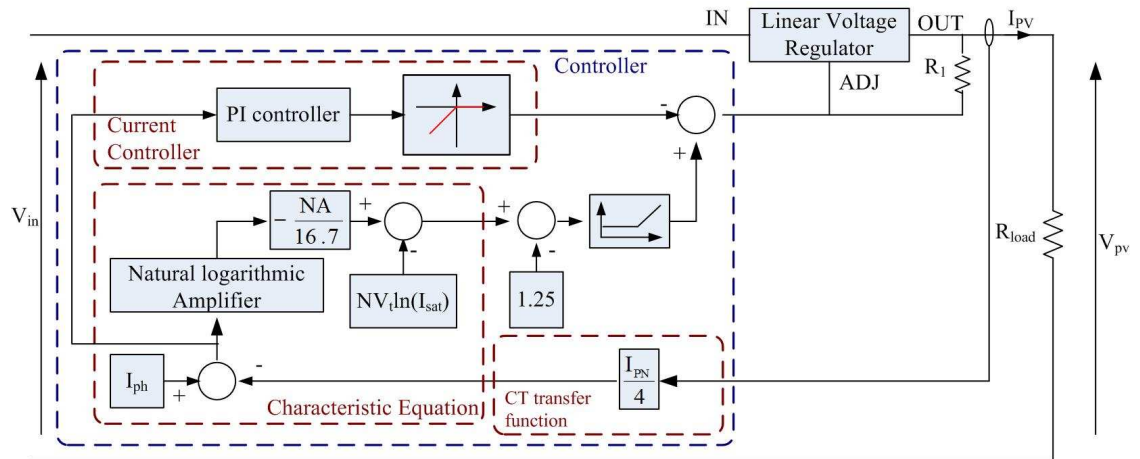
Figure 5-22: Photovoltaic emulator with additional circuitry which behaves properly at low voltages

However, emulator model shown in Figure 5-22 takes the photocurrent as the reference for the current controller. This does not performe well experimentally; therefore the system was slightly changed as shown in Figure 5-23. In this model a separate reference is used for the current controller and this is less than the photovoltaic current. The current reference is approximately equal to the current corresponding to the controller change-over voltage.
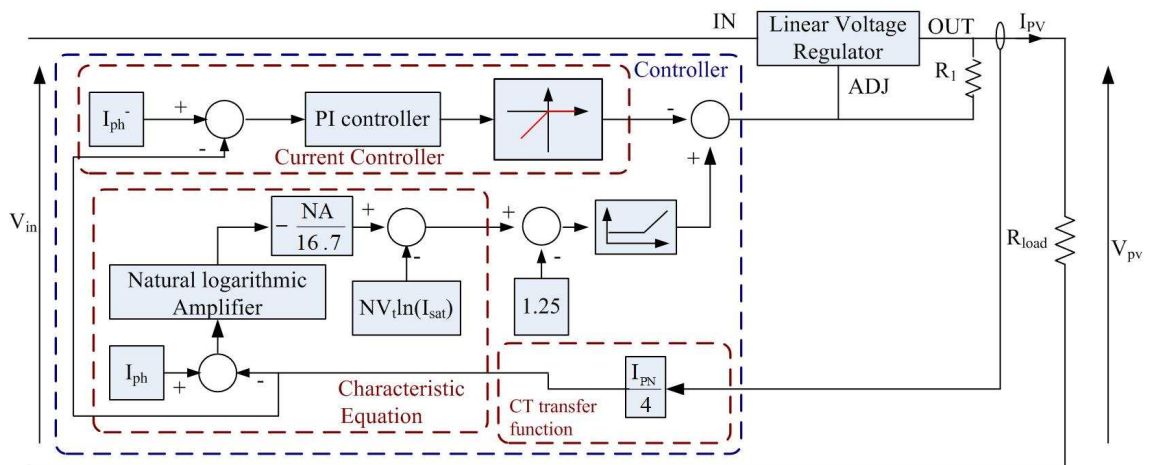
Figure 5-23: Final model of the photovoltaic emulator

5.3.1.3 Results of the photovoltaic emulator

SM110-24P photovoltaic panel was emulated from the adjustable voltage regulator based photovoltaic emulator. Table 5-4 presents the gains theoretically calculated and experimentally used for the photovoltaic emulator for different irradiance conditions

based on the supply voltage applied to the controller. The deviations of theoretical and experimental values are very small.

Figure 5-24 presents the characteristic curves obtained from the simulation model and the photovoltaic emulator for the different irradiance settings. According to the results, it is clear that the photovoltaic emulator follows the characteristic curve.

Table 5-4: Theoretical and experimental gains used for the photovoltaic emulator

Parameter		$400W/m^2$	$600W/m^2$	$800W/m^2$	$1000W/m^2$
I_{ph}	Theoretical	1.38	2.07	2.76	3.45
	Experimental	1.30	2.05	2.70	3.40
V_a	Theoretical	41.2	39.9	38.9	38.2
	Experimental	40.5	38.5	38.5	38.8
I_{ph-}	Experimental	1.26	2.00	2.70	3.35
AN/16.7	Theoretical	7.76	7.76	7.76	7.76
	Experimental	7.76	7.76	7.76	7.76
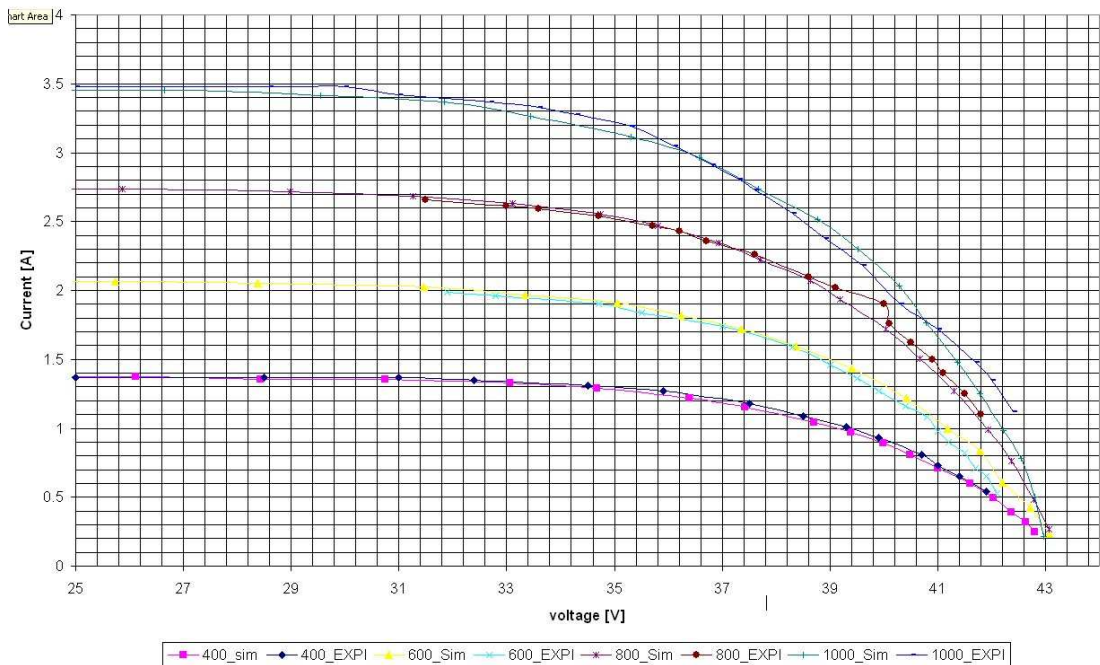
Figure 5-24: Comparison of characteristic curves obtained from simulation model and photovoltaic emulator

5.3.2 Development of photovoltaic emulator capable to emulate five panels

The emulator was extended to emulate five photovoltaic panels which could be operated in parallel. Therefore output power could be increased. Figure 5-25 presents the block diagram of the PV emulator which extended to five photovoltaic panels. The selection switch after current sensor enables to select the number of panels in parallel. Figure 5-26 shows the results obtained from the photovoltaic emulator at different irradiance values compared with the characteristic curve obtained from the simulation model. According the results it is clear that all the panels follow the characteristic curves. A picture of the developed photovoltaic emulator is presented in Figure 5-27.
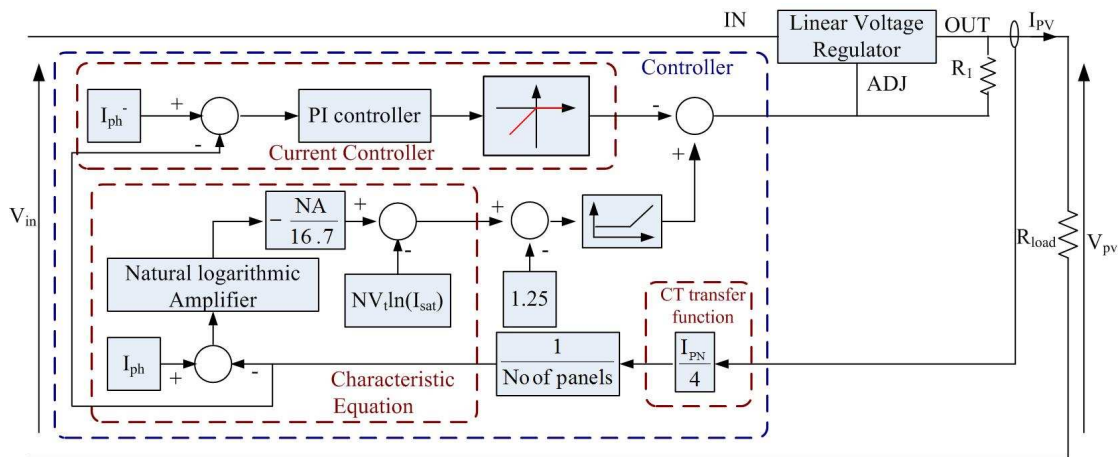
Figure 5-25: Photovoltaic emulator capable of emulating five photovoltaic panels

5.4 SUMMARY

The simulation model of the photovoltaic panel is developed based on the environmental conditions of irradiance and temperature. In order to avoid the numerical failures, it is necessary to insert an inductor in series with the controllable voltage source. A well-behaved photovoltaic panel model is available. An adjustable voltage regulator based photovoltaic emulator was designed, implemented and tested. The characteristic curves of the hardware emulator follows the curves obtained from the simulation model with reasonable accuracy. The single photovoltaic panel was extended to a five panel photovoltaic emulator with a single controller.

$G_a = 400$ W/m^2

$G_a = 600$ W/m^2

$G_a = 800$ W/m^2

$G_a = 1000$ W/m^2
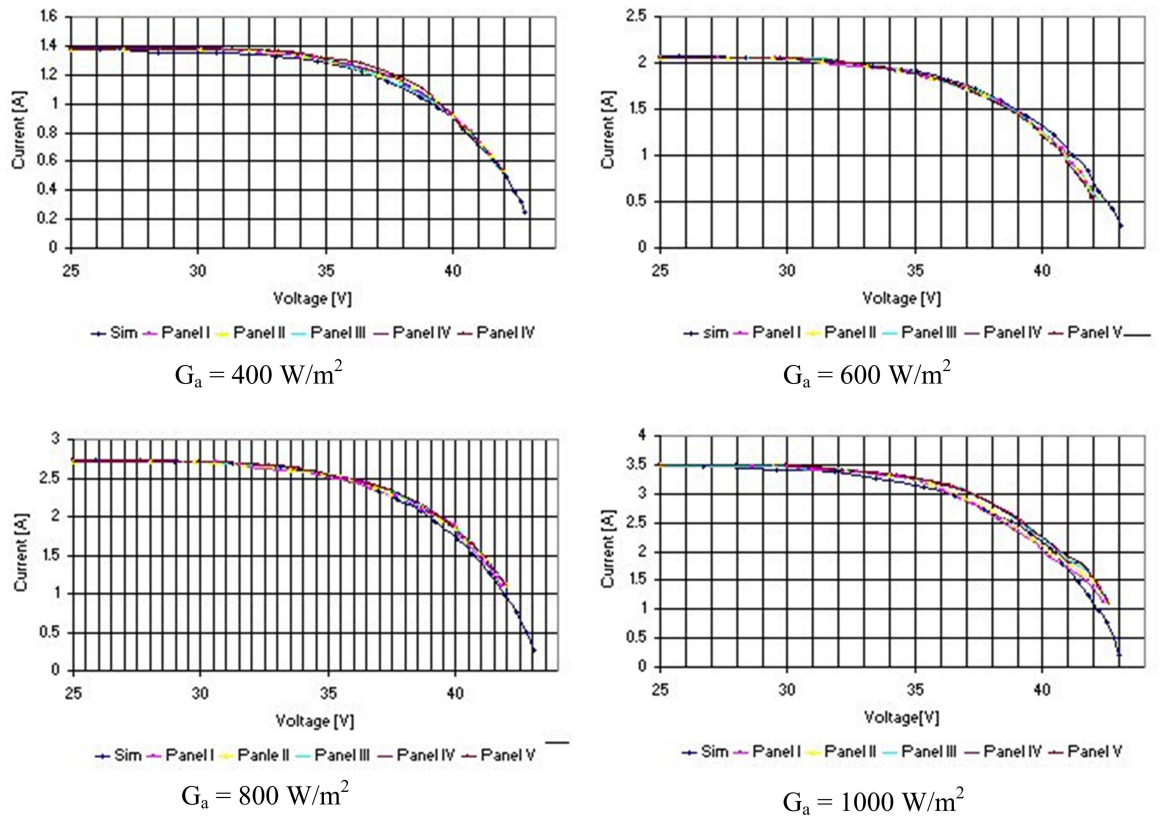
Figure 5-26: Comparison of photovoltaic panels results of simulation model and photovoltaic emulator
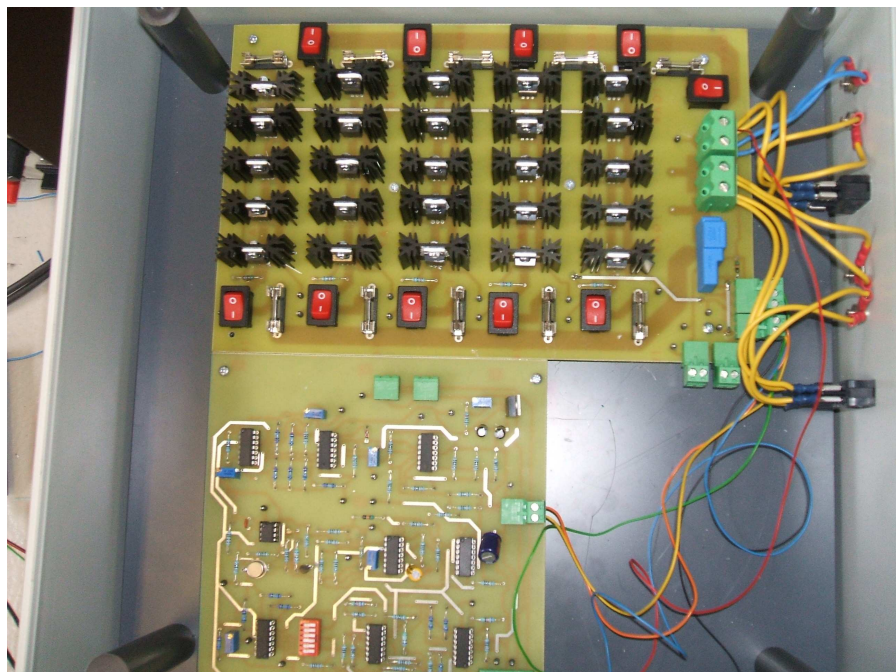
Figure 5-27: Picture of the photovoltaic emulator

CHAPTER 6

DESIGN AND TESTING OF POWER ELECTRONIC CONVERTERS

6.1 INTRODUCTION

The proposed microsource interface contains three power electronic converters. This chapter presents the design of three converters: the unidirectional dc-dc converter, the bi-directional dc-dc converter and the single-phase inverter. The designed converters were modelled and simulated using the EMTDC/PSCAD software. The prototypes of each converter were implemented and were controlled using dSPACE real time software. Simulation and experimental results are also included in this chapter.

6.2 DC-DC CONVERTER

Figure 6-1 shows the schematic diagram of the modified forward dc-dc converter topology. The switches (Q_1 and Q_2) are turned on simultaneously and the energy is transferred to the secondary winding of the transformer during the on-state of the switches. Stored energy in the inductor is released to the load during the turn-off period though the diode D_4. Design requirements of the modified forward dc-dc converter are given in Table 6-1.
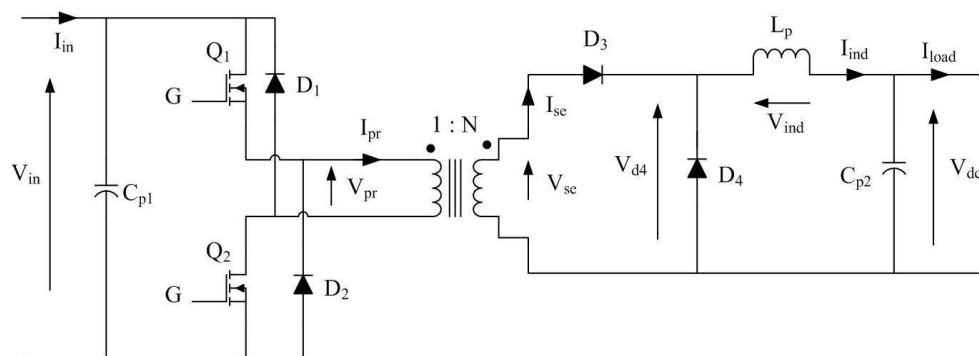
Figure 6-1: Schematic diagram of the modified forward dc-dc converter

Table 6-1: Design requirements of the modified forward dc-dc converter

Parameter	Value
Input voltage[V]	35
Output voltage [V]	360
Rated power [W]	200
Switching frequency [kHz]	40

The relationship between the input voltage and the output voltage of the modified forward dc-dc converter is given in Equation 6-1 where N and D are the turns-ratio of the transformer and the duty ratio respectively. Equation 6-1 is used to calculate the turns-ratio of the transformer. Equation 6-2 is obtained by considering the voltage across the inductor and the current flowing through the inductor during the off-state of switches. Inductance is calculated from Equation 6-2. Δi_{ind} and T_s are the current ripple of the inductor current and the period of the switching signal. For this topology the average inductor current is equal to the output load current.

$$\frac{V_{dc}}{V_{in}} = ND$$ Equation 6-1

$$L_p = \frac{V_{dc}(1-D)T_s}{\Delta i_{ind}}$$ Equation 6-2

Figure 6-2(a) presents the input current and the current flowing through the primary of the transformer. The excess charge (ΔQ_1) is stored in the input capacitor during the off state of the switches and it is related to the input current, the duty ratio and the period as in Equation 6-3. Then the capacitance of the input capacitor can be calculated from Equation 6-4 which is based on Equation 6-3 and the input voltage ripple (ΔV_{in}). Figure 6-2(b) shows the output current of the converter and the current flowing through the inductor. The amount of charge stored in the output capacitor depends on the inductor current ripple and the period of switching signal as in Equation 6-5. Considering the charge to be stored in the capacitor (ΔQ_2) and the output voltage ripple (ΔV_{dc}), the capacitance of the output capacitor is calculated from Equation 6-6. Table 6-2 highlights the details of passive components of the converter calculated using Equation 6-1 to Equation 6-6.

$$\Delta Q_1 = I_{in}(1-D)T_s \qquad\qquad \text{Equation 6-3}$$

$$C_{p1} = \frac{\Delta Q_1}{V_{in} \cdot \left(\dfrac{\Delta V_{in}}{V_{in}}\right)} \qquad\qquad \text{Equation 6-4}$$

$$\Delta Q_2 = \frac{\Delta i_{ind} T_s}{4} \qquad\qquad \text{Equation 6-5}$$

$$C_{p2} = \frac{\Delta Q_2}{V_{dc}\left(\dfrac{\Delta V_{dc}}{V_{dc}}\right)} \qquad\qquad \text{Equation 6-6}$$

(a) Input capacitor   (b) Output capacitor
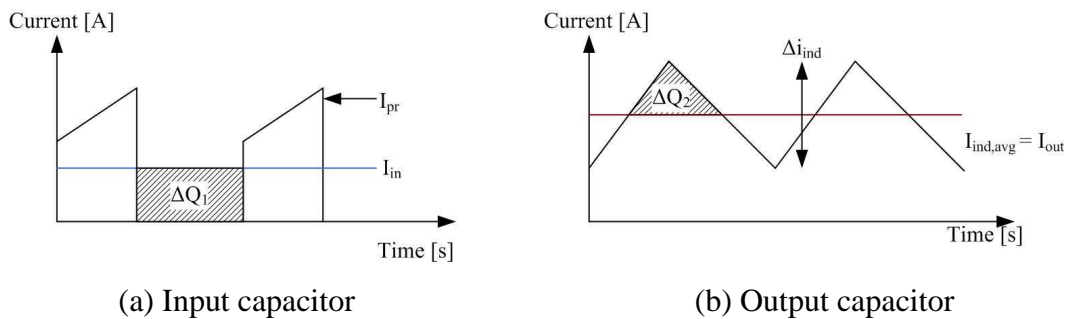
Figure 6-2: Charge stored in the capacitors of the modified forward dc-dc converter

Table 6-2: Passive component data of the modified forward dc-dc converter

Parameter	Values
Turns ratio of the transformer	26
Inductance of inductor [mH]	14.9
Capacitance of the high voltage side capacitor [µF]	220
Capacitance of the low voltage side capacitor [µF]	3300

All the semiconductor devices were selected based on the maximum peak current flowing through the device, rms current flowing through the device and the maximum reverse bias voltage across the devices. Approximately a factor of two was given as a safety margin.

A screen-capture of the modified forward dc-dc converter simulation model is shown in Appendix C. The losses of the semiconductor devices and the inductor are included in

the simulation model based on the values obtained from the datasheets and measured from the prototype.

Electrical isolation between dSPACE outputs and gate drive IC is achieved by means of an optocoupler. The IR2113 gate driver IC was used to drive the MOSFETs in the prototype. The input voltage, the input current and the output voltage were measured and captured into the dSPACE system. All the measurements were filtered by a first order analogue hardware filter with 5 kHz bandwidth before feeding them into the dSPACE system. An emergency switch was connected in series with the supply. An automatic protection system activates the emergency switch although it can be operated manually as well. Further protection via fuses is provided.

6.2.1 Open loop testing of the modified forward dc-dc converter

A 35V voltage source was connected to the input and a 850Ω resistor was connected to the output of the modified forward dc-dc converter for the open loop testing. The duration, step size and channel plot step of the simulation were set to 0.5s, 0.5μs and 1μs respectively. A laboratory power supply (SM2050) was connected to the modified forward dc-dc converter for the prototype testing. The cable connected between the modified forward dc-dc converter and the power supply resulted in a 0.7V drop thus the voltage at the input of the converter was 34.3V. The duty ratio was set to 0.4 and 0.5 for the simulation model and prototype testing respectively. A higher duty ratio was required for prototype to compensate the turn on delay of the switches. Table 6-3 summarises the experimental results.

Table 6-3: Summary of experimental results of the modified forward dc-dc converter

Parameter	Value
Output voltage of the converter [V]	351.3
Output current of the converter [mA]	0.425
Input current of the converter [A]	5.48
Input power [W]	188
Output power [W]	150
Efficiency of power conversion of the converter [%]	79.8

The results of the modified forward dc-dc converter are presented in Figure 6-3 to Figure 6-6. Figure 6-3 presents the pulse width modulation signal applied to the modified forward dc-dc converter. In the simulation model, a triangular wave was compared with a reference value to generate the PWM signal. A reference value was fed into the PWM generation block in dSPACE to generate the PWM signal for the prototype.

(a) Simulation   (b) Experiment
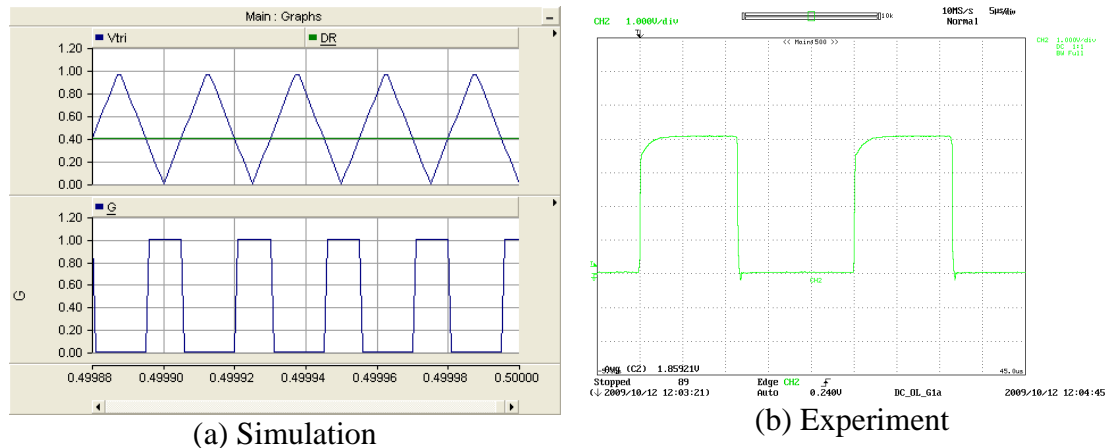
Y axis: Simulations – [top: V_{tri} and Duty ratio, Bottom: Gate signal], Experimental – [Gate signal to G_1: Green (1V/div)]; X axis: Time (Simulations: 20µs/div, Experiment: 5µs/div)

Figure 6-3: PWM signal applied to the modified forward dc-dc converter

Figure 6-4 presents the input voltage and the input current of the modified forward dc-dc converter. Averaged input current is also presented along with the input current of the converter in the simulation results. Average input current is plotted by sending the measured current through a low pass filter. The laboratory power supply current limit was set to 7A. Initially the input capacitor is not charged thus the input voltage dips and the input current is at its maximum. However a high inrush current is visible in the simulation model since there is no current limiter in the voltage source.

The effect of inrush current is visible in the output voltage and the output current (see Figure 6-5). The output voltage of the prototype takes longer time to reach the steady state when compared that with the simulation model.

(a) Simulation   (b) Experiment
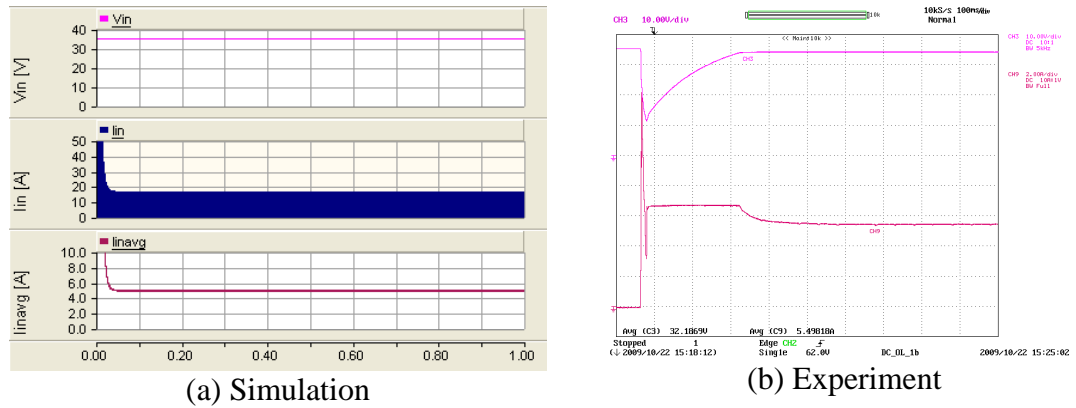
Y axis :V_{in} - Pink (10V/div, top), I_{in} – Maroon (2A/div, bottom) ; X axis: Time (100ms/div)

Figure 6-4: Input voltage and input current of the modified forward dc-dc converter

(a) Simulation   (b) Experiment
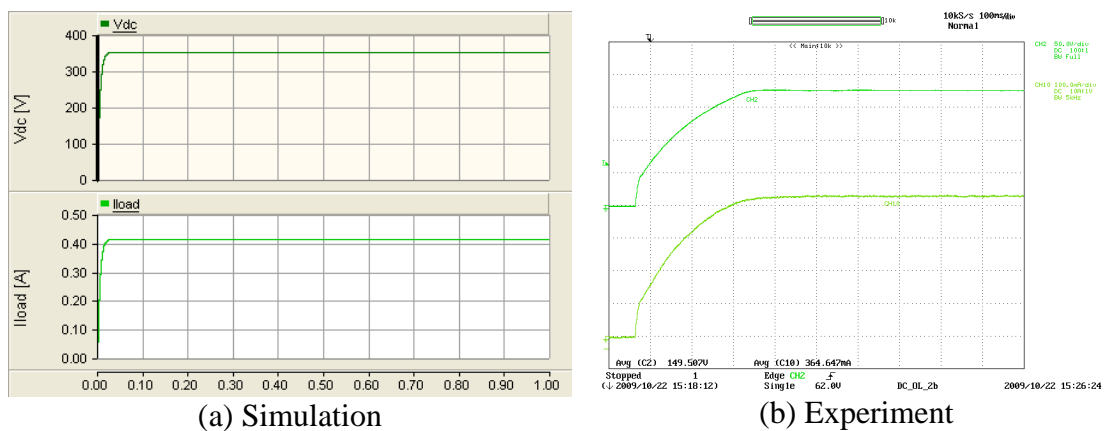
Y axis :V_{dc} – Dark green (100V/div), I_{load} – Light green (100mA/div), Exp. Scope bandwidth 5kHz ; X axis: Time (100ms/div)

Figure 6-5: Output voltage and output current of the modified forward dc-dc converter

The voltage across the inductor and the current flowing through the inductor are presented in Figure 6-6. Current increases when the voltage is positive and the reverse happens when voltage is negative. The inductor current ripple is about 80% and 60% for the simulation model and the prototype respectively. The voltage across the inductor has oscillations during the turn-on period. This is due the parasitic components of the high frequency transformer.

Detailed results of the modified forward dc-dc converter are included in Appendix C. Figure 6-7 presents the screen capture of the measured quantities plotted in the dSPACE real time interface software. The measurements are plotted with time as well as the instantaneous values displayed.

(a) Simulation   (b) Experiment
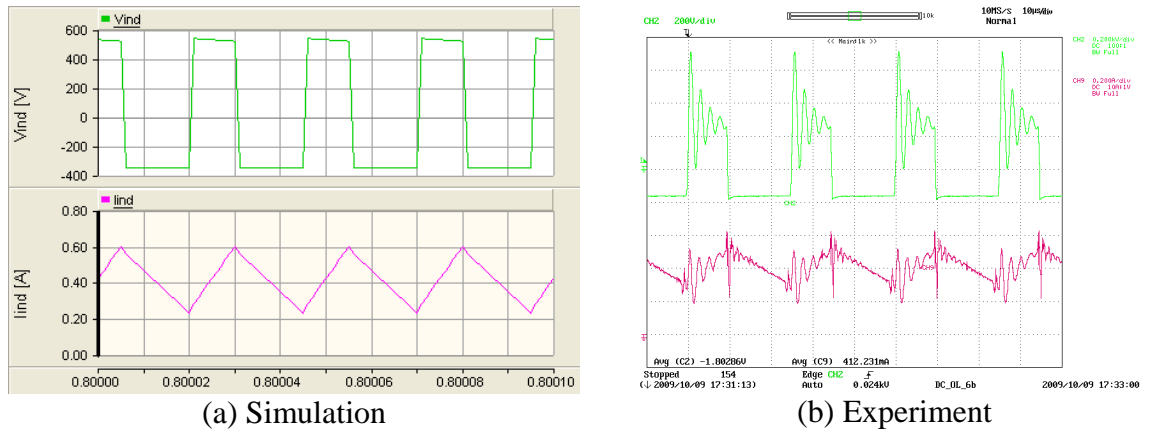
Y axis :V_{ind} - Green (200V/div-simulation, 400V/div-Experiment), I_{ind} - Pink (0.2A/div) ; X axis: Time (10µs/div)

Figure 6-6: Voltage across the inductor and current flowing through the inductor of the modified forward dc-dc converter
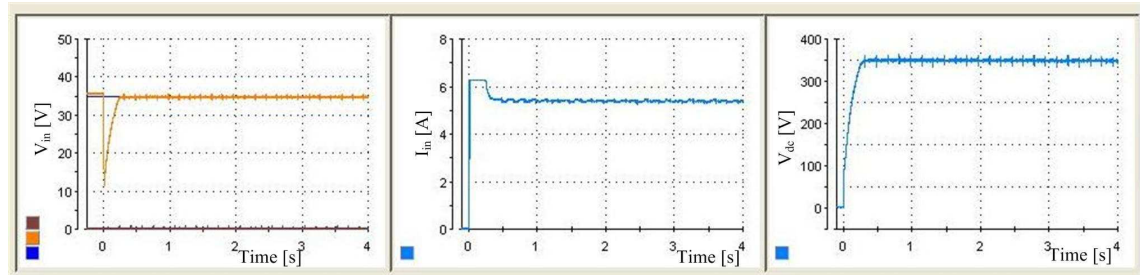
Figure 6-7: Screen capture of measurements plotted in dSPACE

6.3 BI-DIRECTIONAL DC-DC CONVERTER

The schematic diagram of the selected bi-directional dc-dc converter topology is presented in Figure 6-8 and the design requirements of the bi-directional dc-dc converter are given in Table 6-4. Switches Q_1, Q_2, Q_3 and Q_4 are operated during the step-down mode while switches Q_5 and Q_6 are operated during the step-up mode.

Table 6-4: Design requirements of the bi-directional dc-dc converter

Parameter	Values
Voltage at high voltage side, V_{dc} [V]	360
Minimum voltage at low voltage side, V_L [V]	36
Rated power, P [W]	200
Switching frequency, f_s [kHz]	20
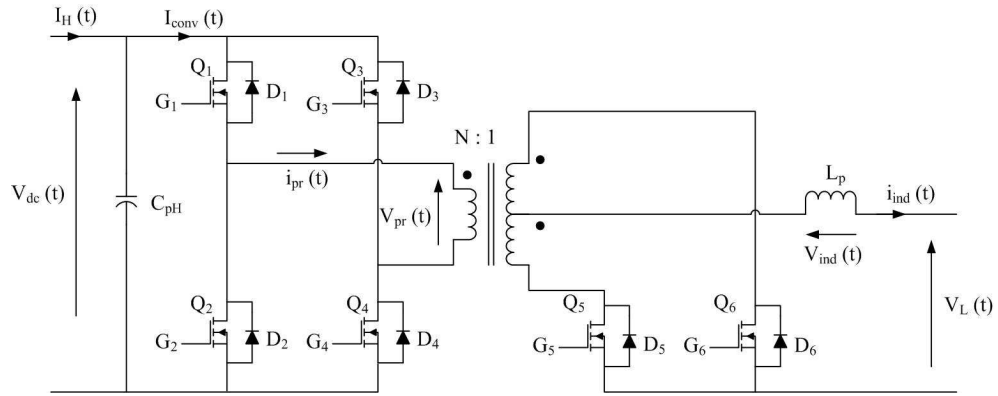
Figure 6-8: Schematic diagram of the bi-directional dc-dc converter

Values for the passive components were calculated considering the step-down mode of the bi-directional dc-dc converter. The relationship between voltage at high-voltage side and low-voltage side voltages is given by the Equation 6-7 where D and N are the duty ratio and the turns-ratio of the transformer respectively. Equation 6-7 is used to calculate the turns-ratio of the converter. The inductance of the inductor in the bi-directional dc-dc converter can be calculated from Equation 6-8 which is derived by considering the voltage across the inductor and the current flowing through the inductor during the on-state of the switches. t_{on} and ΔI_{ind} are turn-on period of the switch and current ripple of the inductor current.

$$\frac{V_L}{V_{dc}} = \frac{2D}{N} \qquad\qquad\qquad \text{Equation 6-7}$$

$$L_p = \left(\frac{V_{dc}}{N} - V_L\right)\frac{t_{on}}{\Delta I_{ind}} \qquad\qquad\qquad \text{Equation 6-8}$$

The capacitance of the high voltage side capacitor can be calculated by considering the currents I_{conv} and I_H (see Figure 6-8) and Figure 6-9 shows the ideal I_{conv} and I_H waveforms. The average current of I_{conv} should be equal to the input current to the converter (I_H). Equation 6-9 represents the amount of charge that should be stored in the capacitor (ΔQ) during steady state. Using Equation 6-10, the capacitance of the high voltage side capacitor could be calculated with the aid of high voltage side ripple (ΔV_{dc}) and the charge which should be stored in the capacitor.

$$\Delta Q = \frac{I_H(0.5 - D)}{f_s}$$

Equation 6-9

$$C_{pH} = \frac{\Delta Q}{V_{dc}\left(\dfrac{\Delta V_{dc}}{V_{dc}}\right)}$$

Equation 6-10
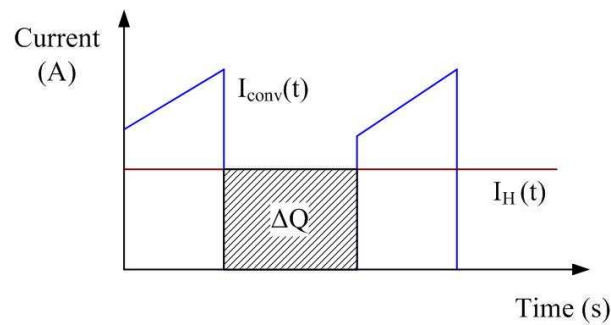
Figure 6-9: Input and output current through the high side capacitor node of the bi-directional dc-dc converter

Table 6-5 shows corresponding component values calculated from above Equation 6-7 to Equation 6-10.

Table 6-5: Details of the passive components of the bi-directional dc-dc converter

Parameter	Values
Turns ratio of the transformer	6
Inductance of inductor [µH]	303
Capacitance of the high voltage side capacitor [µF]	500

All the semiconductor devices were selected based on the maximum peak current flowing through the devices, rms current flowing through the devices and the maximum reverse bias voltage which appears on the devices. Approximately a factor of two was used as a safety margin.

During step-up mode, switches (Q_1, Q_2) and (Q_3, Q_4) operate as pairs and are turned on alternatively. Switches Q_5 and Q_6 are also turned on alternatively during step-up mode. However the PWM signal is generated by comparing a dc reference value with a triangular wave which produces continuous on and off signal. The logic circuitry shown

in Figure 6-10 is used to extract the correct gate signal to each switch from the continuous PWM signal. The behaviour of the logic circuitry is illustrated in Figure 6-11.
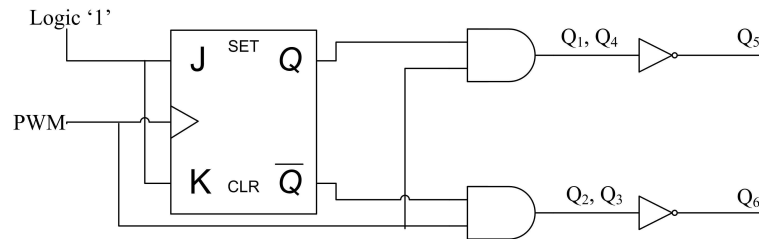
Figure 6-10: Logic circuit used to extract gate signal from PWM signal
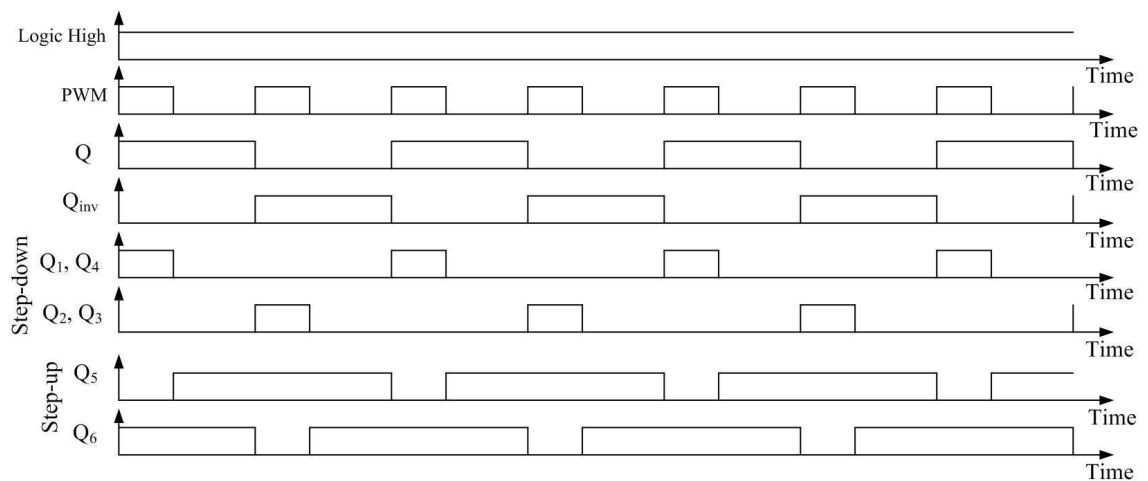
Figure 6-11: Behaviour of the gate signal extractor used in the bi-directional dc-dc converter

A screen capture of the simulation model is included in Appendix C. In the prototype, the PWM signal generated by the dSPACE real-time software is sent through an optical isolator for protection purposes. The PWM signal is then fed to the logic circuitry presented in Figure 6-10 to generate gate signals to each switch. An IR2113 gate driver IC was used to drive the MOSFET switches. The current flowing from the low-voltage side, the voltage of the low-voltage side and the voltage at the high-voltage side of the converter are measured and fed into the dPSACE real time interface. All the measurements are filtered by a first order low pass analogue hardware filter with 5 kHz bandwidth. The bi-directional dc-dc converter automatically shuts down during a fault if the measurements exceed their upper limit. Furthermore, the emergency switches can be operated manually and fuses are placed at appropriate positions.

The gate signals applied during step-down and step-up mode are presented in Figure 6-12 and Figure 6-13 respectively. The duty ratio applied to the PWM generator in simulation model and in prototype was different. Thus the turn-on and the turn-off periods were different. However the logic circuitry performs according to the theoretical analysis.

(a) Simulation　　　　　　　(b) Experiment
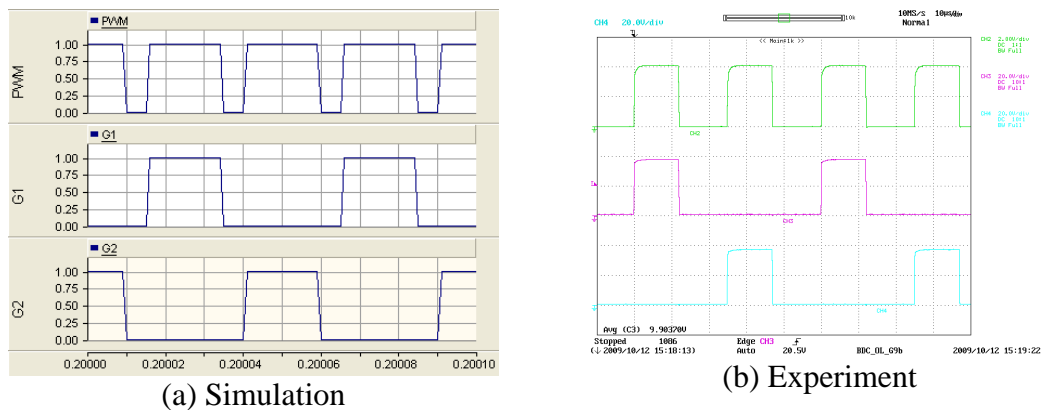
Y axis : Simulations- [Top: PWM, Middle: (Q_1, Q_4), Bottom: (Q_2, Q_3)], Experiment – [Top: PWM - Green (2V/div), Middle: (Q_1, Q_4) - Pink (2V/div), Bottom: (Q_2, Q_3) - Blue (2V/div)] ; X axis: Time (10µs/div)

Figure 6-12: Gate signals during step-down mode of the bi-directional dc-dc converter

(a) Simulation　　　　　　　(b) Experiment
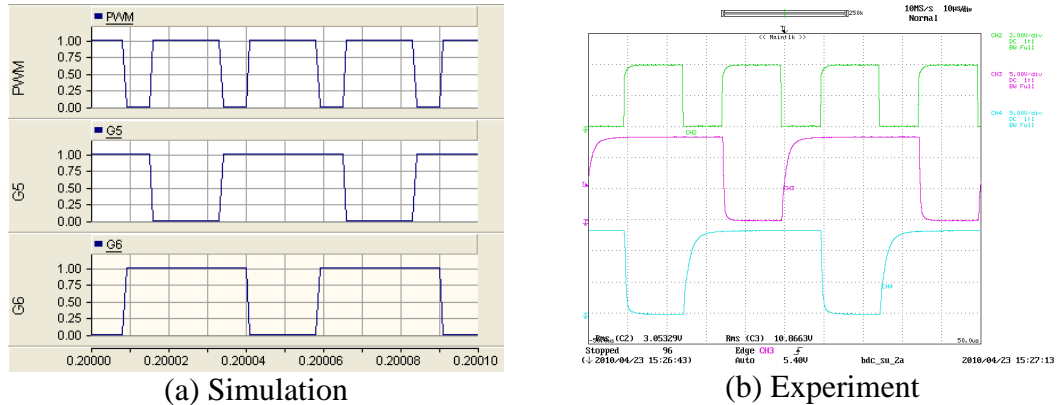
Y axis :Simulations – [Top: PWM, Middle: Q_5, Bottom: Q_6], Experiment - [Top: PWM - Green (2V/div), Middle - Q_5 - Pink (5V/div), Bottom - Q_6 - Blue (5V/div)] ; X axis: Time (10µs/div)

Figure 6-13: Gate signal applied during step-up mode of bi-directional dc-dc converter

6.3.1 Open loop testing of bi-directional dc-dc converter

6.3.1.1 Step-up mode

The test set-up for the step-up mode testing of the bi-directional dc-dc converter is presented in Figure 6-14. A laboratory power supply (Lambda Gen 300-5) was used to

test the prototype. The voltage of the power supply was set to 47.6V and the current limit was set to 3.7A. A negative temperature coefficient resistor was connected in series with the inductor to reduce the inrush current. The inrush current limiter experienced a 2.5V drop in steady state. Therefore the source voltage was set to 45V in the simulation model. A load resistor of 850Ω was connected at the high voltage side of the converter. The duty ratio was set to 0.72 and 0.76 for the simulation model and prototype. The duty ratio is slightly increased in the prototype to compensate delays in the gate drive.
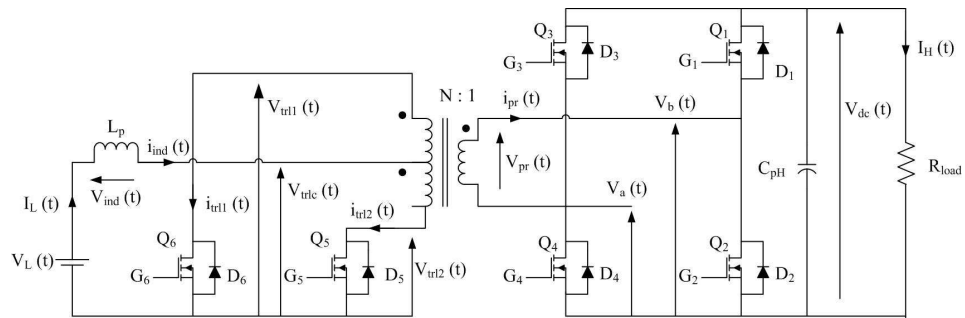
Figure 6-14: Test set-up used to test the operation of the step-up mode of the bi-directional dc-dc converter

The duration, solution time step and channel plot step of the simulation were set to 0.3s, 1μs and 1μs respectively. A summary of experimental results are presented in Table 6-6. Figure 6-15 to Figure 6-17 show the results of the bi-directional dc-dc converter with simulation and experimental results on the left and right hand side.

Table 6-6: Summary of experimental results of the bi-directional dc-dc converter at step-up mode

Parameter	Value
Voltage at high voltage end of the converter [V]	353
Current delivered to the load [mA]	424
Voltage supply output current [A]	3.55
Input power to the converter[W]	159
Output power from the converter[W]	150
Efficiency of power conversion of the converter [%]	94.3

The voltage at the low voltage end of the bi-directional dc-dc converter and the supply current are presented in Figure 6-15. The inrush current limiter is not included in the simulation model thus a high inrush current is experienced. Initially the voltage supply delivers maximum output current, and then decays to the steady state value in the prototype. Figure 6-16 shows the high side voltage and current flowing through the load. The prototype takes longer time to settle because of the operation of inrush current limiter.

(a) Simulation   (b) Experiment
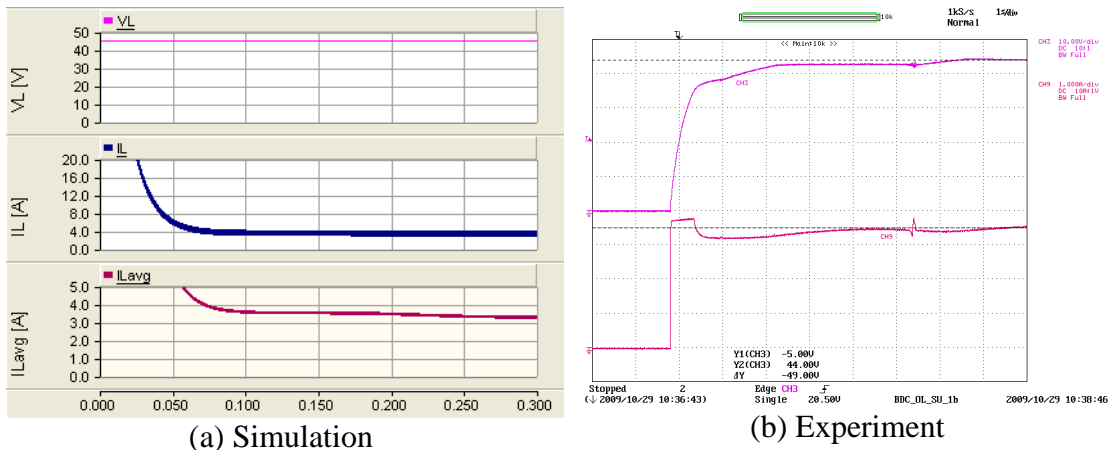
Y axis :V_L - Pink (10V/div), I_L – Maroon (1A/div) ; X axis: Time (50ms/div-Simulation,1s/div-Experiment)

Figure 6-15: Voltage at the low-voltage end of the converter and input current to the bi-directional dc-dc converter (step-up mode)

(a) Simulation   (b) Experiment
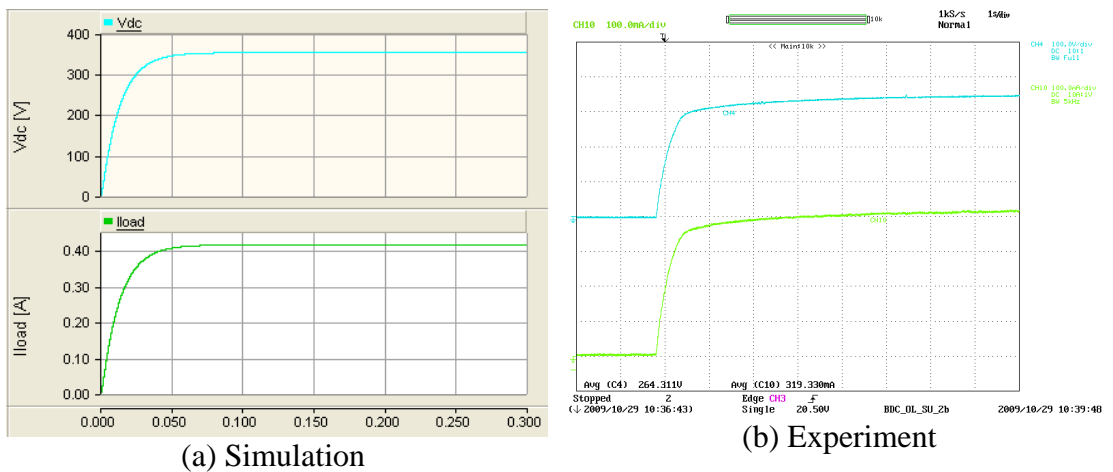
Y axis :V_{dc} – Light blue (100V/div), I_{load} – Light green (100mA/div, 5kHz BW-simulation) ; X axis: Time (50ms/div-Simulation, 1s/div-Experiment)

Figure 6-16: Load voltage and load current of the bi-directional converter (step-up mode)

The voltage at the ends of the inductor and the current flowing through the inductor are presented in Figure 6-17. Inductor ripple is approximately 30% for both simulation model and prototype.
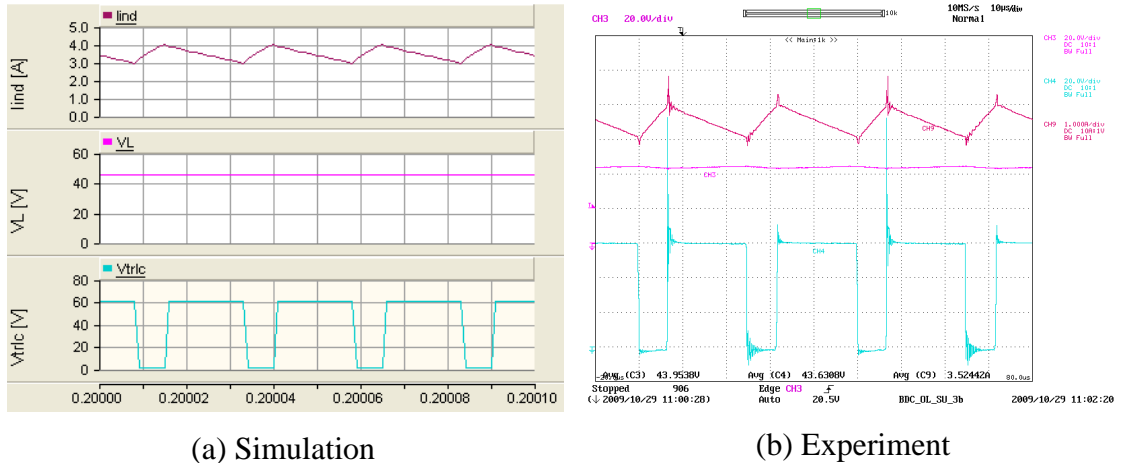
(a) Simulation   (b) Experiment

Y axis : I_L – Brown (1A/div), V_L – Pink (20V/div), V_{trlc} – Blue (20V/div) ; X axis: Time (10µs/div)

Experimental results: I_L ground level is same as V_L ground level

Figure 6-17: Voltage across the ends of the inductor and current flowing through the inductor of the bi-directional dc-dc converter (step-up mode)

Further results of the step-up mode testing of the bi-directional dc-dc converter are included in Appendix C. Figure 6-18 presents a screen capture of the measured waveforms of the bi-directional converter during step up mode which appears in dSPACE real time software interface. The voltage of the high voltage side, battery voltage and current flowing into the battery are measured.
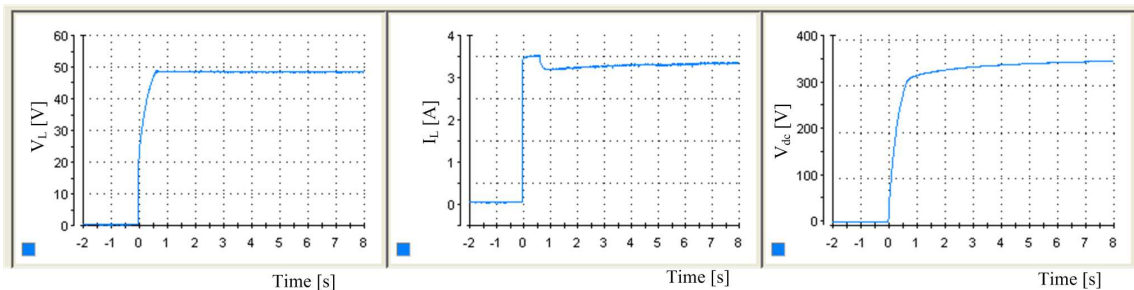
Figure 6-18: Screen capture of the measured waveforms of the bi-directional converter (step-up mode) plotted in dSPACE

6.3.1.2 Step-down mode

The test set-up for the step-down mode testing of the bi-directional dc-dc converter is presented in Figure 6-19. The high voltage side was connected to a 360 V voltage supply. A Xntrex XHR 600-1.7 laboratory power supply was used to test the prototype and the current limit was set to 0.45A. A 15 Ω resistor was connected as the load and a 47µF smoothing capacitor was connected in parallel with load resistor. The operating point duty ratio was set to 0.4. The duration, solution time step and channel plot step of the simulation were set to 0.3s, 0.5µs and 1µs respectively. Table 6-7 presents the summary of experimental results. Results of the converter are presented in Figure 6-20 to Figure 6-22.
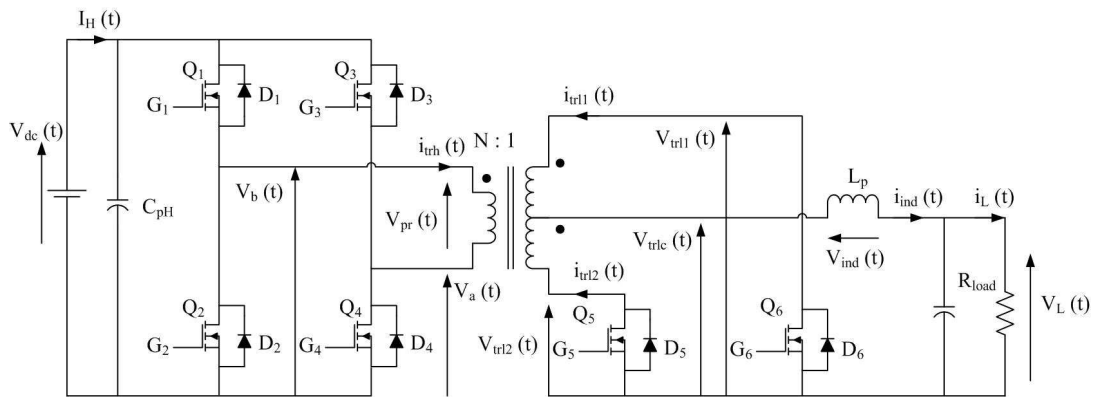
Figure 6-19: Test set-up used to test the operation of the step-down mode of the bi-directional converter

Table 6-7: Summary of results of the bi-directional dc-dc converter during step-down mode

Parameter	Values
Voltage at the low voltage end of the converter [V]	46.7
Current delivered to the load [A]	2.92
Current delivered from the voltage source [mA]	407
Input power [W]	147
Output power [W]	136
Efficiency of power conversion of the converter [%]	92.5

Figure 6-20 presents the input voltage and the current flown into the bi-directional dc-dc converter on the high voltage side. In the simulation model, a high side capacitor does

not filter the current; therefore this measurement was fed through a low pass filter to determine an average value. Initially the high voltage side capacitor in the prototype is not charged; therefore inrush current is experienced in the prototype. The inrush current is limited by the power supply current limit.

(a) Simulation   (b) Experiment
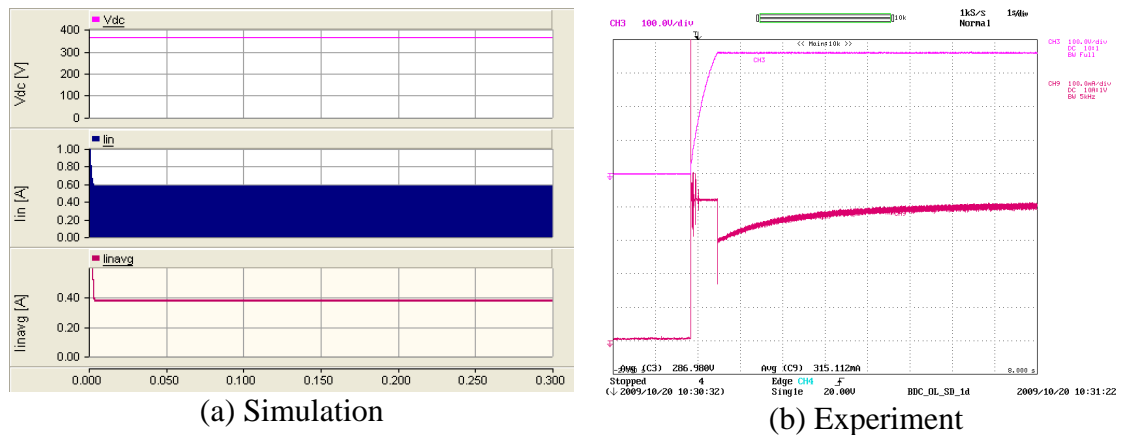
Y axis :V_{dc} - Pink (100V/div), I_{in} – Maroon (Simulation: 0.2A/div, Experiment: 0.1mA/div, 5kHz bandwidth); X axis: Time (0.05s/div-Simulation, 1s/div-Experiment)

Figure 6-20: Input voltage and input current to the bi-directional dc-dc converter (step-down mode)

Figure 6-21 shows the load voltage and the load current. The load voltage reaches the steady state instantaneously in the simulation model. However, the load voltage of the prototype takes longer time to reach the steady state as a result of the inrush current limiter placed at the low voltage side.

(a) Simulation   (b) Experiment
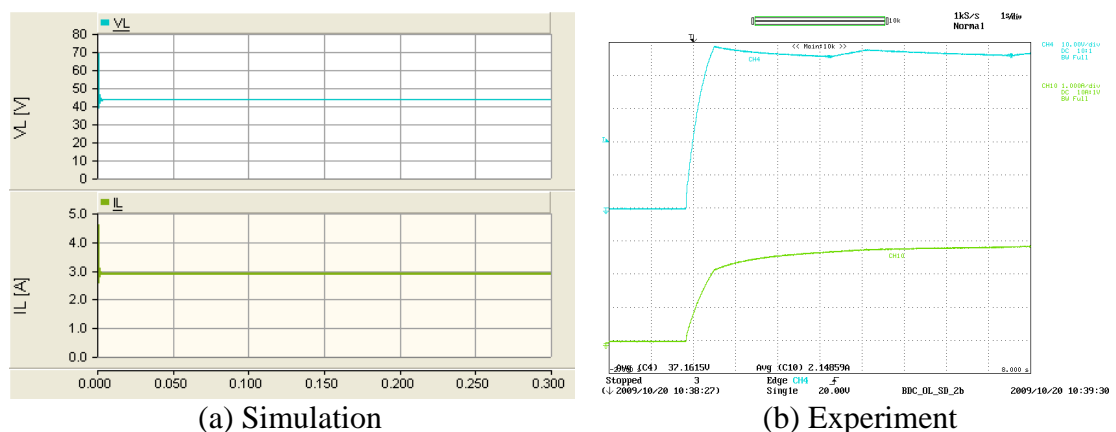
Y axis :V_L – Light blue (10V/div), I_L – Light green (1A/div); X axis: Time (0.05s/div-Simulation, 1s/div-Experiment)

Figure 6-21: Load voltage and load current of the bi-directional dc-dc converter (step-down mode)

The voltage across the inductor and current flowing through the inductor are shown in Figure 6-22. The inductor current linearly increases during the on-state of the switches. Energy stored in the inductor is released to the load during the off-state thus the current through the inductor linearly decays. The inductor ripple current is about 30% and 25% for the simulation model and the prototype respectively. Figure 6-23 presents the screen capture of measurements plotted in dSPACE user interface. Further results of step-up mode testing of the bi-directional converter are included in Appendix C.

(a) Simulation   (b) Experiment
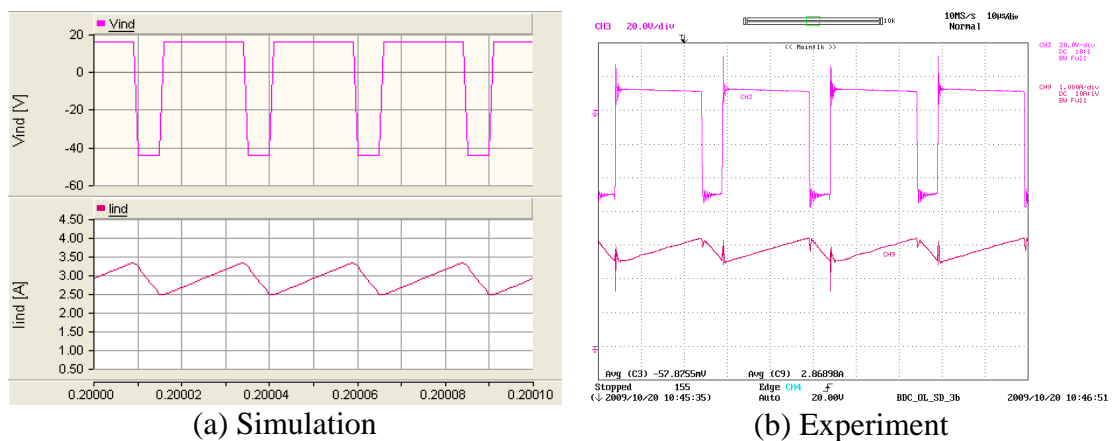
Y axis :V_{ind} – Pink (20V/div), I_{ind} – Maroon (simulation: 0.5A/div, Experiment: 1A/div); X axis: Time (10µs/div)

Figure 6-22: Voltage across the inductor and current flowing through the inductor of the bi-directional dc-dc converter (step-down mode)
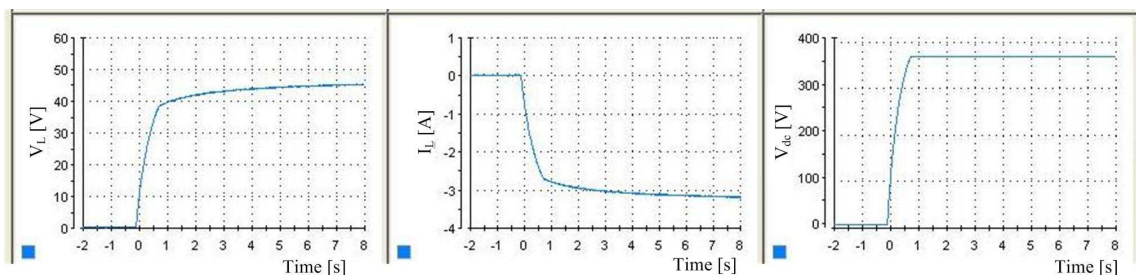
Figure 6-23: Screen capture of the measured waveforms of the bi-directional dc-dc converter (step-down mode) plotted in dSPACE

6.4 SINGLE-PHASE INVERTER

A full-bridge single-phase inverter is used in the proposed system. Pulse Width Modulation (PWM) with a unipolar voltage switching technique was adapted since it produces fewer harmonics compared to PWM with bipolar voltage switching technique. Table 6-8 presents the requirements of the inverter.

Table 6-8: Design requirements of the single-phase inverter

Parameter	Value
Power rating [W]	200
DC voltage [V]	360
Switching frequency [kHz]	10

A screen capture of the single-phase inverter simulation models is presented in Appendix C. Dead time was not introduced into the simulation model and the PWM signal was generated by comparing a sinusoidal wave with a triangular wave. Furthermore the frequency of fundamental component, the modulation index and the load resistance can be adjusted manually. Appropriate voltages and currents were measured in the simulation model. The duration, solution time step and channel plot step of the simulation were set to 0.5s, 1µs and 3µs respectively.

A FSAM20SH60A three-phase inverter module was used as the single-phase inverter hardware. The inverter module has an integrated gate drive circuitry which is driven by external logic signals. Table 6-9 presents the summary of data of the module.

Table 6-9: Summary of data of the FSAM20SH60A inverter module

Parameter	Value
Power rating [W]	1500
DC voltage [V]	600
Switching frequency [kHz]	15

In the prototype, 3µs dead time was introduced to the gate signals which were generated by the dSPACE real-time software to prevent dc-link short-circuit. Electrical isolation between dSPACE outputs and the inverter module was achieved by means of optocouplers. The optocoupler introduces a 1µs delay. Logic signals applied to the inverter module are inverted inside the module before being applied to the gate drive. Turn-on and turn-off switching of the logic signals applied to the gates of a 'leg' are shown in Figure 6-24. The total dead time equals 4µs.
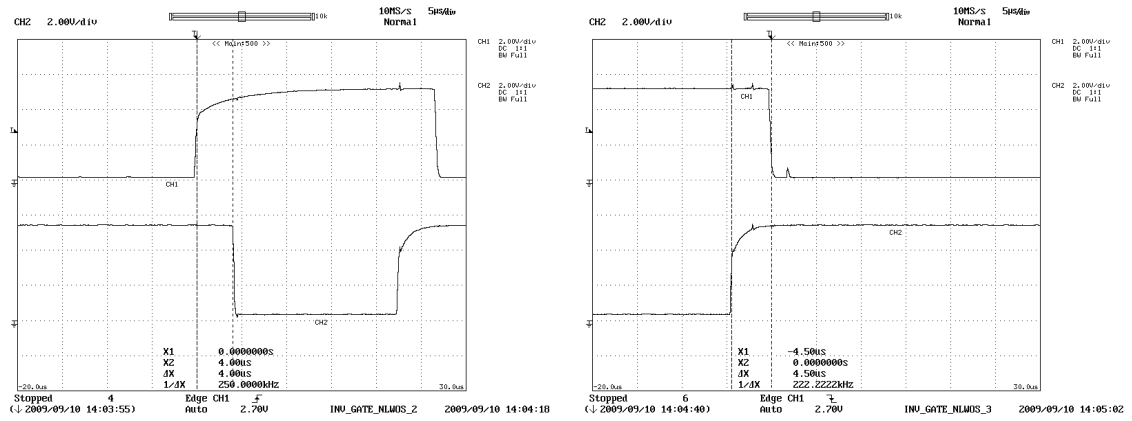
(a) Turn on transient   (b) Turn off transient

Y axis :Top – $\overline{G}_1$ (2V/div), Bottom – $\overline{G}_2$ (2V/div); X axis: Time (5µs/div)

Figure 6-24: Gate signals applied to an arm of the single-phase inverter module

The coupling inductor of inverter is selected to meet the power transfer capability as presented in Chapter 4. Equation 6-11 presents the relationship between inductance of the inductor with voltage at the ends of the inductor, phase angle, active power and frequency. The inductor selected for this application is 54.8mH which is capable of transferring 600W when the phase angle between the voltages at the ends of the inductor. The dc-link capacitance was selected based on the theory presented in the Chapter 4.4.3. The inverter rated power is 200W and the capacitor was selected to achieve a voltage ripple of 1.5V. Therefore a 1250µF capacitor was connected across the dc-link.

$$L_p = \frac{E_{INVrms}V_{INVrms}Sin\delta}{2\pi f P_{max}}$$ Equation 6-11

Behaviour of the inverter under no load (open circuit) was tested initially. Then inverter operation under a resistive load was tested. Simulation and experimental results corresponding to these two test cases are included in Appendix C.

The inverter was connected to series inductive and resistive load as shown in Figure 6-25. The input voltage is set to 360 V and the amplitude modulation ratio is set to one. The load resistance and the inductance are 352 Ω and 54.8 mH respectively. A Xantrex XHR 600-1.7 laboratory power supply was used as the dc voltage source for the inverter.
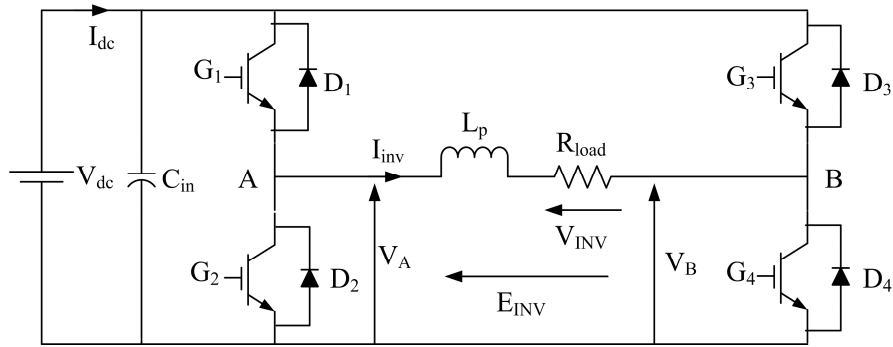
Figure 6-25: Single-phase inverter connected to a series inductive and resistive load

Table 6-10 summarises the experimental results of the single-phase inverter. Figure 6-26 to Figure 6-29 present the simulation and experimental results. Figure 6-26 shows the voltage at the centre of each 'leg' and the output voltage of the inverter.

Table 6-10: Summary of experimental results of the single-phase inverter

Parameter	Values
V_{dc} [V]	360
I_{dc} [A]	0.40
V_{INVrms} [V]	227
I_{INVrns} [V]	0.566
P_{dc} [W]	144
P_{INV} [W]	128
Efficiency [W]	88.8
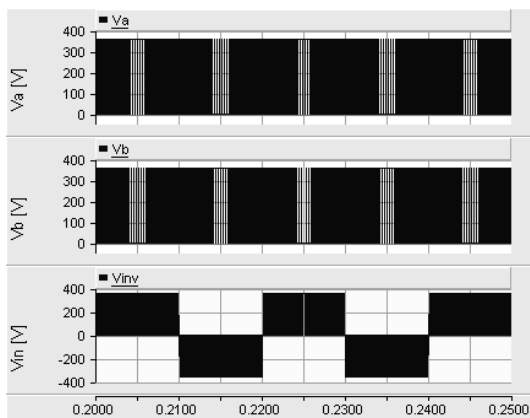
(a) Simulation   (b) Experiment
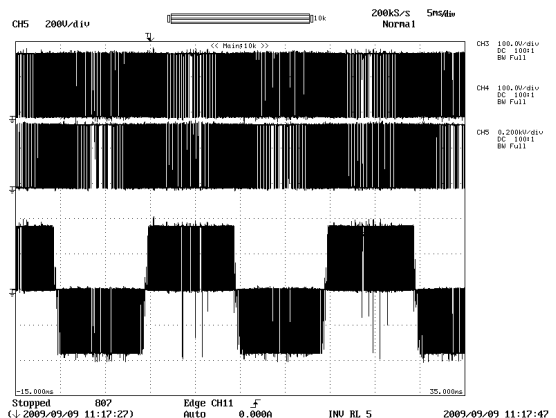
Y axis : Top - V_A (100V/div-simulation, 200V/div-Experiment), Middle –V_B (100V/div-Simulation, 200V/div-Experiment), Bottom – E_{INV} (200V/div); X axis: Time (5ms/div)

Figure 6-26: Voltage at the centre of each arm and inverter output voltage

The voltage across the resistive load and the current flowing through the resistive load is presented in Figure 6-27. In order to measure the load voltage a 1x oscilloscope probe was connected to a resistive voltage divider with attenuation equal to 201. Figure 6-28 presents the load voltage and the load current over few switching cycles.

(a) Simulation   (b) Experiment
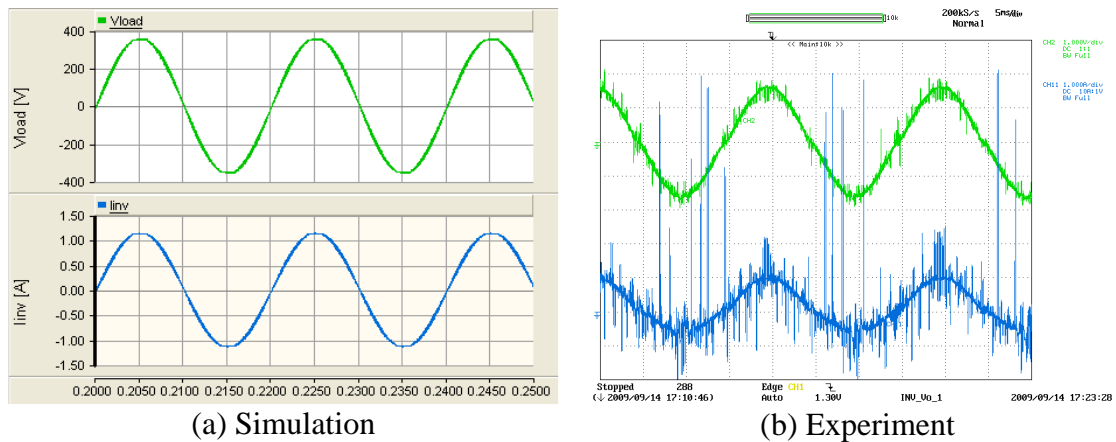
Y axis : V_{lINV} – Green (200V/div), I_{lINV} – Blue (simulation: 0.5A/div, experiment: 1A/div); X axis: Time (5ms/div)

Figure 6-27: Voltage across the load and current flowing through the load

(a) Simulation   (b) Experiment
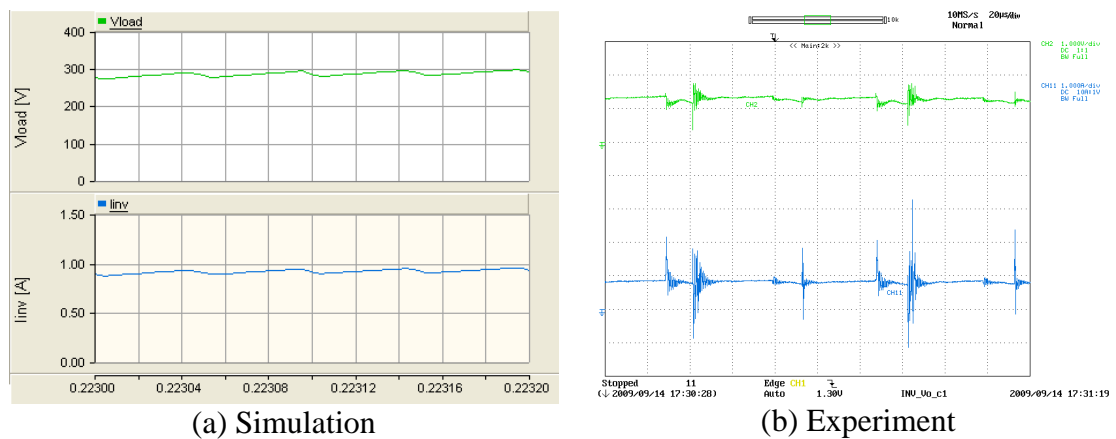
Y axis : V_{lINV} – Green (100V/div-Simulation, 200V/div-Experiment), I_{lINV} – Blue (simulations: 0.5A/div, experiment: 1A/div); X axis: Time (20µs/div)

Figure 6-28: Load voltage and load current over few switching cycles

The input current, the input voltage and the inverter output current are shown in Figure 6-29. The input current is partially filtered in the prototype. A screen capture of the measured waveforms of the inverter which appears in the dSPACE real time interface software is shown in Figure 6-30.

127

(a) Simulation   (b) Experiment
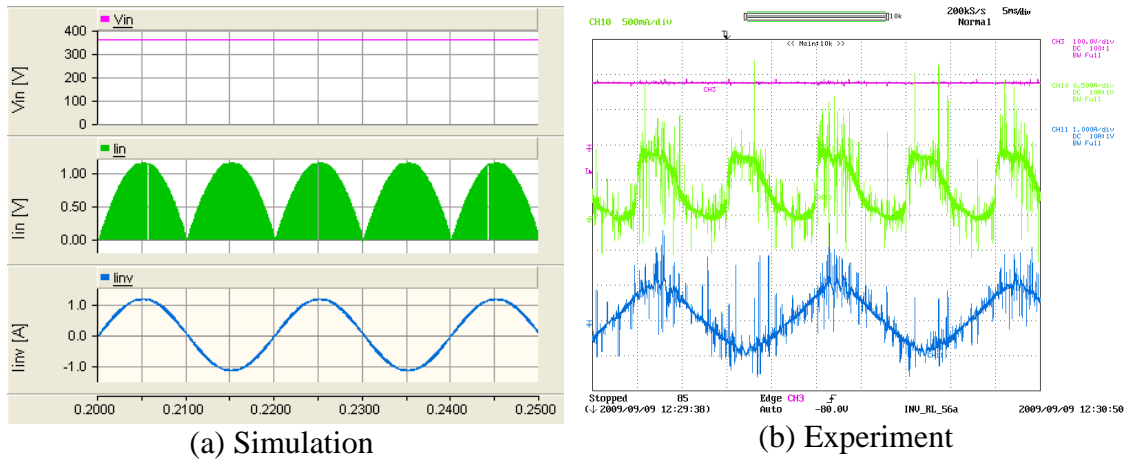
Y axis :V_{dc} – Pink (100V/div-Simulation, 200V/div-Experiment), I_{in} – Light green (0.5A/div), I_{INV} –
Blue (1A/div); X axis: Time (5ms/div)

Figure 6-29: Input voltage, input current and output current of the inverter
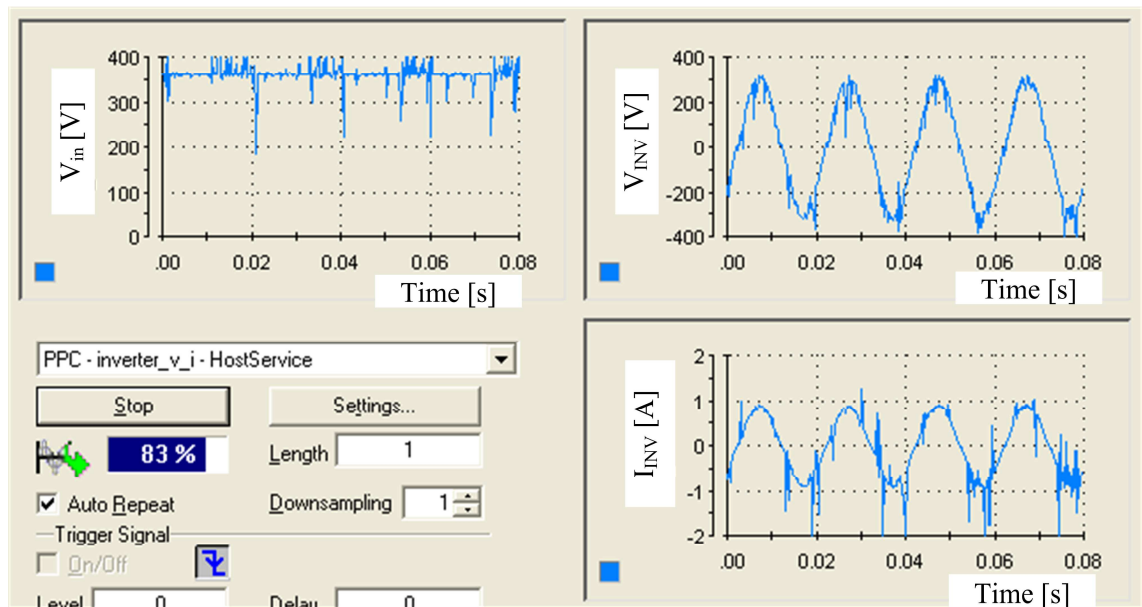
Figure 6-30: Screen capture of the measured quantities of the single-phase inverter
plotted in dSPACE

6.5 SUMMARY

All three converter topologies were modelled and simulated using the EMTDC/PSCAD
software. Hardware prototypes of them were implemented. The prototypes were
controlled using the dSPACE real time controller software. Automatic protection
systems and emergency protection systems were also implemented. Input and output
quantities of the converters are measured and fed into the dSPACE system. A first order

analogue-hardware filter with 5 kHz bandwidth was placed before signals acquired into dSPACE interface.

The efficiency of the unidirectional dc-dc converter is around 80% while the bi-directional converter efficiency is around 90%. Due to the parasitic effects, noise is visible in the turn-on and turn-off transients. However, it does not affect the operation of converters. The single-phase inverter efficiency is about 90% at 75% of full load. It behaves appropriately with inductive load. Thus all the converters are performing as expected.

CHAPTER 7

AUTOMATIC DC-LINK VOLTAGE CONTROL

7.1 INTRODUCTION

As shown in Figure 7-1, the proposed system is divided into two sections based on the system operation. Section-A consists of the microsource, a photovoltaic panel in this case, and an energy storage unit which is battery storage. The grid connected inverter forms Section-B. The output of Section-A should appear to Section-B as a stiff dc voltage source. In other words: the output of the Section-A, which is the dc-link voltage, should remain as constant as possible irrespective of either load or PV panel output power variations.
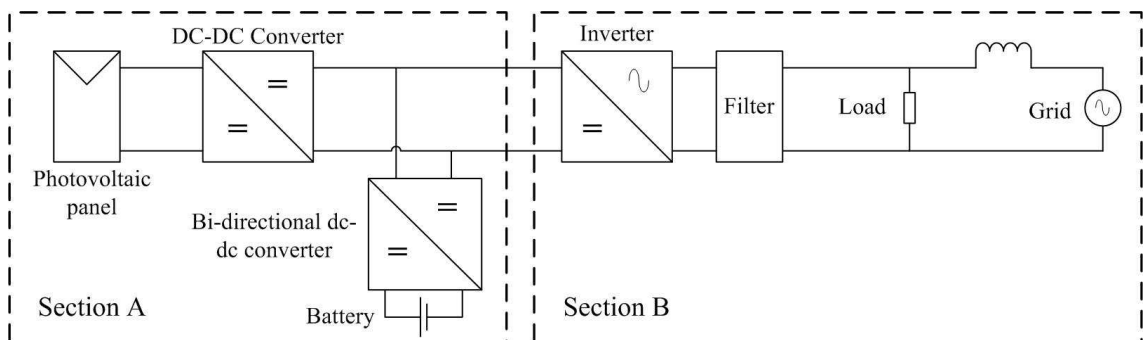
Figure 7-1: Proposed microsource interface

The main goal of this chapter is to present the behaviour of the Section-A under load and for output power variations in the photovoltaic panel. The structure of the controller used, the design criteria and the gains selected for each converter are briefly discussed. Then 'section-A' behaviour is discussed with a resistive load connected to across the dc-link. The system behaviour around the steady state conditions and worst-case conditions are analysed to ensure that the dc-link is acting as a stiff dc voltage source. All the studies were carried out using the simulation model and verified by the hardware prototype. Simulation and experimental results are included for all the case studies.

7.2 CONTROLLER OF THE MODIFIED FORWARD DC-DC CONVERTER

The controller of the modified forward dc-dc converter makes sure that the photovoltaic panel is operating at the maximum power point. The controller consists of two control loops as shown in Figure 7-2. The inner voltage loop ensures that PV panel is operating at the reference voltage generated by the outer loop. The reference voltage is generated by the MPPT which is the outer loop of the controller.
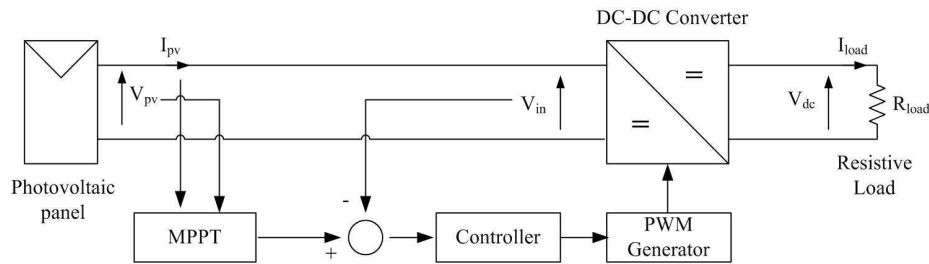
Figure 7-2: Controller of the modified forward dc-dc converter

The inner voltage control loop was designed based on the operating point model of the dc-dc converter. Gains for the controller are selected by considering the dynamic stiffness properties of the system. The design process of the controller is briefly explained in the following paragraphs however Appendix D presents the details of the controller design and modified forward dc-dc converter behaviour with the controller.

The simplified state feedback block diagram of the controller of the modified forward dc-dc converter is shown in Figure 7-3. The dynamic stiffness of the controller with a proportional controller (DS_p) and a PI controller (DS_{pi}) are given in Equation 7-1 and Equation 7-2 respectively.
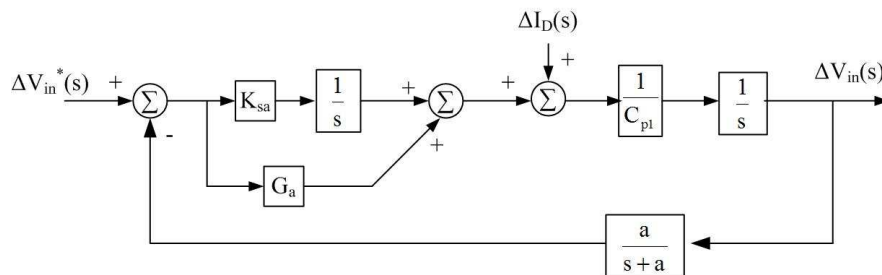
Figure 7-3: Simplified state feedback block diagram of the controller of the modified forward dc-dc converter

$$DS_{pro} : \frac{\Delta I_D(s)}{\Delta V_{in}(s)} = \left[C_{p1}s + \frac{aG_a}{s+a} \right] \qquad \text{Equation 7-1}$$

$$DS_{pi} : \frac{\Delta I_D(s)}{\Delta V_{in}(s)} = \left[C_{p1}s + \frac{a(G_a s + K_{sa})}{s(s+a)} \right] \qquad \text{Equation 7-2}$$

Table 7-1 presents the gains selected for the controller. The eigenvalues of the controller are 4.82 kHz, 8.62 Hz and 2.45 Hz. The gains were selected in such a way that a fast response is achieved. In order to achieve a well-defined and smooth response, real roots for the characteristic equation were selected. The poles corresponding to the gains of the controller were separated by approximately a factor of four.

Table 7-1: Gains selected for the PI controller of the modified forward dc-dc converter

Parameter	Value
G_a	0.25
K_{sa}	3.00

The voltage at the maximum power point is approximately equal to 71-80% of the open circuit voltage of the photovoltaic panel [81-84]. This characteristic is used in this analysis. The goal of this research is to examine the (faster) dynamics of the converter rather than the (relatively slow) behaviour of a MPPT controller. Therefore 80% of the open circuit voltage is fed as the reference to the inner controller of the dc-dc converter as is done in some 'cheap and cheerful' MPPT loops.

7.3 CONTROLLER OF THE BI-DIRECTIONAL DC-DC CONVERTER

The function of the controller of the bi-directional dc-dc converter is to keep the dc-link voltage constant irrespective of variations in either load or PV panel output power. The controller should be operated during step-up and step-down modes.

The controller of the bi-directional dc-dc converter consists of two loops as shown in Figure 7-4. The inner loop controls the average inductor current flowing through the

inductor while the outer loop control the voltage at the high-voltage side of the converter. It is assumed that the inner current loop is faster than the outer voltage loop.
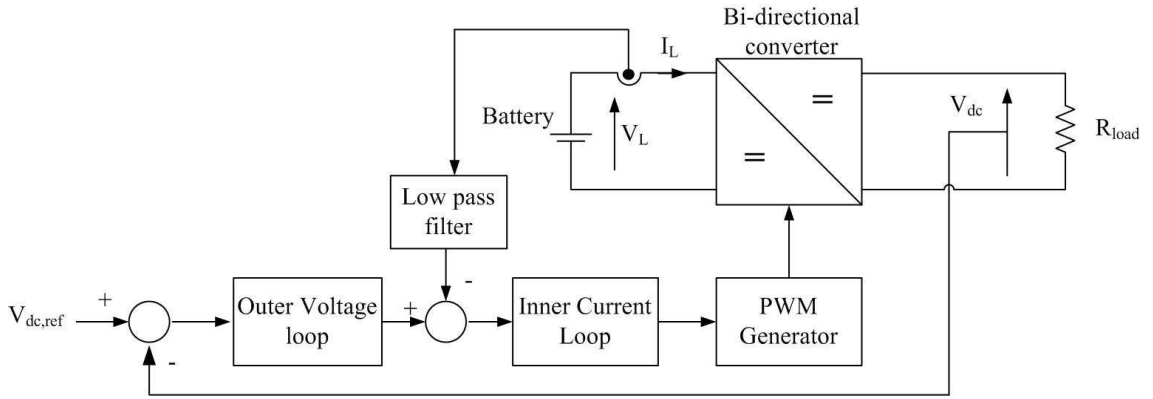
Figure 7-4: Controller of the bi-directional dc-dc converter

The controllers are designed based on the operating point model of the converter. Gains for the inner current loop and the outer voltage loop are selected based on the dynamic stiffness properties of the system. The following paragraphs explain the design process of the controller briefly. Details of controller design are included in Appendix D. Further simulation and experimental results of the controller are also presented in Appendix D.

Simplified state feedback block diagrams of the inner current loop and outer voltage loop are presented in Figure 7-5 and Figure 7-6. Equation 7-3 and Equation 7-4 present the dynamic stiffness of the inner current loop of the controller of the bi-directional dc-dc converter with a proportional controller ($DS_{i,pro}$) and a PI controller ($DS_{i,pi}$). Similarly dynamic stiffness of the controller of the outer voltage of the bi-directional dc-dc converter is given in Equation 7-5 ($DS_{o,pro}$: with a proportional controller) and Equation 7-6 ($DS_{o,pi}$: with a PI controller).
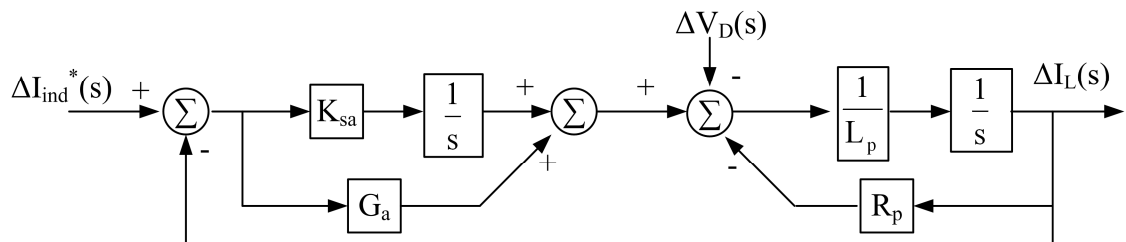
Figure 7-5: Simplified state feedback block diagram of the inner current loop of the bi-directional dc-dc converter

$$DS_{i,pro} : \frac{\Delta V_D(s)}{\Delta I_{ind}(s)} = \left(L_p s + R_p + G_a\right) \qquad \text{Equation 7-3}$$

$$DS_{i,pi} : \frac{\Delta V_D(s)}{\Delta I_{ind}(s)} = \left[L_p s + R_p + G_a + \frac{K_{sa}}{s}\right] \qquad \text{Equation 7-4}$$
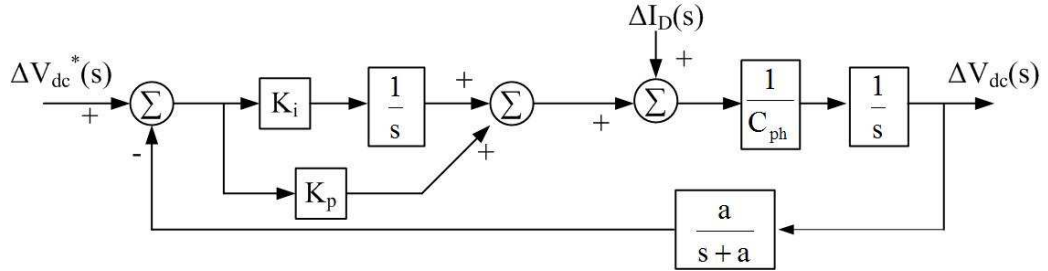
Figure 7-6: Simplified state feedback block diagram of the outer voltage loop of the bi-directional dc-dc converter

$$DS_{o,pro} : \frac{\Delta I_D(s)}{\Delta V_{dc}(s)} = \left[C_{po} s + \frac{aK_p}{s+a}\right] \qquad \text{Equation 7-5}$$

$$DS_{o,pi} : \frac{\Delta I_D(s)}{\Delta V_{dc}(s)} = \left[C_{po} s + \frac{a(K_p s + K_i)}{s(s+a)}\right] \qquad \text{Equation 7-6}$$

Table 7-2 presents the gains selected for the controllers. Eigenvalues of the inner control loops lie at 471 Hz and 133Hz. Eigenvalues corresponding to the outer voltage loops lie at 4.72 kHz, 64.8 Hz and 16.9 Hz. Eigenvalues corresponding to the gains of the controllers were separated by approximately a factor of four. The gains were selected to achieve fast response. Further to achieve well defined and smooth response, real roots were selected for the characteristic equation. Further eigenvalues of inner current loop and outer voltage loop are separated by approximately factor of ten.

Table 7-2: Gains selected for the inner current loop and outer voltage loop

Parameter	Value
G_a	0.75
K_{sa}	750
K_p	0.01
K_i	0.03

The photovoltaic panel and energy storage were connected to form a structure similar to Section-A. Manual operation of the converters was tested. Simulation and experimental results are again included in Appendix D. The following sub-sections present the automatic voltage control of dc-link in response to load and photovoltaic panel output variations.

7.4 AUTOMATIC CONTROL OF THE BI-DIRECTIONAL DC-DC CONVERTER

The function of the controller of the bi-directional dc-dc converter is to keep the dc-link voltage constant. The bi-directional dc-dc converter should switch between its two operating modes automatically depending on the load and PV output power variations.

The mode selection of the bi-directional dc-dc converter is based on hysteresis control technique as shown in Figure 7-7. Hysteresis control was chosen since it is fast and achieves predictable upper and lower boundaries. This methodology avoids unnecessary switching between modes. For each mode, two reference voltage levels were defined. If the dc-link voltage exceeds the step-down turn-on reference (V_{dcsdon}), the bi-directional dc-dc converter operates in the step-down mode until the dc-link voltage drops below the step-down turn-off reference ($V_{dcsdoff}$) value. Similarly the step-up mode is turned on if the dc-link voltage drops below the step-up turn-on reference (V_{dcsuon}). The bi-directional dc-dc converter continues to operate in step-up mode till the dc-link voltage rises above the step-up turn-off reference ($V_{dcsuoff}$). A voltage gap (ΔV) is introduced between turn-on and turn-off levels. However the ability to keep the dc-link within the limits depends on the state of charge of the battery. In the analysis, it is assumed that battery is not fully charged or discharged.

7.5 AUTOMATIC CONTROL OF THE DC-LINK VOLTAGE

Figure 7-8 presents the test set-up used to analyse the automatic voltage control dc-link. The nominal dc-link reference voltage was kept at 360V. The step-up turn-on and turn-off references were set to 340V and 375V respectively. 345V and 380V were the step-down turn-off and turn-on reference voltages respectively. The following sub-sections contain the simulation and experimental results for different scenarios. Current into the

low-voltage (battery) end of the bi-directional dc-dc converter is considered as positive while negative current indicates that the current is flowing out from the low-voltage end as indicated in Figure 7-8.
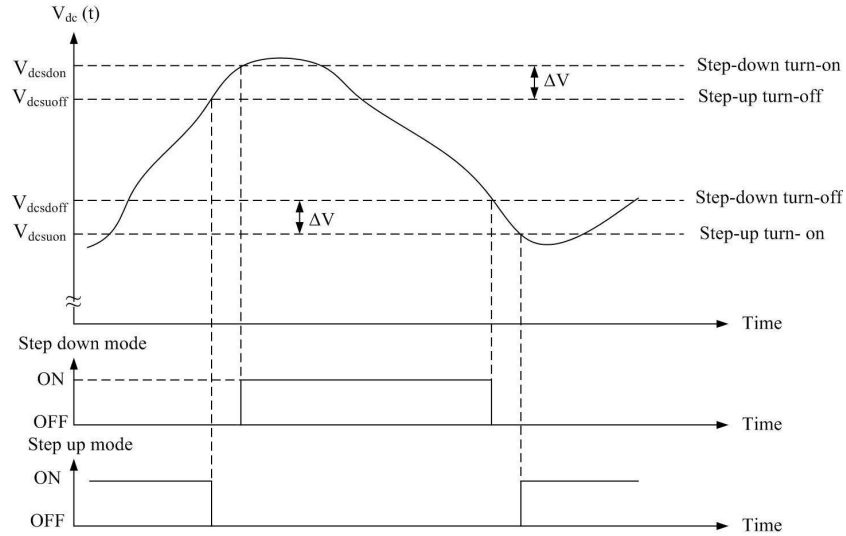
Figure 7-7: Hysteresis control technique used to control the operating modes of the bi-directional dc-dc converter
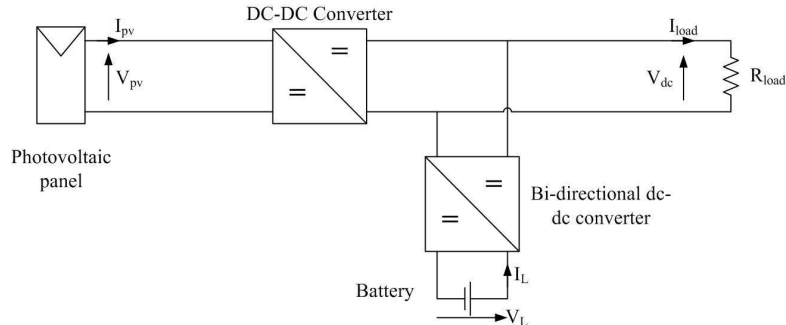
Figure 7-8: Test set-up used to analyse the behaviour of Section-A of the proposed microsource interface

7.5.1 Step-down mode turn-on transient of the bi-directional dc-dc converter

The system behaviour during the step-down mode turn-on transient is discussed in this section. The dc-link voltage increases in response to a decrease in load or an increase in PV output. When the dc-link voltage exceeds the step-down turn-on reference, energy should be transferred into the battery and the dc-link voltage is restored to the nominal reference voltage.

136

In order to observe the step-down mode turn-on transient, a decrease in load is considered. The PV panel (emulator) output corresponds to 1000W/m^2 irradiance at 25°C. A resistive load of 1230Ω was connected to the dc-link. The dc-link voltage is stabilized at its nominal reference voltage with the bi-directional dc-dc converter operating in step-up mode. Then the load resistance was gradually increased from 1230Ω to 1700Ω where the rate of increase was 120Ω per second in the simulation model.

Figure 7-9 to Figure 7-13 present the results of the system during the step-down mode turn-on transient. Figure 7-9 highlights the variation of dc-link voltage and load current. As the load decreases, load voltage increases and load current decreases. Once the dc-link voltage reached the step-down turn-on reference, the dc-link voltage is restored back to nominal reference value. Negative current flowing from the low-voltage end of the bi-directional converter, Figure 7-10, validates the operation of converter in step-down mode. Load resistance variation was carried out manually for the experimental set-up and is not completely identical to the rate of change of load resistance in the simulation model. Thus the complete turn-off period of the bi-directional converter is different for simulation and experimental results. Figure 7-11 presents the photovoltaic panel voltage and current which indicates that photovoltaic panel voltage is not affected by the dc-link dynamics.
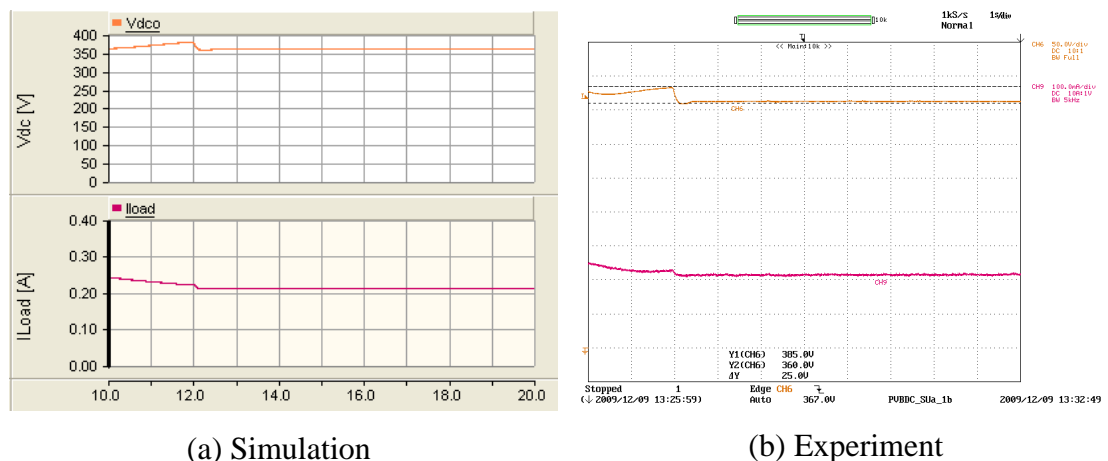
(a) Simulation   (b) Experiment

Y axis: V$_{dc}$ – Orange (50V/div), I$_{load}$ – Maroon (0.1A/div) Experimental oscilloscope channel bandwidth = 5kHz, In the experimental results ground level is same for both channels; X axis: Time (1s/div)

Figure 7-9: DC-link voltage and load current (Automatic step-down mode turn-on transient)

(a) Simulation   (b) Experiment
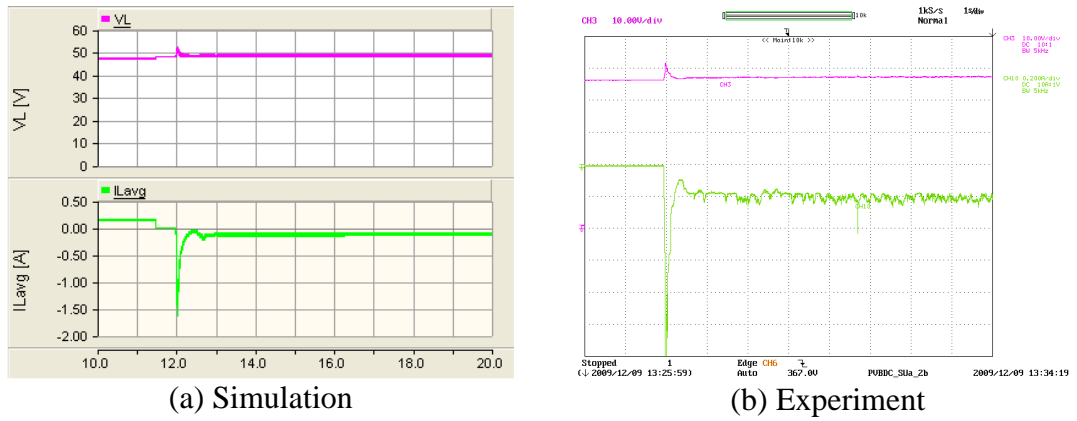
Y axis: V_L – Pink (10V/div), I_L – Green (Simulations-0.5A/div, Experiment-0.2A/div), For Experimental measurements oscilloscope channels bandwidth = 5kHz,; X axis: Time (1s/div)

Figure 7-10: Voltage at the low-voltage end of the bi-directional dc-dc converter and the battery current (Automatic step-down mode turn-on transient)
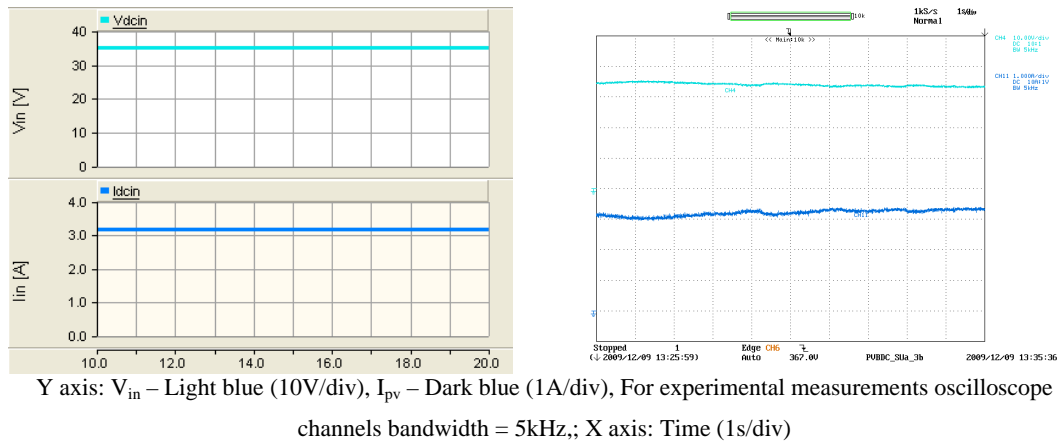
Y axis: V_{in} – Light blue (10V/div), I_{pv} – Dark blue (1A/div), For experimental measurements oscilloscope channels bandwidth = 5kHz,; X axis: Time (1s/div)

Figure 7-11: Photovoltaic panel voltage and current (Automatic step-down mode turn-on transient) – (a) Simulation (left), (b) Experiment (right)

The behaviour of the controller of the bi-directional dc-dc converter is shown in Figure 7-12. Step-down mode was turned on when the dc-link voltage exceeded 380V. The dc-link reaches it nominal reference voltage in less than one second. The average current flowing through the inductor of the bi-directional dc-dc converter starts to follow the current reference as soon as the step-down mode is turned on. Figure 7-13 presents the behaviour of the controller of the modified forward dc-dc converter. The controller of the modified forward dc-dc converter adjusts in such a way that the photovoltaic panel voltage remains constant during the transient. Transients in the dc-link have not significantly affected the PV panel voltage. Gate driver delay in the prototype is responsible for the duty ratio difference in the experimental results when compared with simulation results. This is visible in all the cases presented in this chapter.

Red: Reference, Green: Measured

Red: Reference, Green: Measured, Yellow: Filtered

Blue: Proportional, Green: Integrator, Red: PI

Blue: Proportional, Green: Integrator, Red: PI

Blue: Reference, Green: Measured

Blue: Reference, Green: Measured

Blue: Proportional, Green: Integrator, Red: PI

Blue: Proportional, Green: Integrator, Red: PI

Time [s]

Time [s]
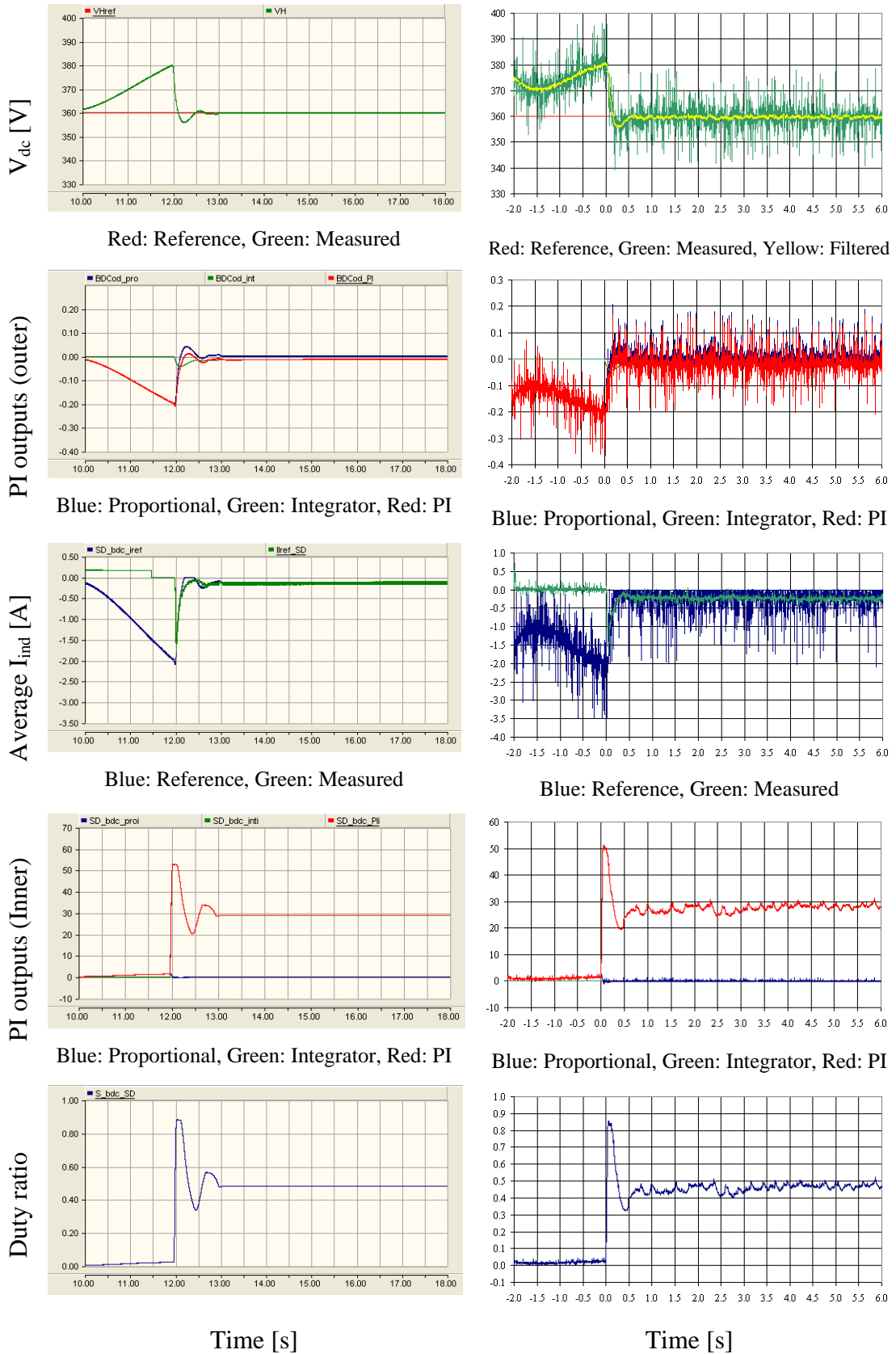
(a) Simulation

(b) Experimental

Figure 7-12: Behaviour of the step-down mode controller of the bi-directional dc-dc
converter (Automatic step-down turn-on transient)

(a) Simulation   (b) Experimental
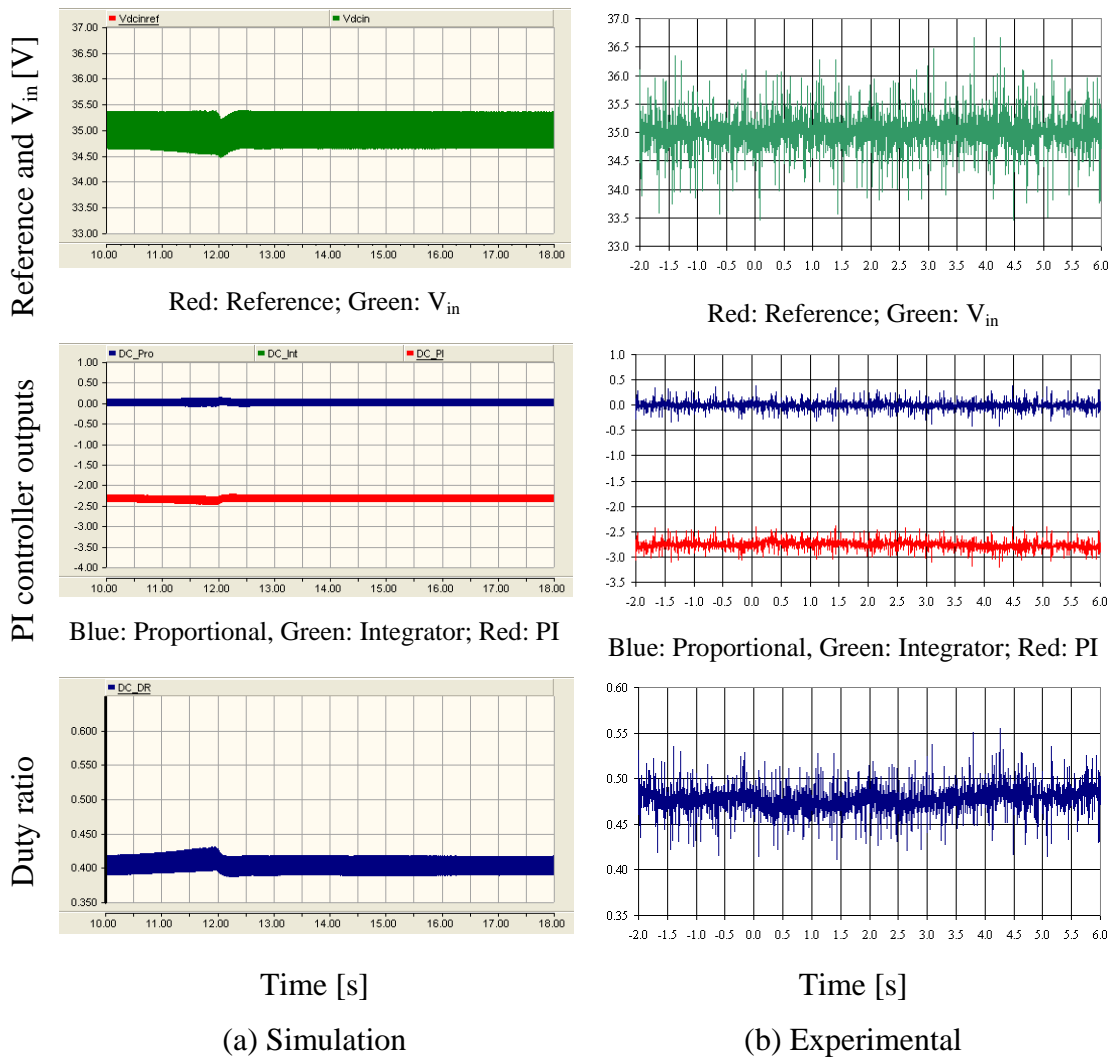
Figure 7-13: Behaviour of the controller of the modified forward dc-dc converter
(Automatic step-down mode turn-on transient)

7.5.2 Step-up mode turn-on transient of the bi-directional converter

The bi-directional dc-dc converter should switch to step-up mode automatically when the dc-link voltage drops below the step-up turn-on reference. The dc-link voltage starts to drop from the nominal value as a result of an increase in load or a drop of output power from the PV panel. A voltage drop due to an increase in load is considered in this test. The PV output corresponds to 1000W/m^2 irradiance at 25°C. A resistive load of 1700Ω was connected across the dc-link. The bi-directional dc-dc converter operates in the step-down mode while keeping the dc-link voltage at its nominal reference. The load resistance was gradually decreased to 1180Ω and in the simulation mode rate was equal to 150Ω per second. Figure 7-14 to Figure 7-18 present the simulation and experimental results during the step-up mode turn-on transient.

The dc-link voltage starts to drop when the load increases as shown in Figure 7-14. The bi-directional dc-dc converter switches to the step-up mode when the dc-link voltage drops below the step-up turn-on reference. Referring to Figure 7-15, current flowing from the low-voltage end of the bi-directional dc-dc converter is positive which indicates that energy is transferred from the battery. The controller of bi-directional dc-dc converter confirms the turn-on of the step-up mode at 340V, referring to Figure 7-16. The voltage differences at the low-voltage end of the bi-directional dc-dc converter are responsible for the duty ratio difference in the simulation and experimental results which is visible in most of the cases presented in this chapter. According to Figure 7-17 and Figure 7-18, the controller of the modified forward dc-dc converter output slightly adjusts during the transient however the photovoltaic panel voltage is not affected.

<table>
<tr><td>(a) Simulation</td><td>(b) Experiment</td></tr>
</table>
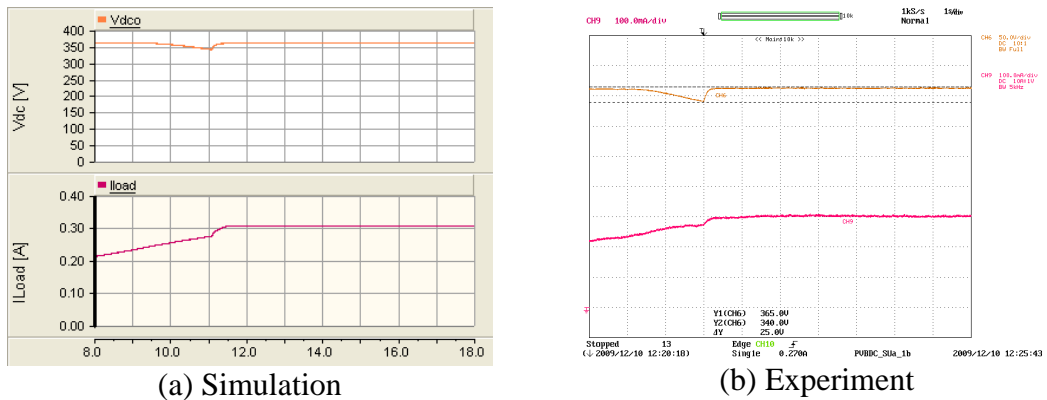
Y axis: V_{dc} – Orange (50V/div), I_{load} Maroon (0.1A/div) Expe. oscilloscope channel BW = 5kHz; X axis: Time (1s/div)

Figure 7-14: DC-link voltage and load current (Automatic step-up mode turn-on transient)

<table>
<tr><td>(a) Simulation</td><td>(b) Experiment</td></tr>
</table>
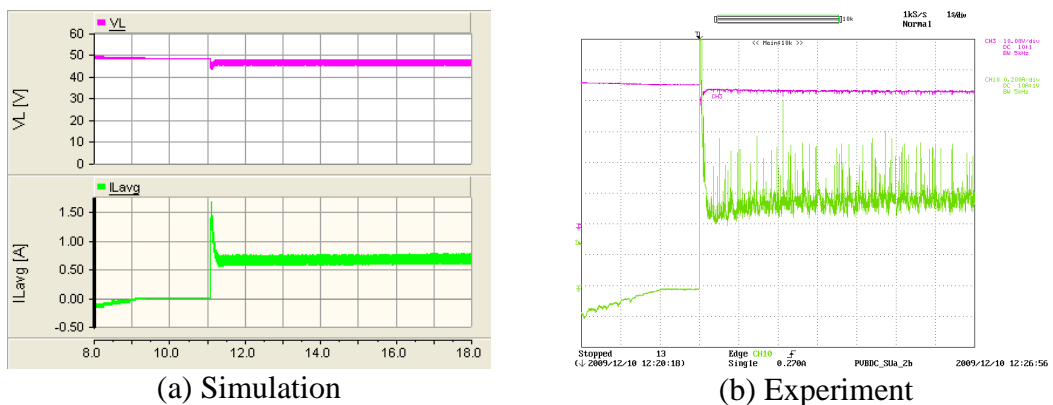
Y axis: V_L – Pink (10V/div), I_L Light Green (0.5A/div-simulation, 0.2A/div-Experiment), For Experimental results oscilloscope channel bandwidth = 5kHz; X axis: Time (1s/div)

Figure 7-15: Voltage at the low-voltage end of the bi-directional dc-dc converter and the battery current (Automatic step-up mode turn-on transient)

Blue: Reference, Green: Measured

Red: Reference, Green: Measured, Yellow: Measured filtered

Blue: Proportional, Green: Integrator, Red: PI

Blue: Proportional, Green: Integrator, Red: PI

Blue: Reference, Green: Measured

Blue: Reference, Green: Measured

Blue: Proportional, Green: Integrator, Red: PI

Blue: Proportional, Green: Integrator, Red: PI

Time [s]

Time [s]
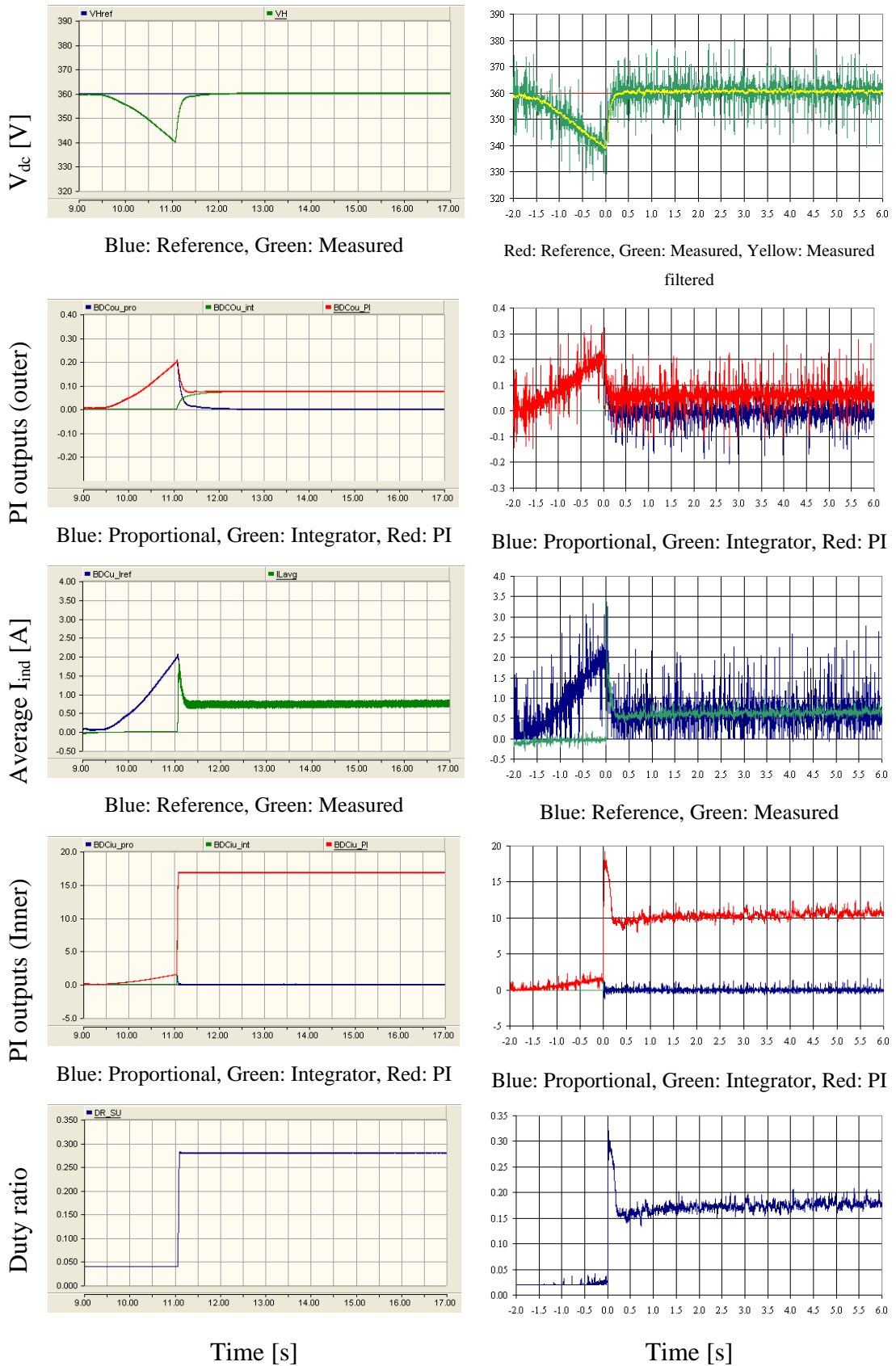
(a) Simulation

(b) Experimental

Figure 7-16: Behaviour of the step-up mode controller of the bi-directional dc-dc converter (Automatic step-up mode turn-on transient)

Red: Reference; Green: V_in   Red: Reference; Green: V_in

Blue: Proportional, Green: Integrator; Red: PI   Blue: Proportional, Green: Integrator; Red: PI

Time [s]   Time [s]

(a) Simulation   (b) Experimental
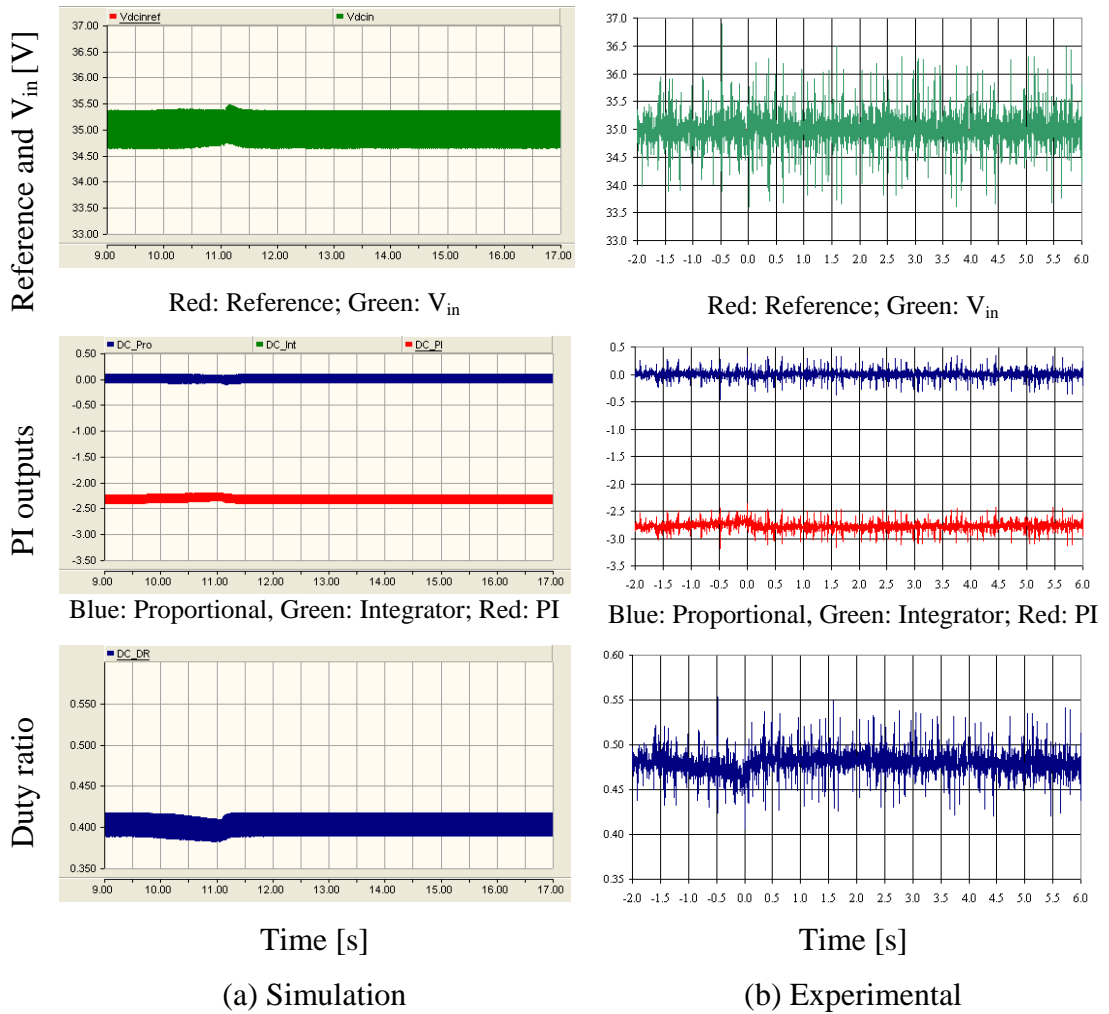
Figure 7-17: Behaviour of the controller of modified forward dc-dc converter
(Automatic step-up mode turn-on transient)
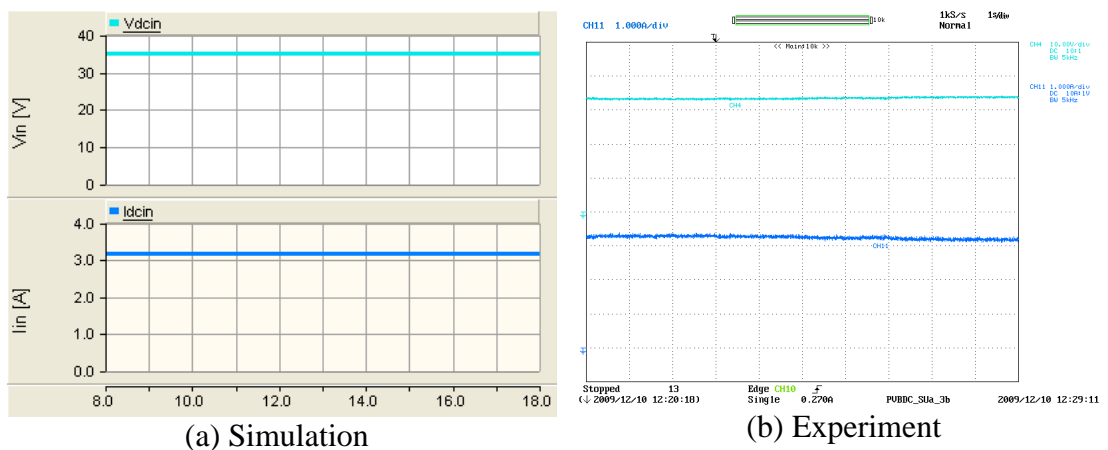
(a) Simulation   (b) Experiment

Y axis: V_in – Light blue (10V/div), I_pv – Dark blue (1A/div), For experimental results oscilloscope channel
bandwidth = 5kHz,; X axis: Time (1s/div)

Figure 7-18: Photovoltaic panel voltage and current (Automatic step-up mode turn-on
transient)

7.5.3 Automatic operation of step-down mode turn-off transient of the bi-directional converter

Either an increase in load or a decrease in PV output corresponds to drop in dc-link voltage which could turn-off the step-down mode. The former reason was selected to observe the behaviour of the system during the step-down mode turn-off transient. Here PV panel emulator output corresponds to 1000W/m^2 at 25°C. A resistive load of 1700Ω was connected as the load. The bi-directional dc-dc converter operates in step-down mode with the dc-link voltage stable at 360V. The load resistance was decreased to 1180Ω gradually where the rate was 150Ω per second in the simulation model.

The transient behaviour of the system during the step-down mode turn-off is presented in Figure 7-19 to Figure 7-23. Figure 7-19 presents the dc-link voltage and the load current variation with time. As the load increases, the dc-link voltage starts to drop and simultaneously the current flowing into the battery decreases to zero as shown in Figure 7-20. The bi-directional dc-dc converter switches to step-up mode when the dc-link voltage crosses the step-up turn-on reference. The behaviour of the controllers is presented in Figure 7-21 and Figure 7-22. The duty ratio applied to the modified forward dc-dc converter is slightly adjusted to compromise the dc-link voltage variations. As the load increases, the duty ratio applied to the bi-directional dc-dc converter reduces. When the dc-link voltage crosses the step-down turn-off reference (345V), the duty ratio becomes zero which indicates the step-down mode is turned off. Considering Figure 7-23 it is possible to state that the dynamics of the dc-link does not affect the photovoltaic panel outputs.

Y axis: V$_{dc}$ – Orange (50V/div), I$_{load}$ – Maroon (50mA/div – Simulation, 0.1A/div-Experimental) Experimental oscilloscope channel bandwidth = 5kHz; X axis: Time (1s/div)
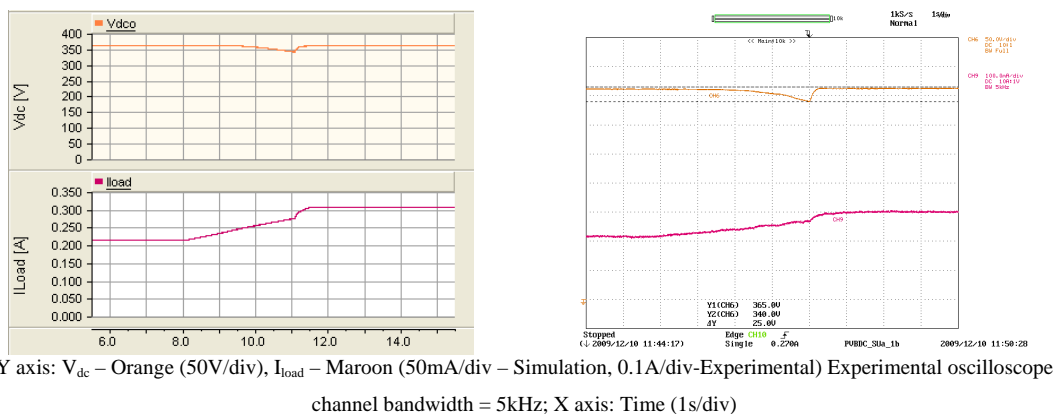
Figure 7-19: DC-link voltage and load current (Automatic step-down mode turn-off transient) – (a) Simulation (left), (b) Experiment (right)

(a) Simulation   (b) Experiment
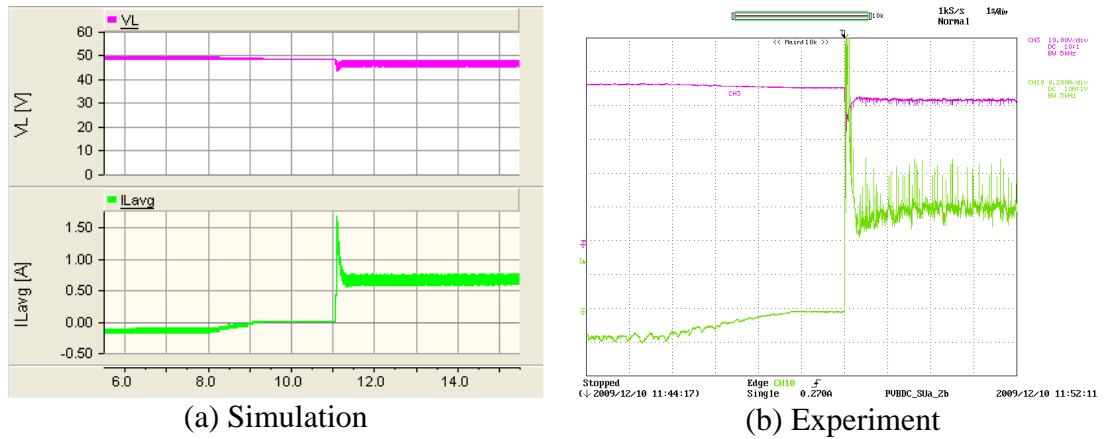
Y axis: V_L – Pink (10V/div) Experimental oscilloscope channel bandwidth = 5kHz, I_L – Green (0.5A/div – Simulations,

0.2A/div-Experimental); X axis: Time (100ms/div)

Figure 7-20: Voltage at the low-voltage end of the bi-directional dc-dc converter and the

battery current (Automatic step-down mode turn-off transient)

Red: Reference; Green: V_{in} Red: Reference; Green: V_{in}

Blue: Proportional, Green: Integrator; Red: PI   Blue: Proportional, Green: Integrator; Red: PI

Time [s]   Time [s]

(a) Simulation   (b) Experimental
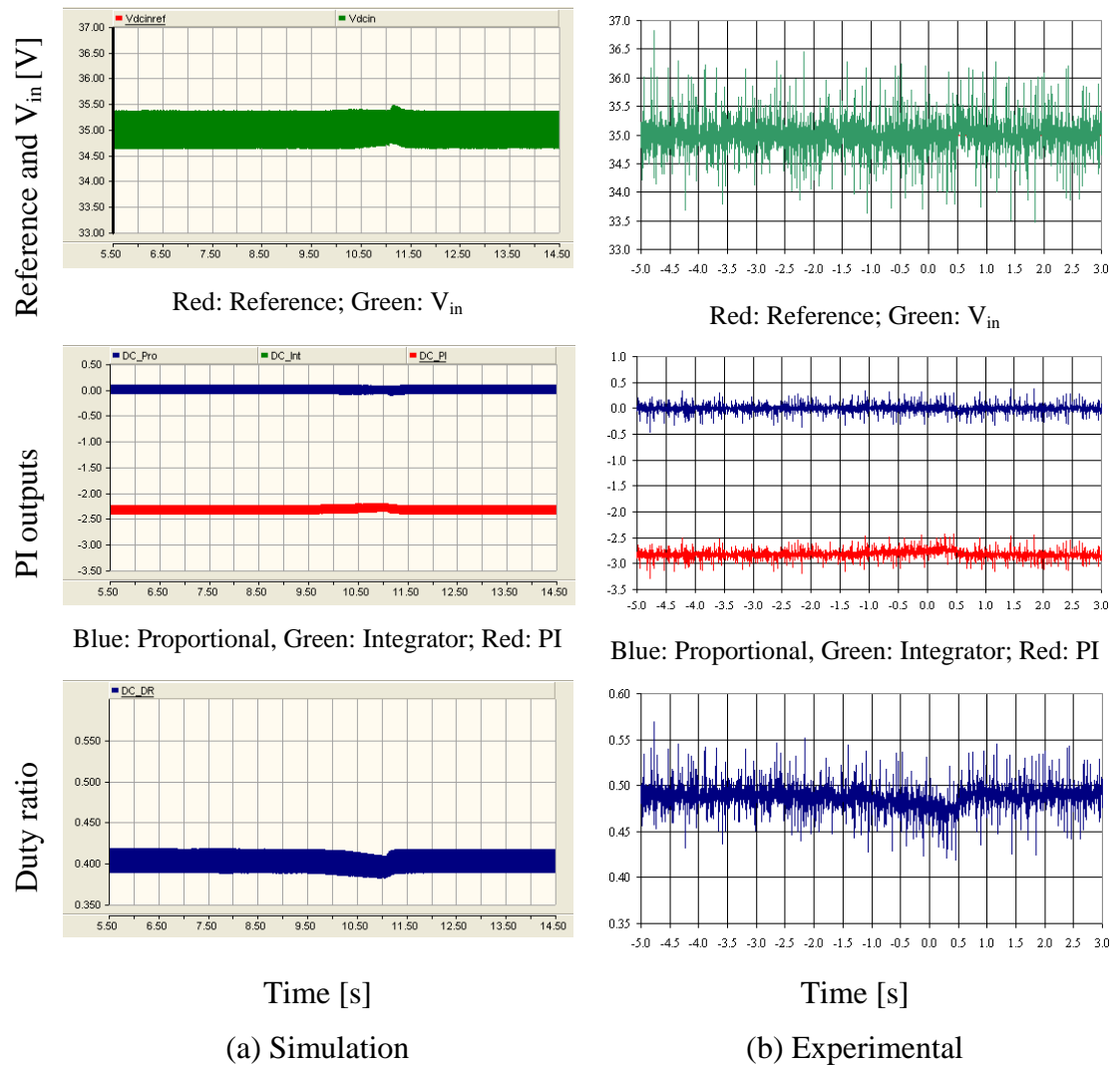
Figure 7-21: Behaviour of the controller of the modified forward dc-dc converter

(Automatic step-down mode turn-off transient)

Blue: Reference, Green: Measured

Red: Reference, Green: Measured, Yellow: Filtered

Blue: Proportional, Green: Integrator, Red: PI

Blue: Proportional, Green: Integrator, Red: PI

Blue: Reference, Green: Measured

Blue: Reference, Green: Measured

Blue: Proportional, Green: Integrator, Red: PI

Blue: Proportional, Green: Integrator, Red: PI

Time [s]

Time [s]
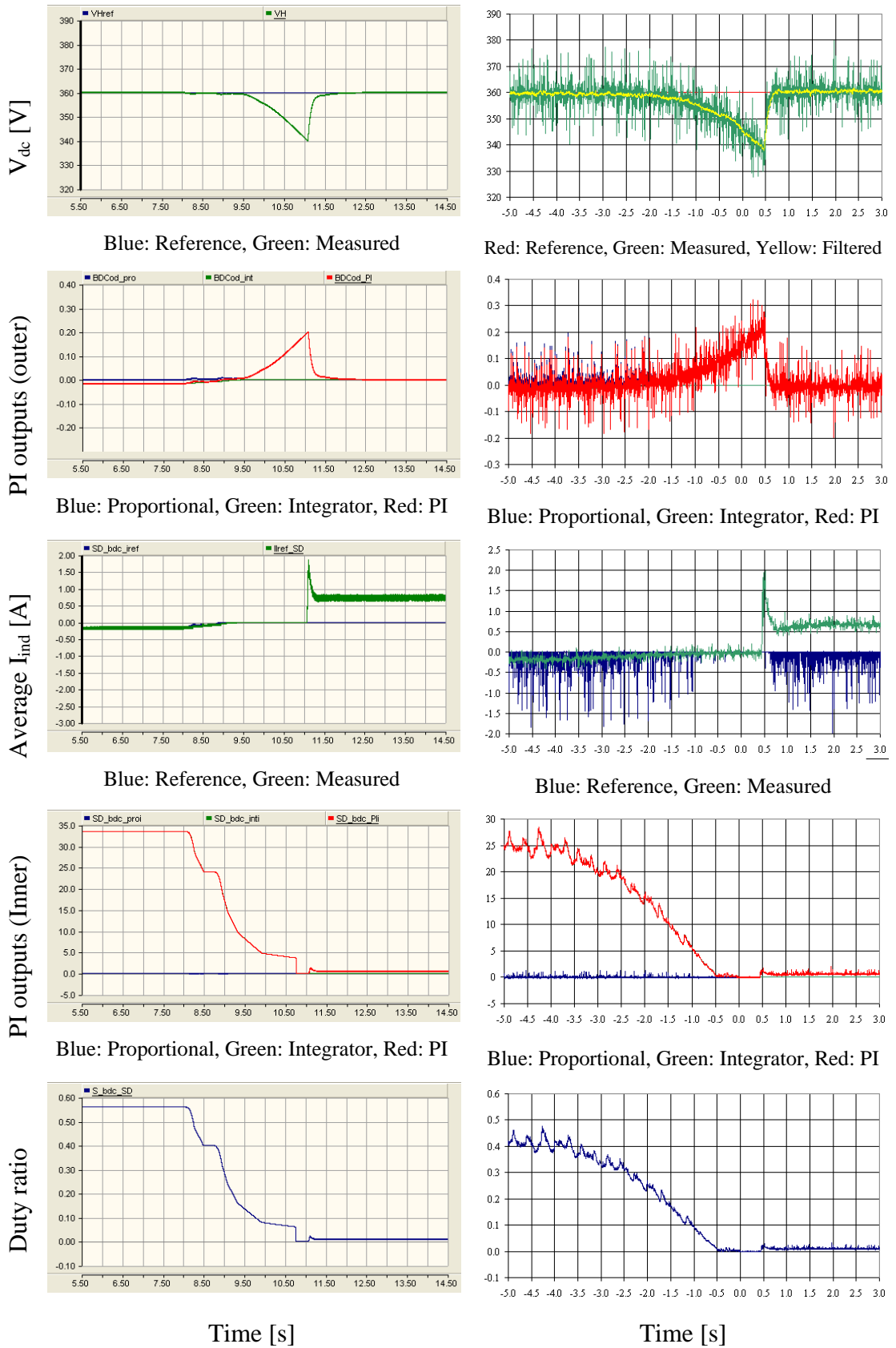
(a) Simulation

(b) Experimental

Figure 7-22: Behaviour of the step-down mode controller of the bi-directional dc-dc
converter (Automatic step-down mode turn-off transient)

Y axis: V$_{in}$ – Light blue (10V/div), I$_{pv}$ – Dark blue (1A/div), For experimental results oscilloscope channel

bandwidth = 5kHz,; X axis: Time (1s/div)
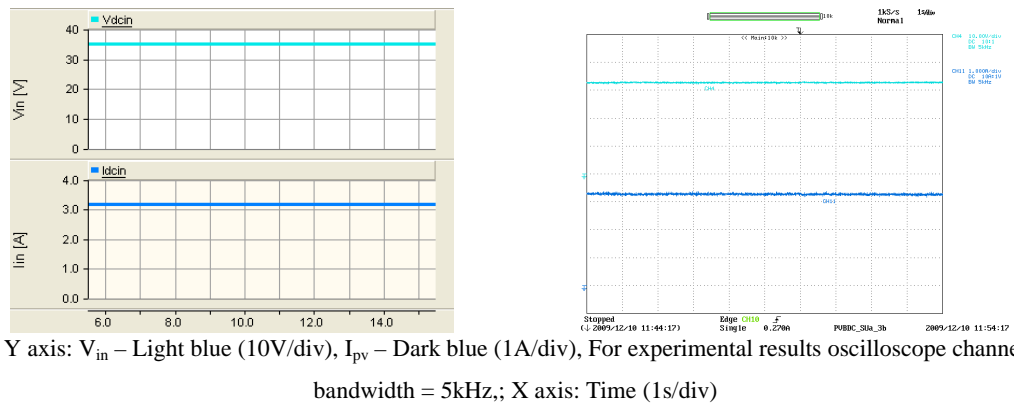
Figure 7-23: Photovoltaic panel voltage and current (Automatic step-down mode turn-off transient) – (a) Simulation (left), (b) Experiment (right)

7.5.4 Automatic turn-off of step-up mode transient of the bi-directional dc-dc converter

Step-up mode would turn off with either an increase in PV output or a decrease in load. This section analyses the transient behaviour during step-up mode turn-off considering a decrease in load. The PV panel emulator output corresponds to 1000W/m^2 and 25°C. Initially the load resistance was set to 1230Ω which would ensure that the bi-directional dc-dc converter is operating in step-up mode with the dc-link voltage at 360V. The load resistance was increased to 1700Ω gradually.

The behaviour of the system during the step-up mode turn-off transient is shown in Figure 7-24 to Figure 7-28. A decrease in current delivered from the battery is visible from Figure 7-24 and simultaneously a dc-link voltage increase is shown in Figure 7-25. Before step-up mode turns off, current delivered from the battery is saturated to a minimum which corresponds to the minimum duty ratio. Once the dc-link voltage cross the reference voltage, current delivered from the battery becomes zero. Figure 7-26 shows the undisturbed photovoltaic panel voltage and current during the transient. Figure 7-27 presents the behaviour of the controller of the bi-directional dc-dc converter. As the dc-link voltage increases, the applied duty ratio decreases and the duty ratio settles to its minimum. When the dc-link voltage crosses the step-up mode turn-off reference (375V), current flowing from the bi-directional dc-dc converter becomes zero. This indicates the turn off operation of the bi-directional converter. As shown in Figure 7-28, the duty ratio applied to the modified forward dc-dc converter is slightly adjusted to compensate the dc-link voltage variations.

(a) Simulation   (b) Experiment
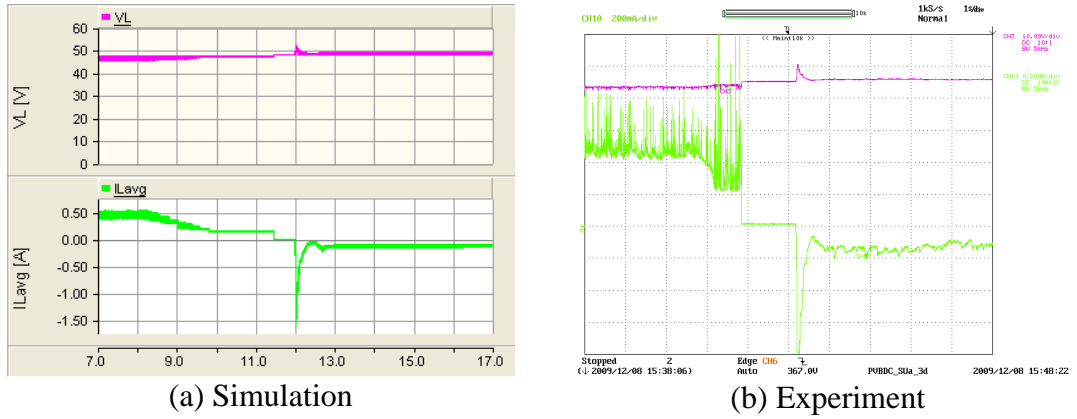
Y axis: V_L – Pink (10V/div), I_L – Green (Simulation-0.5A/div, Experiment-0.2A/div), For experimental measurements oscilloscope channels bandwidth = 5kHz; X axis: Time (1s/div)

Figure 7-24: Voltage at the low-voltage end of the bi-directional dc-dc converter and the battery current (Automatic step-up mode turn-off transient)
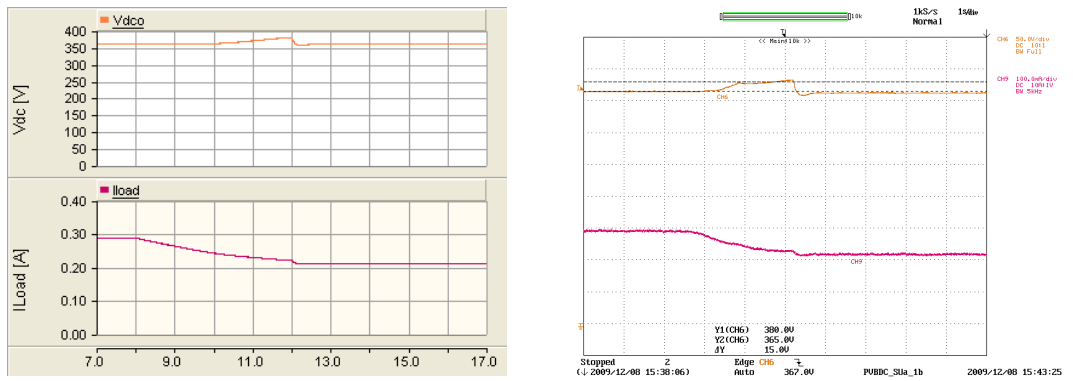
Y axis: V_{dc} – Orange (50V/div), I_{load} – Maroon (0.1mA/div) Experimental oscilloscope channel bandwidth = 5kHz,; X axis: Time (1s/div)

Figure 7-25: DC-link voltage and load current (Automatic step-up mode turn-off transient) – (a) Simulation (left), (b) Experiment (right)
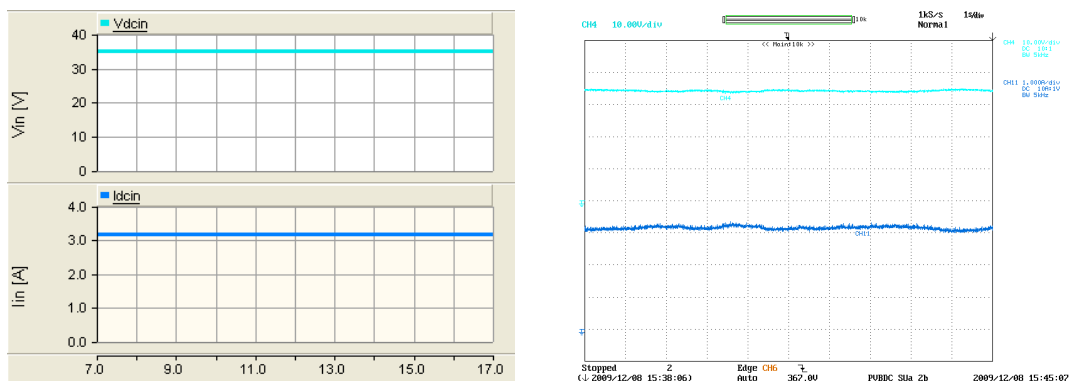
Y axis: V_{in} – Light blue (10V/div), I_{pv} – Dark blue (1A/div), For experimental measurements oscilloscope channels bandwidth = 5kHz,; X axis: Time (1s/div)

Figure 7-26: Photovoltaic panel voltage and current (Automatic step-up mode turn-off transient) – (a) Simulation (left), (b) Experiment (right)

148

Red: Reference, Green: Measured

Blue: Reference, Green: Measured, Yellow: Filtered

Blue: Proportional, Green: Integrator, Red: PI

Blue: Proportional, Green: Integrator, Red: PI

Blue: Reference, Green: Measured

Blue: Reference, Green: Measured

Blue: Proportional, Green: Integrator, Red: PI

Blue: Proportional, Green: Integrator, Red: PI

Time [s]

Time [s]
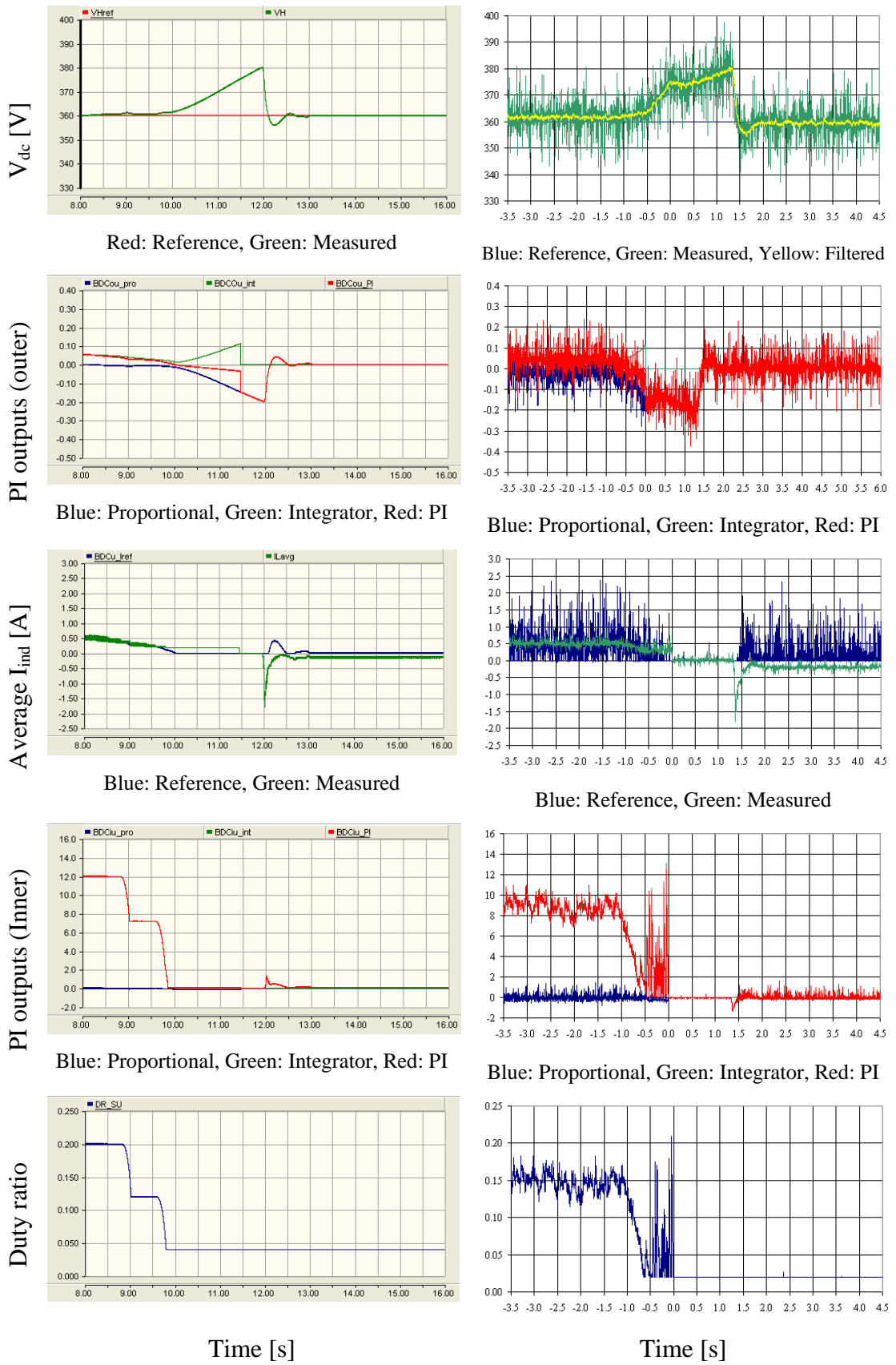
(a) Simulation

(b) Experimental

Figure 7-27: Behaviour of the step-up mode controller of the bi-directional dc-dc converter (Automatic step-up mode turn-off transient)

Red: Reference; Green: V_in   Red: Reference; Green: V_in

Blue: Proportional, Green: Integrator; Red: PI   Blue: Proportional, Green: Integrator; Red: PI

Time [s]   Time [s]

(a) Simulation   (b) Experimental
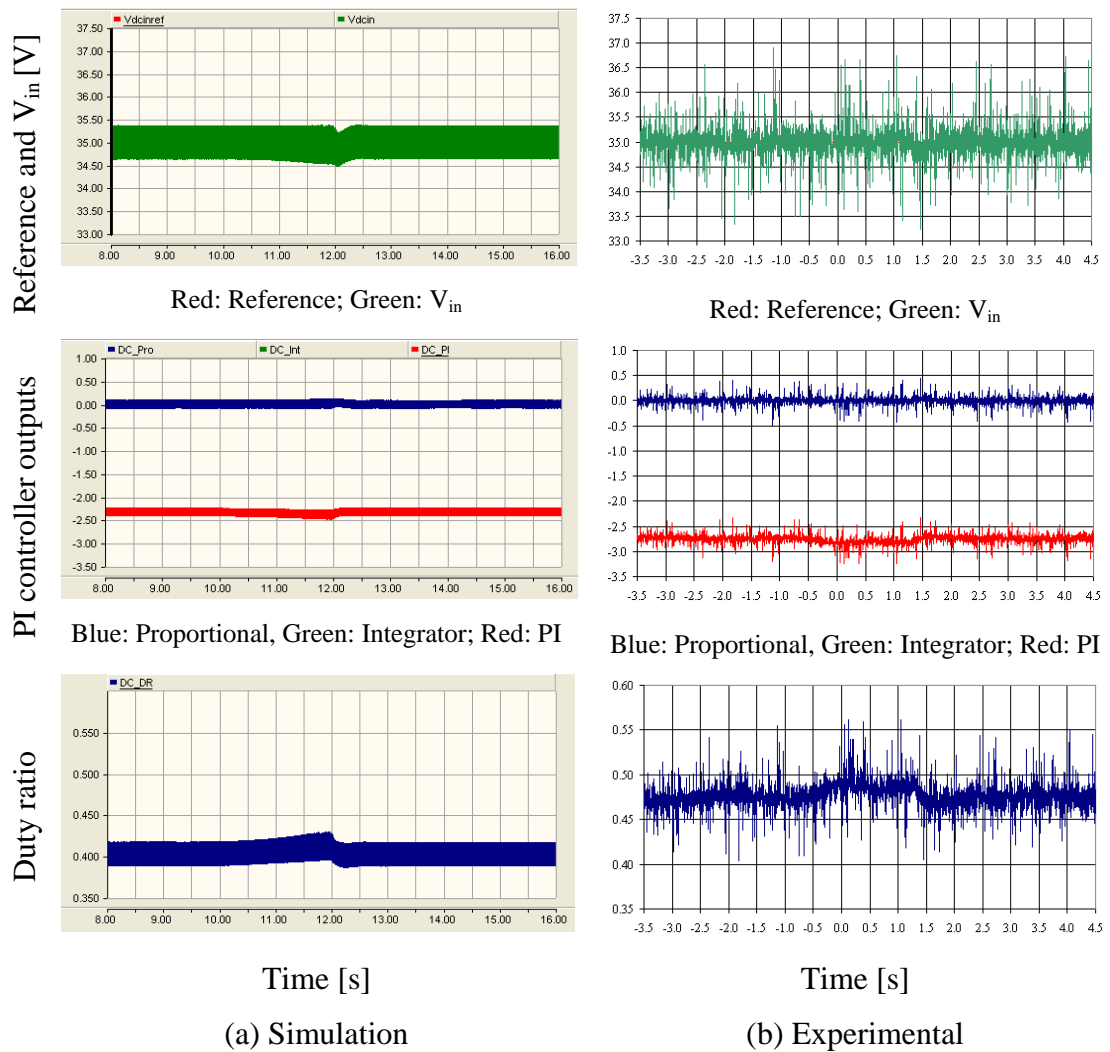
Figure 7-28: Behaviour of the controller of the modified forward dc-dc converter
(Automatic step-up mode turn-off transient)

7.5.5 Worst-case scenario experienced by the step-up mode of the bi-directional dc-dc converter

In case of a sudden disconnection of the photovoltaic panel, the energy storage unit should provide the total load power requirement for an adequate time interval. The dc-link voltage should not experience a significant voltage drop during the transient. Otherwise the power output to the MicroGrid would be disturbed. The PV emulator output again was set to correspond to 1000W/m^2 at 25°C. A resistive load of 1230Ω was connected across the dc-link. The bi-directional dc-dc converter operated in step-up mode while keeping the dc-link voltage at nominal reference in response to the PV output and load. The PV panel was disconnected from the system instantaneously and the transient was captured.

After the disconnection of PV panel, the output current of the PV panel becomes zero as shown Figure 7-29 and the output voltage of the PV corresponds to open circuit voltage. The current delivered by the battery is increased as shown in Figure 7-30 in response to the loss of power from the PV panel. A small drop in dc-link voltage is visible during the transient according Figure 7-31 which shows the dc-link voltage and load current variation. The controller behaviour of the modified forward dc-dc converter is shown on Figure 7-32. The integrator of the controller saturates to its maximum as the input voltage of the converter becomes the open circuit voltage of the PV panel after the disconnection of the PV output power.
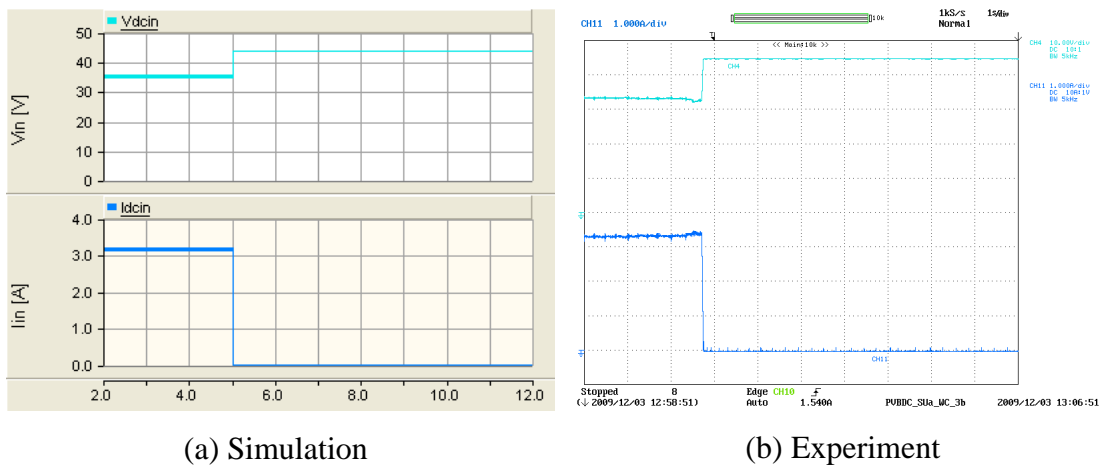
(a) Simulation   (b) Experiment

Y axis: V_{in} – Light blue (10V/div), I_{pv} – Dark blue (1A/div), For experimental results oscilloscope channel bandwidth = 5kHz,; X axis: Time (1s/div)

Figure 7-29: Photovoltaic panel voltage and current (Step-up mode worst-case)

(a) Simulation   (b) Experiment
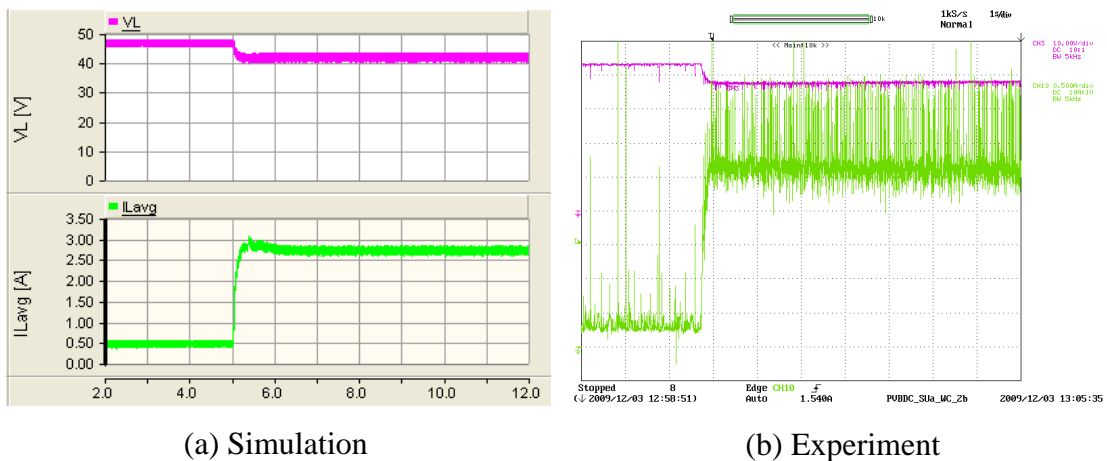
Y axis: V_L – Pink (10V/div), I_L – Green (0.5A/div-Simulation, 0.5A/div-Experimental) Experimental oscilloscope channel bandwidth = 5kHz,; X axis: Time (1s/div)

Figure 7-30: Voltage at the low-voltage end of the bi-directional dc-dc converter and the battery current (step-up mode worst-case)
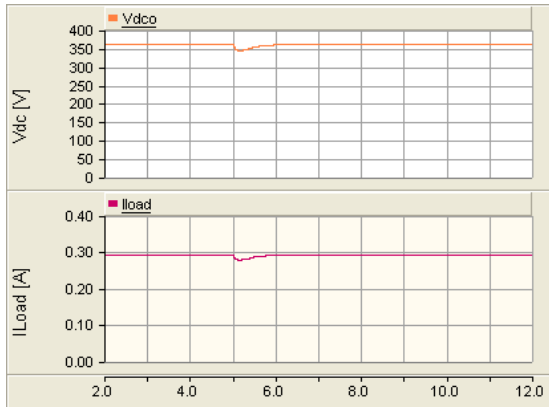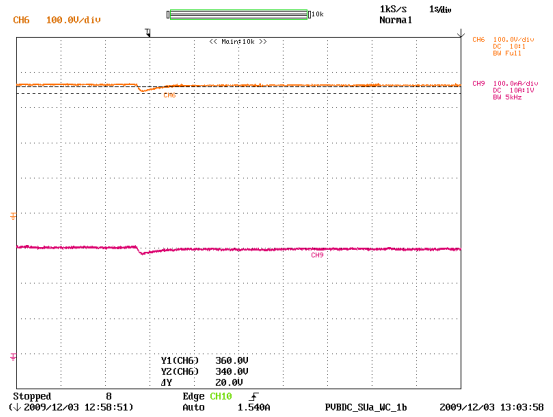
(a) Simulation   (b) Experiment

Y axis: V$_{dc}$ – Orange (50V/div-Simulation, 100V/div-Experiment), I$_{load}$ – Green (0.1A/div) Experimental oscilloscope channel bandwidth = 5kHz; X axis: Time (1s/div)

Figure 7-31: DC-link voltage (V$_{dc}$) and load current (Step-up mode worst-case)
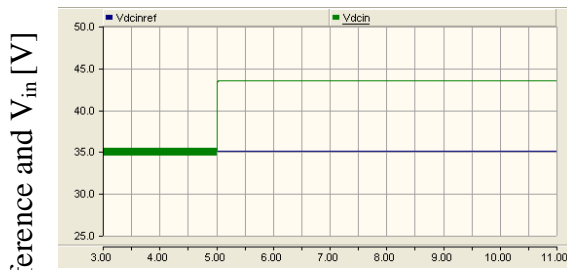
Blue: Reference; Green: V$_{in}$ Red: Reference; Green: V$_{in}$
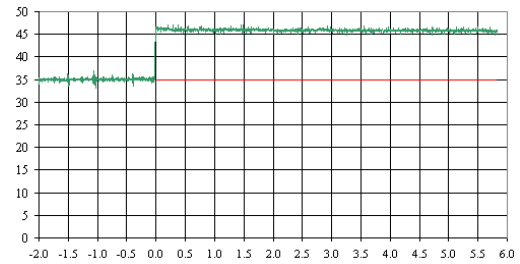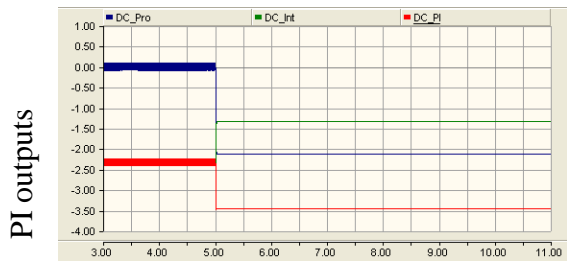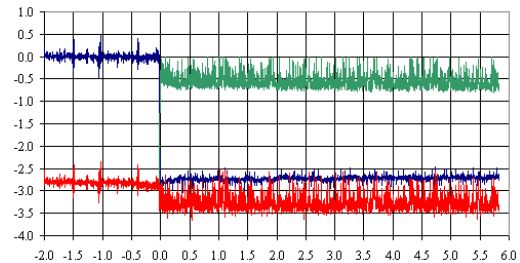
Blue: Proportional, Green: Integrator; Red: PI   Blue: Proportional, Green: Integrator; Red: PI

Time [s]   Time [s]
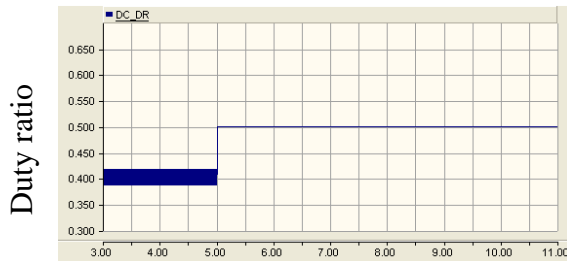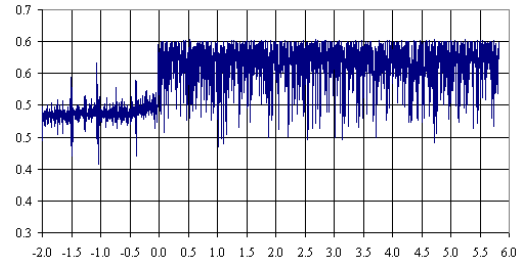
(a) Simulation   (b) Experimental

Figure 7-32: Behaviour of the controller of the modified forward dc-dc converter (step-up mode worst-case)

Figure 7-33 shows the behaviour of the controller of the bi-directional dc-dc converter. The dc-link experiences approximately 20V drop during the loss output power from the PV panel. However, dc-link voltage is restored to the nominal reference value within one second. The outer control loop and average inductor current of the simulation model and experimental results match each other. The difference in duty ratio is due to the difference in voltage at low voltage end of the bi-directional dc-dc converter.

7.5.6 Worst-case scenario experienced by the step-down mode of the bi-directional dc-dc converter

Total power generated by the photovoltaic panel should be diverted to the battery storage in response to a complete loss of load. In such situations the dc-link voltage is subjected to a potentially very severe rise. However the rise should be controlled otherwise the protection system would shut down the complete system. A load of 1642Ω was connected to the dc-link. The photovoltaic panel output was set to correspond to 1000W/m^2 irradiance at 25°C. The system controllers keep the dc-link voltage at the nominal voltage reference with the bi-directional dc-dc converter operating in step-down mode. When the system reached steady state, the load was taken off instantaneously and the transient behaviour was captured.

Figure 7-34 to Figure 7-38 presents the system behaviour during the transient. The load current drops to zero and the current flowing into battery increases simultaneously as shown in Figure 7-34 and Figure 7-35. As shown in Figure 7-36, the photovoltaic voltage or current is not affected significantly even during the worst case scenario.

Figure 7-37 shows the controller behaviour of the bi-directional dc-dc converter. The dc-link experiences about 20V overshoot during the transient before returning to its nominal reference voltage. The duty ratio difference between simulation and experimental results is due to the voltage difference at the low-voltage end of the bi-directional dc-dc converter resulting from the difference between the real battery and its simplified simulation representation. Figure 7-38 shows the behaviour of the controller of the modified forward dc-dc converter. A negligible variation in duty ratio is visible in the controller during the transient.

Blue: Reference, Green: Measured

Red: Reference, Green: Measured

Blue: Proportional, Green: Integrator, Red: PI

Blue: Proportional, Green: Integrator, Red: PI

Blue: Reference, Green: Measured

Blue: Reference, Green: Measured

Blue: Proportional, Green: Integrator, Red: PI

Blue: Proportional, Green: Integrator, Red: PI

Time [s]

Time [s]

(a) Simulation
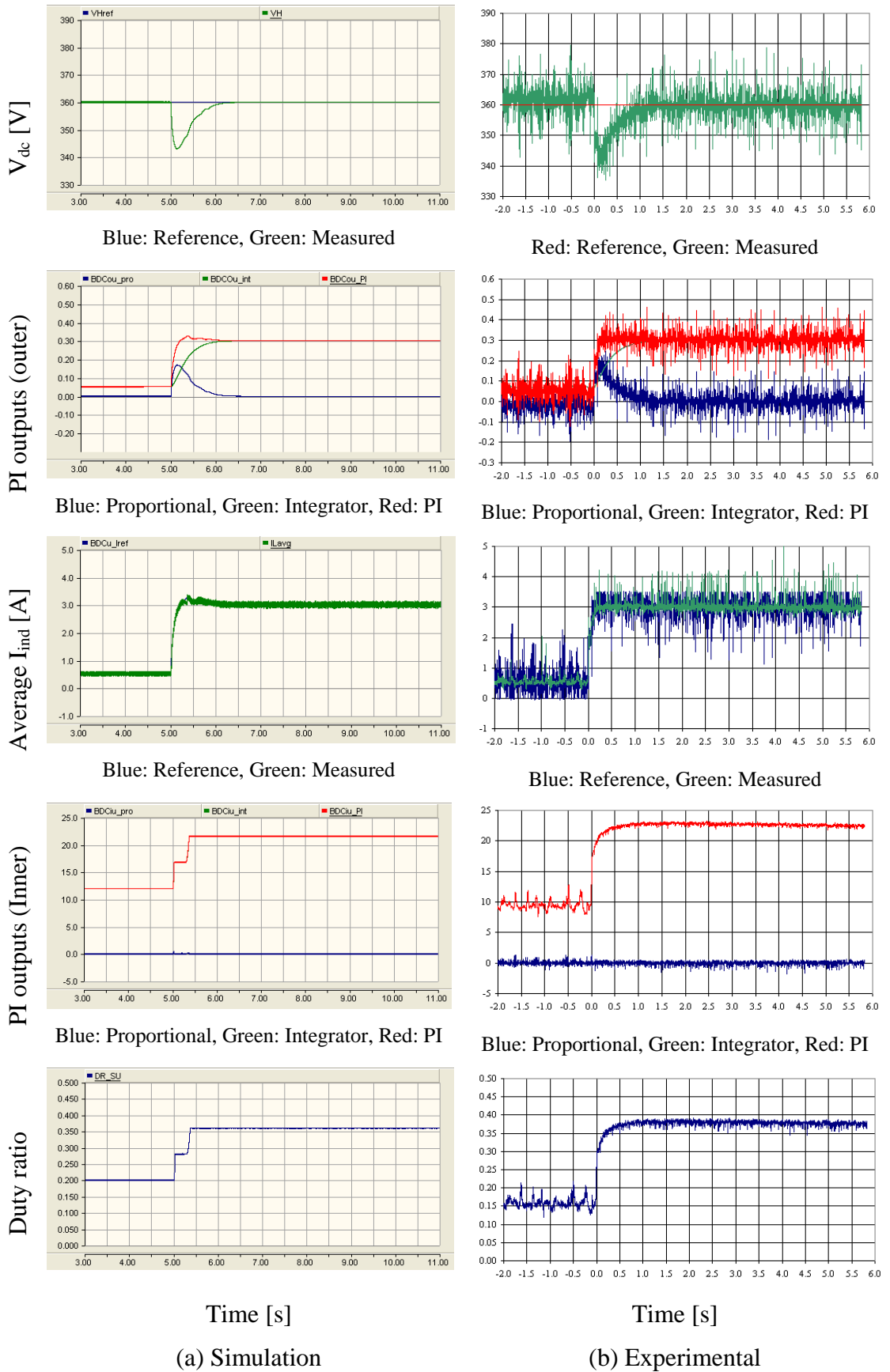
(b) Experimental

Figure 7-33: Behaviour of the step-up mode controller of the bi-directional dc-dc converter (step-up mode worst-case)
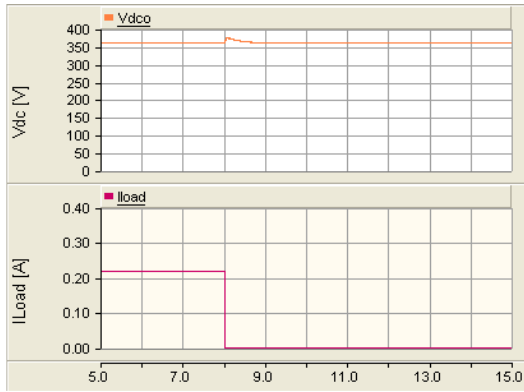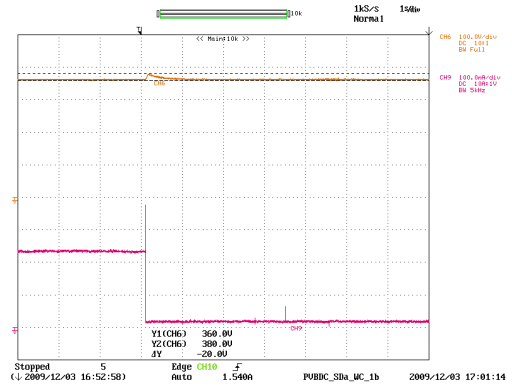
(a) Simulation	(b) Experiment

Y axis: V_{dc} – Orange (50V/div-simulations, 100V/div-Experiment), I_{load} – Maroon (0.1A/div) Experimental oscilloscope channel bandwidth = 5kHz,; X axis: Time (1s/div)

Figure 7-34: DC-link voltage (V_{dc}) and load current (Step-down mode worst-case)
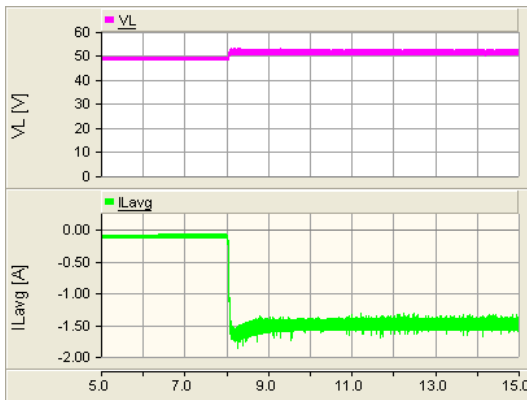
(a) Simulation	(b) Experiment
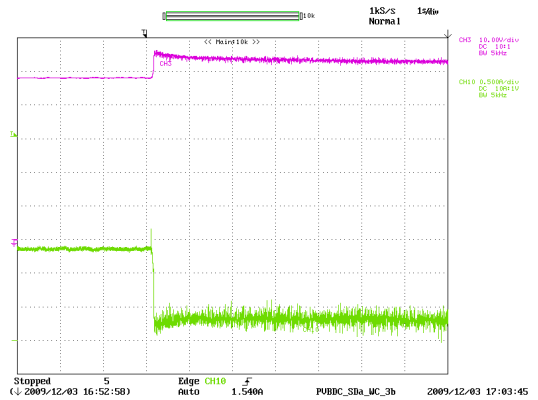
Y axis: V_L – Pink (10V/div), I_L – Green (0.5A/div), Experimental oscilloscope channel bandwidth = 5kHz,; X axis: Time (1s/div)

Figure 7-35: Voltage at the low-voltage end of the bi-directional dc-dc converter and the battery current (Step-down mode worst-case)
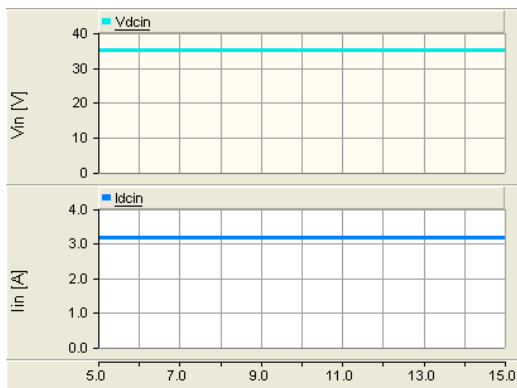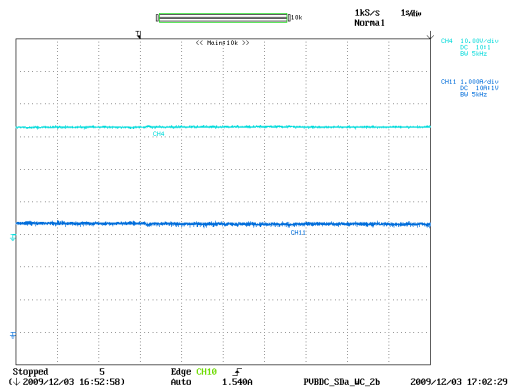
(a) Simulation	(b) Experiment

Y axis: V_{in} – light blue (10V/div), I_{pv} – Dark blue (1A/div), For experimental results oscilloscope channel bandwidth = 5kHz,; X axis: Time (1s/div)

Figure 7-36: Photovoltaic panel voltage and current (Step-down mode worst-case)

Red: Reference, Green: Measured

Red: Reference, Green: Measured

Blue: Proportional, Green: Integrator, Red: PI

Blue: Proportional, Green: Integrator, Red: PI

Blue: Reference, Green: Measured

Blue: Reference, Green: Measured

Blue: Proportional, Green: Integrator, Red: PI

Blue: Proportional, Green: Integrator, Red: PI

Time [s]

Time [s]
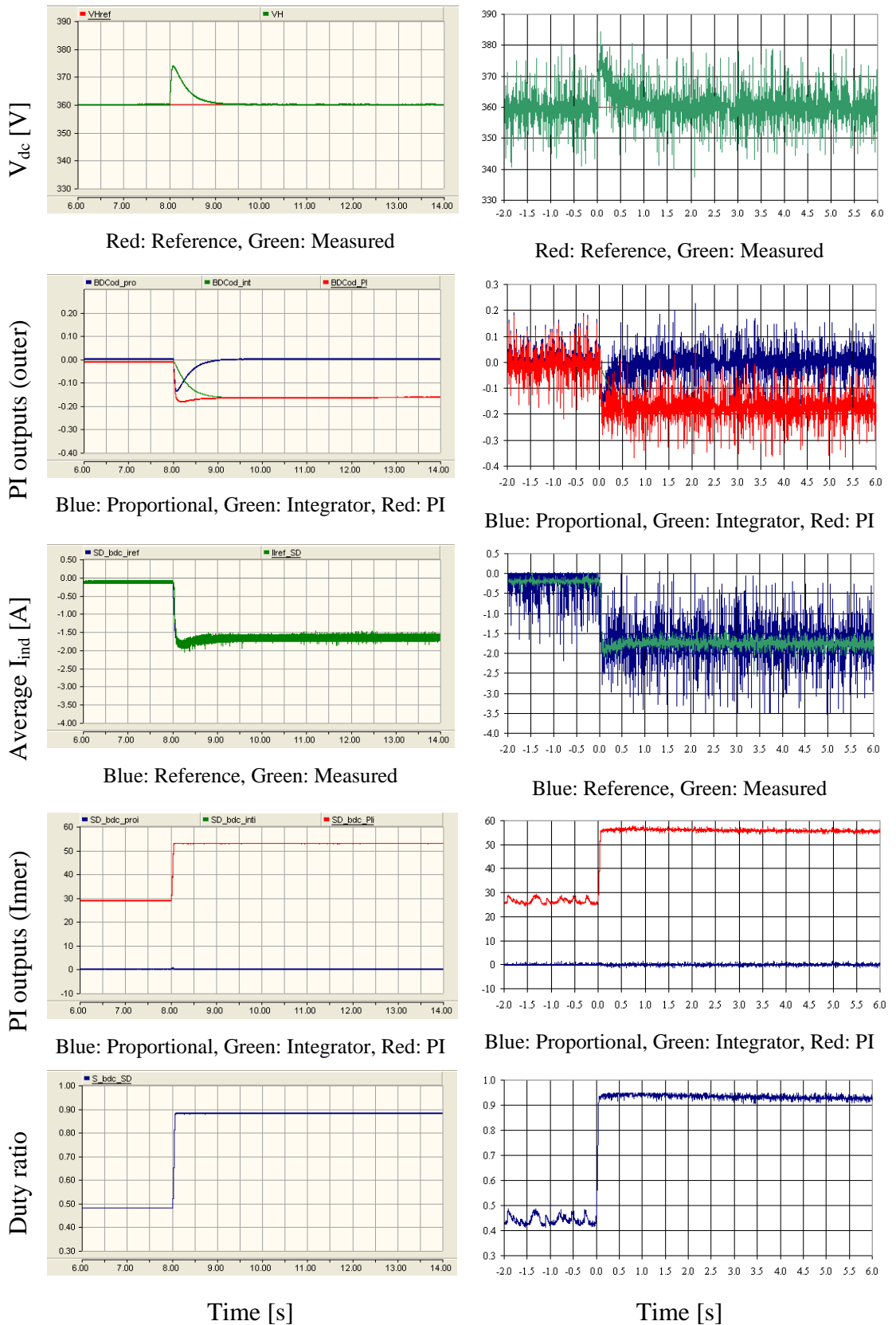
(a) Simulation

(b) Experimental

Figure 7-37: Behaviour of the step-down mode controller of the bi-directional dc-dc converter (Step-down mode worst-case)

(a) Simulation   (b) Experimental
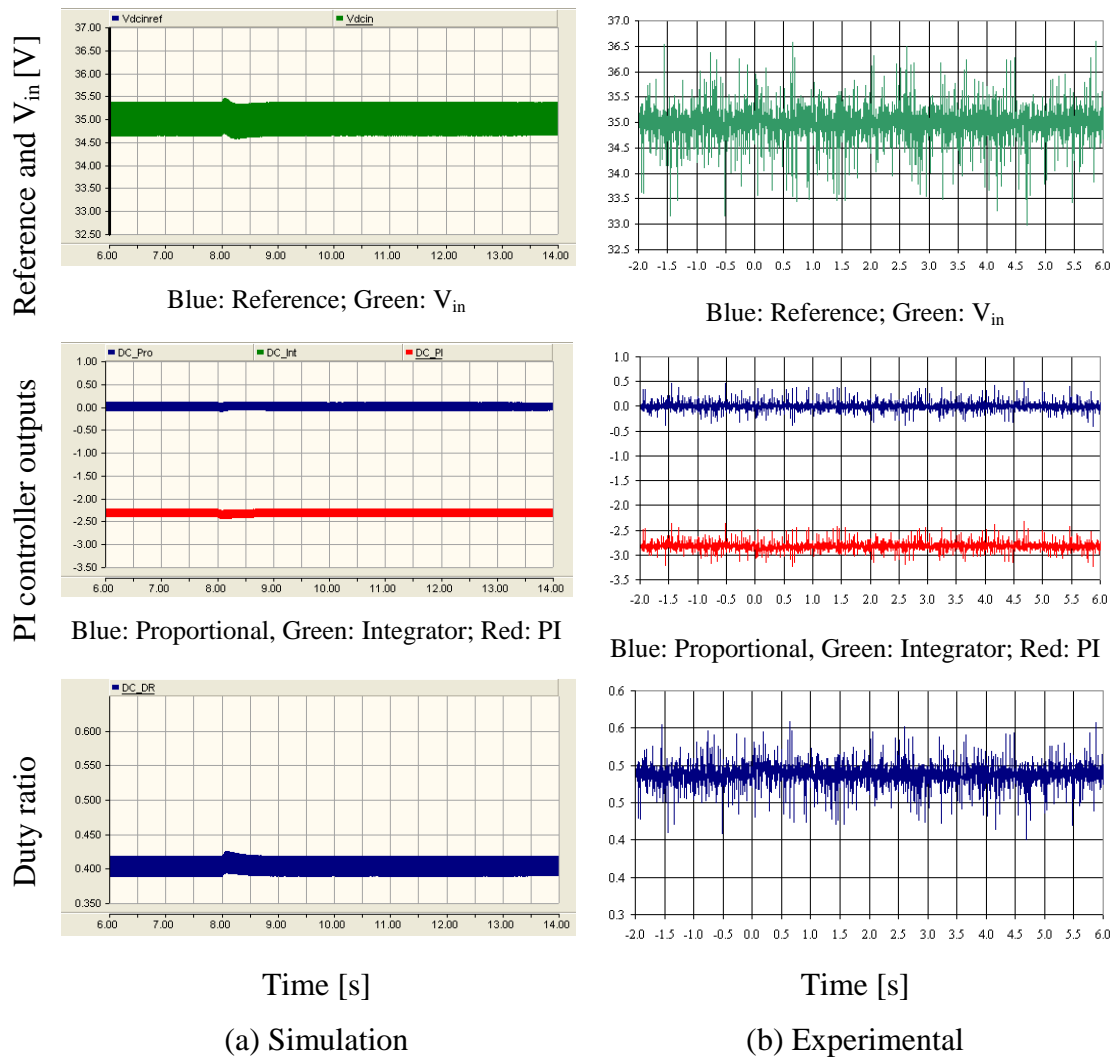
Figure 7-38: Behaviour of the controller of the modified forward dc-dc converter (Step-down mode worst-case)

7.6 SUMMARY

A control scheme for bi-directional dc-dc converter mode selection is introduced which is based on hysteresis control. The system comprising a photovoltaic panel emulator, converters and energy storage was tested with controllers operating automatically. A resistive load was connected to the dc-link. The dc-link voltage was subjected to variations due to PV panel output and load variations with time. Load variation around the operating power range was carried out to observe the dc-link behaviour. In such situations, the bi-directional dc-dc converter switched between modes appropriately while keeping the dc-link voltage with the given limits. The dynamics of the dc-link did not affect the PV panel output voltage which is control variable of the modified forward dc-dc converter. Two worst-case scenarios were studied – complete loss of PV output

power or load. Even in these situations, the dc-link voltage only varied within the limits. Thus it is possible to state that with the proposed controller, a stiff dc-link could be obtained. Further the controller of the modified forward dc-dc converter hardly was affected by the dynamics of the dc-link voltage.

CHAPTER 8

GRID CONNECTION OF SINGLE-PHASE INVERTER

8.1 INTRODUCTION

Figure 8-1 illustrates the controller of the single-phase inverter. The controller consists of an inner current loop and the reference for this inner current loop is generated by the active and reactive power references. This chapter presents the design and implementation of the inner current loop and grid connection of the inverter. Analysis in the chapter assumes that the inverter is powered by a stiff voltage source. Simulation and experimental results corresponding to inner current loop behaviour and grid connection of the inverter are included.
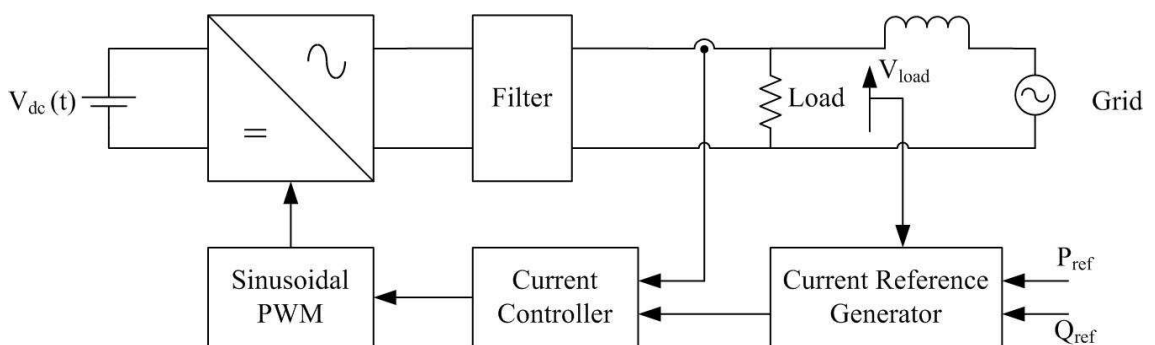
Figure 8-1: Proposed controller for the single-phase inverter

8.2 DEVELOPMENT OF INNER CURRENT LOOP FOR THE INVERTER

8.2.1 Design of current controller

A single-phase inverter connected to a resistive load through an inductive coupler is shown in Figure 8-2. The state feedback block diagram of the system is presented in Figure 8-3 which is based on governing Equation 8-1 and Equation 8-2.

$$L_p s I_{INV}(s) = E_{INV}(s) - R_p I_{INV}(s) - V_{INV}(s) \qquad \text{Equation 8-1}$$

$$E_{INV}(s) = V_{dc} V_c(s) \qquad \text{Equation 8-2}$$
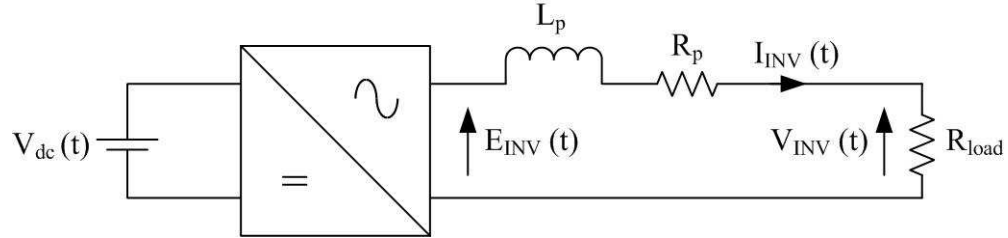
Figure 8-2: Single-phase inverter connected to a series resistive and inductive load
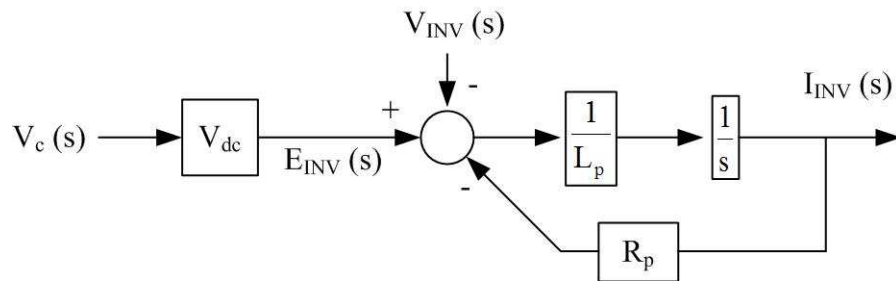
Figure 8-3: State feedback block diagram of the single-phase inverter

Figure 8-4 illustrates the inner current loop of the single-phase inverter which is based on a simple PI controller. The voltage across the load is a disturbance and is decoupled in the controller. The dc supply voltage in the physical system may vary with time. Thus the effect of the dc supply voltage is eliminated in the controller using the measured voltage. Assuming perfect decoupling, the simplified block diagram of the controller is presented in Figure 8-5.
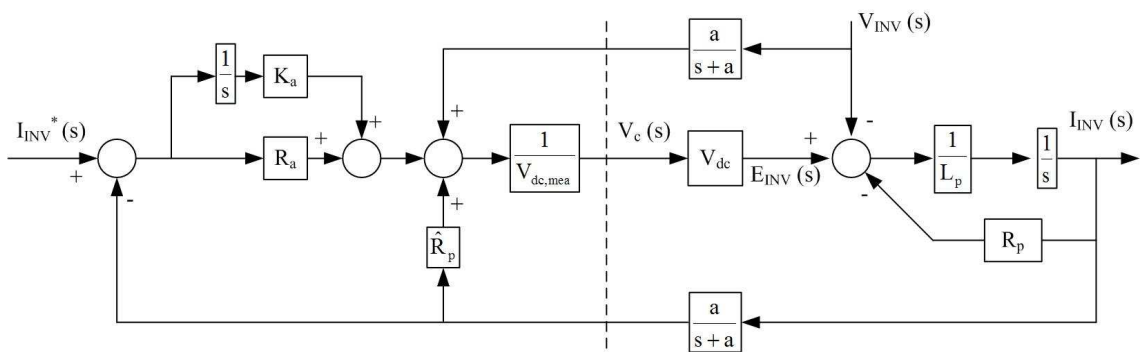
Figure 8-4: Current controller for the single-phase inverter using instantaneous voltage and current measurements
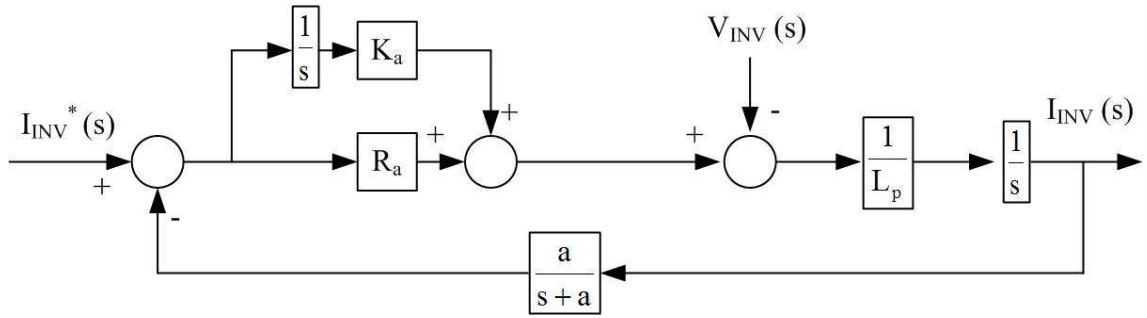
Figure 8-5: Simplified current controller for the single-phase inverter

The dynamic stiffness of the system with a proportional controller (DS_P) and a PI controller (DS_{PI}) is given in Equation 8-3 and Equation 8-4 respectively. It is assumed that disturbance input (V_{INV}) is not decoupled when deriving the dynamic stiffness equations. Further the command tracking (CT) response of the system with a PI controller is given in Equation 8-5.

$$DS_P : \frac{V_{INV}(s)}{I_{INV}(s)} = -\left(L_p s + \frac{R_a}{s+a}\right)$$
<div align="right">Equation 8-3</div>

$$DS_{PI} : \frac{V_{INV}(s)}{I_{INV}(s)} = -\left(L_p s + \frac{aR_a s + aK_a}{s(s+a)}\right)$$
<div align="right">Equation 8-4</div>

$$CT : \frac{I_{INV}(s)}{I_{INV}^*(s)} = \frac{R_a s^2 + (aR_a + K_a)s + aK_a}{L_p s^3 + aL_p s^2 + aR_a s + aK_a}$$
<div align="right">Equation 8-5</div>

The controller dynamic stiffness and command tracking performance were analysed for a set of PI controller gains. A representative sample is presented in Table 8-1.

Table 8-1: PI controller gains for the current controller for selected cases

	R_a	K_a	Eigenvalues (Hz)
Case I	400	600000	3200, 1300, 322
Case II	360	465000	3450, 1000, 273
Case III	320	360000	3660, 929, 236
Case IV	280	270000	3840, 779, 201
Case V	240	200000	4000, 635, 175

Figure 8-6 shows the dynamic stiffness of the current controller. The inductance of the inductor determines the dynamic stiffness at high frequencies. The controller gains could be used to improve the dynamic stiffness properties of the system at low and mid frequencies. As the values of the gains for the controller increases, dynamic stiffness increases. Thus higher gains yield better dynamic stiffness properties.

Legend
Red: Case I
Blue: Case II
Green: Case III
Yellow: Case IV
Black: Case V
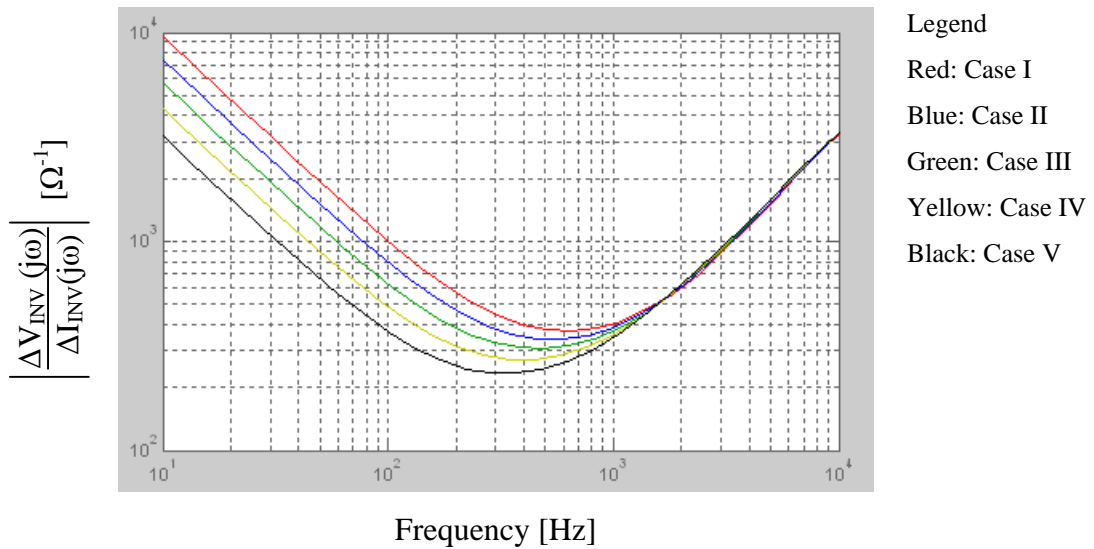
Frequency [Hz]

Figure 8-6: Dynamic stiffness response of the current controller for the selected cases

The command tracking response of the system is presented in Figure 8-7 over a 10Hz to 10kHz frequency range. The system operating frequency is 50Hz thus the frequency response of the system around operating frequency is plotted and presented in Figure 8-8. At 50Hz for the selected cases, a maximum 0.5° phase shift is introduced by the controller. At low frequencies the transfer function of could be approximated to that in Equation 8-6. The magnitude of the imaginary part in the numerator is higher than that of denominator. This is the reason for the small leading phase angle. The phase shift increases as the controller gains increase. Thus lower gains are desirable considering the phase shift of system. However the magnitude error increases as the gains decreases. Therefore a degree of trade-off exists in gain selection.

$$\frac{I_{INV}(s)}{I^*_{INV}(s)} \approx \frac{(aR_a + K_a)s + aK_a}{aR_a s + aK_a} \qquad \text{Equation 8-6}$$

As a result, gains for the case III were selected for the current controller as a reasonable compromise.
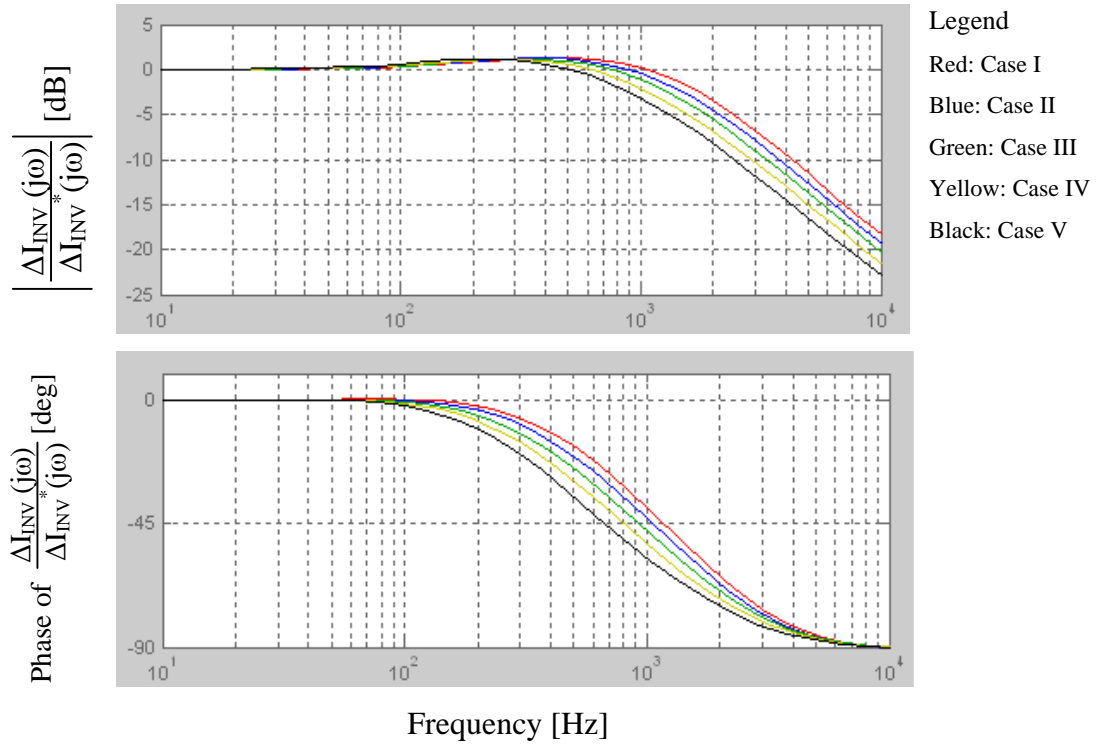
Figure 8-7: Command tracking response of the current controller for the selected cases
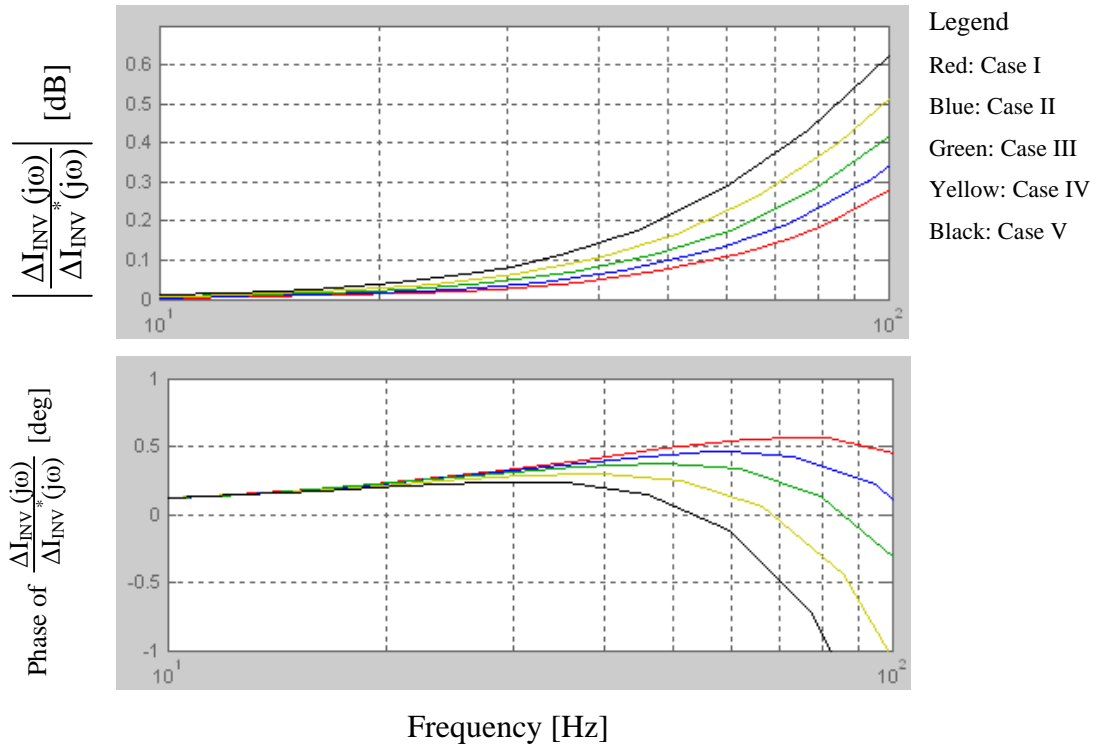
Figure 8-8: Command tracking response of the current controller around 50Hz for the
selected cases

8.2.2 Testing of current controller with resistive load and laboratory power supply

The inverter was connected to a resistive load of 290 Ω as shown in Figure 8-9. A laboratory power supply was used as the dc source and the output voltage of the source was set to 360 V.
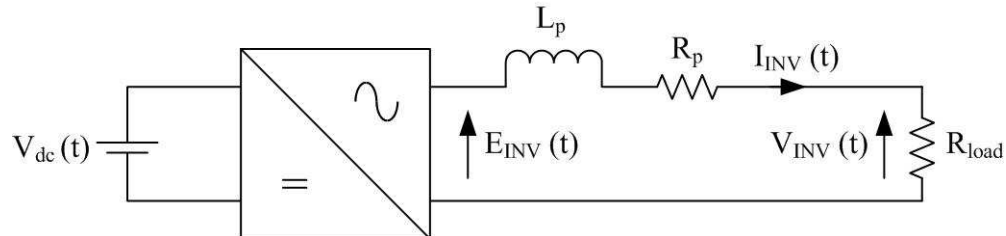
Figure 8-9: Test set-up used for the current controller of the inverter testing

The rms value of the reference current was given a step from 0.5A to 0.7A. Figure 8-10 presents the output voltage and current waveforms of the inverter. The output current of the inverter almost instantaneously changes to the new reference current. The load voltage is adjusted automatically at the same time.

(a) Simulation   (b) Experiment
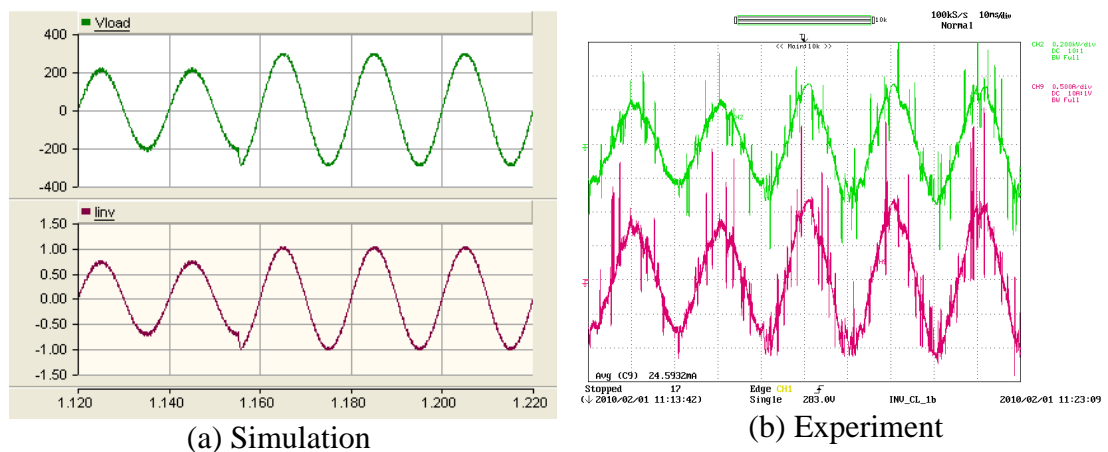
Y axis: V_{INV} – Green (200V/div), I_{INV} – Maroon (0.5A/div); X axis: Time (200ms/div); Step change: just before 1.16 in simulation, at the beginning of 4th time/div block in experimental

Figure 8-10: Inverter output current and voltage across the resistor

The transient response of the current controller is presented in Figure 8-11. The reference was given a step at just before t = 1.16 seconds and t = 0.0 seconds in the simulation model and experimental set-up respectively. The measured current almost instantaneously adjusts to the new reference. The integrator of the PI controller dominates over the proportional controller. The load voltage, which is the disturbance

input decoupling term, is larger compared with the PI controller output and inductor internal resistance (R_p) decoupling term. Thus controller is dominated by the load voltage. Measured voltage and current in the experimental set-up are superimposed with noise which has affected the controller, when compared with controller results of the simulation model.

Red: Reference, Green: Measured

Red: Reference, Green: Measured

Blue: Proportional, Green: Integrator, Red: PI

Blue: Proportional, Green: Integrator, Red: PI

Blue: PI, Green: R_p decoupling, Red: V_{inv}

Blue: PI, Green: R_p decoupling, Red: V_{inv}
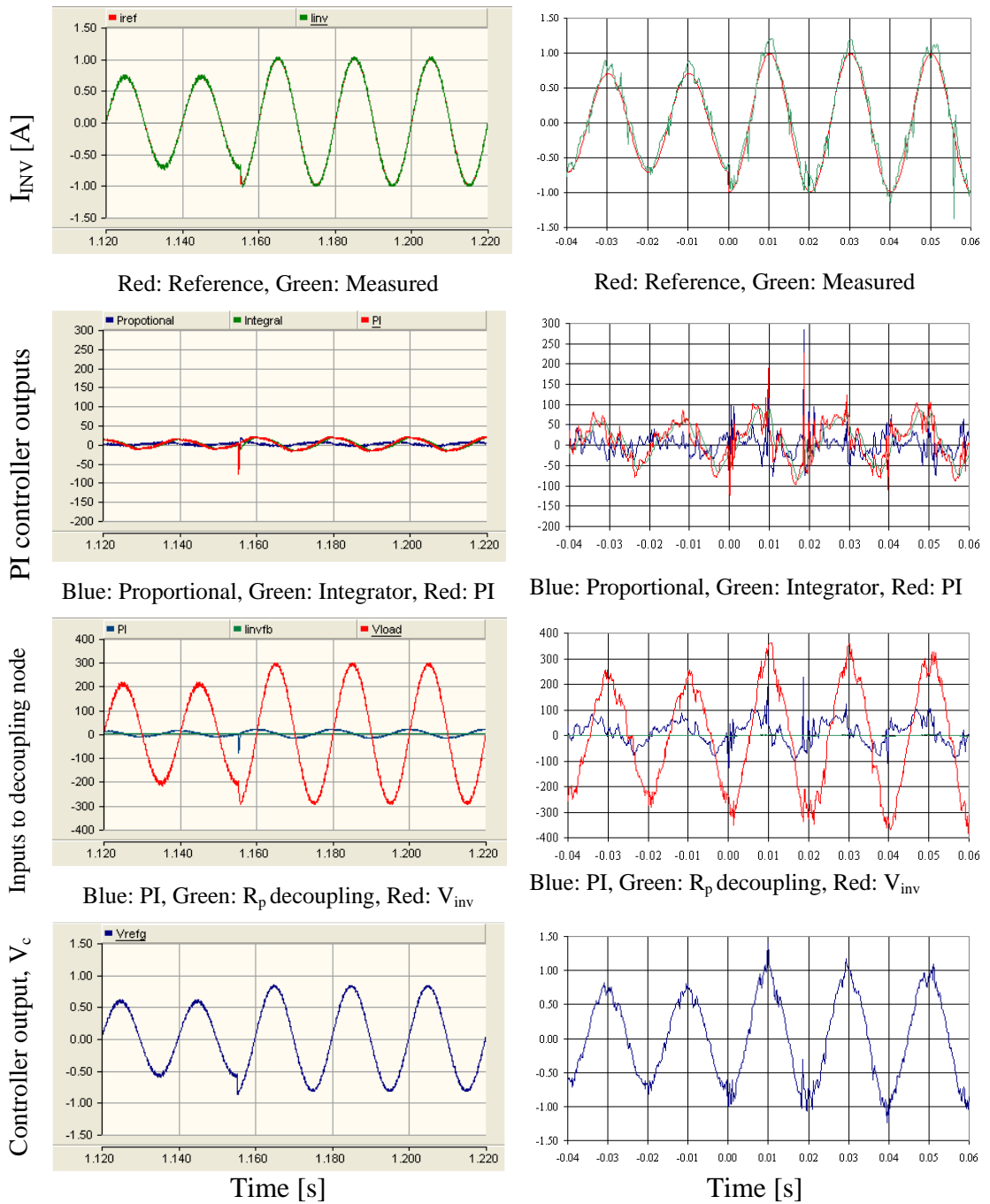
(a) Simulation

(b) Experimental

Figure 8-11: Behaviour of the current controller at the step change current reference

8.3 GRID CONNECTION OF SINGLE-PHASE INVERTER

Figure 8-12 shows the controller block diagram of the inverter which is to be grid connected. In order to interface the inverter to the grid, it is essential to synchronise the two systems. In the proposed system, this is achieved using a Phase Locked Loop (PLL). Grid voltage is fed into the PLL. A synchronised sinusoidal signal is produced using the output of the PLL and this signal is used to generate the current reference to the inner current controller.

The current controller reference needs two inputs which are magnitude and phase. Phase is introduced with respect to grid voltage, allowing the reactive power to be controlled. Current magnitude clearly controls real power, although there is (weak) cross-coupling between the two controllers. In the following sub sections, the magnitude and phase are provided in two different ways. In the first method, magnitude and phase are manually controlled. In the second method, magnitude and phase are calculated from the active and reactive power manual inputs with the aid of rms grid voltage. These two methods are shown in Figure 8-12.
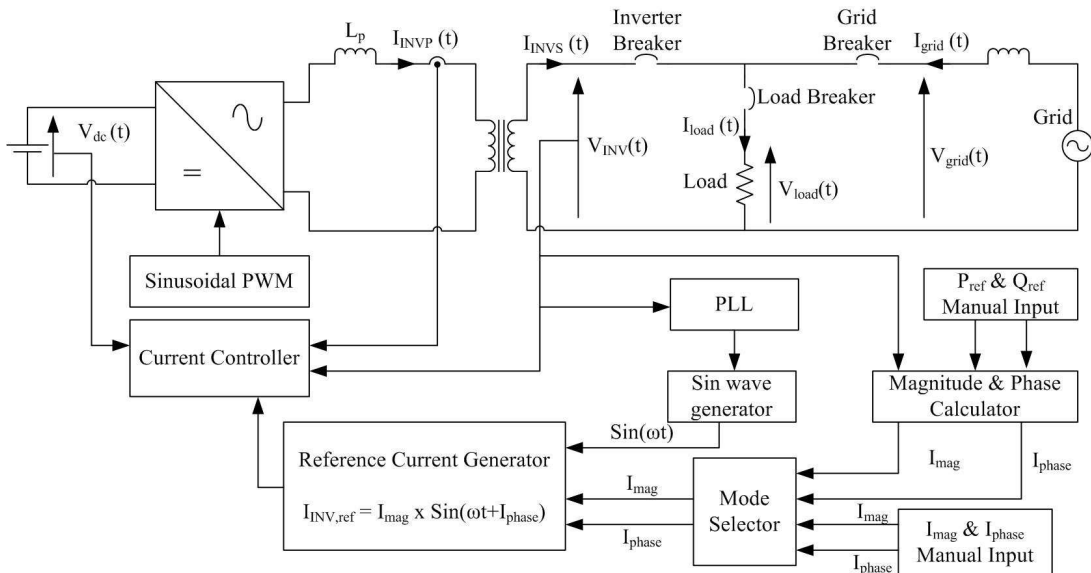
Figure 8-12: Detailed controller of the single-phase inverter

8.3.1 Grid connection with current reference

A resistive load of 290Ω was connected as the load. The system voltage is 240Vrms thus the load consumes 200W. The magnitude of the current reference was set to

0.43Arms. Thus the inverter should supply maximum 90W at the steady-state. The rms current reference is increased at a rate of 0.5A/s to achieve a smooth grid connection.

8.3.1.1 With zero phase shift

Figure 8-13 to Figure 8-17 presents simulation and experimental results of the system. The inverter is connected to the grid at t = 2.0s and t = 0.0s in the simulation model and prototype respectively. According to Figure 8-13 inverter reference current gradually increases after the grid connection which is followed by the inverter output current. Grid current decreases since the load current is constant.

(a) Simulation   (b) Experiment
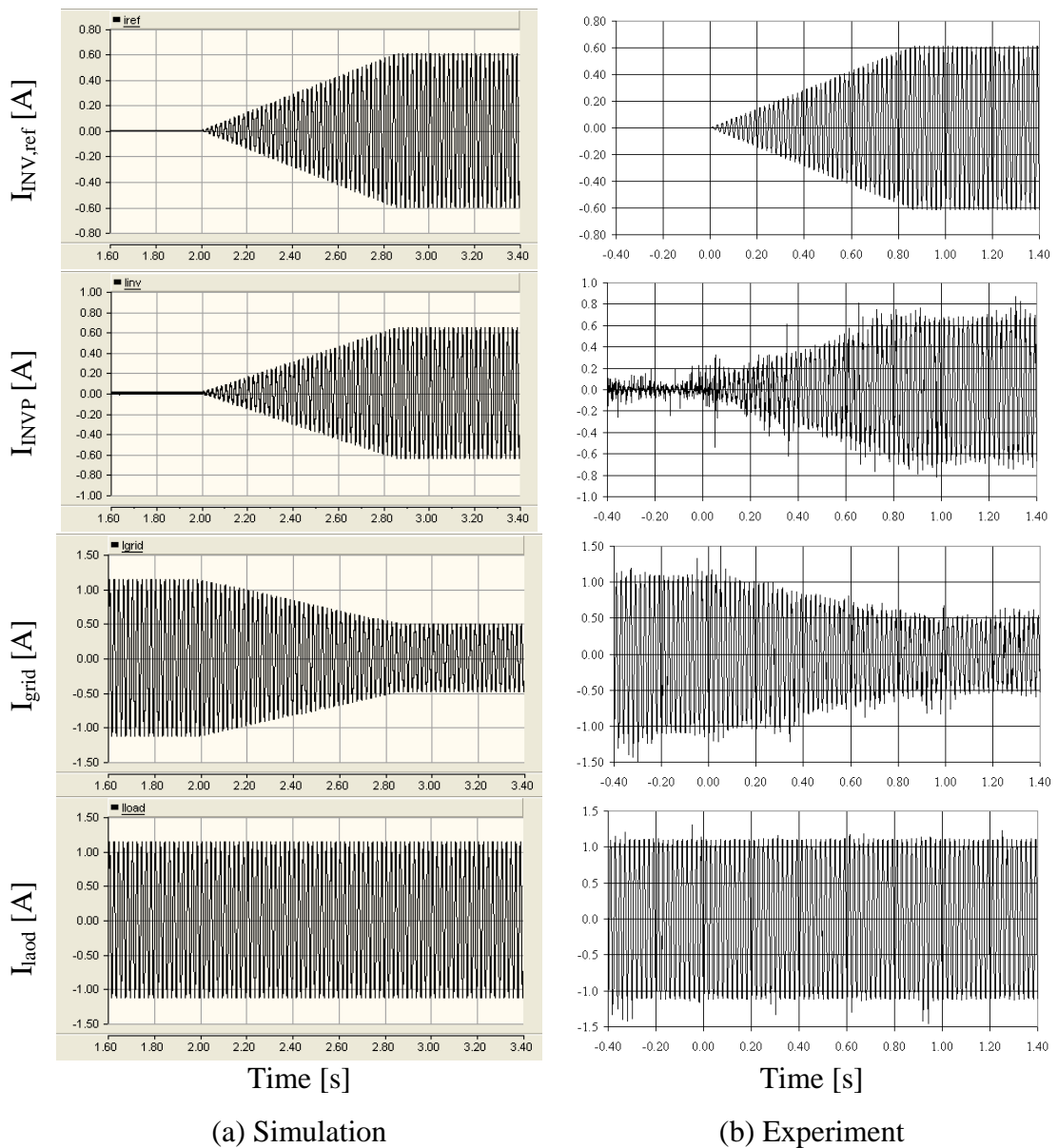
Figure 8-13: Current reference and currents flowing through inverter, load and grid

Figure 8-14 and Figure 8-15 present the voltages and the inverter output current during and after the grid connection respectively. Inverter output current gradually increases after the connection. Load voltage is not distorted at the point of connection or after. This proves that smooth grid connection is possible with this current control technique. Noise superimposed on the inverter output current is reduced once the system has reached the steady state.
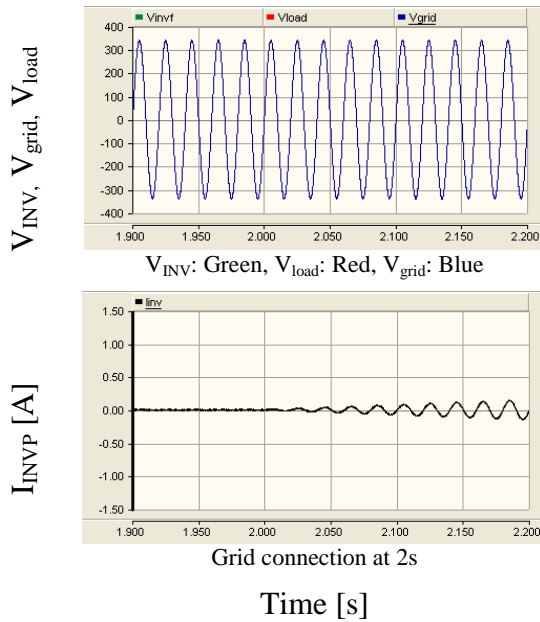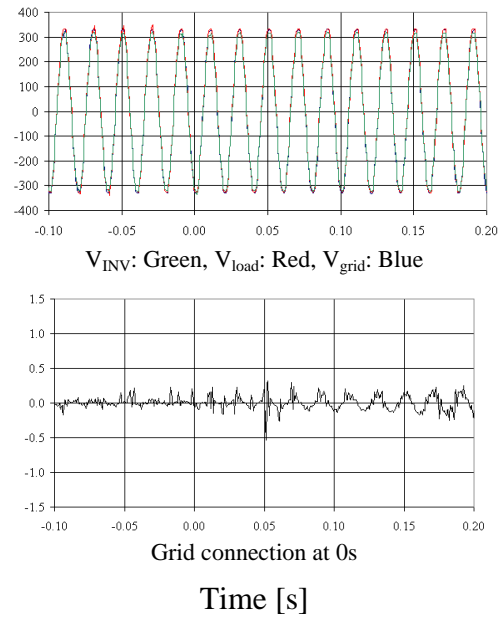
(a) Simulation   (b) Experiment

Figure 8-14: Load voltage and inverter output current at the point of grid connection
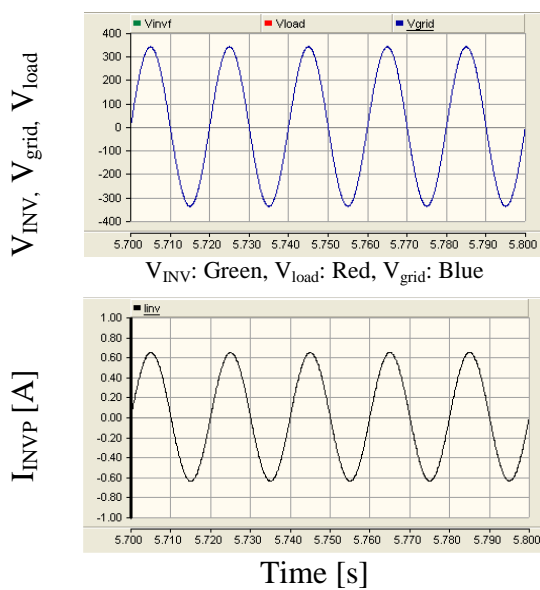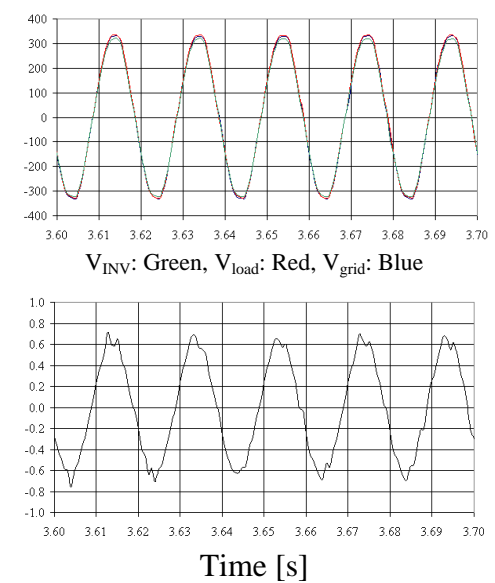
(a) Simulation   (b) Experiment

Figure 8-15: Load voltage and inverter output current after grid connection

Figure 8-16 shows the load voltage (scaled by a factor of 0.004) along with the inverter output current. The phase shift between the load voltage and the inverter output current is zero which indicates that only active power is transferred.

Blue: $0.004 \times V_{load}$, Green: I_{INVP}

Blue: $0.004 \times V_{load}$, Green: I_{INVP}

Blue: $0.004 \times V_{load}$, Green: I_{INVP}

Blue: $0.004 \times V_{load}$, Green: I_{INVP}

Blue: $0.004 \times V_{load}$, Green: I_{INVP}

Blue: $0.004 \times V_{load}$, Green: I_{INVP}

Time [s]   Time [s]

(a) Simulation   (b) Experiment
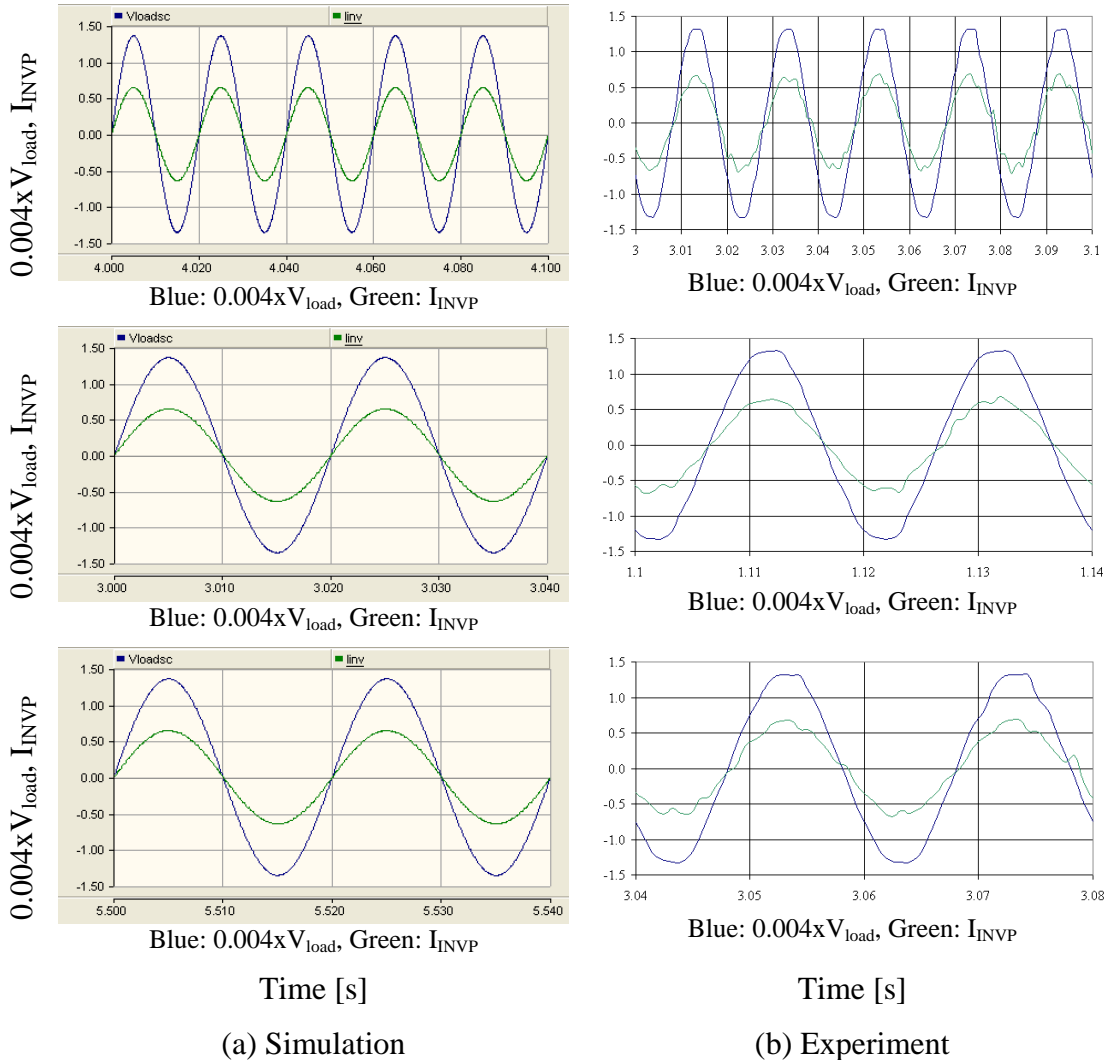
Figure 8-16: Scaled load voltage and inverter output current at the steady state after grid connection

The behaviour of the current controller after grid connection is presented in Figure 8-17. The inverter output current follows the reference current. The load voltage is fed to the controller as disturbance input decoupling and it dominates over the PI controller output. The PI controller outputs of the prototype have additional noise compared with the simulation model PI controller outputs. However, the controller signal applied to the pulse width modulator is similar in magnitude for both simulation model and prototype.
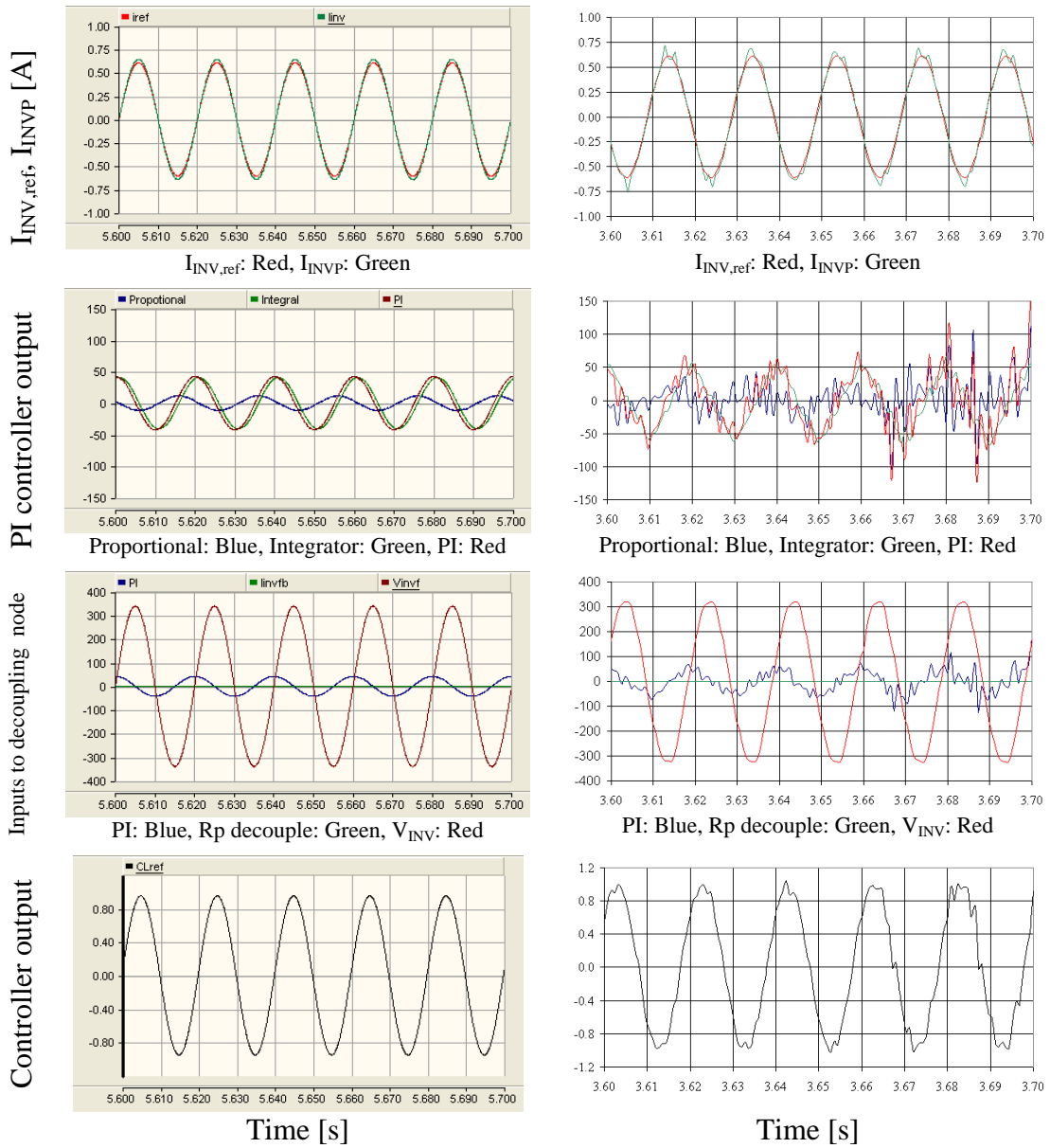
(a) Simulation   (b) Experiment

Figure 8-17: Behaviour of current controller of the inverter

8.3.1.2 With phase shift

A 20° phase shift was added to the current reference with respect to the load voltage. Figure 8-18 to Figure 8-24 shows the simulation and experimental results. The inverter current reference is shown in Figure 8-18. Figure 8-19 presents the load voltage (scaled by a factor of 0.004) and the inverter current reference in the steady state. The inverter current reference lags behind the load voltage. The phase difference is approximately 1ms which is equal to 20°. According to Figure 8-20 the inverter current reference and the output current are in-phase thus correct phase shift is maintained.

(a) Simulation   (b) Experiment
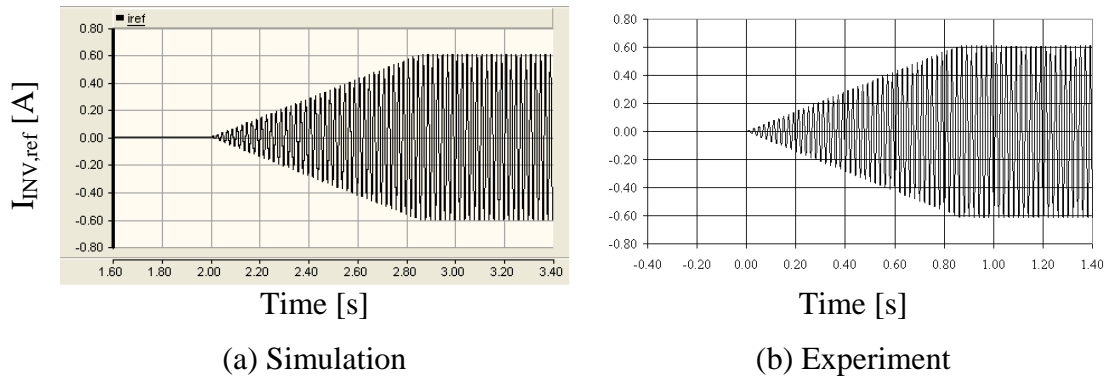
Figure 8-18: Inverter current reference

(a) Simulation   (b) Experiment
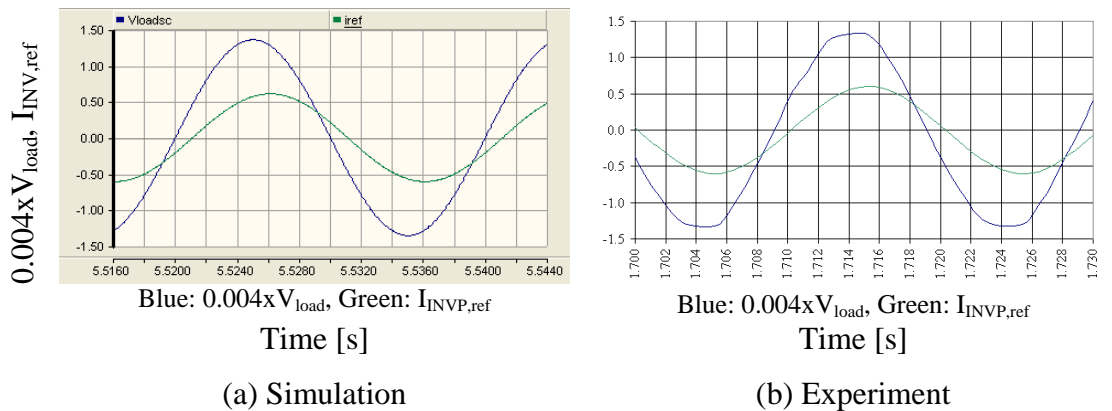
Figure 8-19: Scaled load voltage and inverter current reference

(a) Simulation   (b) Experiment
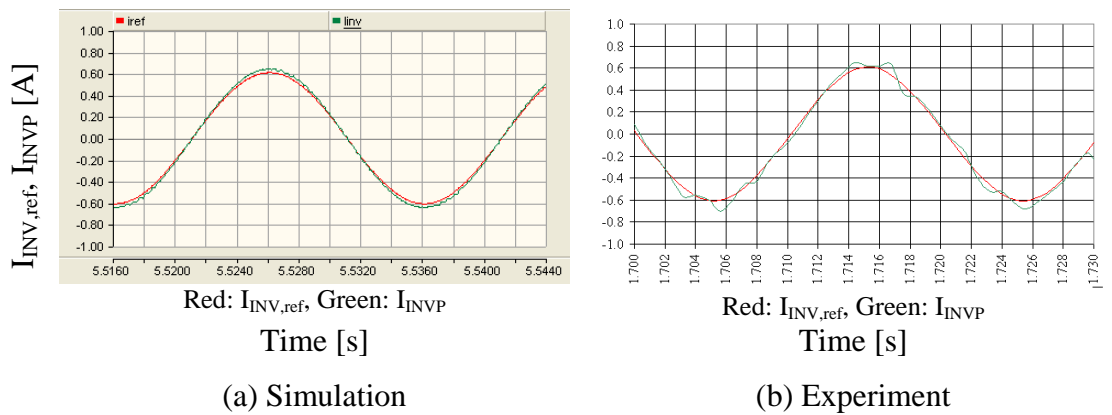
Figure 8-20: Inverter current reference and inverter output current

The behaviour of the inner current controller of the inverter is shown in Figure 8-21. Inverter current follows the reference current command. Again the disturbance input decoupling term, which is the load voltage, dominates the controller signal. PI controller outputs of the prototype are comparatively noisy due to superimposed noise in the current measurement.

$I_{INV,ref}$: Red, I_{INVP}: Green

Proportional: Blue, Integrator: Green, PI: Red

PI: Blue, Rp decouple: Green, V_{INV}: Red

Time [s]

(a) Simulation

$I_{INV,ref}$: Red, I_{INVP}: Green

Proportional: Blue, Integrator: Green, PI: Red

PI: Blue, Rp decouple: Green, V_{INV}: Red

Time [s]

(b) Experiment
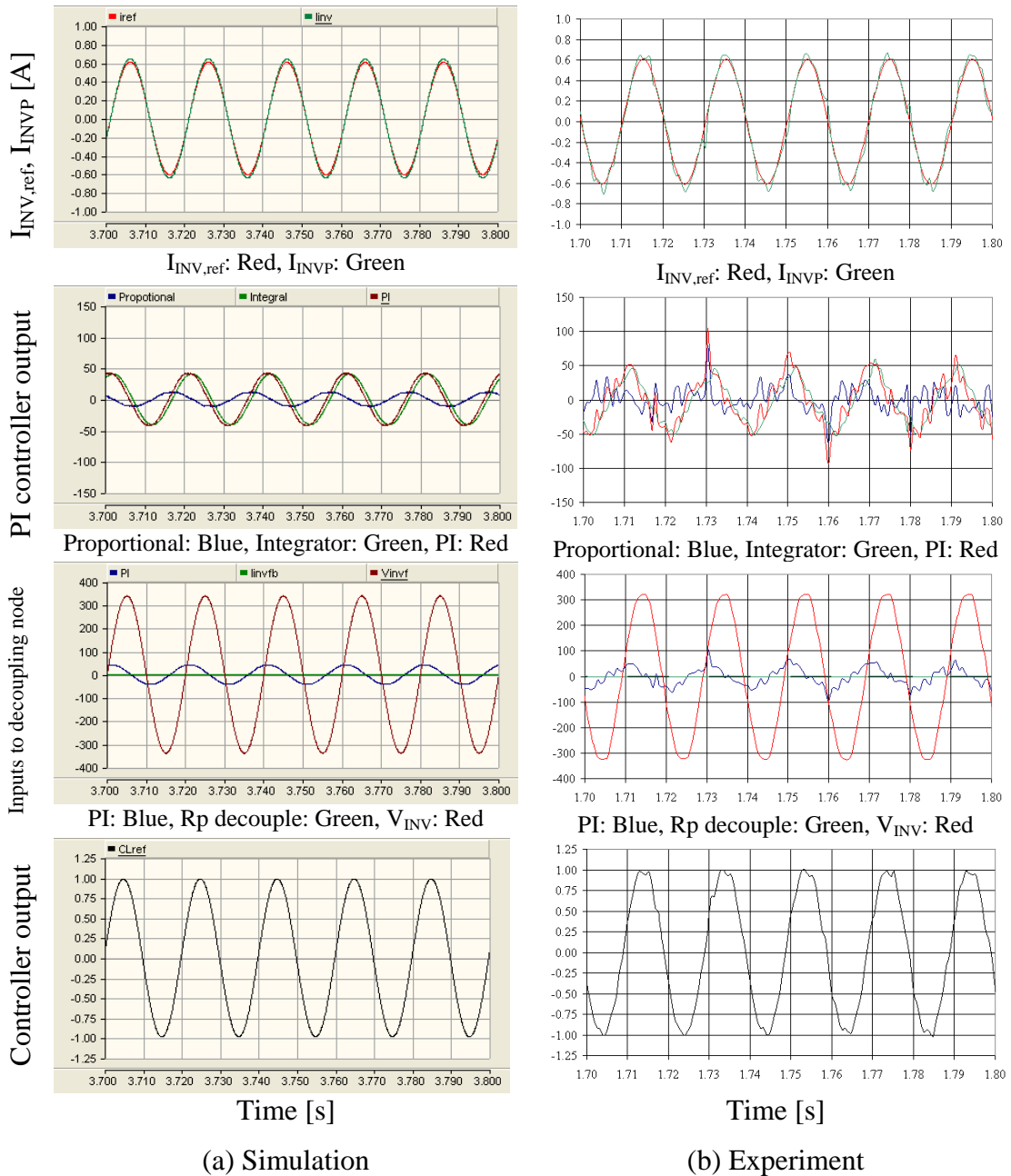
Figure 8-21: Behaviour of the current controller after the grid connection

Figure 8-22 presents the currents flowing through the inverter, the load and the grid. The load current is constant since the grid voltage is constant. Inverter output current increases to follow the inverter current reference. As a result the current contribution from the grid reduces. Inverter, grid and load voltages along with inverter output current at the point of connection are plotted in Figure 8-23. The inverter smoothly connects to the grid thus the voltages do not experience any effect. Figure 8-24 presents the inverter output current and voltages at the steady state after the grid connection.

Time [s]   Time [s]

(a) Simulation   (b) Experiment
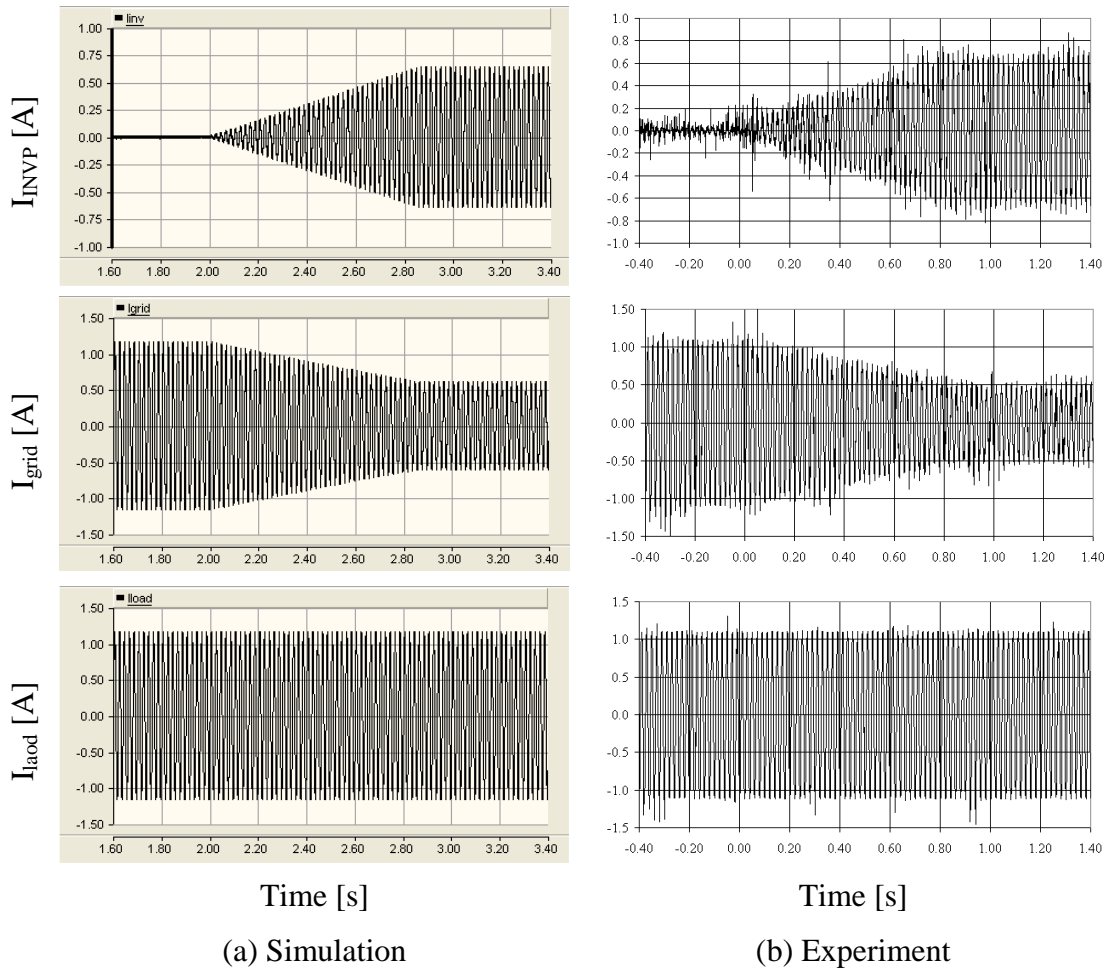
Figure 8-22: Current flowing through the grid, load and inverter

V_INV: Green, V_load: Red, V_grid: Blue   V_INV: Green, V_load: Red, V_grid: Blue

Grid connection at 2s   Grid connection at 0s

Time [s]   Time [s]

(a) Simulation   (b) Experiment
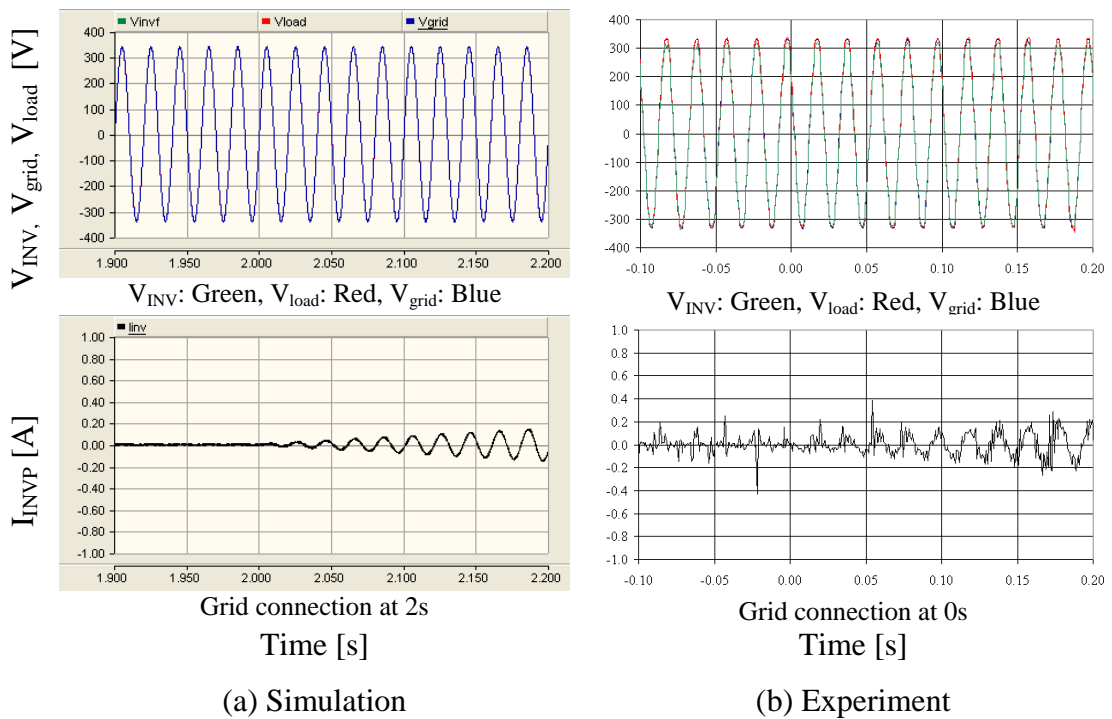
Figure 8-23: Load voltage and inverter output current at the point of grid connection

(a) Simulation   (b) Experiment
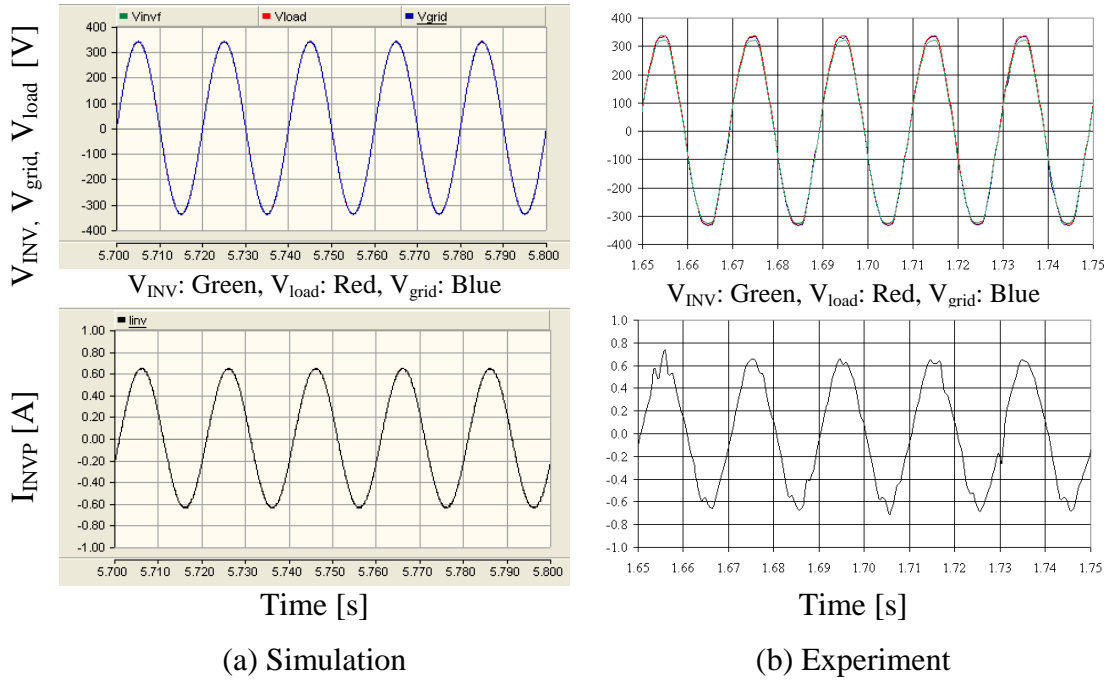
Figure 8-24: Load voltage and inverter output current after grid connection

8.3.2 Grid connection with power references

The current reference can be generated from active and reactive power references with the aid of the RMS voltage according to Equation 8-7 and Equation 8-8. The following sub-section presents the simulation and experimental results of the inverter grid connection using power references.

$$I_{mag} = \sqrt{2}\, \frac{\sqrt{\left(P_{ref}^2 + Q_{ref}^2\right)}}{V_{INVrms}}$$ Equation 8-7

$$I_{phase} = \tan^{-1}\left(\frac{Q_{ref}}{P_{ref}}\right)$$ Equation 8-8

In the simulation model, the FFT block and the harmonic extractor in PSCAD are used to find the magnitude and phase of the fundamental component of voltage and inverter output current. Thereby the active and reactive power outputs are calculated. In the experimental set up, active power is calculated by averaging the product of instantaneous inverter output current and load voltage. Apparent power is calculated by multiplying the RMS inverter output current and RMS load voltage. With the aid of active and apparent power, reactive power is calculated.

A load resistor of 290Ω, which corresponds to 200W at 240Vrms, was connected as the load. Initially the load was fully powered by the grid. Then inverter was connected to the grid with a positive non-zero active power reference and a zero reactive power reference. A step change in reference was not used. Instead the references were ramped at rate of 100W/s and 100VAr/s.

8.3.2.1 With reactive power reference set to zero

An inverter grid connection with 100W active power reference and zero reactive power reference was tested. Figure 8-25 to Figure 8-31 presents the simulation and experimental results of the system. The inverter is connected to the grid at 1.0s and 0.0 seconds in the simulation model and prototype respectively.

Figure 8-25 presents the active power reference and the calculated active power output of the inverter. The current controller introduces a small magnitude error at 50Hz which is the reason for the difference in calculated and reference active power. According to Figure 8-26, phase difference between inverter output current and load voltage (load voltage is scaled by a factor of 0.001 in Figure 8-26) is zero which shows that only active power is transferred by the inverter.

(a) Simulation   (b) Experiment
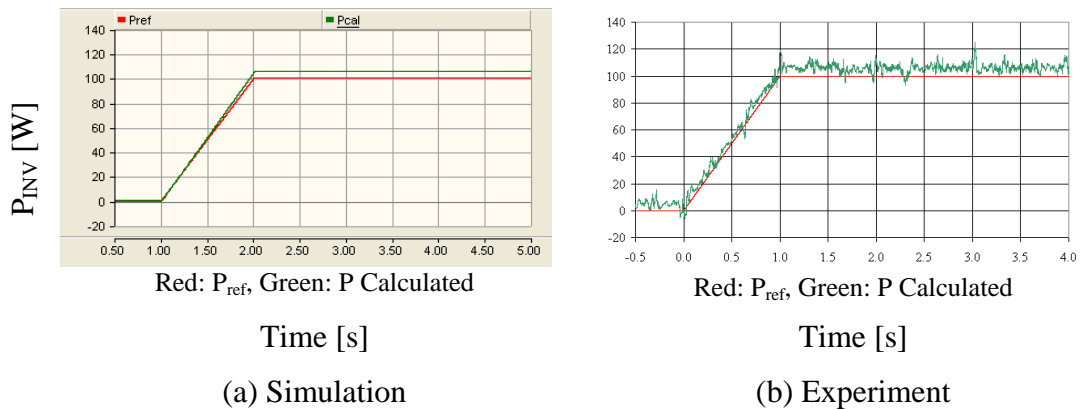
Figure 8-25: Reference and calculated active power of inverter

The magnitude of the current reference increases (see Figure 8-27) in response to increase in active power reference. In response to the current command, the inverter output gradually increases and reaches the steady state value. Load current was constant during the transient. Therefore the grid current reduces. Experimental results are superimposed with noise, thus magnitudes are not clearly visible.

Blue: 0.001xV_load, Green: I_INVP   Blue: 0.001xV_load, Green: I_INVP

Time [s]   Time [s]

(a) Simulation   (b) Experiment
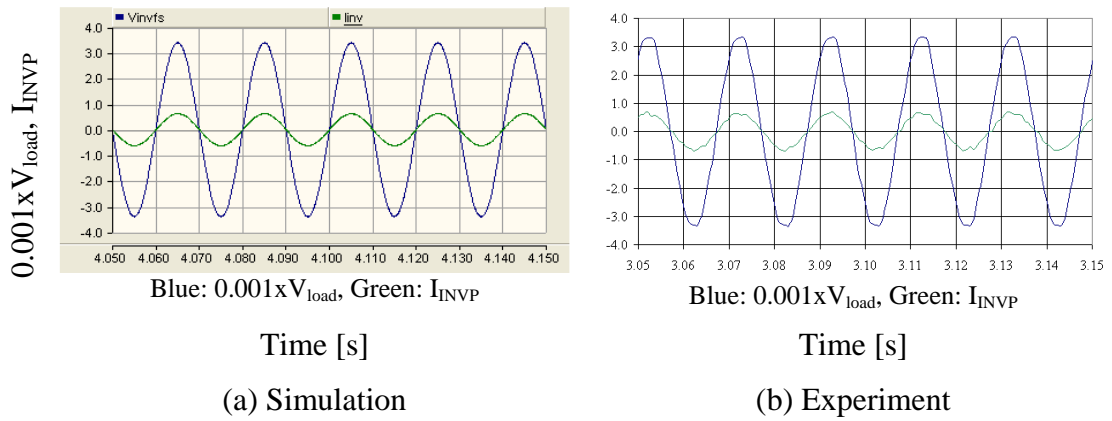
Figure 8-26: Scaled load voltage and inverter output current after the grid connection

Time [s]   Time [s]

(a) Simulation   (b) Experiment
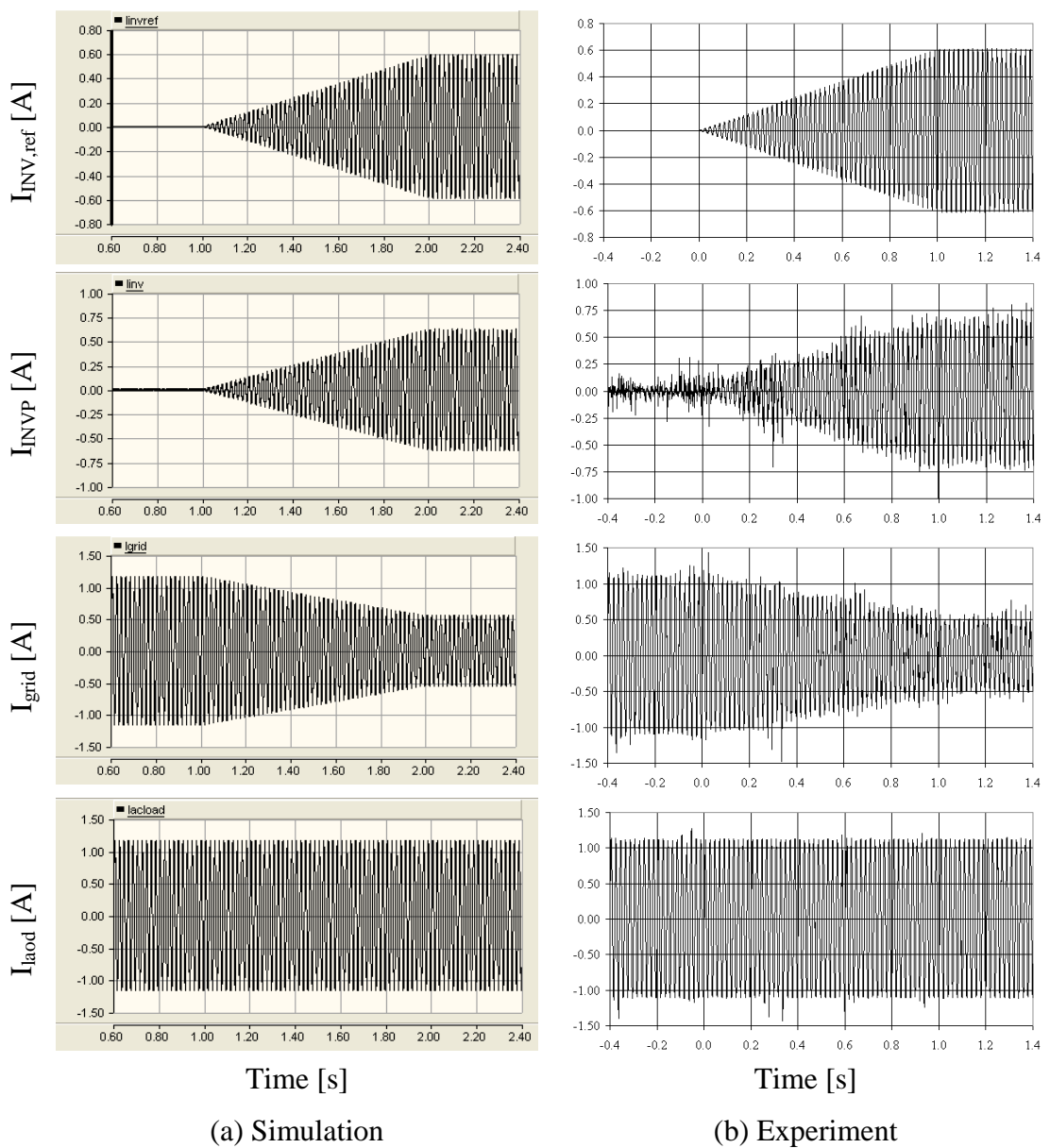
Figure 8-27: Inverter current reference and currents flowing through the inverter, load and grid

Voltages and the inverter output current of the system during and after the grid connection are shown in Figure 8-28 and Figure 8-29 respectively. Load voltage is not distorted when the inverter started to export energy into the load and the grid. Smooth grid connection is achieved.

(a) Simulation   (b) Experiment
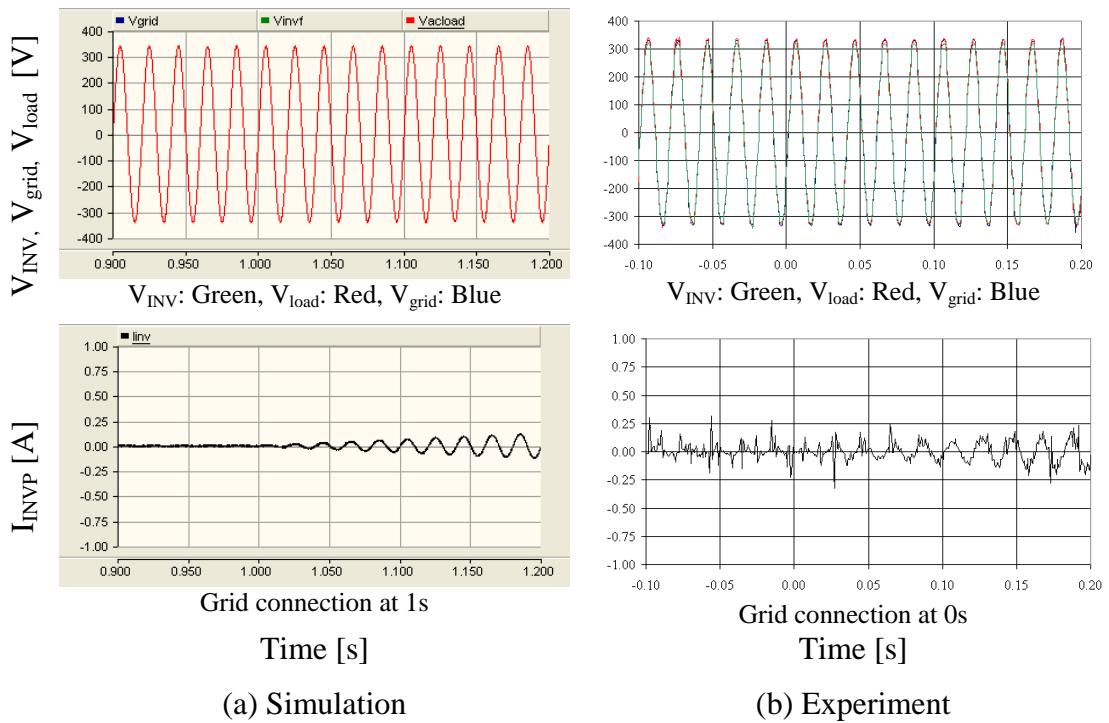
Figure 8-28: Voltages and inverter output current during the grid connection

(a) Simulation   (b) Experiment
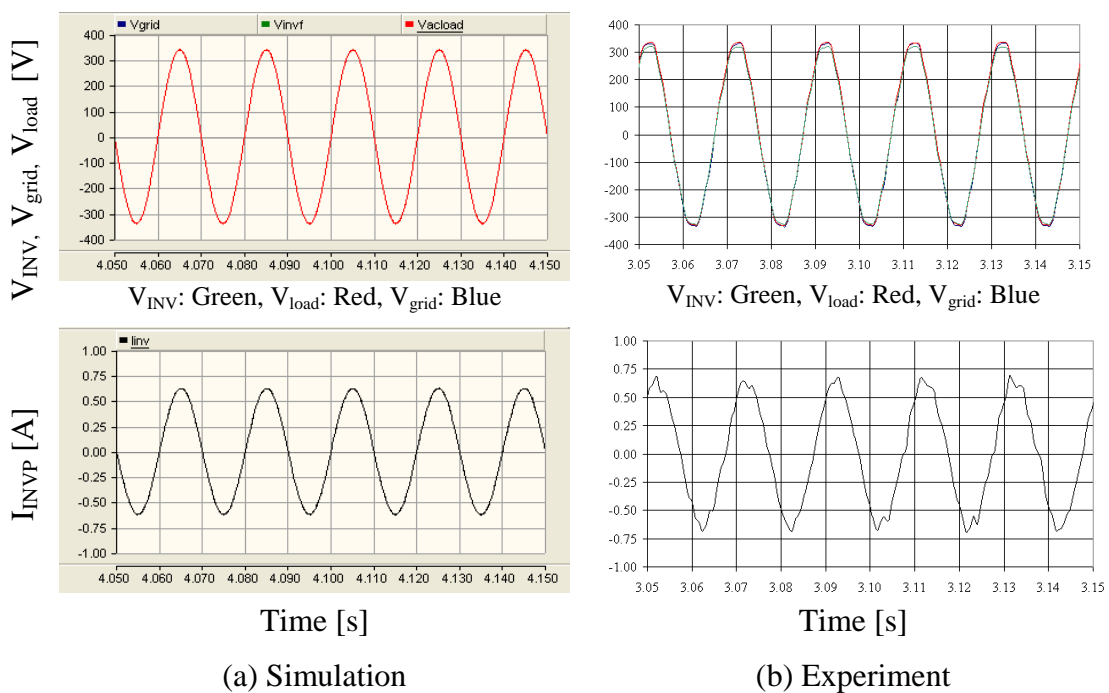
Figure 8-29: Voltages and inverter output current after grid connection

The behaviour of the current controller of inverter is presented in Figure 8-30. The inverter follows the reference current command. The control signal applied to the pulse width modulator is dominated by the load voltage. Noise in the experimental current measurement does not affect the controller output significantly. Figure 8-31 presents the reference and calculated reactive power of the inverter. In the prototype, error is due to the noise superimposed on the voltage and current measurements which affects the respective calculated rms quantities.
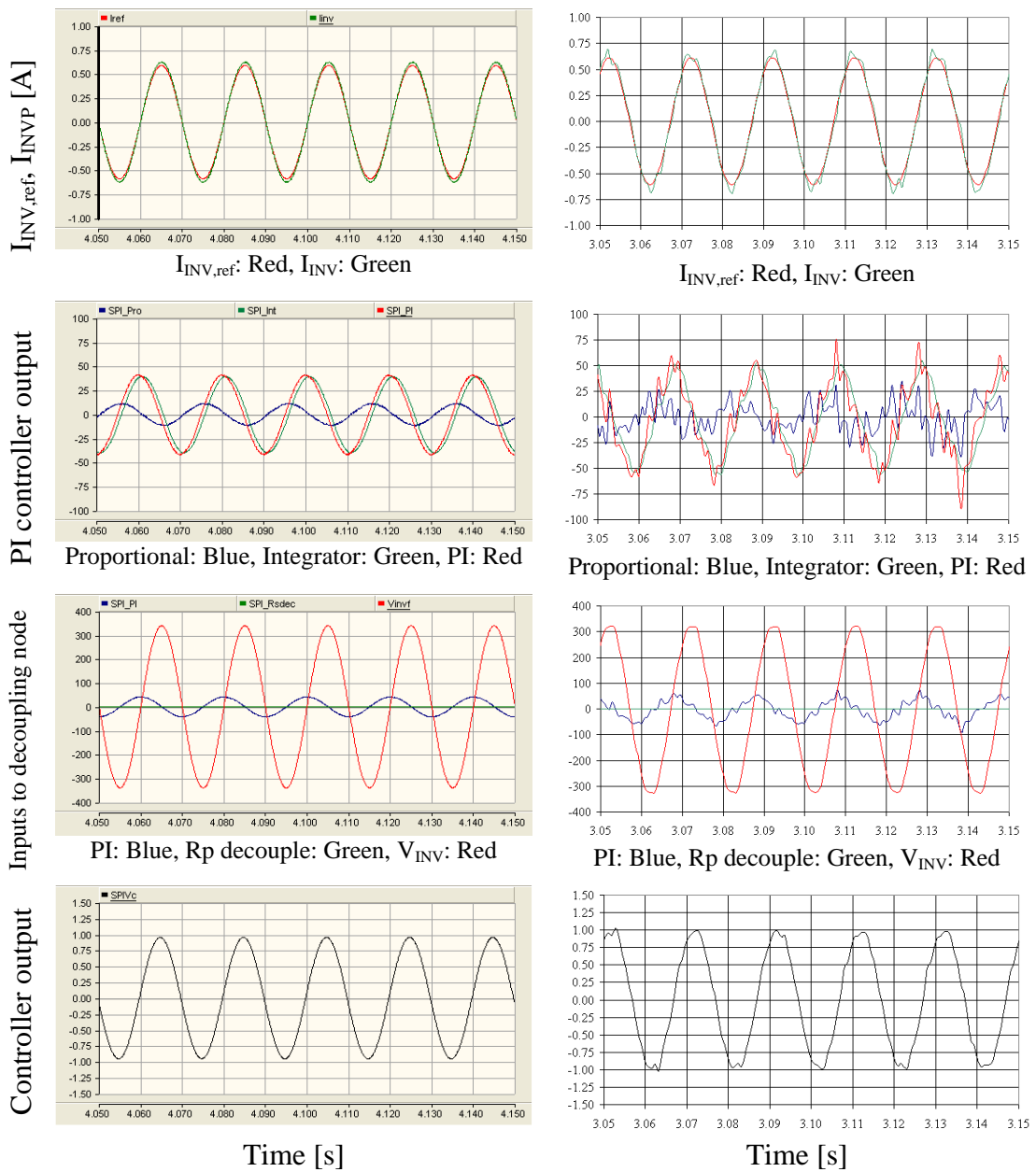
(a) Simulation   (b) Experiment

Figure 8-30: Behaviour of the controller of the current controller

Red: Q$_{ref}$, Green: Q Calculated

Time [s]

(a) Simulation

Red: Q$_{ref}$, Green: Q Calculated

Time [s]

(b) Experiment
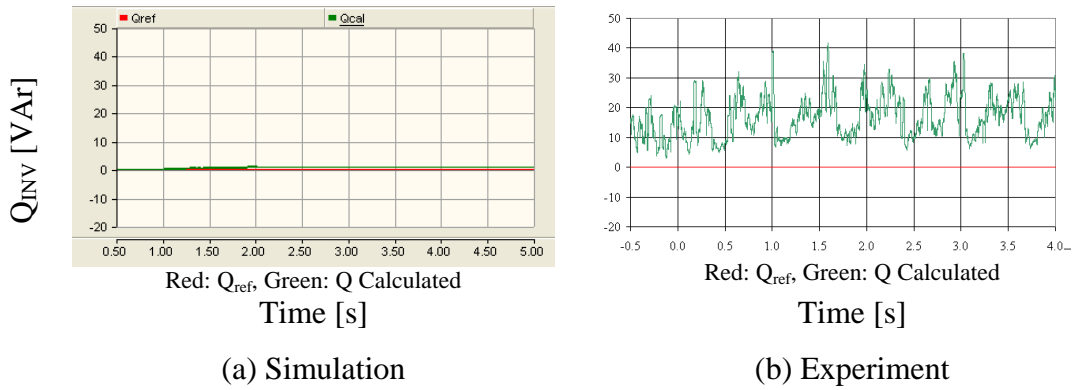
Figure 8-31: Reference and calculated reactive power

8.3.2.2 With reactive power reference

In this sub-section, the ability to export both active and reactive power is studied. Initially the inverter was grid connected with a reactive power reference at zero and the active power reference at 100W. Once the system reached the steady state, the reactive power reference was set to 30VAr. Figure 8-32 to Figure 8-38 presents the simulation and experimental results obtained when a reactive power reference was increased to 60VAr from 30VAr. The reference change occurs at t=3.0s and t=0.0s in the simulation model and prototype respectively. The output active power of the inverter is not changed during the transient (see Figure 8-32). The reactive power output of the inverter is increased to compliment the power reference as shown in Figure 8-33. The current controller introduces a magnitude error which is the reason for small error in active and reactive power. As a result of the reactive power reference increase, the magnitude of the current reference was slightly increased (see Figure 8-34). In the experimental results inverter current increase is not clear due to superimposed noise, however the grid current increases, validating this since the load current is kept constant.

Red: P$_{ref}$, Green: P Calculated

Time [s]

(a) Simulation

Red: P$_{ref}$, Green: P Calculated

Time [s]
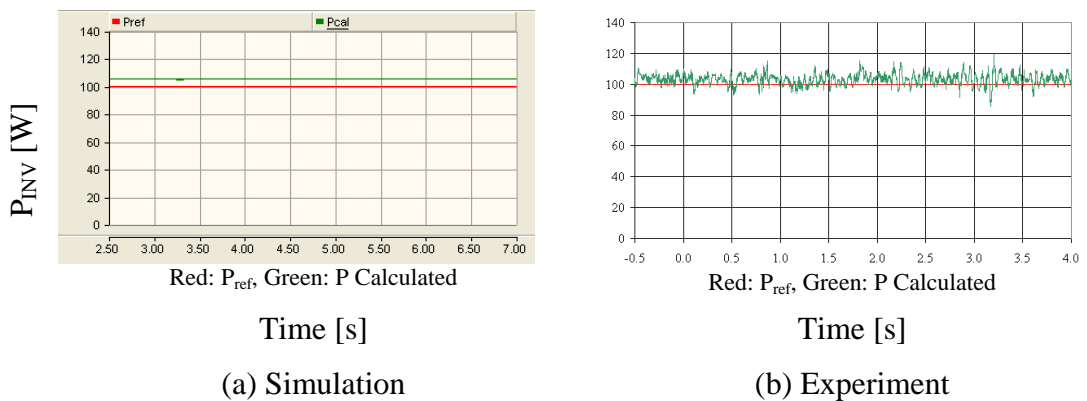
(b) Experiment

Figure 8-32: Reference and calculated active power variation of inverter

Red: Q_ref, Green: Q Calculated

Time [s]

(a) Simulation

Red: Q_ref, Green: Q Calculated

Time [s]
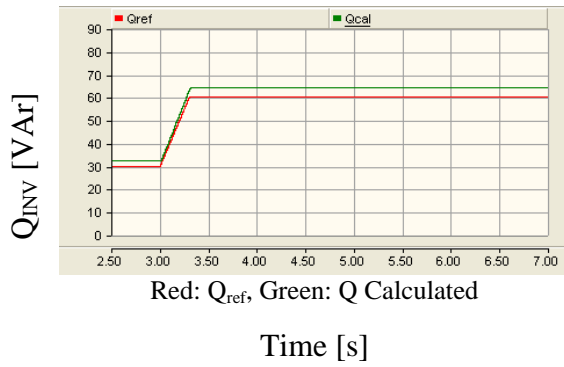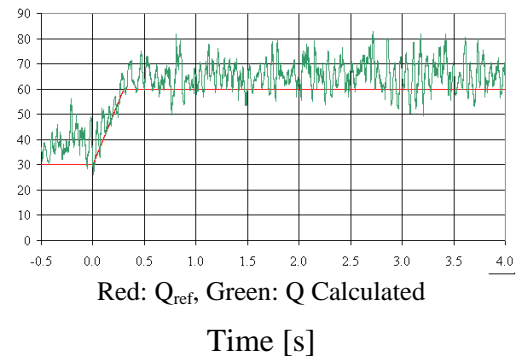
(b) Experiment

Figure 8-33: Reference and calculated reactive power variation of the inverter

Time [s]

(a) Simulation

Time [s]
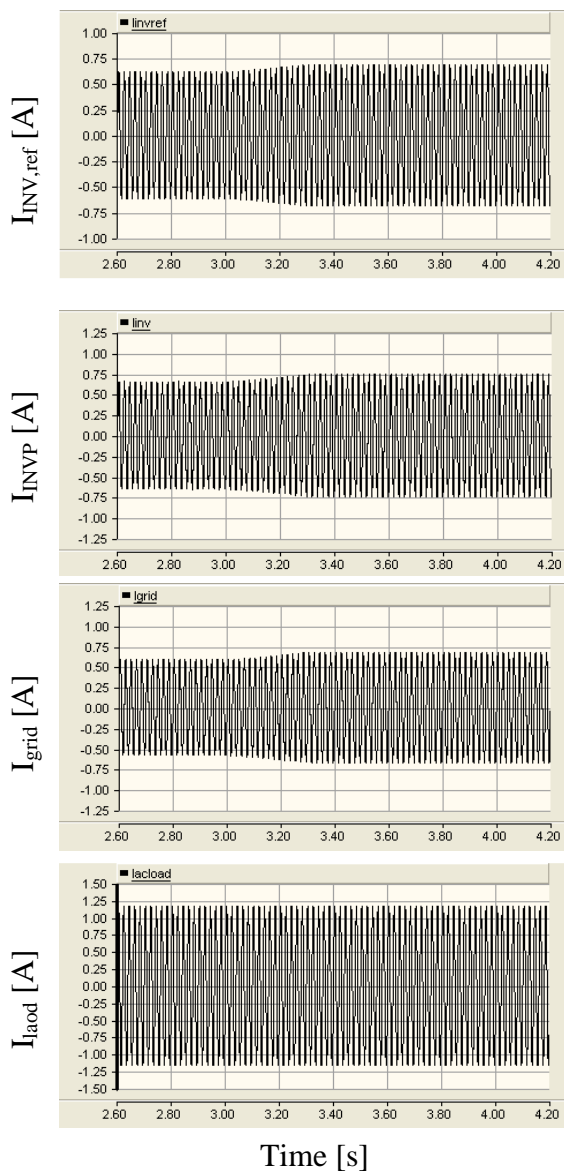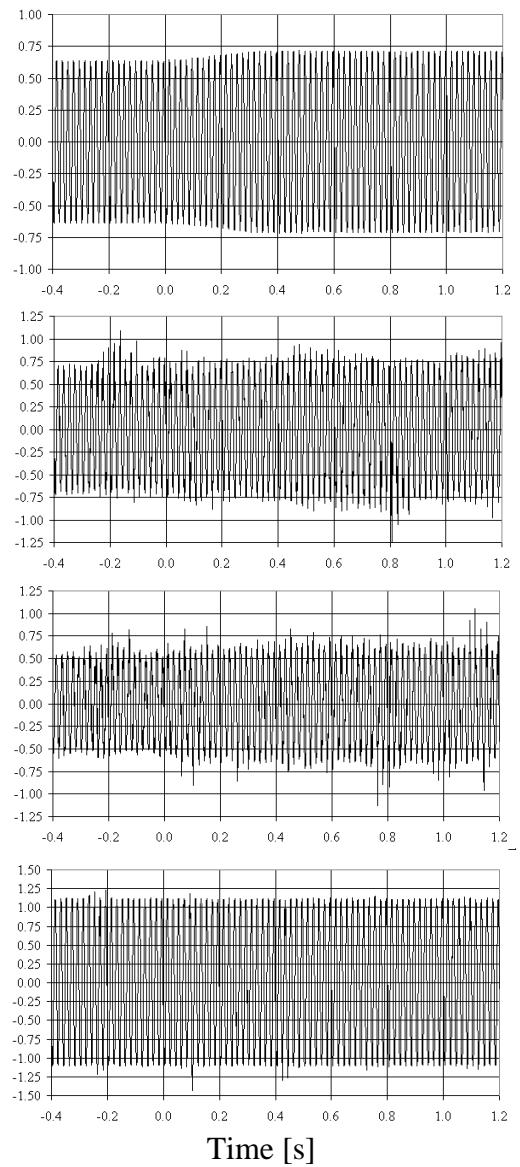
(b) Experiment

Figure 8-34: Inverter current reference and currents flowing through inverter, grid and load

Variation of voltages and the inverter output current during the reactive power increase and in steady state are shown in Figure 8-35 and Figure 8-36 respectively. A slight increase in magnitude of inverter output current is visible.

| (a) Simulation | (b) Experiment |
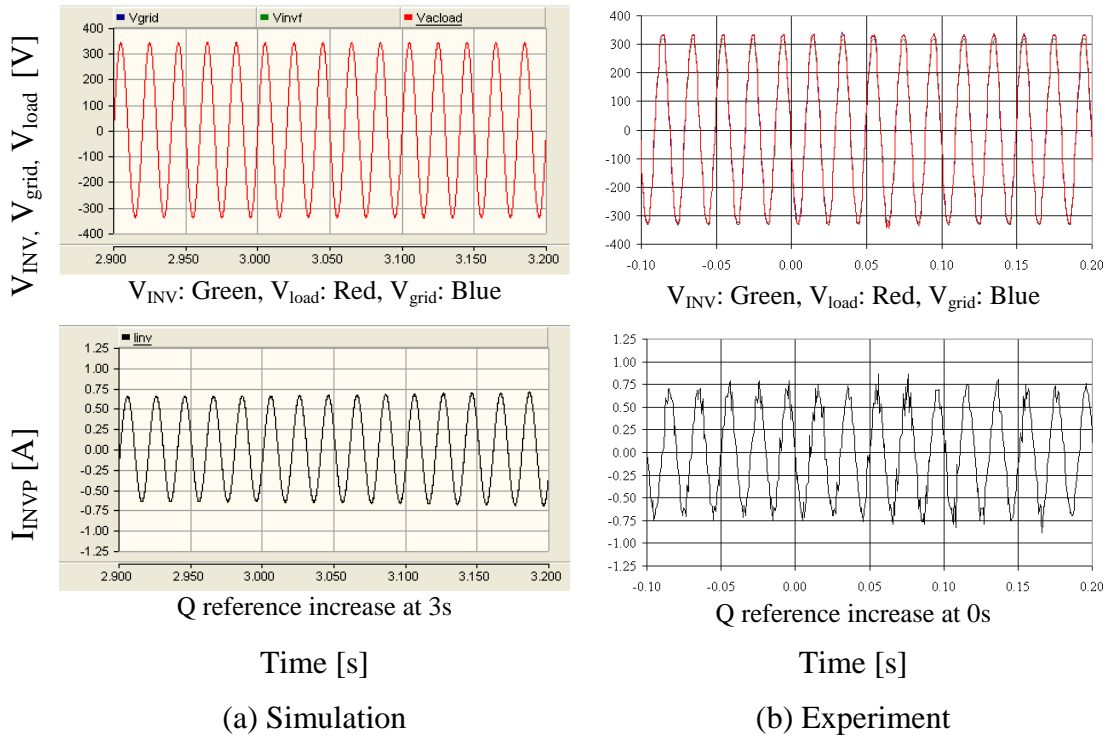
Figure 8-35: Voltages and inverter output current at the increase of reactive power reference

| (a) Simulation | (b) Experiment |
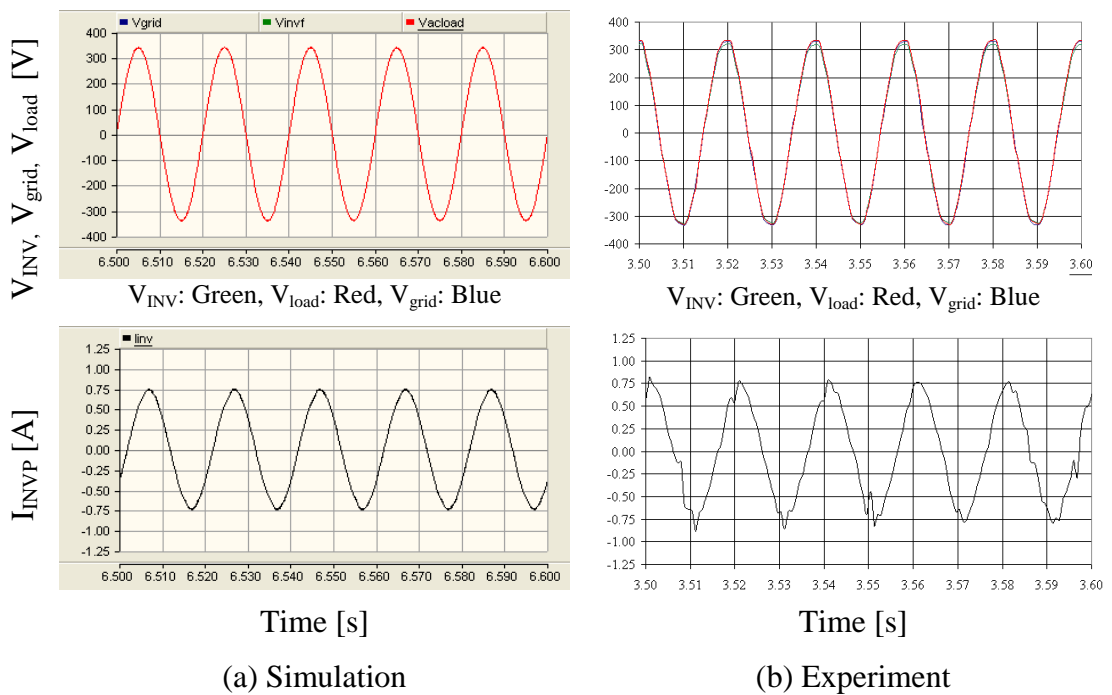
Figure 8-36: Voltages and current after the increase of the reactive power reference

The behaviour of the current controller in steady state after the reference increase is shown in Figure 8-37. The controller ensures that the inverter output current follows the reference current. The controller output is dominated by the load voltage which reduces effect of noisy PI controller output. Figure 8-38 shows the inverter output current and the load voltage (scaled by a factor of 0.004). Inverter output current lags behind the load voltage and the phase difference is around 1.8ms (approximately 32.4°). Therefore current reference produces the correct phase shift. Thus reactive power output is equal to the reference.
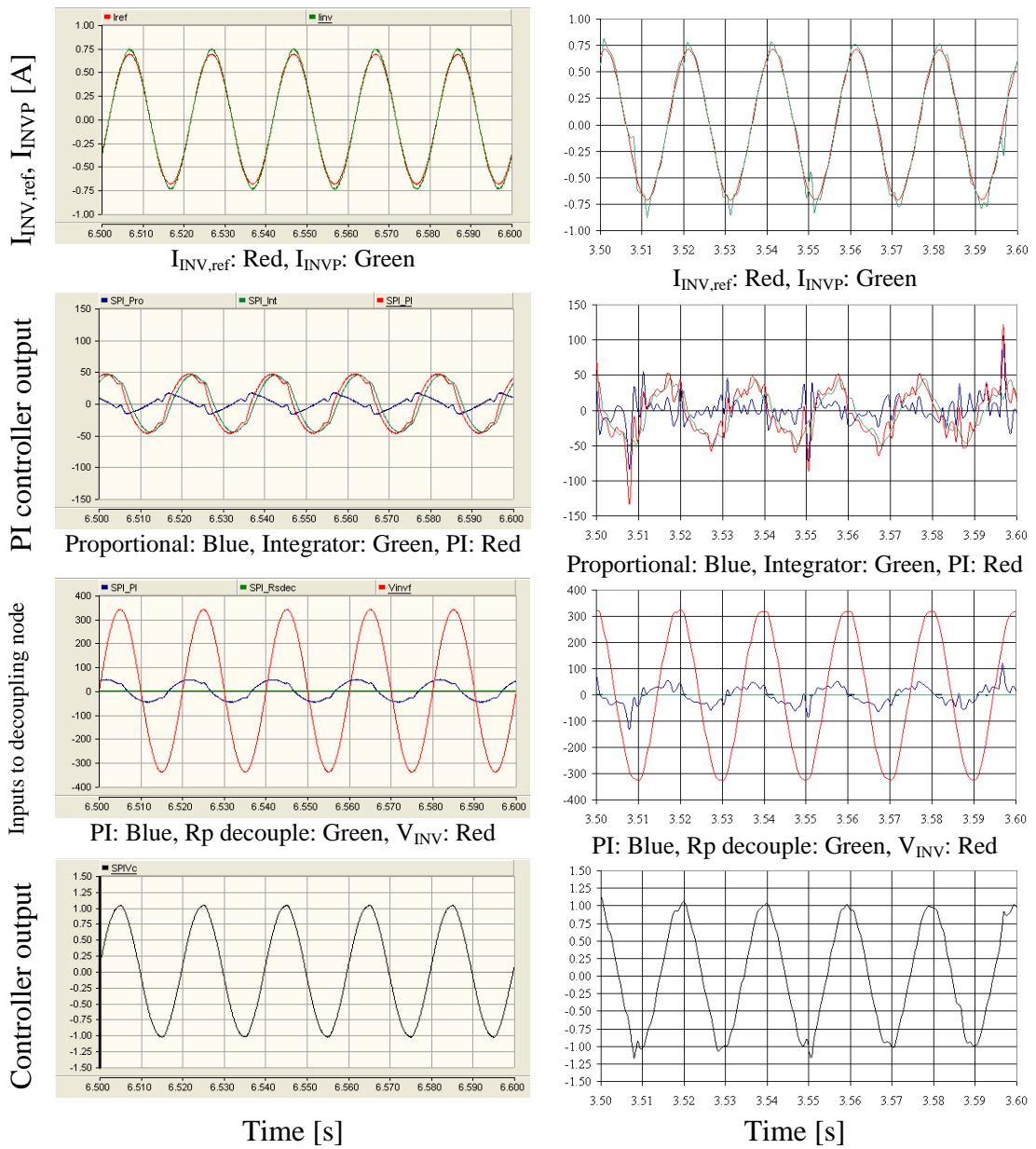
(a) Simulation   (b) Experiment

Figure 8-37: Behaviour of the current controller

(a) Simulation   (b) Experiment
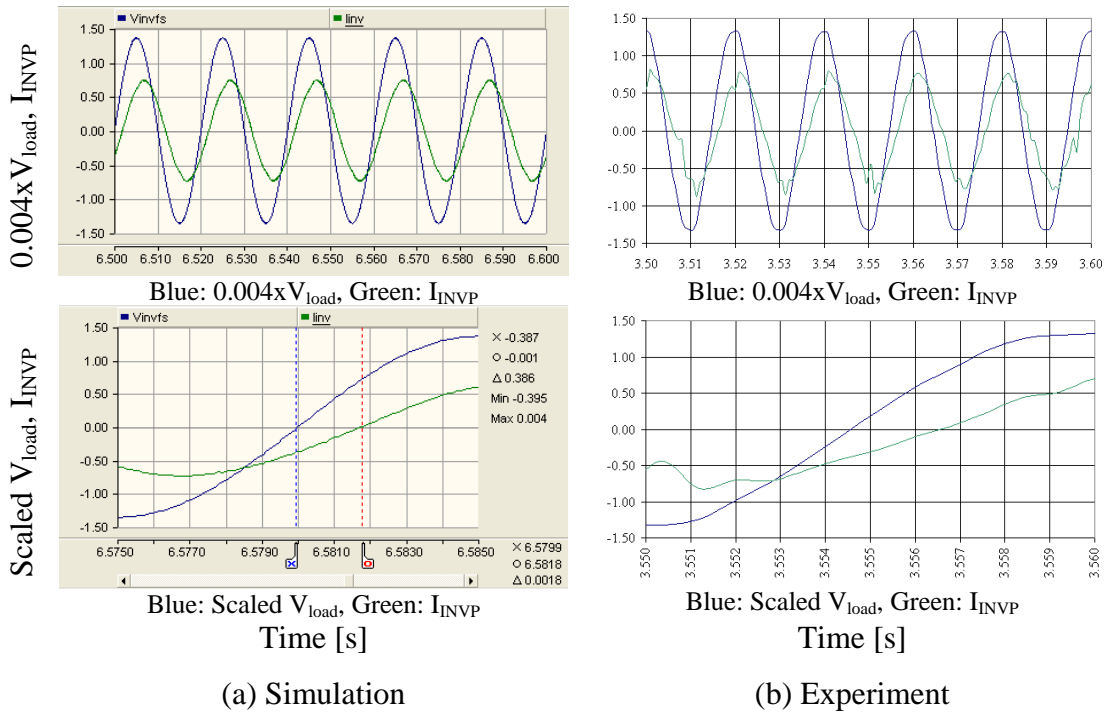
Figure 8-38: Scaled load voltage and inverter output current after the increase of current reference

8.4 SUMMARY

The controller of the single-phase inverter consists of two loops. The inner control loop controls the output current of the inverter and the outer control loop synchronises the inverter to the grid. In this section it is assumed that a stiff dc voltage source is supplying power to the inverter. Thus a voltage source is connected to the input of the inverter.

A fast current controller was designed based on dynamic stiffness properties and command tracking properties.

Smooth grid connection is achieved using the proposed current controller. A reference sinusoidal signal was synchronised with the grid voltage. Initially magnitude and phase of the current reference is given manually. Then active and reactive power references are used to calculate the magnitude and phase of the current reference. The simulation results are verified by experimental results. The grid connected inverter was transferring active and reactive power corresponding to respective references.

CHAPTER 9

BEHAVIOUR OF PROPOSED MICROSOURCE INTERFACE

9.1 INTRODUCTION

A block diagram of the proposed microsource interface is presented in Figure 9-1. The previous chapters presented the development of the converters and associate individual controllers. Further the proposed system was divided into two sections and the behaviour of the parts was analysed separately. Grid connected inverter operation was analysed assuming that the inverter is powered by a stiff dc voltage source. Also it was shown that when the microsource, energy storage unit and dc-dc converters are designed to operate collectively, a stiff dc voltage could be achieved in the dc-link.

This chapter analyses the behaviour of the complete system using the simulation models which have been validated against hardware (see Chapter 7 and 8). The system should withstand load variations as well as microsource output power variations. Therefore the microsource output power was varied while keeping the output power reference of the inverter constant. Similarly the inverter output power reference was varied while keeping the microsource output power constant. Simulation results are presented for each case. Finally a starting method for the proposed microsource interface is presented.
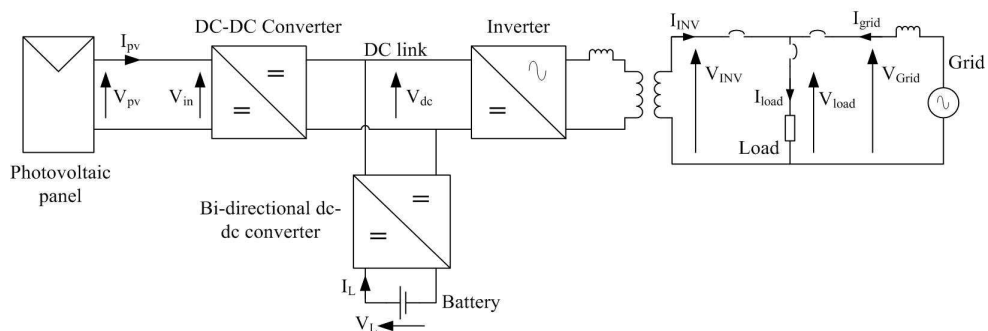
Figure 9-1: Proposed Microsource interface

9.2 SYSTEM RESPONSE TO MICROSOURCE POWER VARIATIONS

The output power of a photovoltaic panel depends on the irradiance incident on the panel and its temperature. The integrated energy storage unit in the proposed system should decouple the dynamics of the microsource. The inverter should provide the power according to the references at least until the central controller of the MicroGrid responds to the change in microsource available power with a new reference command for the inverter interface. The central controller ensures the stable operation of the MicroGrid and it coordinates with the microsources and loads within the MicroGrid (see section 2.3.5 of Chapter 2). This sub-section presents the system response to microsource output power variations.

The initial output power of the PV panel corresponds to 800W/m^2 irradiance and 25°C temperature. The active and reactive power references were set to 100W and 0VAr respectively. At t = 4 seconds, irradiance was increased to 1000W/m^2 and decreased to 600W/m^2 in two separate case studies. As a response to the increase and decrease of irradiance, the output power of the PV panel increases and decreases respectively. Figure 9-2 to Figure 9-8 present simulation results corresponding to these two cases. The system start-up transient response is visible before t = 2.5 seconds in some of the results. However the step change is applied after the system reached the steady state. Thus the start-up does not affect the system behaviour.

Figure 9-2 presents the output voltage and the output current of the photovoltaic panel. In response to irradiance increase, the output current of the photovoltaic panel was increased. The voltage at maximum power point was also increased. Conversely the output voltage of the photovoltaic panel was decreased as the voltage of the maximum power point decreased in response to irradiance decrease.

The behaviour of the controller of the modified forward dc-dc converter is shown in Figure 9-3. In both cases, the controller responds to reference changes quickly and restores the input voltage of the modified forward dc-dc converter to the reference. The duty ratio of the modified forward dc-dc converter was appropriately adjusted.
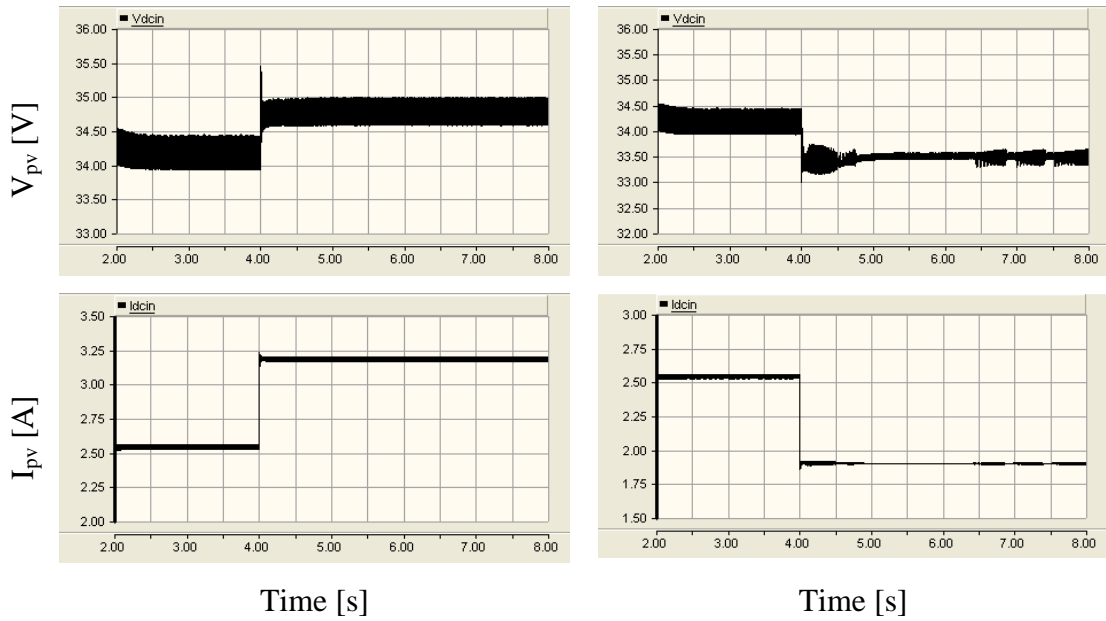
(a) Increase in irradiance   (b) Decrease in irradiance

Figure 9-2: Output voltage and current of the photovoltaic panel
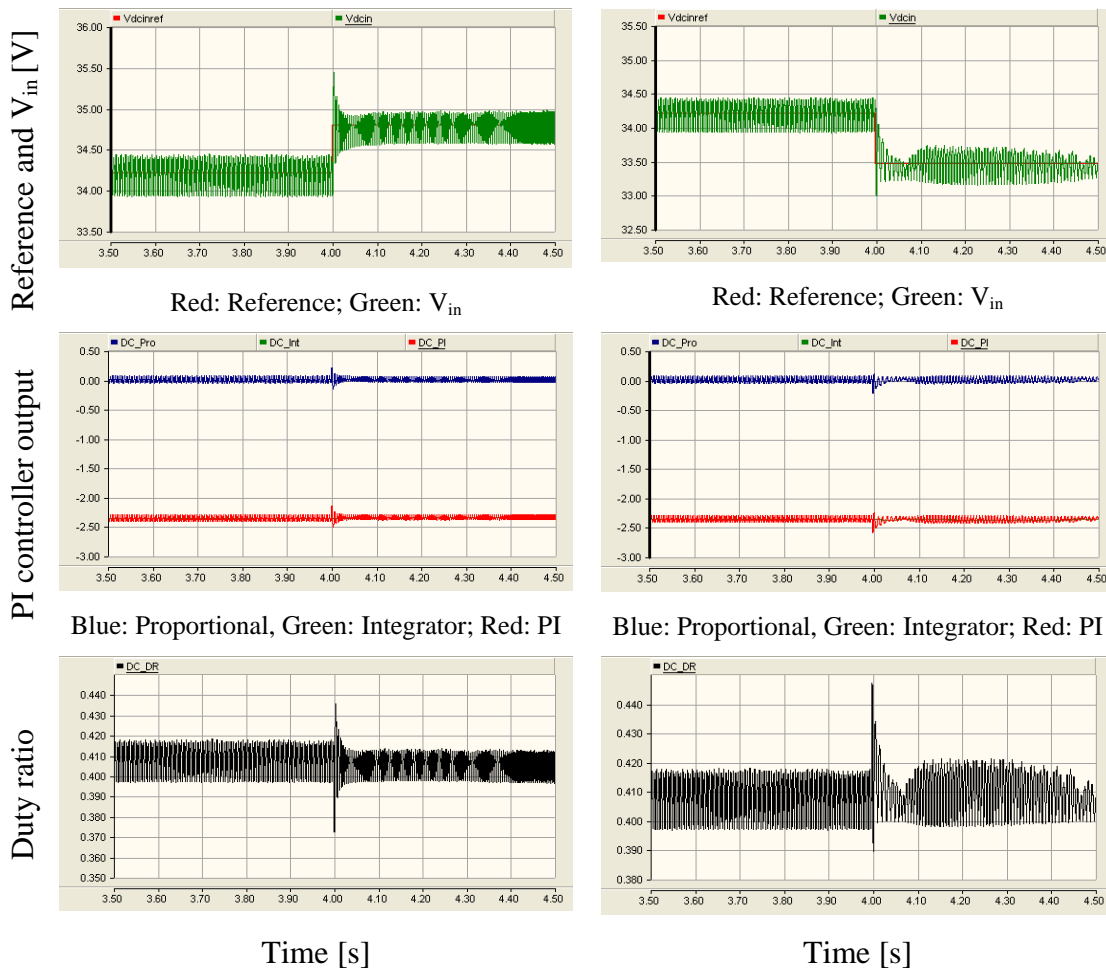
(a) Increase in irradiance   (b) Decrease in irradiance

Figure 9-3: Behaviour of the controller of the modified forward dc-dc converter

The dc-link voltage variation during the step change in irradiance is shown in Figure 9-4 while Figure 9-5 presents the battery voltage and battery current. The battery was discharging before the step change in irradiance (before t = 4s) which is indicated by the positive battery current. The increase in irradiance also increases the output power from the PV panel thus the dc-link voltage was increased. Then the controller of the bi-directional dc-dc converter responds and reduces the battery discharge current. Finally the dc-link voltage settles to reference voltage which is 360V. On the other hand dc-link voltage drops when irradiance is decreased. Battery current was increased to restore the dc-link voltage to the nominal value. Thus the controller of the bi-directional dc-dc converter ensures that the dc-link voltage variations are within the limits.

(a) Increase in irradiance   (b) Decrease in irradiance
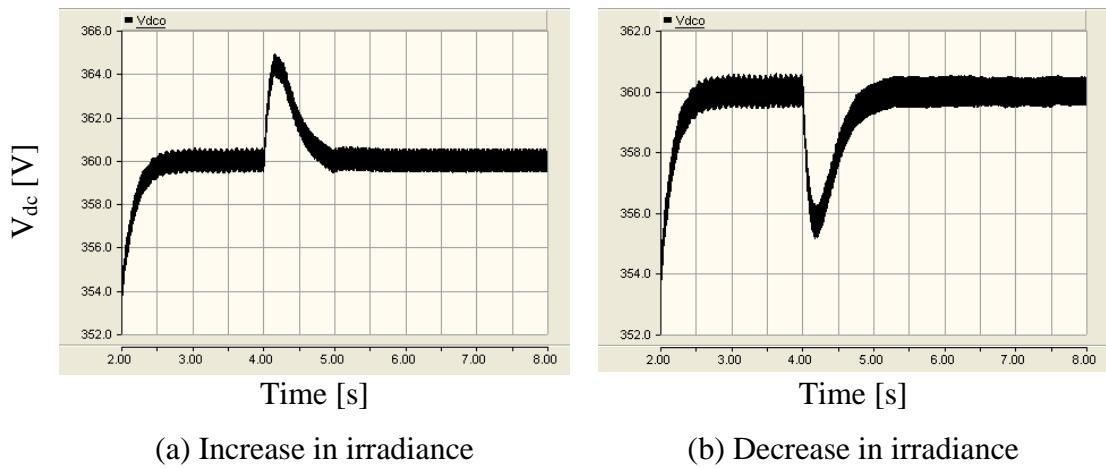
Figure 9-4: Variation of dc-link voltage

(a) Increase in irradiance   (b) Decrease in irradiance
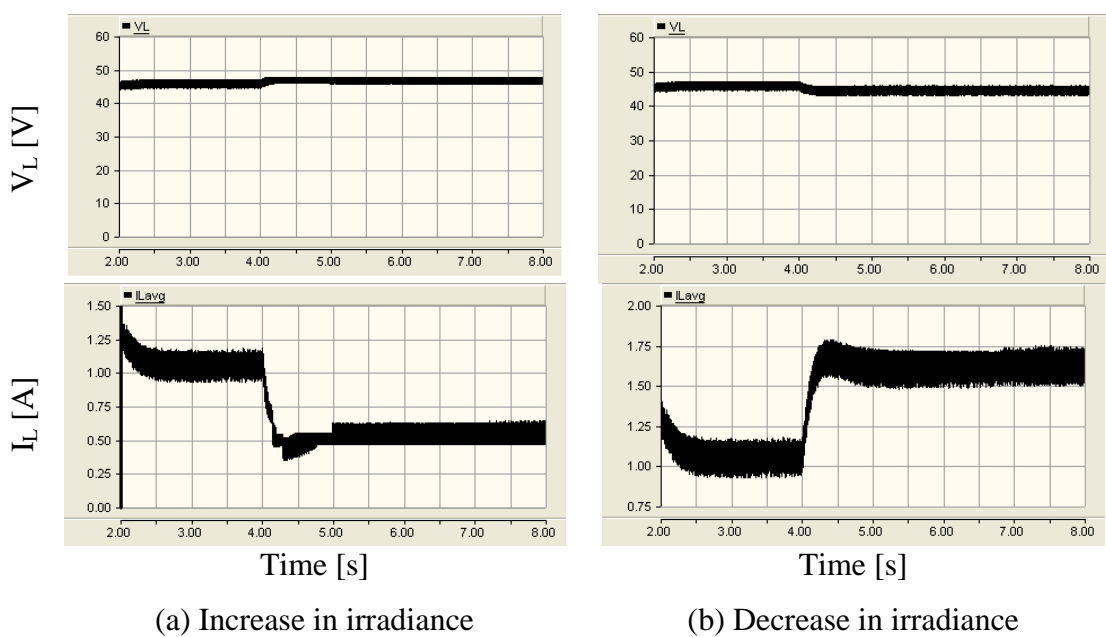
Figure 9-5: Battery voltage and battery current

Figure 9-6 shows the inverter output current and the inverter output voltage just before and after the transients. The inverter outputs were not affected by the variations of the microsource output power.

Time [s]   Time [s]

(a) Increase in irradiance   (b) Decrease in irradiance
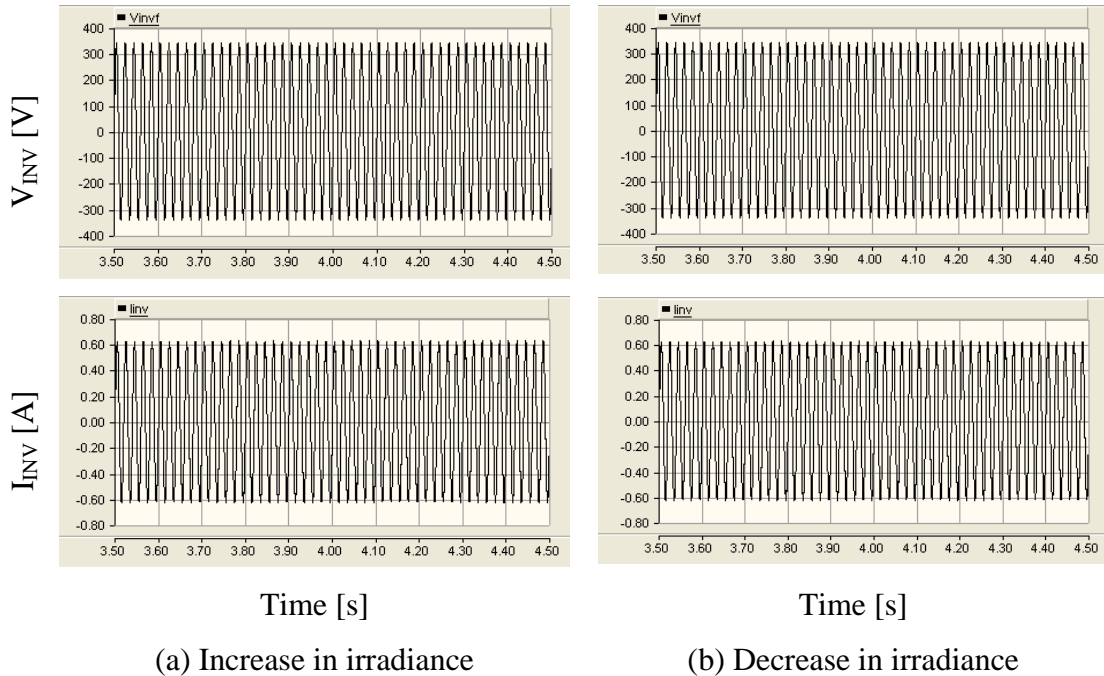
Figure 9-6: Inverter output current and voltage

Figure 9-7 presents the behaviour of the step-up mode controller of the bi-directional dc-dc converter. For these two cases, the controller operates in the step-up mode before the step change in irradiance. The controller restored the dc-link voltage within one second after the irradiance changes were applied in the test cases. The inner current loop effectively controls the output current of the battery. The outer voltage control loop provides a new battery current reference when dc-link varies from the reference. The inner current loop ensures that the battery current is following the reference current. In order to reduce the battery current, the duty ratio is reduced in the case corresponding to increase in irradiance. On the other hand the duty ratio is increased to enable higher current to flow when irradiance is decreased.

Steady state behaviour of the current controller of the single-phase inverter after the step change in irradiance is presented in Figure 9-8. The current controller ensures that the current reference was followed. Thus the MicroGrid is not disturbed by the microsource output power variations.

Blue: Reference, Green: Measured   Blue: Reference, Green: Measured

Blue: Proportional, Green: Integrator, Red: PI   Blue: Proportional, Green: Integrator, Red: PI

Blue: Reference, Green: Measured   Blue: Reference, Green: Measured

Blue: Proportional, Green: Integrator, Red: PI   Blue: Proportional, Green: Integrator, Red: PI

Time [s]   Time [s]
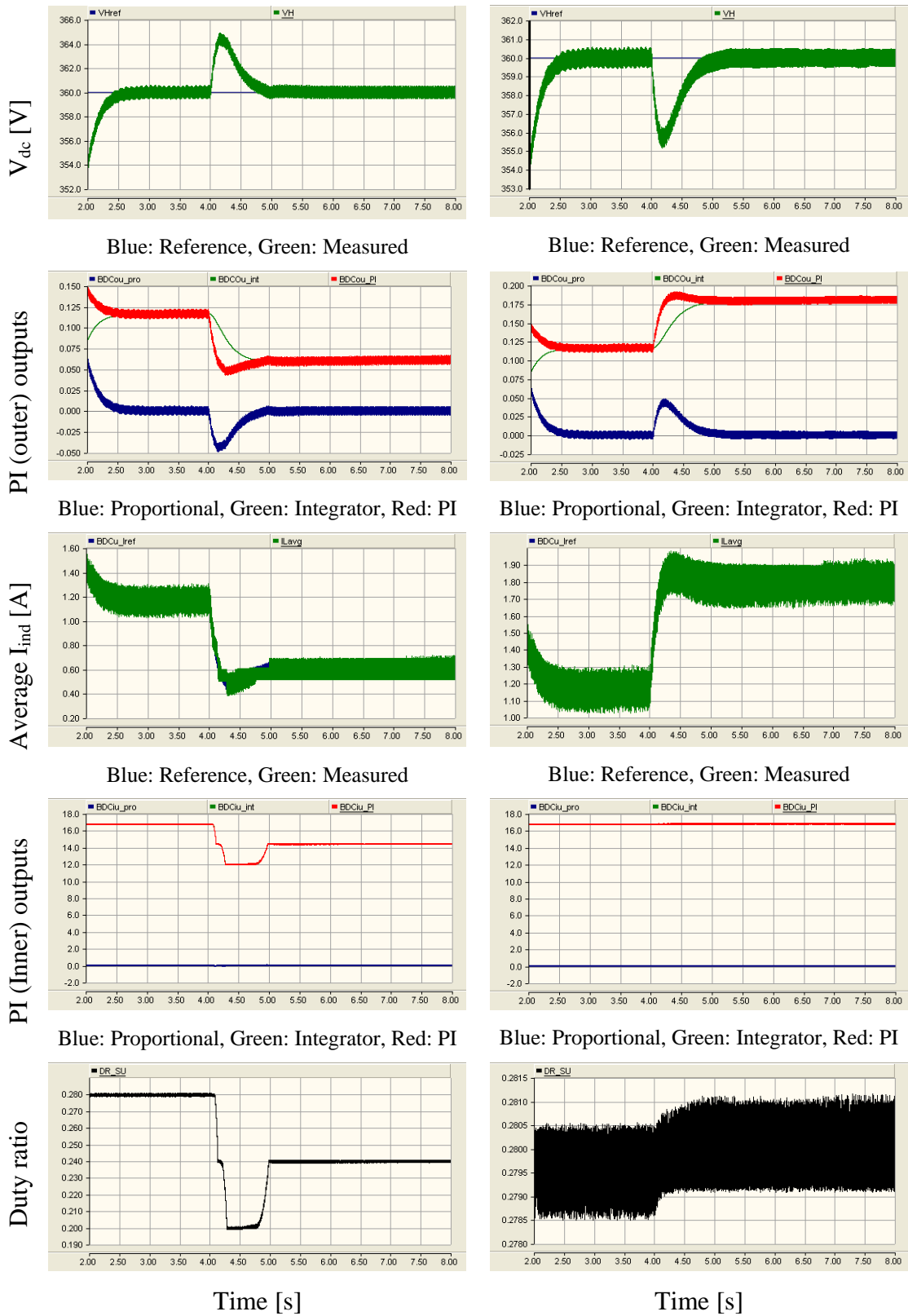
(a) Increase in irradiance   (b) Decrease in irradiance

Figure 9-7: Behaviour of the step-up mode controller of the bi-directional dc-dc converter
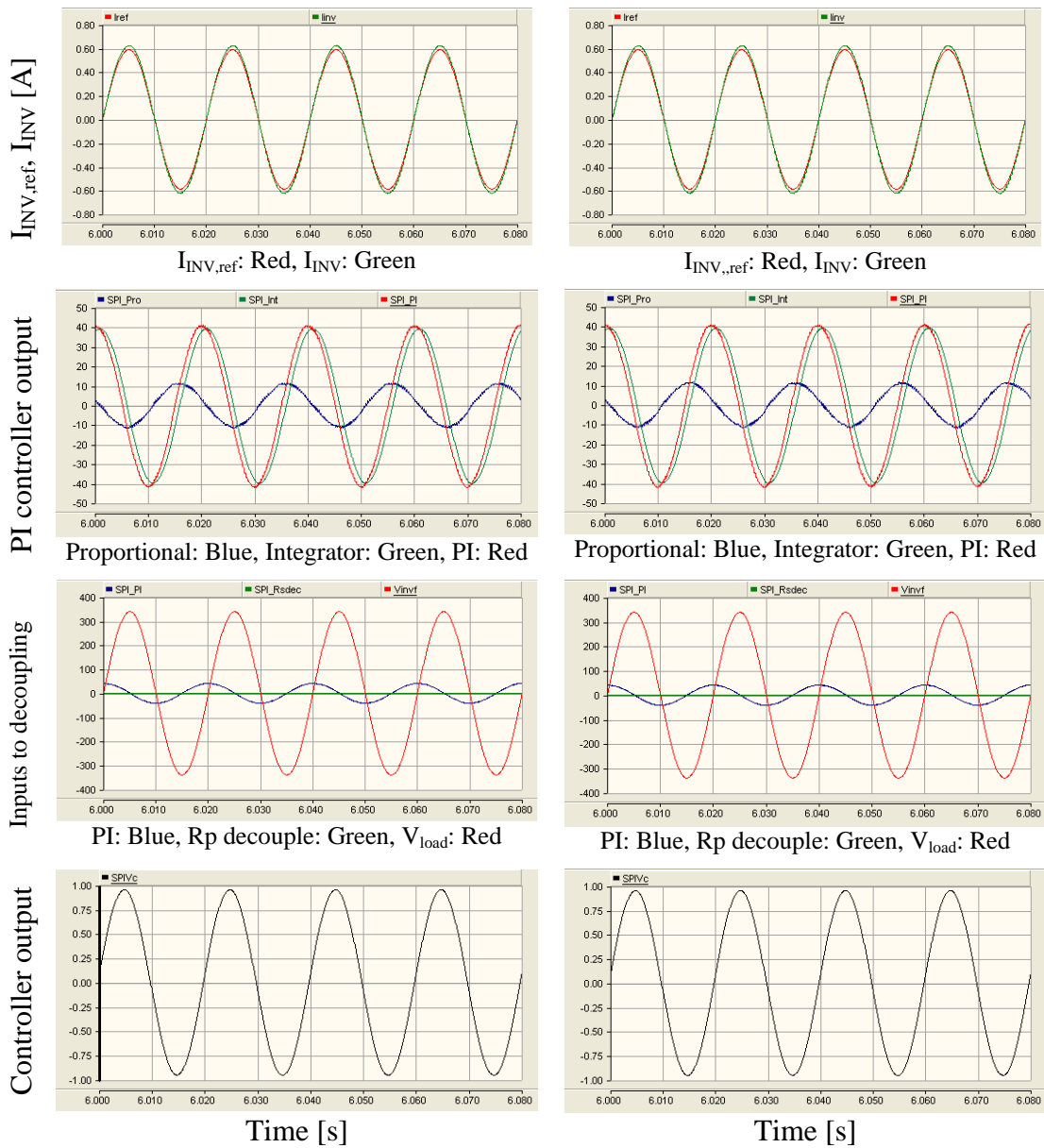
(a) Increase in irradiance   (b) Decrease in irradiance

Figure 9-8: Behaviour of the current controller of the single-phase inverter

9.3 RESPONSE OF THE SYSTEM TO OUTPUT POWER REFERENCE VARIATIONS

Similar to microsource output power variations, the microsource interface should respond to power reference changes applied to the inverter in a robust manner with minimal disturbances. In other words the energy storage should respond appropriately by storing excess energy or providing energy to cover a shortage. The proposed microsource interface response to active and reactive power variations is presented in the following sections.

9.3.1 Active power reference change

The behaviour of the microsource interface in response to active power reference variations, while reactive power reference is kept constant, is presented in this sub-section. In response to an increase in active power reference, the battery should discharge more or charge less depending on operating mode prior to the reference change. Similarly the battery should discharge less or charge more in response to active power reference decrease.

The PV panel output power corresponds to 1000W/m^2 irradiance and 25°C temperature. Initial active and reactive power references were set to 100W and 0VAr. Two scenarios were simulated. The active power reference was increased to 125W in one case while in other case the active power reference was reduced to 75W. The power reference change was applied at a rate of 100 W/s at t = 4 seconds. Again the system start-up transient response is visible before t = 2.5 seconds in some of the results. The active power reference change was applied only after system reached the steady state.

Figure 9-9 to Figure 9-19 present the simulation results of the system corresponding to the active power reference change. Figure 9-9 presents the variation of inverter current reference when active power reference variation was introduced. The magnitude of the current was increased and decreased when active power reference was increased and decreased respectively. In Figure 9-10 load voltage (scaled by a factor of 0.004) and the inverter output current, during the steady state after the reference variations, are plotted together. In both cases, load voltage is in-phase with the inverter output current. Therefore only active power is transferred.

(a) Increase in active power   (b) Decrease in active power
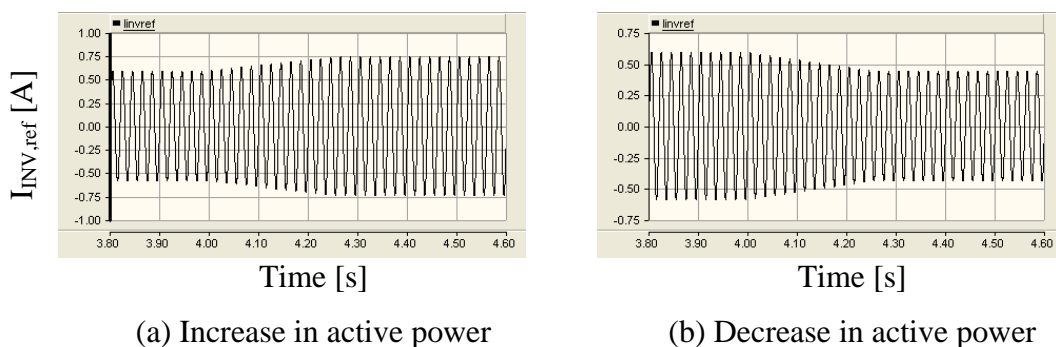
Figure 9-9: Inverter current reference

Blue: 0.004xV_load, Green: I_INV　　　　　　　Blue: 0.004xV_load, Green: I_INV

Time [s]　　　　　　　　　　　　　　　Time [s]

(a) Increase in active power　　　　　　(b) Decrease in active power
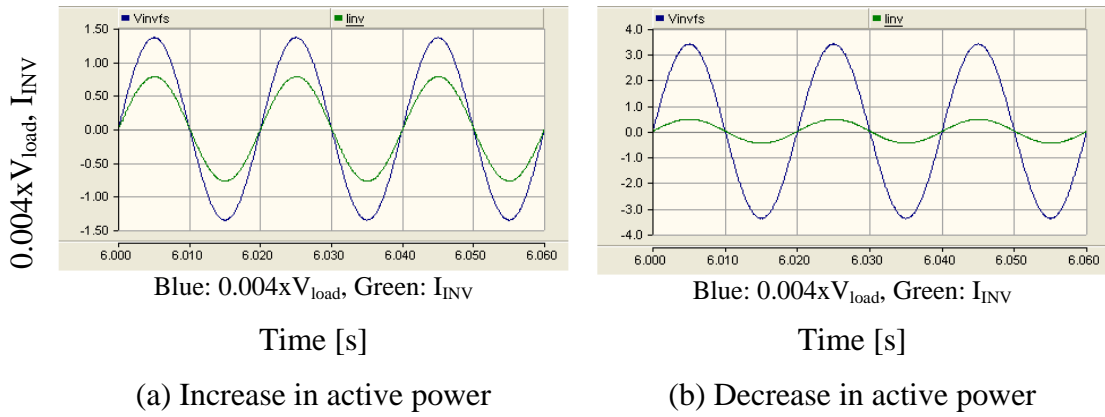
Figure 9-10: Scaled load voltage and inverter output current

Figure 9-11 presents power references along with the calculated output power values. In both cases, calculated active power output is approximately equal to the active power reference. According to the frequency response of the command tracking of the current controller (see Chapter 8), a magnitude and phase error is introduced at 50Hz which is the reason for the error in calculated power and reference power. However, the error is slightly higher than the amount which was predicted at the design stage of the current controller for the inverter. This is due to fact that transformer leakage inductance was not taken into consideration during the controller design. Reactive power output is almost zero.

Red: Reference, Green: Calculated　　　　　　Red: Reference, Green: Calculated

Red: Reference, Green: Calculated　　　　　　Red: Reference, Green: Calculated

Time [s]　　　　　　　　　　　　　　　Time [s]

(a) Increase in active power　　　　　　(b) Decrease in active power
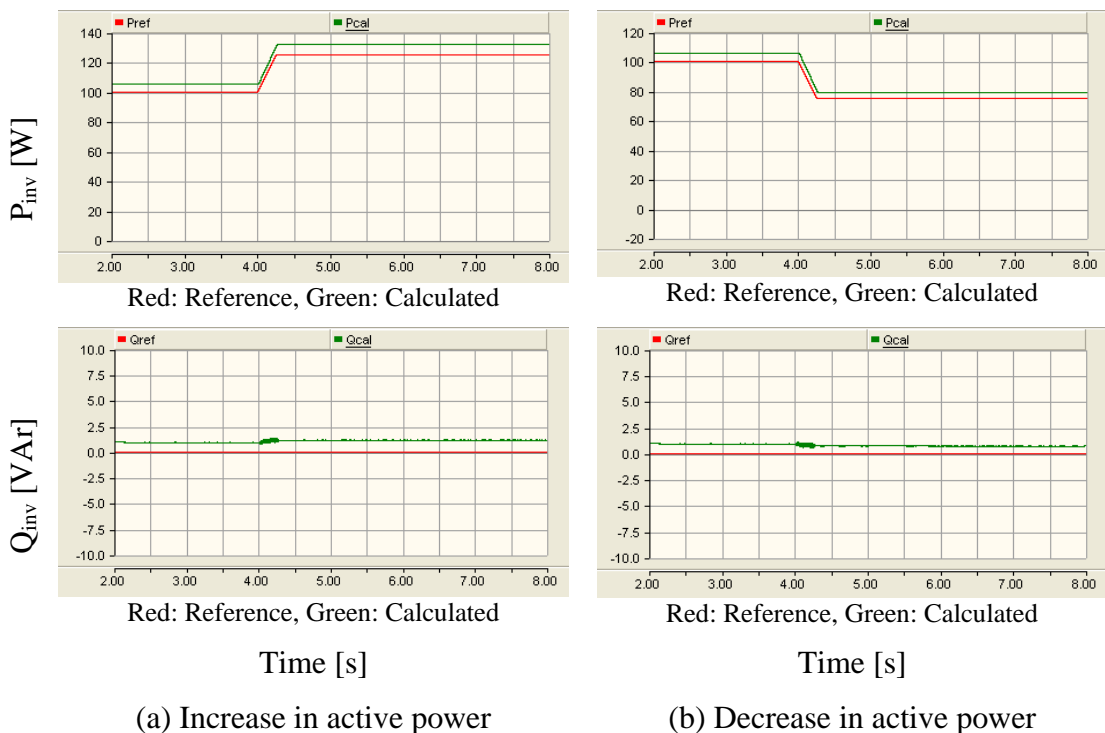
Figure 9-11: Active and reactive power output of the inverter

Figure 9-12 presents inverter output current, grid current and load current. As the active power reference is increased, the magnitude of the inverter output current is also increased. Since the load current is constant, grid current is reduced. Conversely the inverter output current dropped when the active power reference is decreased. As a result the grid current is increased and load current is constant.

(a) Increase in active power   (b) Decrease in active power
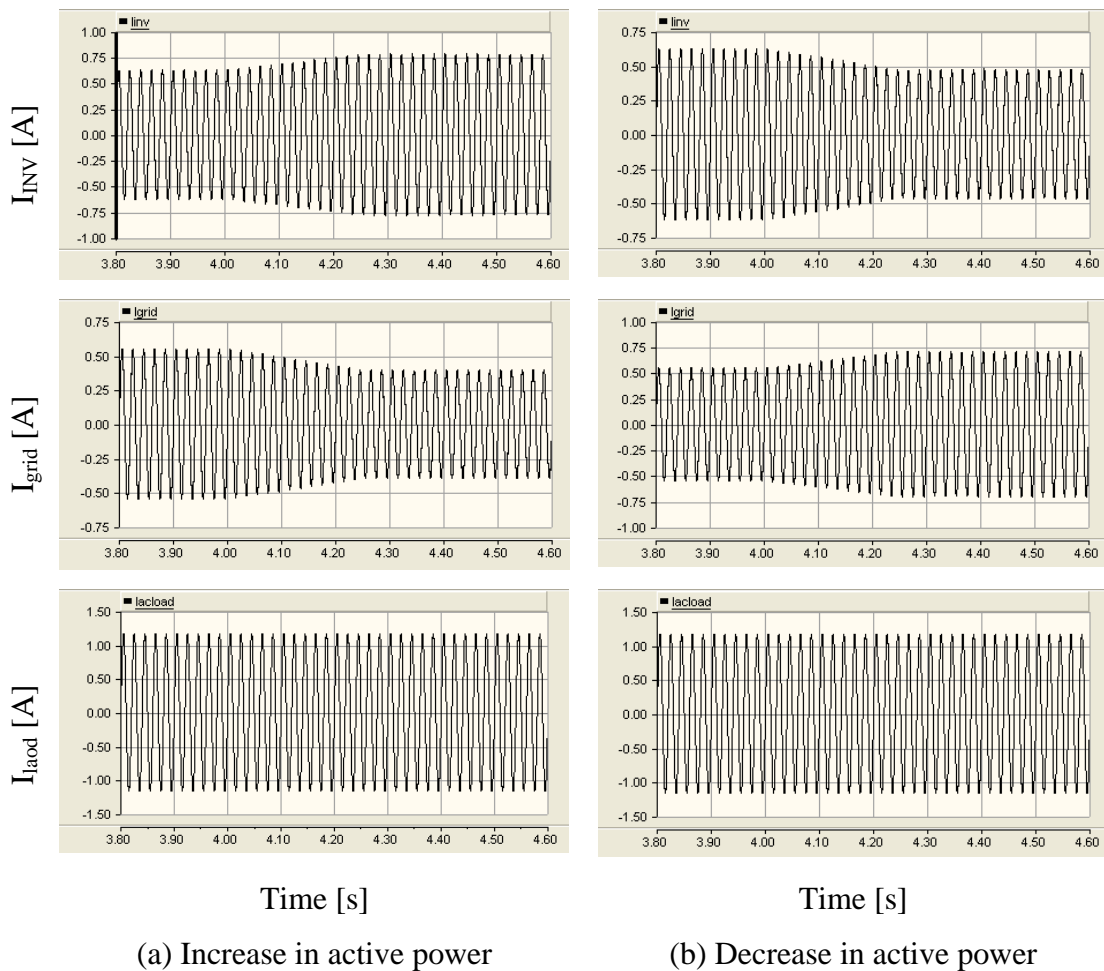
Figure 9-12: Inverter output current, grid current and load current

The variation of the dc-link voltage is presented in Figure 9-13, and Figure 9-14 shows the battery voltage and battery current. The dc-link voltage dropped when the active power reference was increased since the output power of PV panel was not increased simultaneously. Thus battery discharge current was increased to restore the dc-link voltage to nominal value. For the "decrease" case, the dc-link voltage increased in response to the decrease in the active power reference before being restored back to its nominal value. Battery current changed from positive to negative which indicates that the bi-directional dc-dc converter operating mode changed from step-up to step-down.

(a) Increase in active power   (b) Decrease in active power
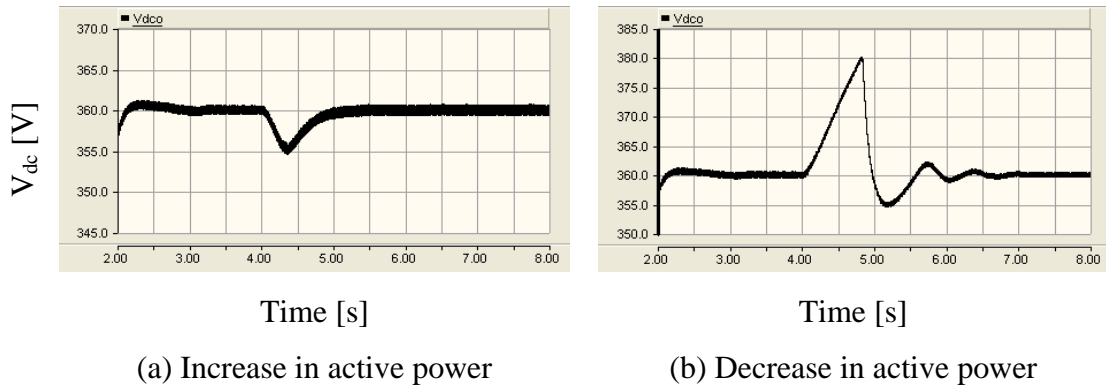
Figure 9-13: Variation of dc-link voltage

(a) Increase in active power   (b) Decrease in active power
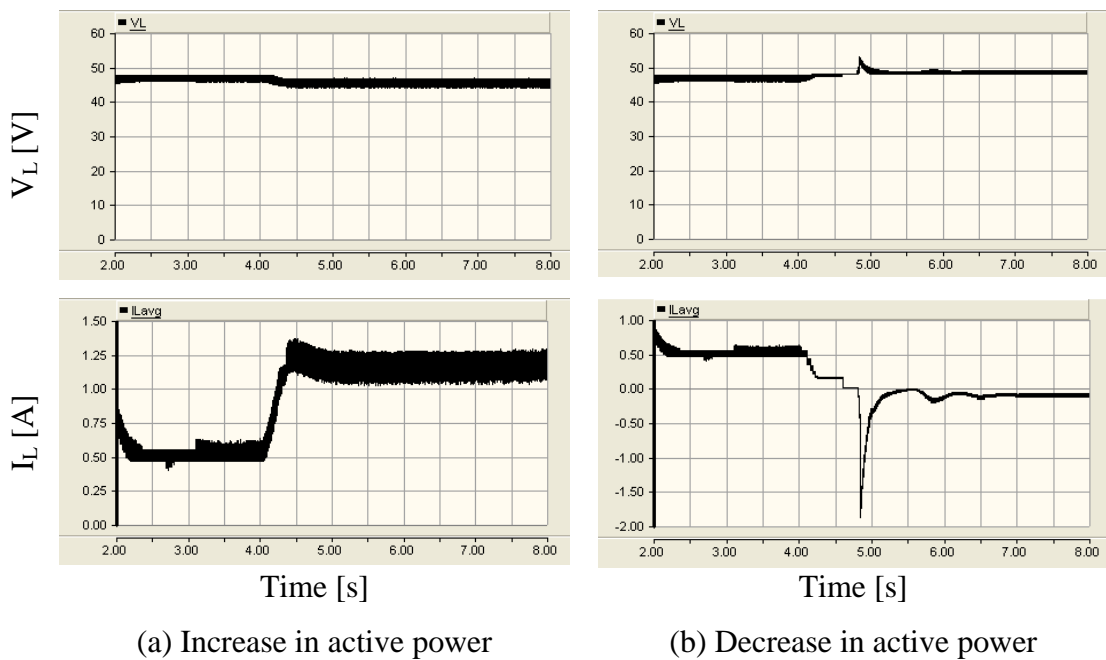
Figure 9-14: Battery voltage and battery current

The behaviour of the controller of the bi-directional dc-dc converter is shown in Figure 9-15 and Figure 9-16. For the active power increase case, the bi-directional dc-dc converter only operates in step-up mode. In response to the dc-link voltage error, the outer control loop of the step-up mode controller increased the battery current reference. Finally the duty ratio is increased to increase the battery current. In response to the decrease in power output, the battery discharge current was reduced as the dc-link voltage increased. The step-up mode of bi-directional dc-dc converter was turned off when the dc-link voltage crossed the step-up turn-off reference (375V). For the decrease in active power case, the bi-directional dc-dc converter step-down mode was turned on once the step-down turn-on reference (380V) was crossed. Within 1s the dc-link voltage was restored to nominal.

Blue: Reference, Green: Measured   Blue: Reference, Green: Measured

Blue: Proportional, Green: Integrator, Red: PI   Blue: Proportional, Green: Integrator, Red: PI

Blue: Reference, Green: Measured   Blue: Reference, Green: Measured

Blue: Proportional, Green: Integrator, Red: PI   Blue: Proportional, Green: Integrator, Red: PI

Time [s]   Time [s]
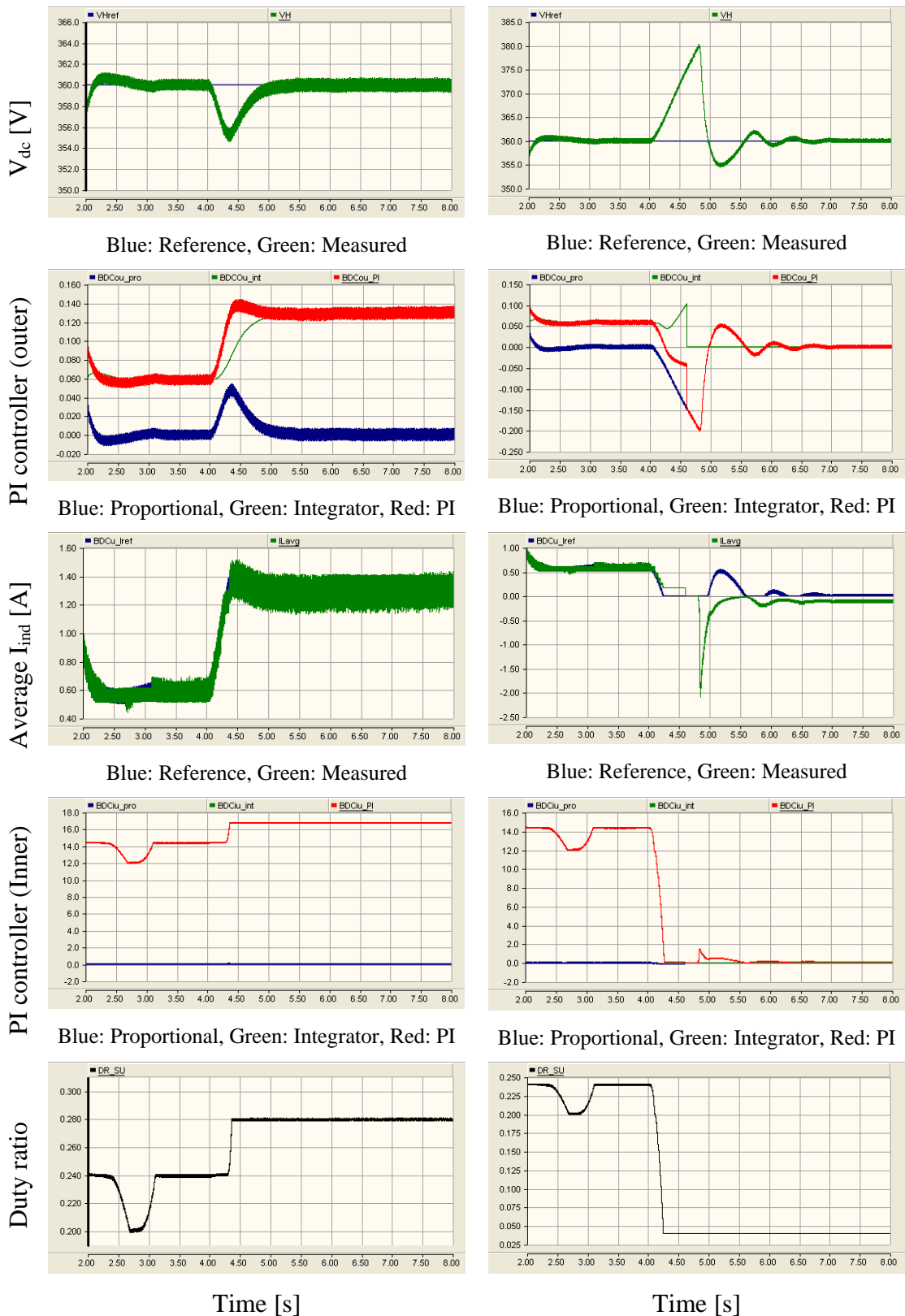
(a) Increase in active power   (b) Decrease in active power

Figure 9-15: Behaviour of the step-up mode controller of the bi-directional dc-dc converter

Blue: Reference, Green: Measured   Blue: Reference, Green: Measured

Blue: Proportional, Green: Integrator, Red: PI   Blue: Proportional, Green: Integrator, Red: PI

Blue: Reference, Green: Measured   Blue: Reference, Green: Measured

Blue: Proportional, Green: Integrator, Red: PI   Blue: Proportional, Green: Integrator, Red: PI

Time [s]   Time [s]
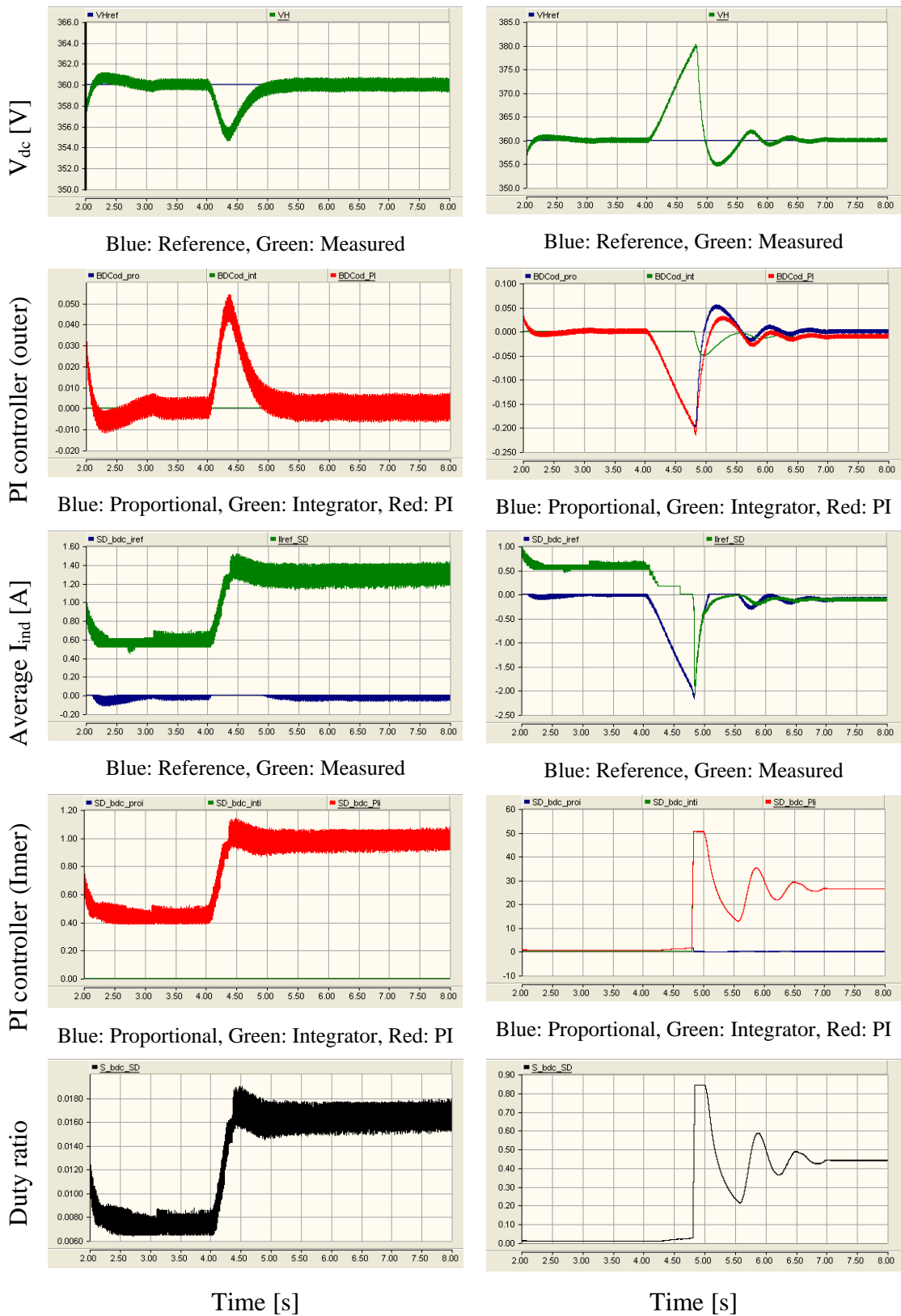
(a) Increase in active power   (b) Decrease in active power

Figure 9-16: Behaviour of the step-down mode controller of the bi-directional dc-dc

converter

The response of the current controller of the single-phase inverter is shown in Figure 9-17. The inverter output current follows the reference current; however a slight error between the two is visible. The PV panel voltage or current is not affected by the inverter output active power variations (see Figure 9-18). Figure 9-19 presents the behaviour of the controller of the modified forward dc-dc converter. The controller automatically adjusts the duty ratio of this converter to match the dc-link voltage to the required panel voltage.
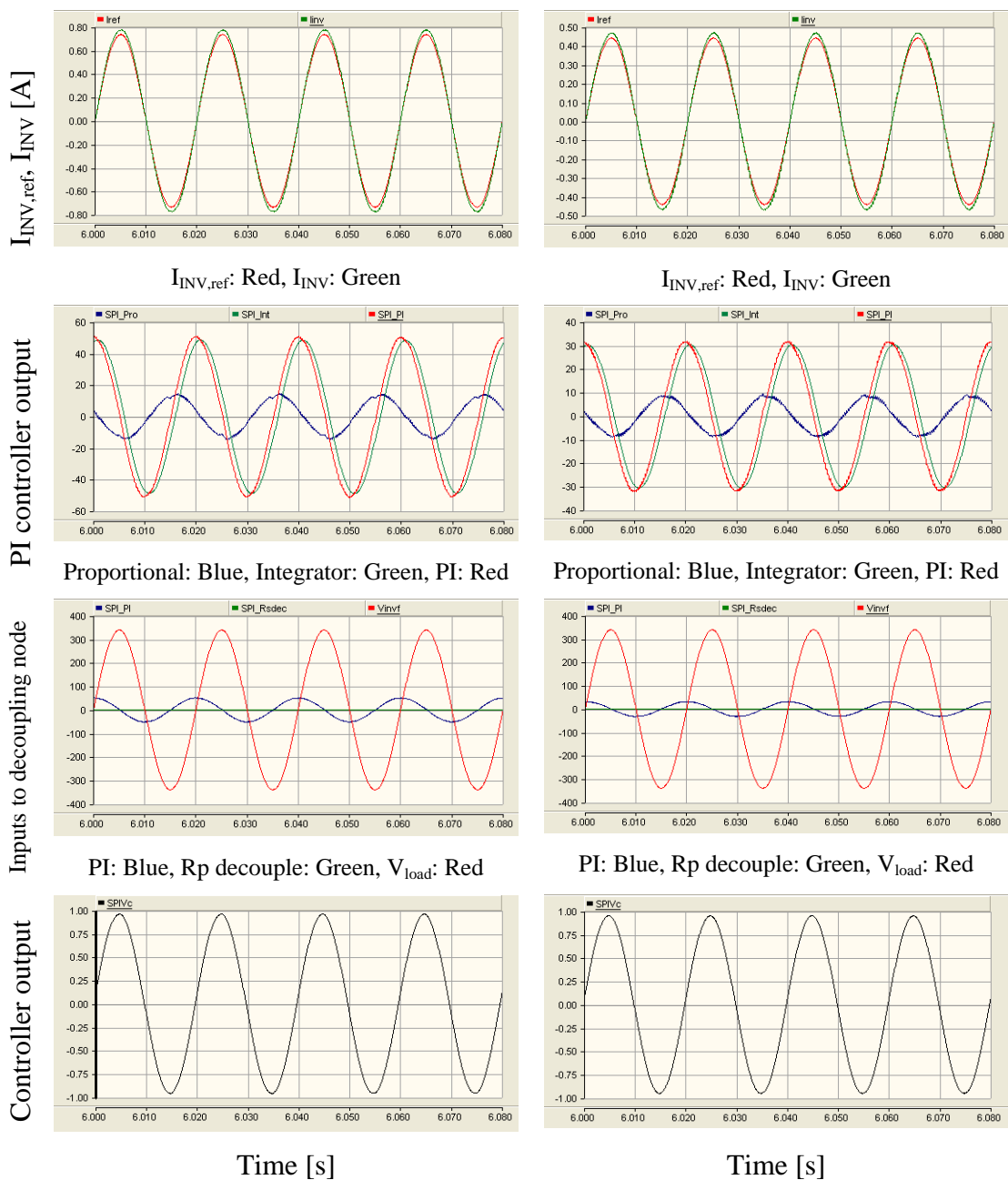
(a) Increase in active power   (b) Decrease in active power

Figure 9-17: Behaviour of the current controller of the inverter
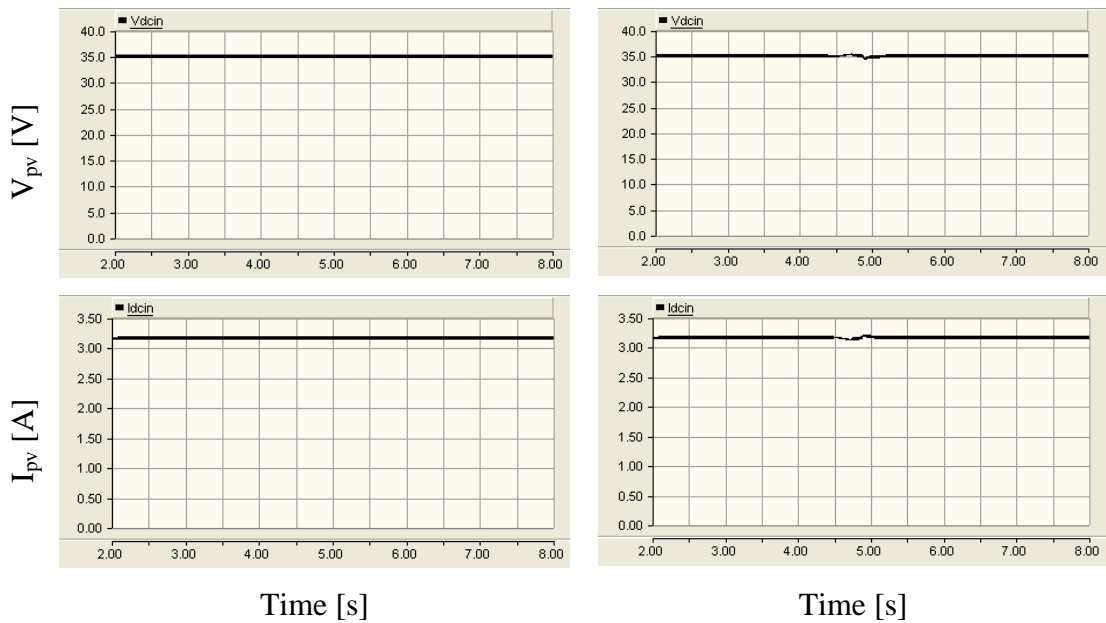
(a) Increase in active power   (b) Decrease in active power

Figure 9-18: Output current and voltage of the PV panel
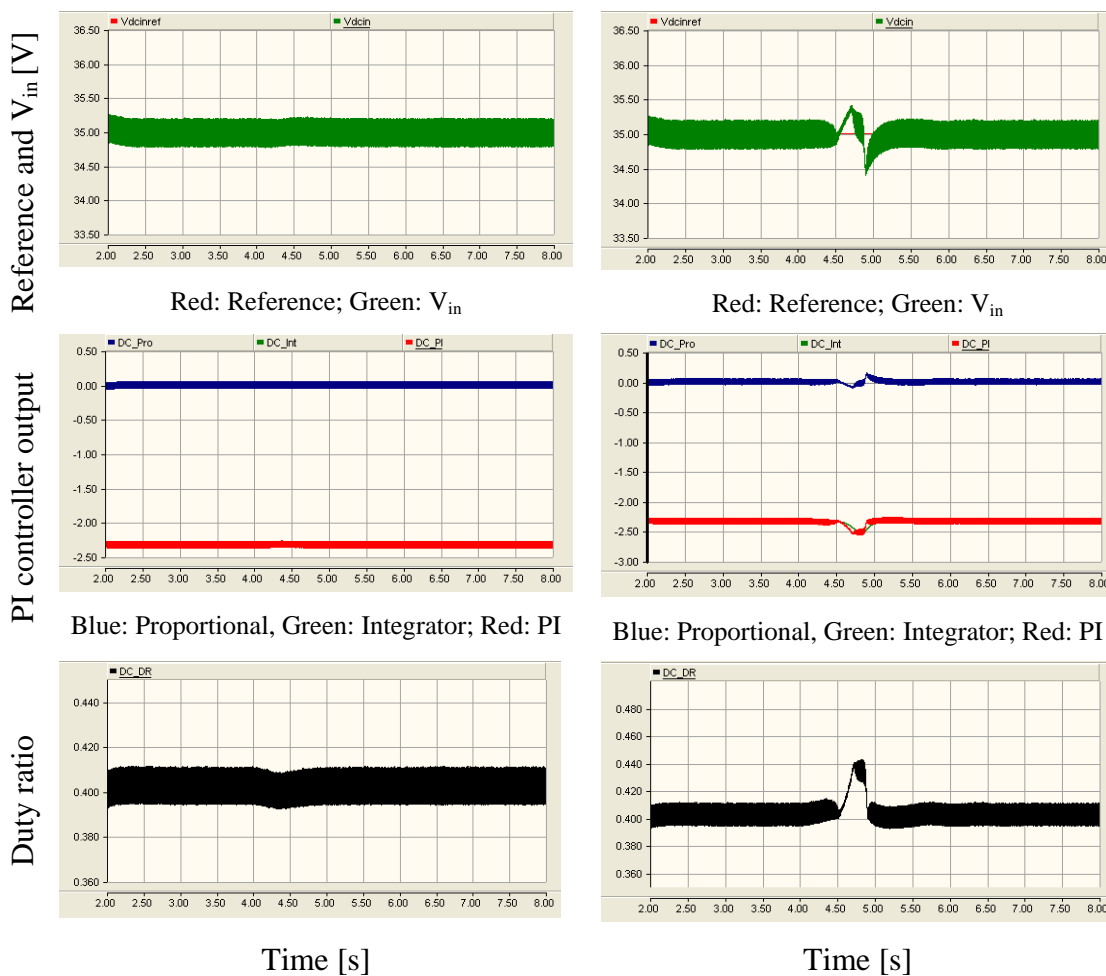
(a) Increase in active power   (b) Decrease in active power

Figure 9-19: Behaviour of the controller of the modified forward dc-dc converter

9.3.2 Reactive power change

The proposed system behaviour in response to reactive power reference variations is analysed in this section. The controllers of the dc-dc converters should not be affected by the reactive power reference. The PV panel output power corresponds to $1000W/m^2$ and 25°C. Initially the inverter output active and reactive power references were set to 100W and 30VAr. Two scenarios were considered. The reactive power reference was increased to 50VAr in one case while it was decreased to 10VAr in the other case. Reactive power was increased or decreased at a rate of 100VAr/s at t = 4 seconds.

Figure 9-20 to Figure 9-25 present the simulation results corresponding to the two cases. Figure 9-20 shows the load voltage (scaled by a factor of 0.004) and inverter output current for the steady state case after the reference change. The phase difference was 1.5ms (27°) and 0.3ms (5.4°) for two cases which approximately equals with the theoretical phase differences (26.6° and 5.71°) for the cases.

Blue: $0.004xV_{load}$, Green: I_{INV} Blue: $0.004xV_{load}$, Green: I_{INV}

Time [s]   Time [s]

(a) Increase in reactive power   (b) Decrease in reactive power
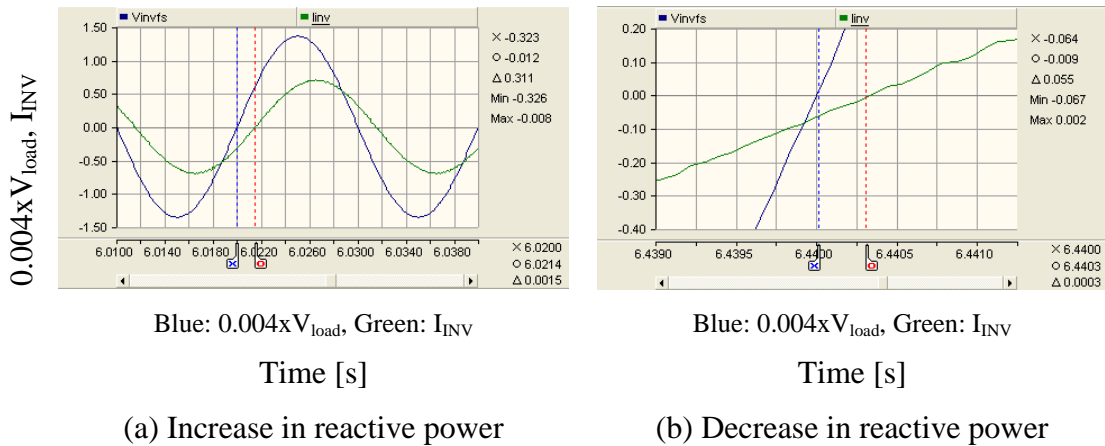
Figure 9-20: Scaled load voltage and inverter output current

The magnitude of inverter output current was slightly increased when the reference increased while the opposite happens when the reference decreased (see Figure 9-21). Figure 9-22 presents the variation of the dc-link voltage which is constant at the nominal reference of 360V. Therefore the dc-link voltage was not significantly affected by the reactive power reference change
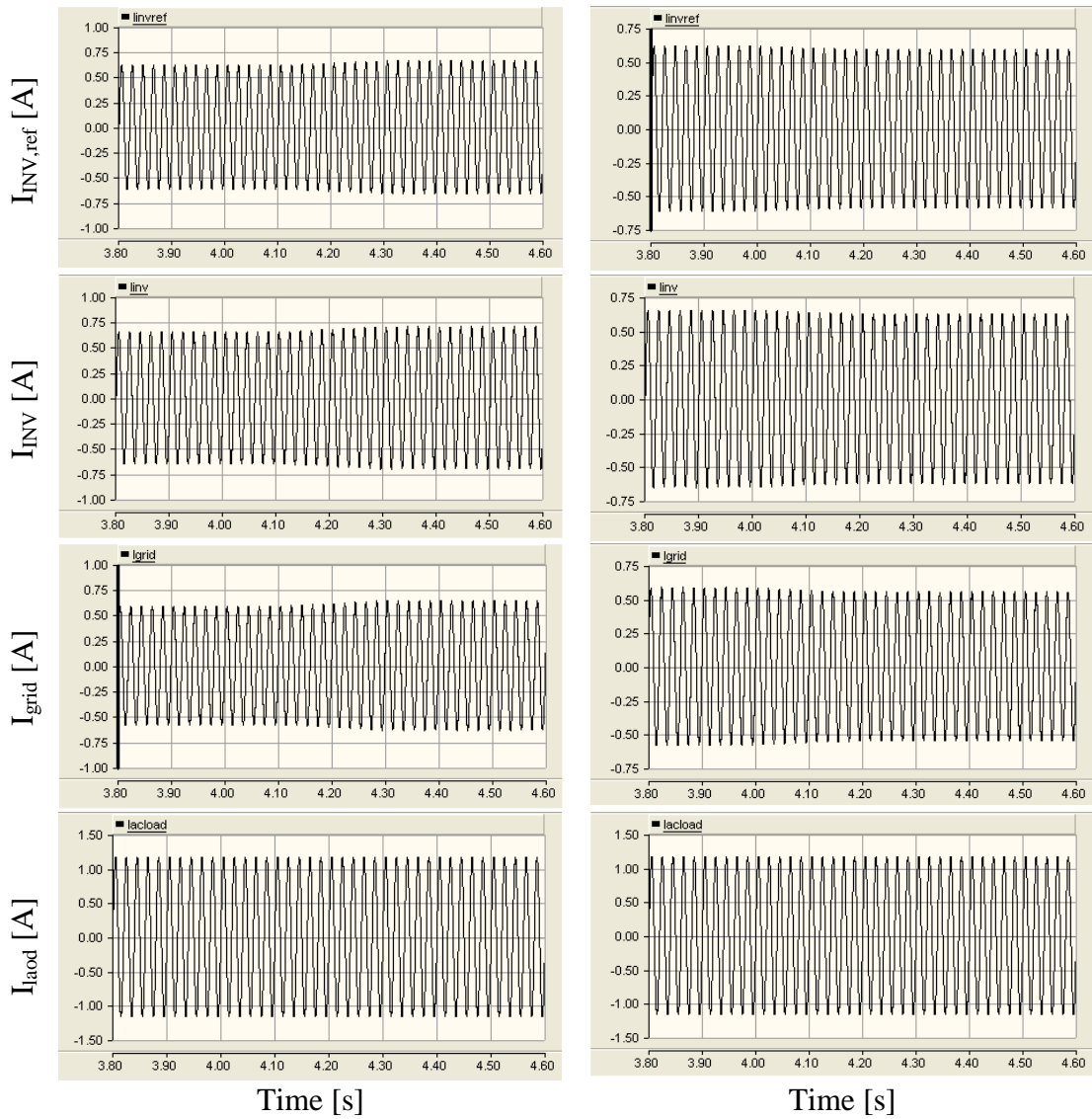
(a) Increase in reactive power   (b) Decrease in reactive power

Figure 9-21: Inverter output current reference, inverter output current, grid current and load current
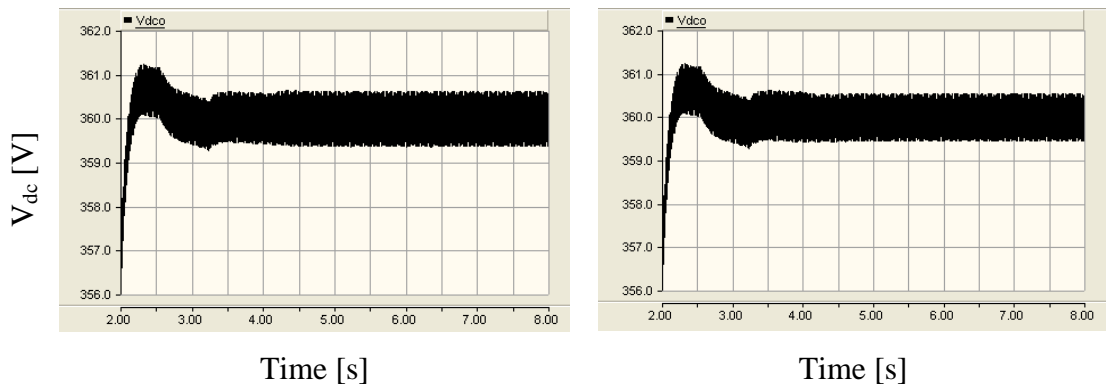
(a) Increase in reactive power   (b) Decrease in reactive power

Figure 9-22: Variation of dc-link voltage

As a result the battery voltage or battery current are not affected which is shown in Figure 9-23. Figure 9-24 shows the output voltage and current of the PV panel. Similar to the battery output quantities, photovoltaic panel output quantities are also not affected by the reactive power references change.

Time [s]   Time [s]

(a) Increase in reactive power   (b) Decrease in reactive power
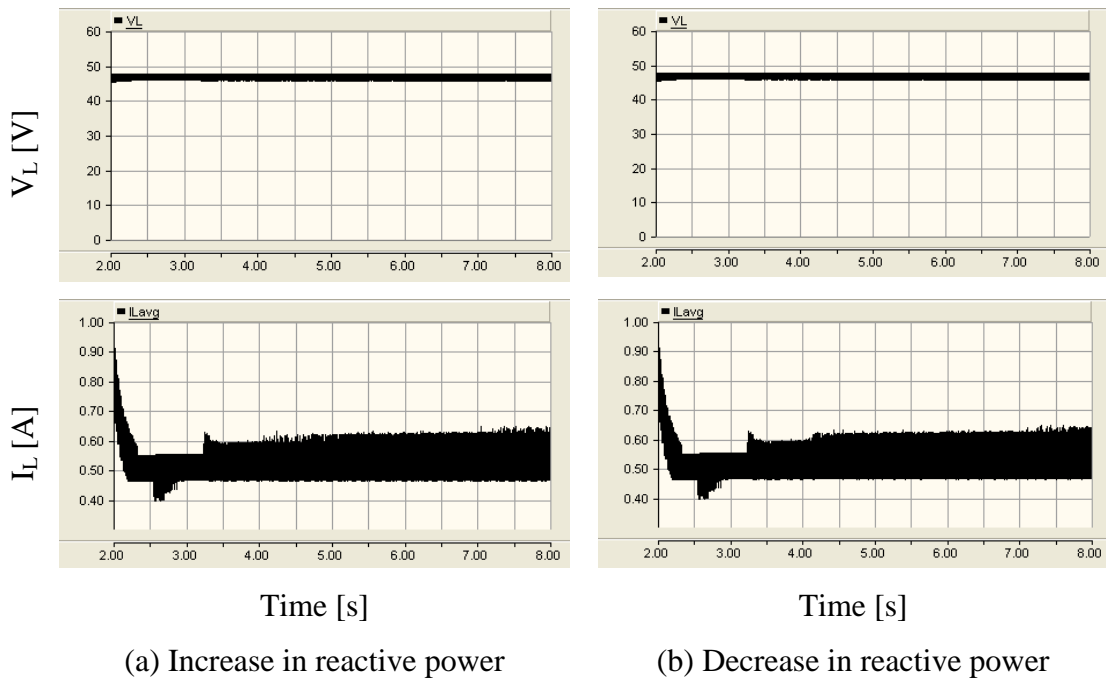
Figure 9-23: Battery voltage and battery current

Time [s]   Time [s]

(a) Increase in reactive power   (b) Decrease in reactive power
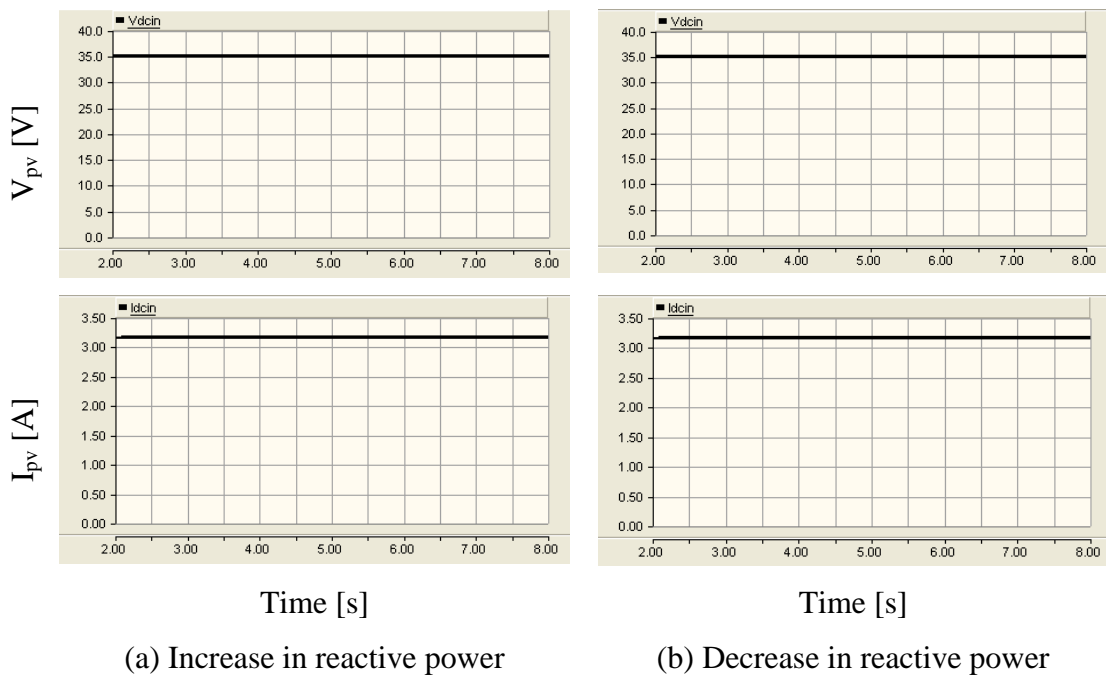
Figure 9-24: Photovoltaic panel voltage and current

According to Figure 9-25, the calculated reactive power follows the reference. Again the calculated power differs slightly from the reference. At 50Hz, the command tracking response of the current controller introduces a magnitude and phase error which is reason for this difference (see Chapter 8). The error is also affected by the fact that the leakage inductance of the transformer is not included in the controller design.
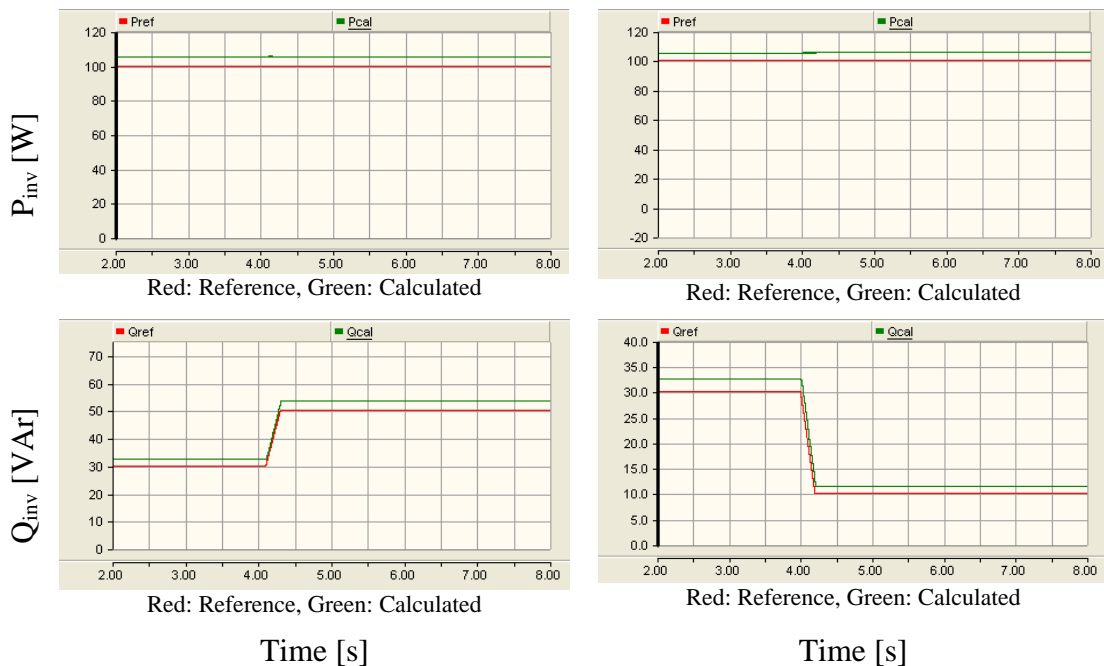
(a) Increase in reactive power   (b) Decrease in reactive power

Figure 9-25: Active and reactive power outputs of the inverter

9.4 START-UP PROCEDURE

When the proposed system is initially started, the dc-link voltage is zero. Thus it is not possible to integrate the microsource interface to the MicroGrid directly at this point. A suitable starting method is required and this section explains the start-up process used.

It is necessary to charge the dc-link capacitors to their nominal voltage before the connection of the inverter to the MicroGrid. There are three ways to charge the dc-link capacitors: using the PV panel, using the battery and using the grid. Capacitors could be charged through the diodes of the inverter using energy from the MicroGrid; however an inrush current limiter is required to avoid the damage to the inverter. Similarly there is a possibility for inrush current when charging from the battery. Charging the capacitors using PV output power would yield least inrush currents since the short

circuit current of the PV panel is limited. Overcharging should be avoided irrespective of the charging method. Otherwise the protection system would shut down the system.

In the proposed start-up method, dc-link capacitors were charged from the PV panel output power. The bi-directional dc-dc converter and inverter were turned off at the start. In addition the circuit breaker, which is in between the inverter and MicroGrid, was also turned off. The dc-link capacitors were charged to 360V. The circuit breaker in between the inverter and the MicroGrid was closed when the dc-link voltage exceeded 350V. This avoids the inrush current which would flow from the MicroGrid to dc-link capacitors through the diodes of the inverter. At the same time the bi-directional dc-dc converter and the inverter were also turned on. A positive active power reference was applied to the inverter at a 100W/s rate. This would remove any current spikes at the grid connection.

Figure 9-26 to Figure 9-30 shows the simulation results during the start-up of the proposed system. Figure 9-26 shows the output voltage and current of the photovoltaic panel. The controller of the modified forward dc-dc converter keeps the input voltage of the converter, which is the PV panel voltage, constant through out the process.
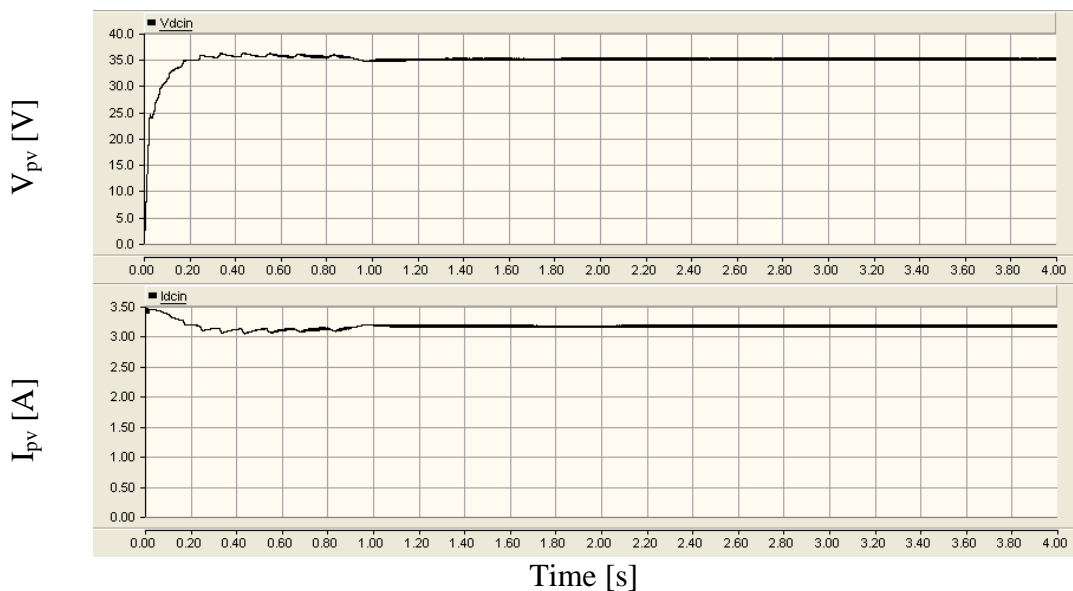
Figure 9-26: Photovoltaic panel voltage and current

The dc-link voltage is shown in Figure 9-27 which starts to increase smoothly at the beginning and crosses the 350V line at around t = 0.7 second. The voltage started to

drop just after t= 0.8 second until t = 1.8 second. Then dc-link voltage again increased and stabilised at 360V. Figure 9-28 presents the battery voltage and battery current during the start-up of the microsource interface. Battery current was zero initially since the bi-directional dc-dc converter was turned off. The battery started to discharge current at around t = 0.7 second since the bi-directional dc-dc converter was turned on when the dc-link voltage crossed 350V. Positive current indicates that the battery is discharging. After t = 0.8 second, dc-link voltages cross the step-down turn-on reference, thus the operating mode of the bi-directional dc-dc converter changes to step-down mode. As a result, the battery current becomes negative. The dc-link voltage continues drop and at around t = 1.8 second the dc-link voltage crosses the step-up turn-on reference. Thus bi-directional dc-dc converter operates in step-up mode and the battery current becomes positive.
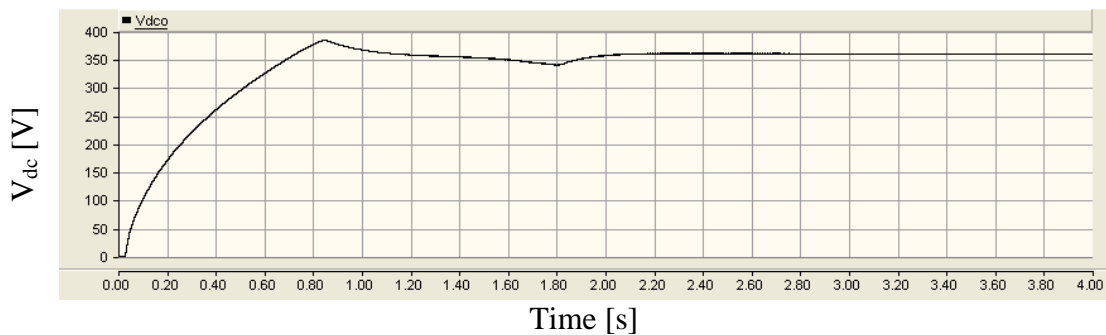
Figure 9-27: DC-link voltage
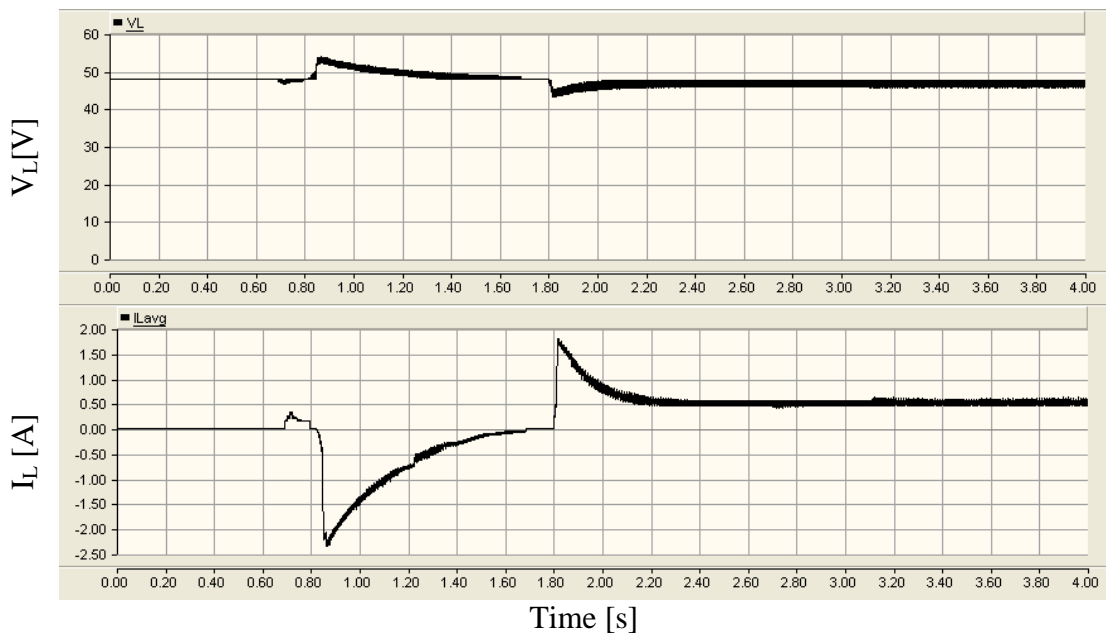
Figure 9-28: Battery voltage and current

The inverter output current reference, inverter output current, grid current and load current are shown in Figure 9-29. At around t = 0.7 second, the inverter current reference starts to increase followed by the inverter output current. Initially the load is fully powered from the grid. The current contributed by the grid decreases after t = 0.7 second. Load current is constant over the periods and is not disturbed by the inverter grid connection.
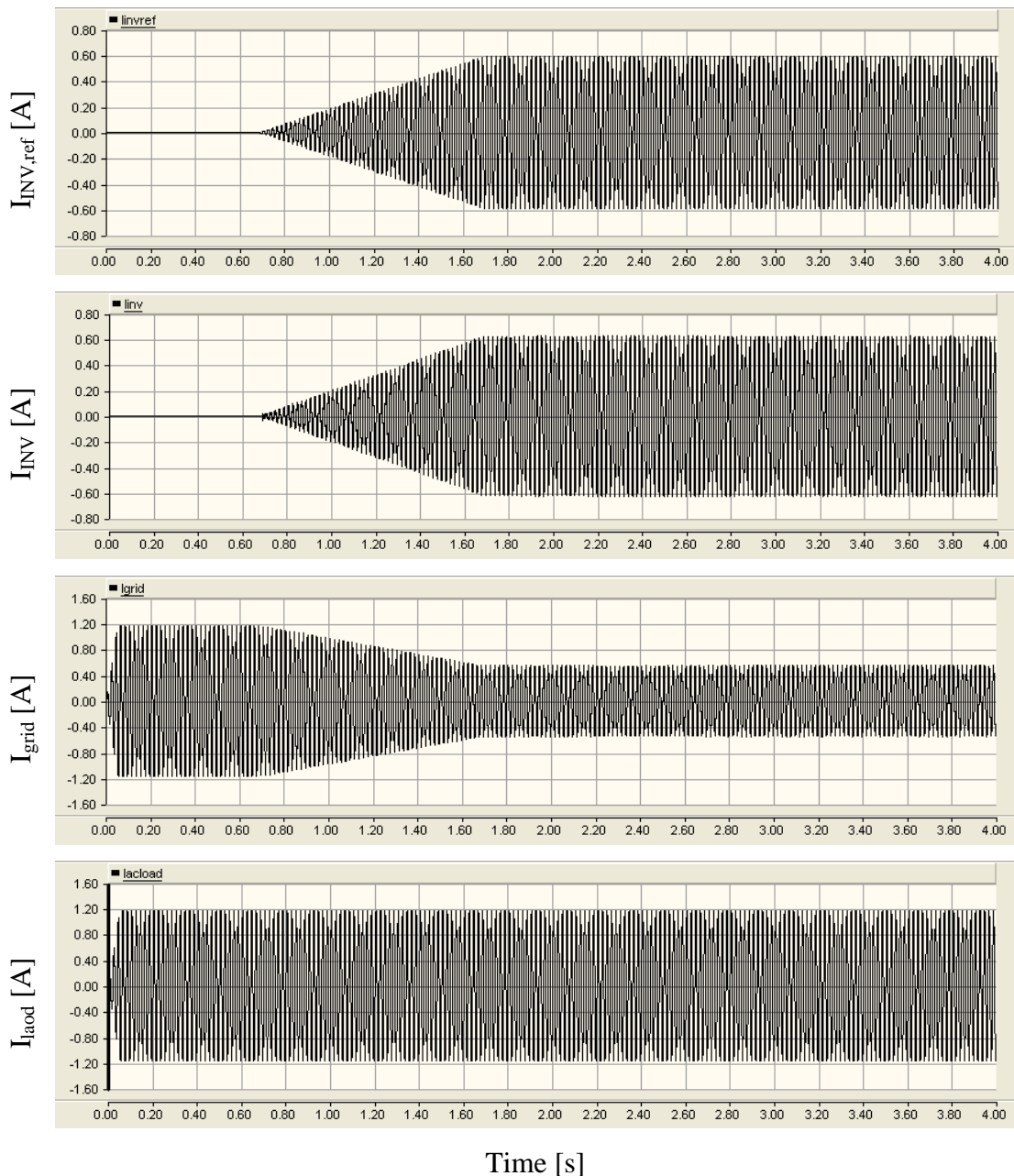
Figure 9-29: Inverter output current reference, inverter output current, grid current and load current

Figure 9-30 presents the inverter output voltage, grid voltage and inverter output current at the grid connection point. Just before t = 0.7 second the inverter was connected to the MicroGrid. The inverter output voltage starts to follow the grid voltage. The inverter output current was zero before the grid connection. However the current before t = 0.7 second is insignificant. Grid voltage (in blue) is equals to load voltage thus not visible.

V_{INV}: Green, V_{load}: Red, V_{grid}: Blue

Time [s]
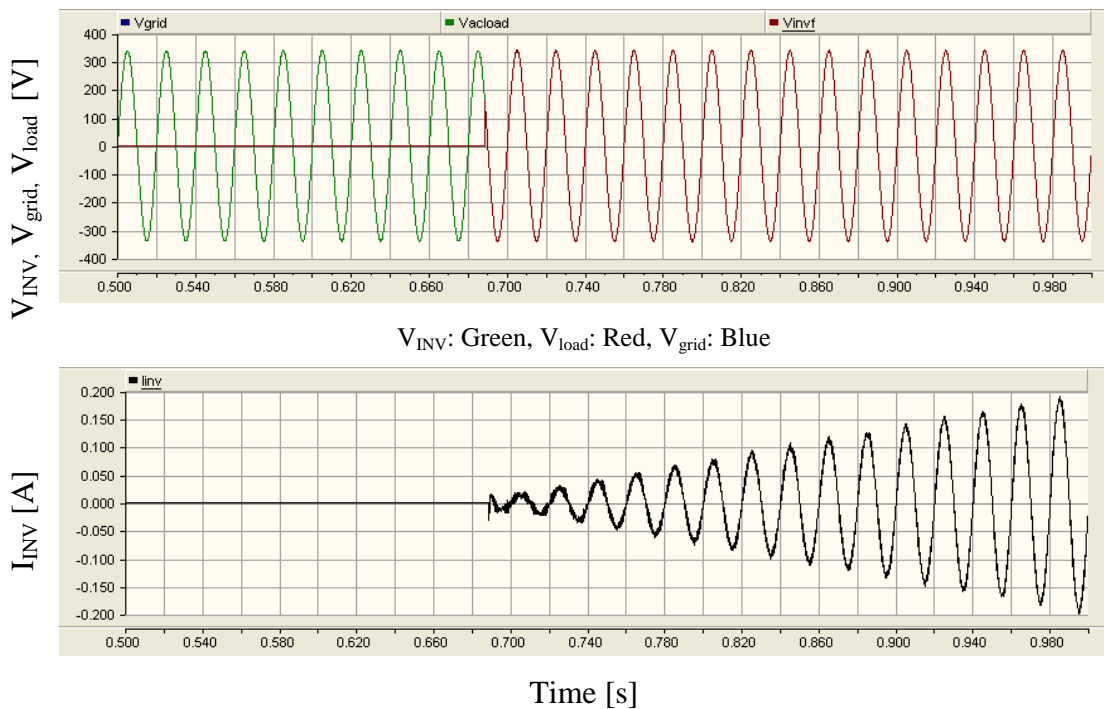
Figure 9-30: Inverter load current and load voltage

9.5 SUMMARY

This chapter presents the behaviour of the proposed system when integrated. System response to load variations and microsource output power variations were discussed. Finally a start-up method was presented.

According to the simulation results, the controller of the bi-directional dc-dc converter, which controls the energy in and out from the battery, kept the dc-link voltage constant in response to irradiance changes and microsource output power variations. Thus inverter output power was not affected during microsource output power variations. Similarly the microsource was not affected by the inverter output power variations. Thus the controllers decoupled the dynamics of the load variations and microsource output power variations.

Since the dc-link voltage is zero at the start, integration of inverter to the grid is not possible at this point. In the proposed start-up method, dc-link capacitors were charged using the PV panel output power to a minimum before operating the inverter and the bi-directional dc-dc converter. The inverter was then integrated to the MicroGrid smoothly. Further the dc-link voltage was kept with the pre-defined limits.

CHAPTER 10

DISCUSSION AND CONCLUSIONS

10.1 INTRODUCTION

The objective of this thesis was to develop a single-phase microsource interface for a MicroGrid and investigate the issues surrounding its 'system integration'. A key element of this system is the energy storage unit integrated into the proposed microsource interface. Therefore the proposed system can improve 'plug-and-play' functionality within the MicroGrid.

A review of MicroGrids was presented in Chapter 2 of this thesis which included the definition and brief description of major components of a typical MicroGrid. A review on operational real-world MicroGrids was also included. Microsource interfacing methods were also discussed. Chapter 3 presented the basics of photovoltaic (PV) cells. PV cell electrical models were discussed. Grid connected PV systems and maximum power point tracking methods were reviewed briefly. In chapter 4 the power electronic converters used in the proposed system were presented. Mathematical models were obtained for the converters which were used later in designing the controllers. A simulation model of a photovoltaic panel was developed and an emulator was designed and implemented. Chapter 5 included the details of the PV model and emulator. Open loop test results of three converters were presented in Chapter 6. The system behaviour with the microsource and energy storage unit operating together was presented in Chapter 7. In Chapter 8, grid connection of the single-phase inverter was discussed. Finally simulation results of the proposed system were presented in Chapter 9.

A summary and discussion of the outcome of the research are presented in the discussion sub-section of this chapter. Then conclusions of the thesis are presented. Finally the possible ways to extend this work are included in the future work sub-section.

10.2 DISCUSSION

10.2.1 Microsource

A photovoltaic panel was selected as the microsource to validate the proposed microsource interface.

10.2.1.1 Simulation model of photovoltaic panel

A photovoltaic panel model was developed in EMTDC/PSCAD software which was presented in Chapter 5. The model was based on the characteristic equation of a PV panel and was represented by a controllable voltage source. Appropriate equations were used to relate irradiance and temperature to the variables in the characteristic equation. Thus irradiance and temperature were inputs to the model. However the simulation model based on the characteristic equation failed at voltages below and near the maximum power point. Numerical instability during the iteration process was the reason for this failure. An inductor in series with the voltage source extended the operating region of the simulation model of the photovoltaic panel. Again the failure point was predicted from mathematical analysis and verified using the simulation results.

The following are the contributions to knowledge from this modelling of the photovoltaic panel: a) The reason for failure of the simulation model of photovoltaic panel developed in EMTDC/PSCAD software is mathematically shown; b) A method was proposed to extend of safe operating region of the model with known limitations.

10.2.1.2 Photovoltaic emulator

A simple, but reasonably accurate, photovoltaic emulator based on an adjustable linear voltage regulator was designed and implemented which was used in the experimental set-up. The output voltage of the regulator was controlled by an analogue circuit. The function of the controller differs depending on the operating point on the characteristic curve of the PV panel. At higher voltages, the output voltage of the linear voltage regulator was controlled using the characteristic equation of the PV panel. In contrast the output current of a PV panel is almost constant at low voltages: thus in this region a current controller was used to keep the output current constant. Variable resistors were

used in the controller to change the characteristic curves for different irradiance conditions. However, fast irradiance changes were difficult to emulate as several variable resistors would need to be adjusted simultaneously. The characteristic curves obtained from the emulator matched with the characteristic curves obtained from the simulation model.

The design and implementation method of a simple and low cost hardware photovoltaic emulator is a contribution to knowledge from this thesis. The proposed hardware emulator will accelerate the initial research related to photovoltaic systems.

10.2.2 Open loop testing of power electronic converters

The photovoltaic panel was connected to the dc-link through a modified forward dc-dc converter and the energy storage unit was connected through a bi-directional dc-dc converter. The system was connected to the grid via a single-phase inverter.

The power conversion efficiency of the bi-directional dc-dc converter was approximately 90%. The experimental results of the bi-directional dc-dc converter matched with the theoretical waveforms and simulation results. The effects of parasitic components were not significant. An inrush current limiter was required at the low voltage end of the bi-directional dc-dc converter to limit the battery discharge current at the start.

Efficiency of the modified forward dc-dc converter efficiency was found to be 75-80%. The modified forward dc-dc converter is derived from buck dc-dc converter. Thus the transformer turns-ratio was comparatively large. As a result, the voltage across the secondary winding of the transformer was more than twice the dc-link voltage. Thus the effect of parasitic components was significant. Oscillations were experienced during turn-on transient of the switch (a MOSFET in this case). Further, a larger inductor was required since the current flowing through the inductor is small and the voltage across the inductor is large. The equivalent circuit of the bi-directional dc-dc converter during step-up mode is similar to a boost derived dc-dc converter. Thus a boost derived dc-dc converter would have been better than a modified forward converter, which would have

reduced the parasitic effects and improved the efficiency of the unidirectional dc-dc converter.

A full-bridge single-phase inverter was used to convert the dc voltage into ac voltage. The inverter was coupled to the grid through an inductor. The open loop control results of the inverter validated the proper operation of the inverter. Power conversion efficiency of the inverter is over 90%.

Following are the contributions to knowledge from the testing of switch-mode power electronic converters: a) It has been confirmed that in this system that approximately 90% power conversion efficiency can be achieved with appropriately selected topologies. b) Appropriate selection of topologies should be undertaken to avoid introducing parasitic effects which are difficult to eliminate after the implementation.

10.2.3 Closed loop controllers of converters

The controllers were developed for all three converters. Dynamic stiffness properties and command tracking properties were used to design the controllers

10.2.3.1 Modified forward dc-dc converter

The function of the controller of the modified forward dc-dc converter is to keep the input voltage of the converter at the maximum power point (MPP). In this analysis, the photovoltaic panel emulator was operated at nominal 1000W/m^2 irradiance at 25°C. The voltage at MPP corresponds to 35V which was the reference to the controller of the modified forward dc-dc converter. According to the simulation and experimental results, the controller kept the input voltage constant at that reference. Further, dc-link voltage transients due to load variations did not affect the input voltage of the modified forward dc-dc converter.

10.2.3.2 Bi-directional dc-dc converter

The controller of the bi-directional dc-dc converter is responsible for keeping the dc-link voltage approximately constant within pre-defined limits. An operating model of the bi-directional dc-dc converter is used to design the controller. Operating modes of

the bi-directional dc-dc converter are selected by the controller based on the dc-link voltage. A hysteresis control technique was adapted to avoid unnecessary oscillations between modes. Simulation and experimental results validated that the converter was switching between the modes at pre-defined voltages.

10.2.3.3 Single-phase inverter

A fast inner-loop current controller was designed based on the required dynamic stiffness properties and the command tracking properties. Further, in the controller, load voltage was fed back to the controller as a disturbance input decoupling signal. This further increased the dynamic stiffness of the system. The designed controller was implemented in the simulation model and the simulated results matched with the experimental results.

The following are contributions to knowledge from the design of the controllers: a) State feedback block diagram based controller design can be used to allow improved performance of the controller (either disturbance input decoupling or feedforward control); b) An instantaneous current controller, which is used to control the output current of the inverter can be integrated with limited magnitude and phase error.

10.2.4 Automatic dc-link voltage control

The dc-link should represent a stiff voltage source in the proposed system. The photovoltaic panel, energy storage unit and dc-dc converters were connected together to evaluate the behaviour of the dc-link voltage. A resistive load was connected to the dc-link. The dc-link voltage was held to be effectively constant for the load variations. Even for complete power loss from the photovoltaic panel or complete load removal, the dc-link voltage was kept with the proposed limits. Thus the controllers ensured that a stiff dc-link voltage is achieved. Such minor voltage variations can be compensated by dc-link voltage feedforward control to the inverter.

The contributions to knowledge of this work are: a) An energy storage unit can be used to produce a stiff dc voltage source to the inverter; b) The dynamic stiffness based controller allows the decoupling of the dynamics of the microsource and load, thus stiff dc-link and undisturbed microsource operation can be achieved.

10.2.5 Grid connection of single-phase inverter

The controller of the single-phase inverter is responsible for the synchronisation of the inverter with grid, the connection of inverter to the grid and output power flow control. A phased-locked loop was used to generate a sinusoidal signal in-phase with the load voltage, and this signal was used to generate the current reference to the current controller. The magnitude and the phase with respect to load voltage of the current reference were calculated from the power references and measured load voltage. According to the simulation results, the inverter delivered the active and reactive power according to the given reference values with only minor errors. The results were also validated by the experimental results. Current controlled grid connection removed the necessity to match the magnitude of the voltage waveforms. Smooth grid connection was achieved and distortions were not visible in the load voltage.

The contributions to knowledge are: a) Smooth grid connection can be achieved from the current controlled grid connection; b) with this control method, it is only necessary to generate a sinusoidal signal in-phase with the grid voltage with current controlled grid connection. Voltage magnitude and phase matching is not required. This simplifies the grid connection process.

10.2.6 Proposed system behaviour

Simulation results of the proposed microsource interface were presented in Chapter 9. The system was tested under different load and microsource conditions. An energy storage unit decoupled the dynamics of the microsource and inverter output power variations. Furthermore, a stiff dc voltage source to the inverter was achieved. As a result, the inverter output power was not affected by the microsource dynamics and the PV panel was not affected by inverter output power variations. Therefore the proposed system functioned properly under different conditions.

The inverter cannot integrate to the MicroGrid at zero seconds when the microsource unit is first switched on, as the dc-link voltage is zero. In the proposed start-up method, the dc-link capacitors were charged from the PV panel output power. Once the minimum dc-link voltage achieved, both the inverter and the bi-directional dc-dc converter are allowed to operate. This avoided the inrush current flow either from the

battery or MicroGrid through the diodes of the inverter. According to the simulation results smooth grid connection is possible using the proposed start-up method.

The contributions to knowledge from the proposed interface are: a) Energy storage unit can be used to decouple the dynamics of the microsource and variations in the power output of the inverter; b) A complex system can be controlled from simple controllers with the aid of appropriate controller design. This results in an implementation which is easier to design and will be potentially cheaper; c) A start-up problem occurs when the energy storage unit is connected to the dc-link through a bi-directional dc-dc converter. This is not an issue when energy storage unit is directly connected to the dc-link. However, it is possible to overcome this problem.

10.3 CONCLUSIONS

The proposed microsource interface was simulated and experimentally validated. The following conclusions are reached from the proposed microsource interface development.

A simulation model of a photovoltaic panel was developed with known limitations. The failure point of the simulation model can be calculated mathematically, thus a simulation system failure due to PV panel operation can be easily indentified beforehand. Further a simple and low cost adjustable linear voltage regulator based photovoltaic emulator was designed which can be used to accelerate the testing of laboratory PV systems.

The controllers of modified forward dc-dc converter ensured that the maximum power from the PV panel was delivered and PV panel operation was not disturbed by the load variations connected at the output of the modified forward dc-dc converter. The controller of the bi-directional dc-dc converter kept the dc-link voltage constant within a tight range even in worst-case scenarios while discharging and charging the battery appropriately. A very quick but simple PI based current controller was developed to control the inverter output current using the instantaneous inverter output current and load voltage. A smooth grid connection was achieved and the required output power was delivered.

The simulation model of the proposed system complemented the predicted results. The inverter delivered the active and reactive power corresponding to the reference. The controller of the bi-directional dc-dc converter ensured that the dc-link voltage was kept within the tight limits specified irrespective of the microsource and inverter output conditions. The controller of the modified forward dc-dc converter, which controls the microsource output power, ensured that it was not disturbed by the system behaviour. A start-up method was proposed which ensured smooth grid connection and smooth operation of all converters. The proposed start-up method reduced the inrush current flowing from the various power sources. This reduced the required protection components.

Finally it is possible to conclude that proposed microsource interface embedded with energy storage unit decoupled the dynamics of the microsource and can help to ensure the proper operation of a MicroGrid.

10.4 FUTURE WORK

The proposed microsource interface presented in this thesis and associated components could be improved. Thereby a better microsource interface could be achieved.

Either a P-Q power reference control or a droop-line control method could be used to control the output power of a microsource. The system presented in thesis uses a P-Q control technique which requires power references from the central MicroGrid controller. Droop-line controller operates based on the inverter terminal quantities which would not require communication between central controller of the MicroGrid and microsource. Thus the system could be made more robust by using the droop-line control method.

It would be desirable to improve the behaviour of the current controller of the single-phase inverter. Even though the error cannot be made zero, it could be minimised. Thus further research could be carried out to improve the behaviour of the current controller.

The controller in this thesis does not consider the state of the battery. System malfunction during a fully charged or discharged battery state could be removed by enhancing the controller to take the state of the battery into account.

It would be highly desirable to test with a real panel to investigate the operation of the proposed system which would prove the system behaviour with real components. In this thesis, a static voltage maximum power point tracker was incorporated with the photovoltaic panel. It would be interesting to examine the effects of having a slow dynamic MPPT with the controller of the proposed system.

The ability to use the proposed controller with other microsources could also be tested. The proposed microsource interface could be proposed as the standard microsource interface if the proposed structure and control scheme could be made to incorporate other types of microsources as well.

In this research an analogue electronic controller was used in the photovoltaic emulator. It would be more user-friendly if a digital controller is used instead of the analogue controller. Then the output of the photovoltaic panel could be varied based on pre-defined environmental conditions. Further the characteristics of the emulator could be compared with those of a real panel. This would help to develop the transient behaviour of the emulator.

REFERENCES

[1] "The growth potential for Microgeneration in England, Wales and Scotland," Element Energy Limited, 2008, pp. 136, http://www.berr.gov.uk/files/file46003.pdf last accessed on 2010-04-09.

[2] R. Lasseter, A. Akhil, C. Marnay, J. Stephens, J. Dagle, R. Guttromson, A.S. Meliopoulous, R. Yinger, and J. Eto, *White Paper on Integration of Distributed Energy Resources The CERTS MicroGrid Concept - Appendices*, Consortium for Electric Reliability Technology Solutions, 2002.

[3] R.H. Lasseter, "MicroGrids," *IEEE Power Engineering Society Winter Meeting*, 2002, pp. 305-308, Vol. 1.

[4] T. Funabashi and R. Yokoyama, "Microgrid field test experiences in Japan," *IEEE Power Engineering Society General Meeting*, 2006, p. 2 pp.

[5] C. Marnay and R. Firestone, "An Emerging Paradigm for Meeting Building Electricity and Heat Requirements Efficiently and with Appropriate Energy Quality," *European Council for an Energy Effecient Economy 2007 Summer Study*, La Colle sur Loup, France: 2007.

[6] J.A.P. Lopes, C.L. Moreira, and A.G. Madureira, "Defining control strategies for MicroGrids islanded operation," *IEEE Transactions on Power Systems,*, vol. 21, 2006, pp. 916-924.

[7] M. Barnes, A. Dimeas, A. Engler, C. Fitzer, N. Hatziargyriou, C. Jones, S. Papathanassiou, and M. Vandenbergh, "MicroGrid Laboratory Facilities," *International Conference on Future Power Systems*, 2005, pp. 1-6.

[8] S. Bando, H. Asano, T. Tokumoto, T.A.T.T. Tsukada, and T.A.O.T. Ogata, "Optimal Operation Planning of a Photovoltaic-Cogeneration-Battery Hybrid System," *International Conference on Power System Technology, PowerCon*, 2006, pp. 1-8.

[9] C.L. Moreira, F.O. Resende, and J.A.P. Lopes, "Using Low Voltage MicroGrids for Service Restoration," *IEEE Transactions on Power Systems*, vol. 22, 2007, pp. 395-403.

[10] N. Hatziargyriou, H. Asano, R. Iravani, and C.A.M.C. Marnay, "Microgrids,"

Power and Energy Magazine, IEEE, vol. 5, 2007, pp. 78-94.

[11] B. Kroposki, R. Lasseter, T. Ise, S. Morozumi, S. Papatlianassiou, and N. Hatziargyriou, "Making microgrids work," *IEEE Power and Energy Magazine*, vol. 6, 2008, pp. 40-53.

[12] Y. Kojima, M. Koshio, S. Nakamura, H.A.M.H. Maejima, Y.A.F.Y. Fujioka, and T.A.G.T. Goda, "A Demonstration Project in Hachinohe: Microgrid with Private Distribution Line," *IEEE International Conference on System of Systems Engineering, SoSE*, 2007, pp. 1-6.

[13] A. Yokoyama, "Overview of Microgrid R&D in Japan," *Symposium on MicroGrids*, University of California, San Diego: 2009.

[14] S. Tagami, Y. Sasaki, T. Tsukada, T. Tokumoto, J. Ichimura, Y. Watanabe, H. Asano, and S. Bando, "Development and evaluation of microgrids islanded operation method with demand side control," *16th Power Systems Computation Conference*, Glasgow, Scotland: 2008, p. 7.

[15] N. Hatziargyriou, "The More Microgrids Project," *SMART ELECTRICITY NETWORKS, Demonstration of smart distribution network solutions, Contractors meeting*, Brussels: 2009.

[16] R.H. Lasseter and P. Paigi, "Microgrid: a conceptual solution," *IEEE 35th Annual Power Electronics Specialists Conference, PESC*, 2004, pp. 4285-4290, Vol.6.

[17] A. Invernizzi, "Technologies to innovate distribution network with DG," *Workshop on Electricity Transmission and Distribution Technology and R&D*, Paris 2004: http://www.iea.org/work/2004/distribution/presentations/invernizzi.pdf last access on 2010.02.11, .

[18] T. Tsukada, T. Tokumoto, T. Ogata, and S. Tagami, "DEMONSTRATION OF MICROGRID THROUGH THE ACTIVITIES TOWARD HOLONIC ENERGY SYSTEMS," *6th International Conference on Indoor Air Quality, Ventilation & Energy Conservation in Buildings - IAQVEC*, Sendai, Japan, 2007: http://www.inive.org/members_area/medias/pdf/Inive%5CIAQVEC2007%5CTsukada.pdf accessed on 2010.02.11, .

[19] Y. Zoka, H. Sasaki, N. Yorino, K.A.K.K. Kawahara, and C.C.A.L.C.C. Liu, "An interaction problem of distributed generators installed in a MicroGrid," *Proceedings of the IEEE International Conference on Electric Utility*

Deregulation, Restructuring and Power Technologies, (DRPT), H. Sasaki, Ed., 2004, pp. 795-799 Vol.2.

[20] B. Lasseter, "Microgrids [distributed power generation]," *IEEE Power Engineering Society Winter Meeting*, 2001, pp. 146-149, Vol.1.

[21] T. Funabashi, "Efficient operation of distributed energy resources in microgrid," *IEEE International Conference on Sustainable Energy Technologies*, Singapore, 2008: http://www.ieee-icset.org/keynotes/Keynote_Address_Funabashi.pdf last accessed on 2010.02.11, .

[22] A. Denda, "Shimizu's Microgrid Research Activities," *Symposium on Microgrids*, Canada, 2006: http://der.lbl.gov/new_site/2006microgrids_files/Japan/Presentation_6_Atsushi_d enda.pdf access on 2010.02.11, .

[23] C.E. Jones, C. Fitzer, and M. Barnes, "Investigation of Microgrids," *The 3rd IET International Conference on Power Electronics, Machines and Drives*, 2006, pp. 510-514.

[24] H. Al-Nasseri, M.A. Redfern, and R. O'Gorman, "Protecting micro-grid systems containing solid-state converter generation," *International Conference on Future Power Systems*, 2005, p. 5 pp.

[25] H. Nikkhajoei and R.H. Lasseter, "Microgrid Protection," *IEEE Power Engineering Society General Meeting*, 2007, pp. 1-6.

[26] N. Jayawarna, C. Jones, M. Barnes, and N.A.J.N. Jenkins, "Operating MicroGrid Energy Storage Control during Network Faults," *IEEE International Conference on System of Systems Engineering, SoSE*, 2007, pp. 1-7.

[27] M. Barnes, "An Evaluation of Microgrid Structures and their Relative Merits," *IET Power Convention*, 2007, pp. 1-34.

[28] M. Barnes and P. Binduhewa, "Asynchronous interconnection of a microgrid," *CIRED Seminar SmartGrids for Distribution, IET-CIRED.*, 2008, pp. 1-4.

[29] A. Amorim, A.L. Cardoso, J. Oyarzabal, and N.A.M.N. Melo, "Analysis of the Connection of a Microturbine to a Low Voltage Grid," *International Conference on Future Power Systems*, 2005, pp. 1-5.

[30] P. Piagi and R.H. Lasseter, "Autonomous control of microgrids," *IEEE Power Engineering Society General Meeting*, 2006, p. 8 pp.

[31] M. Barnes, J. Kondoh, H. Asano, J. Oyarzabal, G. Ventakaramanan, R. Lasseter, N. Hatziargyriou, and T. Green, "Real-World MicroGrids - An Overview," *IEEE*

International Conference on System of Systems Engineering, SoSE, 2007, pp. 1-8.

[32] J. Lynch, "Update on Mad River MicroGrid Project," *Consortium for Electric Reliability Technology Solutions Berkeley, Symposium on Microgrids*, U.C. Berkeley Faculty Club, Heyns Room: 2005.

[33] Resource Dynamics Corporation, *Characterization of Microgrids in the United States - Final Whitepaper*, 2005.

[34] F. Katiraei, C. Abbey, S. Tang, and M. Gauthier, "Planned islanding on rural feeders — utility perspective," *IEEE Power and Energy Society General Meeting - Conversion and Delivery of Electrical Energy in the 21st Century*, 2008, pp. 1-6.

[35] R. Fulton and C. Abbey, "Planned Islanding of 8.6 MVA IPP for BC Hydro System Reliability," *First International Conference on the Integration of RE and DERIntegration of Renewable Energy Sources and Distributed Energy Resources*, 2004, p. 9.

[36] P. Agrawal, "Overview of DOE Microgrid Activities," *Symposium on Microgrids*, Québec, Canada: 2006.

[37] C. Marnay, "Overview of Microgrid R&D in the U.S.," *Symposium on Microgrids*, Nagoya, Japan: 2007.

[38] T. Tanabe, Y. Ueda, T. Funabashi, S. Numata, K. Morino, and E. Shimoda, "An active network control method using distributed energy resources in microgrids," *13th Power Electronics and Motion Control Conference, EPE-PEMC*, 2008, pp. 2478-2480.

[39] A.L. Dimeas and N.D. Hatziargyriou, "Operation of a Multiagent System for Microgrid Control," *IEEE Transactions on Power Systems*, vol. 20, 2005, pp. 1447-1455.

[40] A.L. Dimeas and N.D. Hatziargyriou, "A MAS architecture for microgrids control," *Proceedings of the 13th International Conference on Intelligent Systems Application to Power Systems*, 2005, p. 5 pp.

[41] M. Prodanovic and T.C. Green, "High-Quality Power Generation Through Distributed Control of a Power Park Microgrid," *IEEE Transactions on Industrial Electronics*, vol. 53, 2006, pp. 1471-1482.

[42] "Laboratory Grid for Distributed Generation," *Accessed through http://www.iset.uni-kassel.de/abt/FB-A/demotec/bilder/demotec.pdf on 2010-02-12*.

[43] E. Zabala, "ANALYSIS OF THE MICROGRID AT THE TECHNOLOGY PARK OF BIZKAIA," *2nd International Conference on Integration of Renewable and Distributed Energy Resources*, Napa, CA: 2006.

[44] J.E. Nielsen, "MORE Microgrids - Demonstration sites," Dec. 2008.

[45] S.J. Chatzivasiliadis, N.D. Hatziargyriou, and A.L. Dimeas, "Development of an agent based intelligent control system for microgrids," *IEEE Power and Energy Society General Meeting - Conversion and Delivery of Electrical Energy in the 21st Century,*, 2008, pp. 1-6.

[46] G. Venkataramanan and M. Illindala, "Microgrids and sensitive loads," *Power Engineering Society Winter Meeting*, 2002, pp. 315-322, Vol.1.

[47] L. Yunwei, D.M. Vilathgamuwa, and L. Poh Chiang, "Design, analysis, and real-time testing of a controller for multibus microgrid system," *IEEE Transactions on Power Electronics*, vol. 19, 2004, pp. 1195-1204.

[48] N. Pogaku, M. Prodanovic, and T.C. Green, "Modeling, Analysis and Testing of Autonomous Operation of an Inverter-Based Microgrid," *IEEE Transactions on Power Electronics*, vol. 22, 2007, pp. 613-625.

[49] J.A. Pecas Lopes, C.L. Moreira, A.G. Madureira, F.O.A.R.F.O. Resende, X.A.W.X. Wu, N.A.J.N. Jayawarna, Y.A.Z.Y. Zhang, N.A.J.N. Jenkins, F.A.K.F. Kanellos, and N.A.H.N. Hatziargyriou, "Control Strategies for MicroGrids Emergency Operation," *International Conference on Future Power Systems*, 2005, pp. 1-6.

[50] Y. Zhao and L. Guo, "Dynamical Simulation of Laboratory MicroGrid," *Asia-Pacific Power and Energy Engineering Conference, APPEEC*, 2009, pp. 1-5.

[51] European Photovoltaic Industry Association and Greenpeace, *Solar Generation IV – 2007*, Accessed from http://www.greenpeace.org/raw/content/international/press/reports/solar-generation-iv.pdf on 2010.02.23, 2007.

[52] S. Davidson, *National Survey Report of PV Power Applications in the United Kingdom 2006*, Department for Business Enterprise and Regulatory Reform, Accessed through http://www.iea-pvpsuk.org.uk/resources/resources.shtml#status on 2010.02.24, 2007.

[53] S. Davidson, *National Survey Report of PV Power Applications in the United Kingdom 2007*, Department for Business Enterprise and Regulatory Reform, Accessed through http://www.iea-pvpsuk.org.uk/resources/resources.shtml#status

on 2010.02.24, 2008.

[54] European Photovoltaic Industry Association and Greenpeace, *Solar Generation V – 2008*, Accessed through http://www.epia.org/publications/epia-publications.html on 2010.02.24, 2008.

[55] "Photovoltaic modules," *Accesed from pvresources.com website: http://www.pvresources.com/en/module.php on 2010.02.24*.

[56] International Energy Agency, *TRENDS IN PHOTOVOLTAIC APPLICATIONS Survey report of selected IEA countries between 1992 and 2005*, Accessed via http://www.iea-pvps.org/products/rep1_15.htm on 2010.02.24, 2006.

[57] International Energy Agency, *TRENDS IN PHOTOVOLTAIC APPLICATIONS Survey report of selected IEA countries between 1992 and 2008*, Accessed via http://www.iea-pvps.org/products/rep1_18.htm on 2010.02.24, 2009.

[58] Weidong Xiao, W. Dunford, and A. Capel, "A novel modeling method for photovoltaic cells," *IEEE 35th Annual Power Electronics Specialists Conference, PESC*, 2004, pp. 1950-1956, Vol.3.

[59] T. Markvart, *Solar Electricity*, John wiley & Sons, LTD, 2003.

[60] Sanyo Energy corp., *HIT Double Brochure*, Accessed through http://us.sanyo.com/HIT-Power-Double/HIT-Double-Bifacial-Photovoltaic-Module on 2010.02.24, 2009.

[61] "Solar trackers and concentrators," *Accessed from pvsources.com website: http://www.pvresources.com/en/concentrator.php on 2010.02.24*.

[62] Chihchiang Hua and Chihming Shen, "Control of DC/DC converters for solar energy system with maximum power tracking," *23rd International Conference on Industrial Electronics, Control and Instrumentation, IECON*, 1997, pp. 827-832, Vol.2.

[63] W. Swiegers and J. Enslin, "An integrated maximum power point tracker for photovoltaic panels," *Proceedings of IEEE International Symposium on Industrial Electronics, ISIE*, 1998, pp. 40-44 vol.1.

[64] J. Enslin, M. Wolf, D. Snyman, and W. Swiegers, "Integrated photovoltaic maximum power point tracking converter," *IEEE Transactions on Industrial Electronics,*, vol. 44, 1997, pp. 769-773.

[65] M. Ayres, D. Wait, M. Weiderholt, and Truong Le, "Pholtovoltaic cell model for the International Space Station," *Conference Record of the Twenty-Eighth IEEE Photovoltaic Specialists Conference*, 2000, pp. 1301-1303.

[66] Weidong Xiao, M. Lind, W. Dunford, and A. Capel, "Real-Time Identification of Optimal Operating Points in Photovoltaic Power Systems," *IEEE Transactions on Industrial Electronics,*, vol. 53, 2006, pp. 1017-1026.

[67] Y. Yusof, S. Sayuti, M. Abdul Latif, and M. Wanik, "Modeling and simulation of maximum power point tracker for photovoltaic system," *Proceedings of National Power and Energy Conference, PECon*, 2004, pp. 88-93.

[68] E. Matagne, R. Chenni, and R. El Bachtiri, "A photovoltaic cell model based on nominal data only," *International Conference on Power Engineering, Energy and Electrical Drives, POWERENG*, 2007, pp. 562-565.

[69] F. Albuquerque, A. Moraes, G. Guimaraes, S. Sanhueza, and A. Vaz, "Optimization of a photovoltaic system connected to electric power grid," *IEEE/PES Transmission and Distribution Conference and Exposition: Latin America,*, 2004, pp. 645-650.

[70] Il-Song Kim, Myung-Bok Kim, and Myung-Joong Youn, "New Maximum Power Point Tracker Using Sliding-Mode Observer for Estimation of Solar Array Current in the Grid-Connected Photovoltaic System," *IEEE Transactions on Industrial Electronics,*, vol. 53, 2006, pp. 1027-1035.

[71] Petronio Vieira Junior, Pedro Ivan G. Palheta, Denis Marcelo B. da Silva, Miguel P. do Nascimento, Alex Ramos Costa, Pedro S. Ferreira Filho, and Jose Gilson Siqueira, "Applied Digital Control for Localization of the Maximum Power of Photovoltaic Generators," *28th Annual International Telecommunications Energy Conference, INTELEC*, 2006, pp. 1-6.

[72] D. Sera, R. Teodorescu, and P. Rodriguez, "PV panel model based on datasheet values," *IEEE International Symposium on Industrial Electronics, ISIE*, 2007, pp. 2392-2396.

[73] D. Dondi, D. Brunelli, L. Benini, P. Pavan, A. Bertacchini, and L. Larcher, "Photovoltaic cell modeling for solar energy powered sensor networks," *2nd International Workshop on Advances in Sensors and Interface, IWASI*, 2007, pp. 1-6.

[74] T. Elshatter, M. Elhagry, E. Abou-Elzahab, and A. Elkousy, "Fuzzy modeling of photovoltaic panel equivalent circuit," *Conference Record of the Twenty-Eighth IEEE Photovoltaic Specialists Conference*, 2000, pp. 1656-1659.

[75] M. Wanzeller, R. Alves, J. da Fonseca Neto, and W. Fonseca, "Current control loop for tracking of maximum power point supplied for photovoltaic array,"

IEEE Transactions on Instrumentation and Measurement,, vol. 53, 2004, pp. 1304-1310.

[76] S. Kjaer, J. Pedersen, and F. Blaabjerg, "A review of single-phase grid-connected inverters for photovoltaic modules," *IEEE Transactions on Industry Applications,*, vol. 41, 2005, pp. 1292-1306.

[77] A. Kajihara and A. Harakawa, "Model of photovoltaic cell circuits under partial shading," *IEEE International Conference on Industrial Technology, ICIT*, 2005, pp. 866-870.

[78] C. Prapanavarat, M. Barnes, and N. Jenkins, "Investigation of the performance of a photovoltaic AC module," *IEE Proceedings- Generation, Transmission and Distribution,*, vol. 149, 2002, pp. 472-478.

[79] "Shell SM110-24P photovoltaic solar module datasheet," *http://www.powerupco.com/panels/shell/Shell%20SM110-24P.pdf last accessed on 2010.02.24.*

[80] L. Castaner and S. Silvestre, *Modeliing Photovoltaic Systems using PSPice*, John wiley & Sons, LTD, 2002.

[81] A. Tariq and J. Asghar, "Development of an Analog Maximum Power Point Tracker for Photovoltaic Panel," *International Conference on Power Electronics and Drives Systems, PEDS*, 2005, pp. 251-255.

[82] T. Esram and P. Chapman, "Comparison of Photovoltaic Array Maximum Power Point Tracking Techniques," *IEEE Transactions on Energy Conversion,*, vol. 22, 2007, pp. 439-449.

[83] Abu Tariq and M. Jamil Asghar, "Development of microcontroller-based maximum power point tracker for a photovoltaic panel," *IEEEPower India Conference,*, 2006, p. 5 pp.

[84] D. Sera, T. Kerekes, R. Teodorescu, and F. Blaabjerg, "Improved MPPT Algorithms for Rapidly Changing Environmental Conditions," *12th International Power Electronics and Motion Control Conference, EPE-PEMC*, 2006, pp. 1614-1619.

[85] D. Snyman, "Centralized PV generation and decentralized battery storage for cost effective electrification of rural areas," *Proceedings of 3rd AFRICON Conference, AFRICON*, 1992, pp. 235-239.

[86] S. Yuvarajan and Shanguang Xu, "Photo-voltaic power converter with a simple maximum-power-point-tracker," *Proceedings of the International Symposium on*

Circuits and Systems, ISCAS, 2003, pp. III-399-III-402, Vol.3.

[87] Chihchiang Hua and Chihming Shen, "Study of maximum power tracking techniques and control of DC/DC converters for photovoltaic power system," *29th Annual IEEE Power Electronics Specialists Conference, PESC Record.*, 1998, pp. 86-93 vol.1.

[88] E. Koutroulis, K. Kalaitzakis, and N. Voulgaris, "Development of a microcontroller-based, photovoltaic maximum power point tracking control system," *IEEE Transactions on Power Electronics,*, vol. 16, 2001, pp. 46-54.

[89] M. Mather, M. Malengret, and J. Le Claire, "110 W low cost, efficient PV-grid interface for rural electrification," *Eighth International Conference on Power Electronics and Variable Speed Drives, (IEE Conf. Publ. No. 475)*, 2000, pp. 136-139.

[90] M. Ciobotaru, R. Teodorescu, and F. Blaabjerg, "Control of single-stage single-phase PV inverter," *European Conference on Power Electronics and Applications,*, 2005, pp. 10 pp.-P.10.

[91] Tae-Yeop Kim, Ho-Gyun Ahn, Seung Kyu Park, and Youn-Kyun Lee, "A novel maximum power point tracking control for photovoltaic power system under rapidly changing solar radiation," *Proceedings of IEEE International Symposium on Industrial Electronics, ISIE*, 2001, pp. 1011-1014 vol.2.

[92] N. Khaehintung, C. Kangsajian, P. Sirisuk, and A. Kunakorn, "Grid-connected Photovoltaic System with Maximum Power Point Tracking using Self-Organizing Fuzzy Logic Controller," *International Conference on Power Electronics and Drives Systems, PEDS*, 2005, pp. 517-521.

[93] F. Chan and H. Calleja, "Reliability: A New Approach in Design of Inverters for PV Systems," *10th IEEE International Power Electronics Congress,*, 2006, pp. 1-6.

[94] J.M. Chang, W.N. Chang, and S.J. Chung, "Single-phase grid-connected PV system using three-arm rectifier-inverter," *IEEE Transactions on Aerospace and Electronic Systems,*, vol. 42, 2006, pp. 211-219.

[95] M. Nikraz, H. Dehbonei, and C. Curtin, "Digital control of a voltage source inverter in photovoltaic applications," *IEEE 35th Annual Power Electronics Specialists Conference, PESC*, 2004, pp. 3266-3271 Vol.5.

[96] J. Myrzik and M. Calais, "String and module integrated inverters for single-phase grid connected photovoltaic systems - a review," *IEEE Bologna Power Tech*

Conference Proceedings,, 2003, p. 8 pp. Vol.2.

[97] G. Walker and P. Sernia, "Cascaded DC-DC converter connection of photovoltaic modules," *IEEE Transactions on Power Electronics,*, vol. 19, 2004, pp. 1130-1139.

[98] Yang Chen and K. Smedley, "A cost-effective single-stage inverter with maximum power point tracking," *IEEE Transactions on Power Electronics,*, vol. 19, 2004, pp. 1289-1294.

[99] R. Gonzalez, J. Lopez, P. Sanchis, and L. Marroyo, "Transformerless Inverter for Single-Phase Photovoltaic Systems," *IEEE Transactions on Power Electronics,*, vol. 22, 2007, pp. 693-697.

[100] C. Meza, D. Biel, J. Negroni, and F. Guinjoan, "Considerations on the control design of DC-link based inverters in grid-connected photovoltaic systems," *Proceedings of IEEE International Symposium on Circuits and Systems, ISCAS*, 2006, pp. 4 pp.-5070.

[101] Xiaofeng Sun, Weiyang Wu, Xin Li, and Qinglin Zhao, "A research on photovoltaic energy controlling system with maximum power point tracking," *Proceedings of the Power Conversion Conference, PCC Osaka*, 2002, pp. 822-826 vol.2.

[102] C. Meza, D. Biel, J. Negroni, and F. Guinjoan, "Boost-buck inverter variable structure control for grid-connected photovoltaic systems with sensorless MPPT," *Proceedings of the IEEE International Symposium on Industrial Electronics, ISIE*, 2005, pp. 657-662 vol. 2.

[103] E. Roman, R. Alonso, P. Ibanez, S. Elorduizapatarietxe, and D. Goitia, "Intelligent PV Module for Grid-Connected PV Systems," *IEEE Transactions on Industrial Electronics,*, vol. 53, 2006, pp. 1066-1073.

[104] N. Khaehintung, P. Sirisuk, and A. Kunakorn, "Grid-connected Photovoltaic System with Maximum Power Point Tracking using Self-Organizing Fuzzy Logic Controller," *IEEE Region 10 TENCON*, 2005, pp. 1-4.

[105] J. Alfonso-Gil, F. Gimeno-Sales, S. Segui-Chilet, S. Orts, J. Calvo, and V. Fuster, "New optimization in photovoltaic installations with energy balance with the three-phase utility," *Proceedings of the IEEE International Symposium on Industrial Electronics, ISIE*, 2005, pp. 981-987 vol. 3.

[106] K. Billings, *Switchmode Power Supply Handbook*, McGraw-Hill, 2nd Edition, 1999.

[107] A.I. Pressman, K. Billings, and T. Morey, *Switching Power Supply Design*, McGraw-Hill, 3rd Edition, 2009.

[108] N. Mohan, T.M. Undeland, and W.P. Robbins, *Power Electronics: Converters, Applications and Design*, John wiley & Sons, LTD, 1995.

[109] T. Mishima and E. Hiraki, "A Dual Voltage Power System by Battery/Supercapacitors Hybrid Configuration," *IEEE 36th Power Electronics Specialists Conference, PESC*, 2005, pp. 1845-1850.

[110] M. Cacciato, F. Caricchi, F. Giuhlii, and E. Santini, "A critical evaluation and design of bi-directional DC/DC converters for super-capacitors interfacing in fuel cell applications," *Conference Record of the IEEE 39th IAS Annual Meeting, Industry Applications Conference*, 2004, pp. 1127-1133 vol.2.

[111] Energy Networks Association, *Engineering Recommendations G83/1 - Recommendation for the connection of small-scale embedded generators (up to 16A per phase) in parallel with public low-voltage distribution networks*, Energy Networks Association, 2003.

[112] N. Pogaku, M. Prodanovic, and T.C. Green, "Inverter-based microgrids: Small-signal modelling and testing," *The 3rd IET International Conference on Power Electronics, Machines and Drives*, 2006, pp. 499-504.

[113] R.E. Best, *Phase-Locked Loops: Design, Simulation, and Applications*, McGraw-Hill, 1999.

[114] Philips Semiconductors, "HEF4046B datasheet," Philips Semiconductors, 1995, pp. 16, http://www.datasheetcatalog.org/datasheet/philips/HEF4046.pdf last accessed on 2010.03.05.

[115] "AN 177 - An overview of the phase-locked loop (PLL)," Philips Semiconductors, 1988, pp. 6, http://kitsrus.com/pdf/an177.pdf last accessed on 2010.03.05.

[116] A. Hood, "Convergence of Fixed-Point Iteration, Error Analysis," *http://www-solar.mcs.st-and.ac.uk/~lan/MT2003/Numerical/node11.html*, 01.02.2000: last accessed on 19.04.2010, .

[117] Texas Intruments, "TL783 HIGH-VOLTAGE ADJUSTABLE REGULATOR datasheet," 2008, pp. 20, http://focus.ti.com/lit/ds/symlink/tl783.pdf last accessed on 2010.03.07.

[118] Texas Intruments, "LM317 3-TERMINAL ADJUSTABLE REGULATOR datasheet," Texas Intruments, 2008, pp. 23,

http://focus.ti.com/lit/ds/symlink/lm317.pdf last accessed on 2010.03.07.

[119] National Semiconductor, "LM138/LM338 5-Amp Adjustable Regulators datasheet," National Semiconductor, 1998, pp. 16, http://www.national.com/ds/LM/LM138.pdf last accessed on 2010.03.07.

[120] LEM, "LEM Current Transducers HY 5..25-P datasheet," LEM, , pp. 2, http://www.lem.com/docs/products/hy_e.pdf last accessed on 2010.03.07.

[121] National Semiconductor, "Theory and Applications of Logarithmic Amplifiers - Application note 311," National Semiconductor, 1991, pp. 6, http://www.national.com/an/AN/AN-311.pdf last accessed on 2010.03.07.

LIST OF PUBLICATIONS

Conference papers

[1] P. Binduhewa, A. Renfrew, and M. Barnes, "MicroGrid power electronics interface for photovoltaics," *4th IET Conference on Power Electronics, Machines and Drives, PEMD 2008*, 2008, pp. 260-264.

[2] P. Binduhewa, A. Renfrew, and M. Barnes, "Ultracapacitor energy storage for MicroGrid micro-generation," *4th IET Conference on Power Electronics, Machines and Drives, PEMD*, 2008, pp. 270-274.

[3] P. Binduhewa, M. Barnes, and A. Renfrew, "Standard microsource interface for a MicroGrid," *CIRED Seminar on SmartGrids for Distribution, IET-CIRED*, 2008, pp. 1-4.

APPENDIX A

REVIEW OF LEAD ACID BATTERIES

A.1 INTRODUCTION

Unlike the large generators used in conventional power systems, microsources store very little energy internally. Therefore some form of energy storage must be integrated into a MicroGrid in order to provide additional power during transients. Pilot MicroGrids across the globe have used batteries, ultracapacitors and flywheels as their storage methods [A1-A6]. This appendix provides a review on lead acid batteries since this technology is most suited to longer term energy supply/absorption necessary for MicroGrids.

A.2 PRINCIPLE OF OPERATION

In a battery, energy is stored in the form of chemical energy [A7]. Chemical energy is converted into electrical energy during discharging and the reverse occurs in the charging mode. Figure A-1 shows the structure of a lead acid battery [A7]. There are two electrodes which are immersed in an electrolyte. A lead oxide electrode is the positive terminal while a lead electrode is the positive terminal. Sulphuric acid in water acts as the electrolyte.
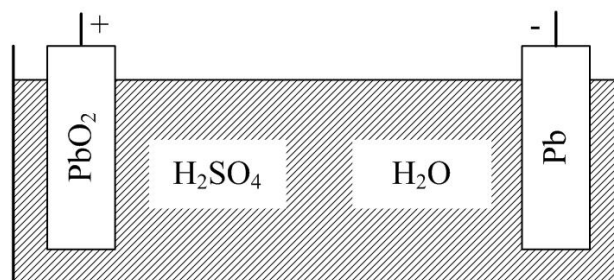
Figure A-1: Structure of a lead-acid battery

Equation A-1 presents the chemical reaction which occurs during charging and discharging of such a battery [A8, A9].

$$Pb + 2H_2SO_4 + PbO_2 \underset{\leftarrow Discharging}{\overset{Charging \rightarrow}{\Leftrightarrow}} PbSO_4 + 2H_2O + PbSO_4 \qquad \text{Equation A-1}$$
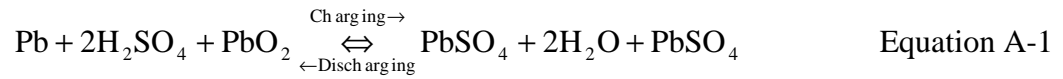
The battery starts to discharge when a load such as resistor is connected across the terminals of a battery as shown Figure A-2(a). At the negative electrode, lead reacts with sulphuric acid and produces lead sulphate, two hydrogen ions and two electrons. At the same time at the positive electrode lead oxide reacts with sulphuric acid, two hydrogen ions and electrons. As a result lead sulphate and water are produce at the positive electrode. Electrons travel through the external circuit path.

The battery starts to store energy when a power source is connected across the terminals of the battery as shown in Figure A-2(b). At the negative electrode, lead is formed from lead sulphate reacting with two electrons. At the positive electrode, lead sulphate is converted to lead oxide and two electrons are released. Sulphuric acid is formed in the process.

(a) Discharging   (b) Charging
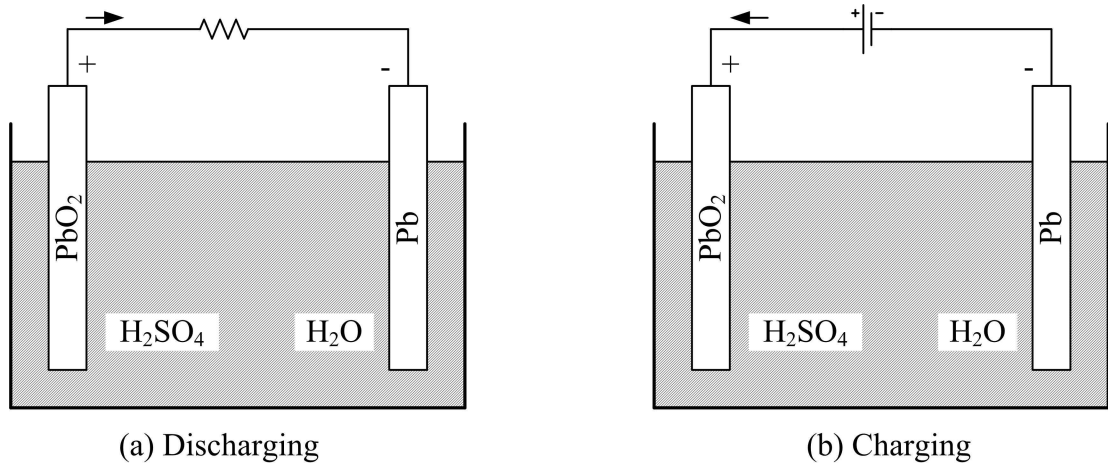
Figure A-2: Structure of a Lead acid battery [A8]

Equation A-2 presents the chemical reactions at each electrode during charging and discharging process.

Negative electrode

$$Pb \underset{discharge}{\overset{charge}{\Leftrightarrow}} Pb^{2+} + 2e$$

$$Pb^{2+} + SO_4^{2-} \underset{discharge}{\overset{charge}{\Leftrightarrow}} PbSO_4$$

Positive Electrode

$$PbO_2 + 4H^+ + 2e \underset{discharge}{\overset{charge}{\Leftrightarrow}} Pb^{2+} + 2H_2O$$

$$Pb^{2+} + SO_4^{2-} \underset{discharge}{\overset{charge}{\Leftrightarrow}} PbSO_4$$

Equation A-2
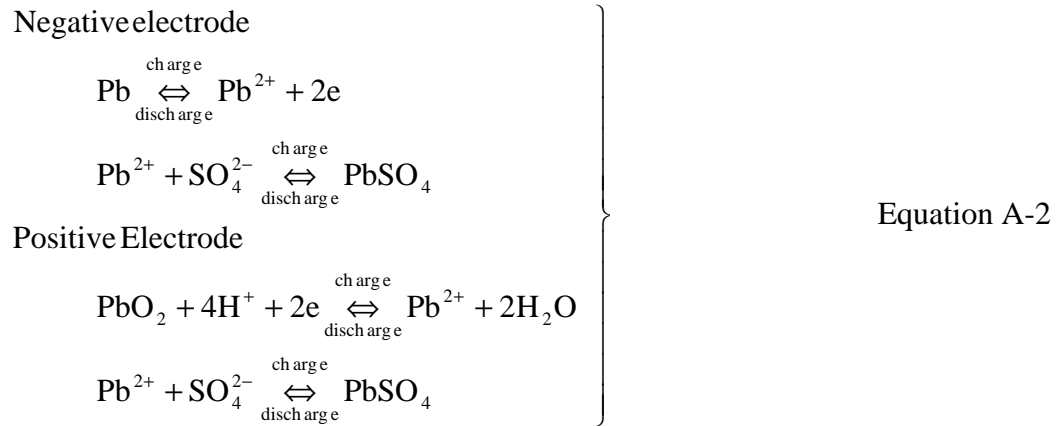
The voltage of a lead acid cell is around 2 volts [A7]. In commercial lead acid batteries a number of cells are connected is series to increase voltage. Lead acid batteries with voltages of 12V, 24V and 48V can be found in market.

A.3 CAPACITY

The capacity of a battery describes the amount of energy stored in the battery. It is usually expressed in ampere-hours and is calculated by integrating current delivered with respect to time as in Equation A-3 [A10]. Alternatively capacity is represented in Watt-hours according to Equation A-4 [A10].

$$C_{Ah} = \int_0^t I(t)dt$$

Equation A-3

$$C_{Wh} = \int_0^t E(t)I(t)dt$$

Equation A-4

The remaining stored energy depends on the ambient temperature and the amount of energy discharged from the battery. Typically rated capacity provided in datasheets corresponds to a battery at 20°C. The capacity of a battery increases with temperature. An increase of temperature to increase the capacity has a negative effect on the lifetime of the battery. Every 10°C temperature increase would result in decrease of lifetime by half. Commercial lead acid battery capacities typically vary from 0.5Ah to 210Ah [A8].

A.4 CHARACTERISTICS

A.4.1 Discharging

The discharge characteristics of a typical lead acid battery are presented in Figure A-3 and depend on the rate of discharge [A8, A10]. Usually battery discharge current is represented as a multiple of rated discharge current which is denoted by letter 'C'. Battery terminal voltage decreases as the battery starts to discharge. If the battery is discharged below the voltage specified by the manufacturer, known as deep discharge, the lifetime of the battery would be negatively affected.
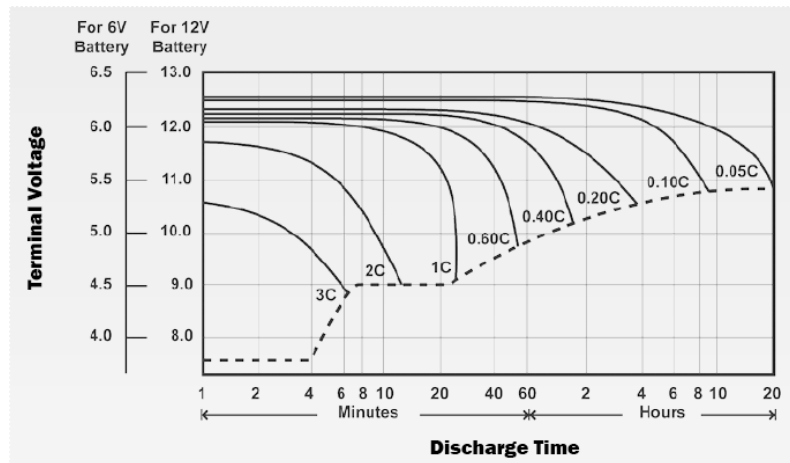
Figure A-3: Discharge characteristics

A.4.2 Open circuit voltage

The open circuit voltage of a battery is a function of energy remaining in the battery and the temperature [A8, A10]. The variation of open circuit voltage of the battery with remaining energy is presented in Figure A-4 [A11]. Under loaded conditions battery voltage may drop below the open circuit voltage, however the voltage will rise again when the load is removed.
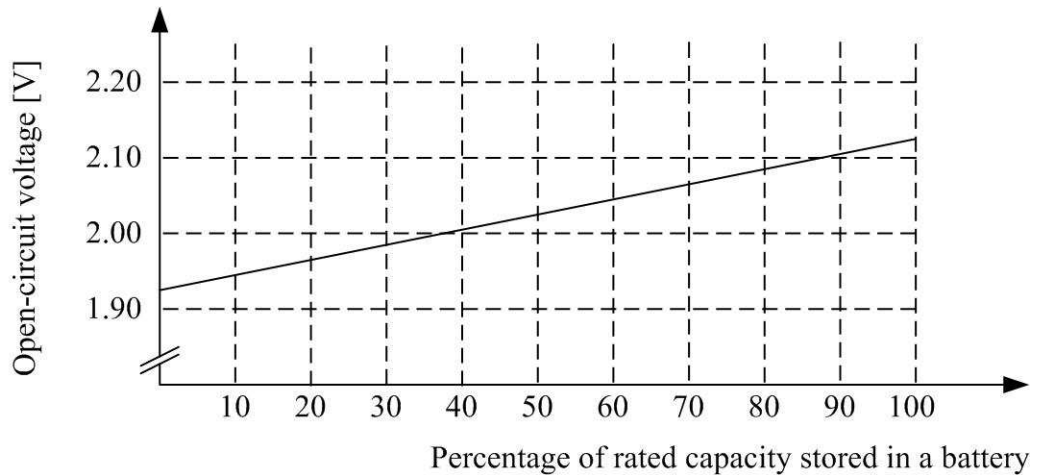
Figure A-4: Variation of open circuit voltage with energy storage in a battery

A.4.3 Internal resistance

The lower the internal resistance of a battery, the higher the discharge rates which can be achieved [A10]. This is not a constant and depends on the state of charge of the battery. It increases as the temperature decreases. Also the value is different for charging and discharging cycles. Redesigning battery geometry to decrease internal resistance is possible, but not without negatively affecting other battery properties (like lifetime).

A.4.4 Battery life

Battery life is dependent on the discharge level over the cycles it is used. In an application where the battery is discharged for a small percentage, the number of charge/discharge cycles which can be achieved is higher. On the other hand the number of charge/discharge cycles is minimal if the battery is fully discharged and charged every cycle. Operating temperature also affects the life time of a battery.

A.4.5 Self-discharge

A battery undergoes self-discharge when it is not in use. The rate of self-discharge depends on the temperature of the battery and battery discharge is higher as the temperature increases [A8, A10]. Therefore it is important to recharge the battery regularly to avoid complete discharge of the battery.

A.5 CHARGING TECHNIQUES

The desirable performance and the life time of a battery depend on the charging technique. Several charging methods are adopted for lead acid batteries namely constant voltage, constant current, taper charging and boost charging.

The output voltage of the battery is kept constant in the constant voltage method and this is also known as float charging [A8, A10]. This method is used for many applications. Figure A-5 shows the voltage and the current waveforms of battery under constant voltage charge. Initially the battery takes a higher current which is limited by the maximum output current of the power source. During this stage the power source may not be constant voltage. Then current flowing into the battery is reduced and a constant voltage is applied to the battery. Initial charging current determines the time taken to for the battery voltage to be constant. Over-discharged batteries may not be able to charge using this method.
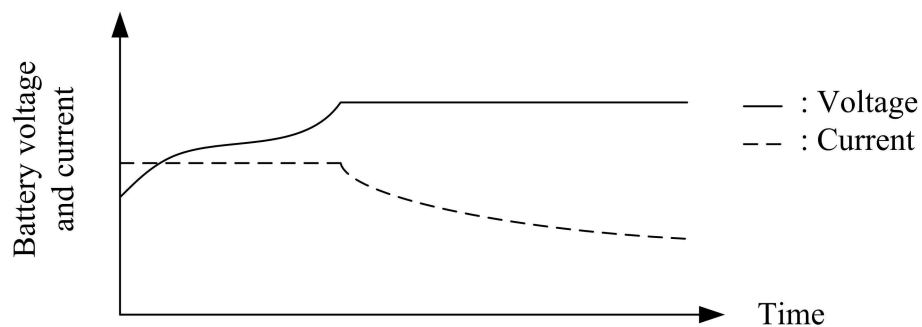

Figure A-5: Voltage and current variation of a battery during constant voltage charging

In the constant current charging technique, the charging current controlled [A8, A10]. This method is useful for charging batteries which have not been used for long periods. Since the voltage is uncontrolled, this method is not suitable for general usage. Charging batteries in parallel using constant current charging is not suitable as current distribution cannot be controlled [A8, A10]. Overcharging should be avoided by measuring the voltage or limiting charge time. In order to keep the battery fully charged, the battery can be charged at a very small rate. Then it is known as trickle charging [A10].

Taper charging is an inexpensive method used for charging a battery. The variation of charging current and voltage are presented in Figure A-6 and the reason for the name 'taper charging' can be deduced by looking at the characteristic curves [A8, A10]. In this method, current is controlled by the external resistor connected to the battery.
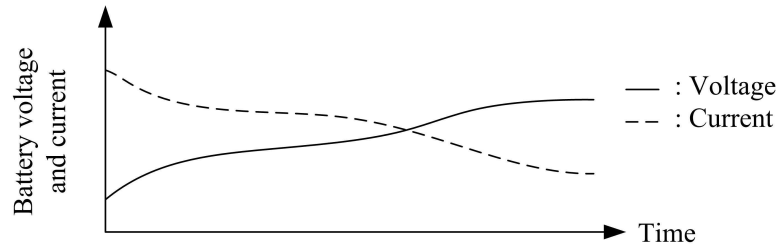

Figure A-6: Variation of voltage and current during charging

A.6 MODELLING OF BATTERIES

Electrical models of batteries are important to conduct computer based simulations. Over the years different battery models have been proposed from simple to more detailed [A12-A18]. More accurate representations of a battery can be obtained from more complex models. However unnecessary complexity should be avoided – the most suitable model should therefore be chosen.

The simplest form of representation is an ideal voltage source in series with impedance as shown in Figure A-7 [A6,A12,A19-A20]. The voltage of the ideal voltage source is equal to the open circuit voltage of the battery which is dependent on its state of charge. Impedance is represented by a resistor which represents the internal resistance [A6]. Internal resistance is not a constant. This model does not represent the characteristics explicitly as the variables do not represent the exact values over the characteristic curve. In [19], an extended model is presented where the internal resistance varies with the state of charge.
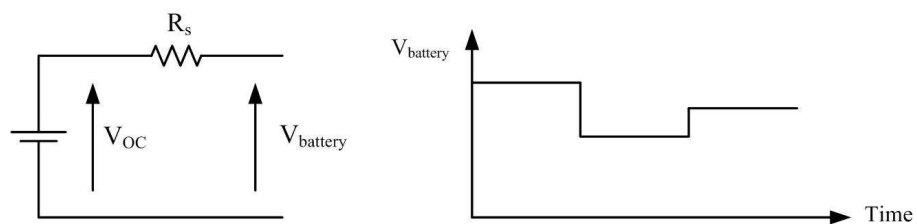

Figure A-7: Simplest battery equivalent circuit

The Thevenin equivalent battery model is presented in Figure A-8 which comprises a voltage source, two resistors and a capacitor [A9, A12, A18-A19]. A voltage source (V_{OC}) represents the open circuit voltage of the battery while the internal resistance of the battery is represented by the resistor R_{bs}. The capacitance C_b represents the effect of the larger initial current one gets from a battery. According to [A19], contact resistance between the electrolyte and plate is represented by the resistor R_b. The resistor in parallel to voltage source R_{bp} represent the self discharge of the battery. Similar to earlier models, the components of this model are also dependent on the history and operating conditions of the battery [A18]. In some cases the parallel resistor and capacitor are neglected and then the model is more suitable for short term discharge applications [A18]. The resistances are different for charging and discharging mode. The model presented in Figure A-9 enables the use of separate resistor values with the aid of ideal diodes.
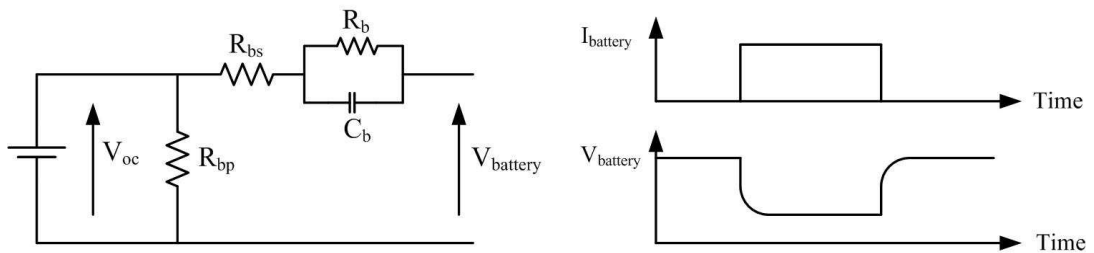

Figure A-8: Thevenin's equivalent circuit of a battery
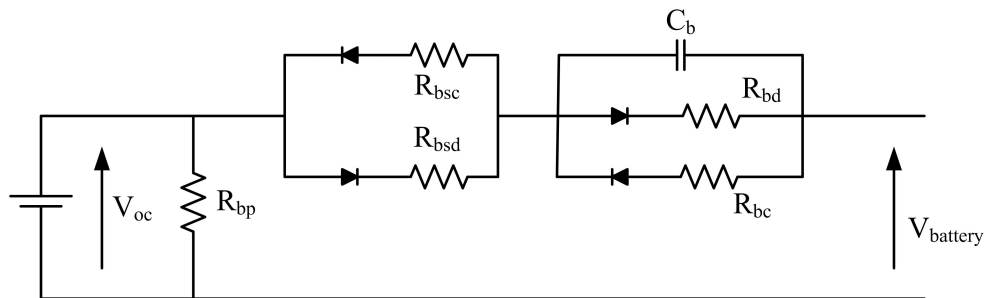
Figure A-9: Modified thevinin's equivalent circuit of a battery

Figure A-10 represents the model presented in [A15-A16]. In this model a capacitor is used instead of a voltage source. The resistance parallel to the capacitor again represents the self discharge of a battery. An extension of this is presented in [A9] which uses two separate resistor values for charging and discharging modes.
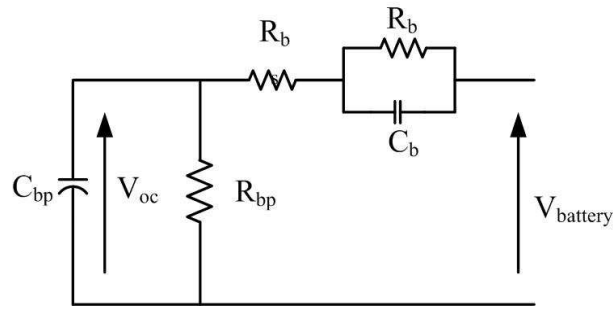
Figure A-10: Lead-acid battery electrical model

A.7 SELECTION OF BATTERIES

The selection of batteries depends on several factors: type of battery, voltage, load current, load current profile, duty cycle, temperature requirements, charge –discharge cycle, safety and reliability, and cost. The capacity of the storage is an important parameter thus the designer should calculate the necessary ampere-hours for the application. The maximum charging and maximum discharging currents are also need to calculate and the datasheets of a battery provide the maximum charging and discharging currents of a battery. The voltage rating of the battery also needs to be considered. The battery voltage varies between limits at fully charged level and discharged level. The discharge level should be select appropriately.

A.8 SUMMARY

In this chapter, the principles of operation of a lead acid battery are reviewed. Further the major characteristics are introduced. Constant voltage, constant current and trickle charging are main charging techniques used to charge a battery. In the literature it is possible to find wide variety of electrical models for a lead acid battery. The simplest model is the fixed voltage source which does not provide any transient characteristics. Complex models may be more accurate however the user needs to perform specific tests to find out the required parameters. For this study a voltage source model was selected based on the simplicity.

A.9 REFERENCES

[A1] M. Barnes, A. Dimeas, A. Engler, C. Fitzer, N. Hatziargyriou, C. Jones, S. Papathanassiou, and M. Vandenbergh, "MicroGrid Laboratory Facilities,"

International Conference on Future Power Systems, 2005, pp. 1-6.

[A2] T. Funabashi and R. Yokoyama, "Microgrid field test experiences in Japan," *IEEE Power Engineering Society General Meeting*, 2006, p. 2 pp.

[A3] A. Yokoyama, "Overview of Microgrid R&D in Japan," *Symposium on MicroGrids*, University of California, San Diego: 2009.

[A4] Y. Kojima, M. Koshio, S. Nakamura, H.A.M.H. Maejima, Y.A.F.Y. Fujioka, and T.A.G.T. Goda, "A Demonstration Project in Hachinohe: Microgrid with Private Distribution Line," *IEEE International Conference on System of Systems Engineering, SoSE*, 2007, pp. 1-6.

[A5] A. Denda, "Shimizu's Microgrid Research Activities," *Symposium on Microgrids*, Canada, 2006: http://der.lbl.gov/new_site/2006microgrids_files/Japan/Presentation_6_Atsushi_denda.pdf access on 2010.02.11, .

[A6] G. Venkataramanan and M. Illindala, "Microgrids and sensitive loads," *Power Engineering Society Winter Meeting*, 2002, pp. 315-322, Vol.1.

[A7] M. Anderson and D. Carr, "Battery energy storage technologies," *Proceedings of the IEEE*, vol. 81, 1993, pp. 475-479.

[A8] POWER-SONIC, *Sealed Lead-Acid Batteries Technical Manual*, http://www.power-sonic.com/index.php?id=98 last accessed on 2010.02.15: Power-Sonic Corporation, .

[A9] Z. Salameh, M. Casacca, and W. Lynch, "A mathematical model for lead-acid batteries," *IEEE Transactions on Energy Conversion,*, vol. 7, 1992, pp. 93-98.

[A10] D. Berndt, *Maintenance-Free Batteries Lead-Acid, Nickel/Cadmium*, Research Studies Press LTD and John Wiley & Sons Inc, 2nd Edition, 1997.

[A11] D. Linden, *Handbook of Batteries*, McGraw-Hill, 2nd edition, 1999.

[A12] Min Chen and G. Rincon-Mora, "Accurate electrical battery model capable of predicting runtime and I-V performance," *IEEE Transactions on Energy Conversion,*, vol. 21, 2006, pp. 504-511.

[A13] Shuo Pang, J. Farrell, Jie Du, and M. Barth, "Battery state-of-charge estimation," *Proceedings of the American Control Conference*, 2001, pp. 1644-1649 vol.2.

[A14] M. Glavin, P. Chan, S. Armstrong, and W. Hurley, "A stand-alone photovoltaic supercapacitor battery hybrid energy storage system," *13th Power Electronics and Motion Control Conference, EPE-PEMC*, 2008, pp. 1688-1695.

[A15] Jie Zeng, Buhan Zhang, Chengxiong Mao, and Yunling Wang, "Use of Battery Energy Storage System to Improve the Power Quality and Stability of Wind Farms," *International Conference on Power System Technology, PowerCon*, 2006, pp. 1-6.

[A16] M. Casacca and Z. Salameh, "Determination of lead-acid battery capacity via mathematical modeling techniques," *IEEE Transactions on Energy Conversion,*, vol. 7, 1992, pp. 442-446.

[A17] G. Tina and G. Capizzi, "Improved lead -acid battery modelling for photovoltaic application by Recurrent Neural Networks," *International Symposium on Power Electronics, Electrical Drives, Automation and Motion, SPEEDAM*, 2008, pp. 1170-1174.

[A18] C. Zhan, X. Wu, S. Kromlidis, V. Ramachandaramurthy, M. Barnes, N. Jenkins, and A. Ruddell, "Two electrical models of the lead-acid battery used in a dynamic voltage restorer," *IEE Proceedings Generation, Transmission and Distribution,*, vol. 150, 2003, pp. 175-182.

[A19] M. Dᵣrr, A. Cruden, S. Gair, and J. McDonald, "Dynamic model of a lead acid battery for use in a domestic fuel cell system," *Journal of Power Sources*, vol. 161, Oct. 2006, pp. 1400-1411.

[A20] M. Ceraolo, "New dynamical models of lead-acid batteries," *IEEE Transactions on Power Systems,*, vol. 15, 2000, pp. 1184-1190.

APPENDIX B

## SIMULATION MODEL OF THE PHOTOVOLTAIC PANEL

Figure B-1 presents the MATLAB code used to find the ideality factor the photovoltaic panel. The results shown in Chapter 5 are based on this code.

```
clc;
clear all;

% Find ideality factor

% Model no: SM 110-24P
% Brand: Shell

% Data

N = 72; % No of cells in series
Pmpp = 110; % Power at MPP in W
Vmpp = 35.0; % Voltage at MPP in V
Impp = 3.15; % Current at MPP in A
Voc = 43.5; % Open-circuit voltage in V
Isc = 3.45; % Short-circuit current in A

k = 1.38*10^-23; % Boltzmann's contant
T = 298 % Temperature in K at 25C
q = 1.6*10^-19 % Charge of electron

Vocpc = Voc/N; % Open circuit voltage per cell in V
Vmpppc = Vmpp/N; % Votlage at MPP per cell in V
Iph = Isc; % Photocurrent in A

i = 0;

for A =1:0.005:2
    i=i+1;
    B(i)=A;
    Vt=A*k*T/q; % Thermal Voltage
    Isat = Iph/(exp(Vocpc/Vt)-1); % Saturation current
    Rs = (Vt/Impp)*log((Iph+Isat-Impp)/Isat) - (Vmpppc/Impp); % Series resistance
    Y(i)=Rs;
    W = -((Isat/Vt)*exp((Vmpppc+Impp*Rs)/Vt))/(1+(Isat*Rs/Vt)*exp((Vmpppc+Impp*Rs)/Vt));
    % dI/dV @ MPP
    X(i)= abs(W+Impp/Vmpppc); % |dI/dV + I/V| @ MPP
end

subplot(2,1,1);plot(B,X) % |dI/dV + I/V| @ MPP with ideality factor
subplot(2,1,2);plot(B,Y) % Rs with ideality factor
```

Figure B-1: MATLAB code used to find the ideality factor

Simulation model of the photovoltaic emulator connected to a resistor is shown in Figure B-2. The inputs the photovoltaic emulator are irradiance and temperature. Figure B-3 and Figure B-4 presents the simulation model of photovoltaic panel with and without the inductor in series with the controllable voltage source. The output current of the voltage source is fed back to the controller. Photocurrent, open circuit voltage, thermal voltage and diode saturation current are calculated from the inputs according to the equations presented in Chapter 5. Then the characteristic equation is implemented.
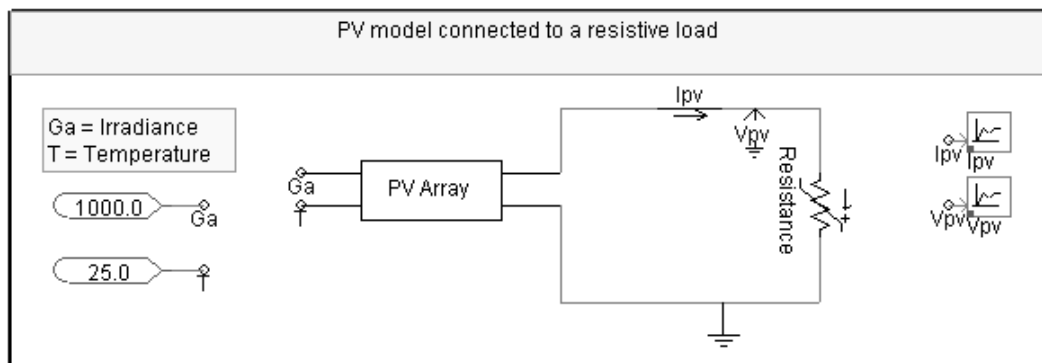
Figure B-2: Screen capture of the simulation model of the photovoltaic panel
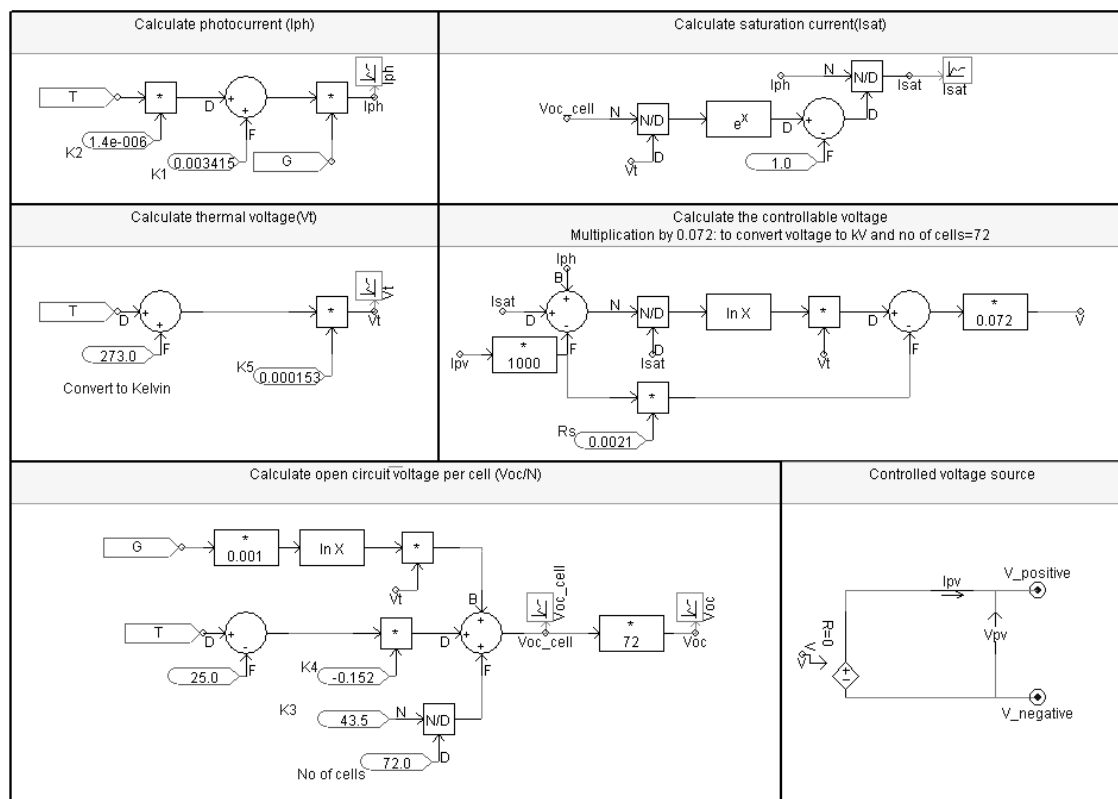
Figure B-3: Screen capture of the simulation model of the photovoltaic panel purely based on the characteristic curve
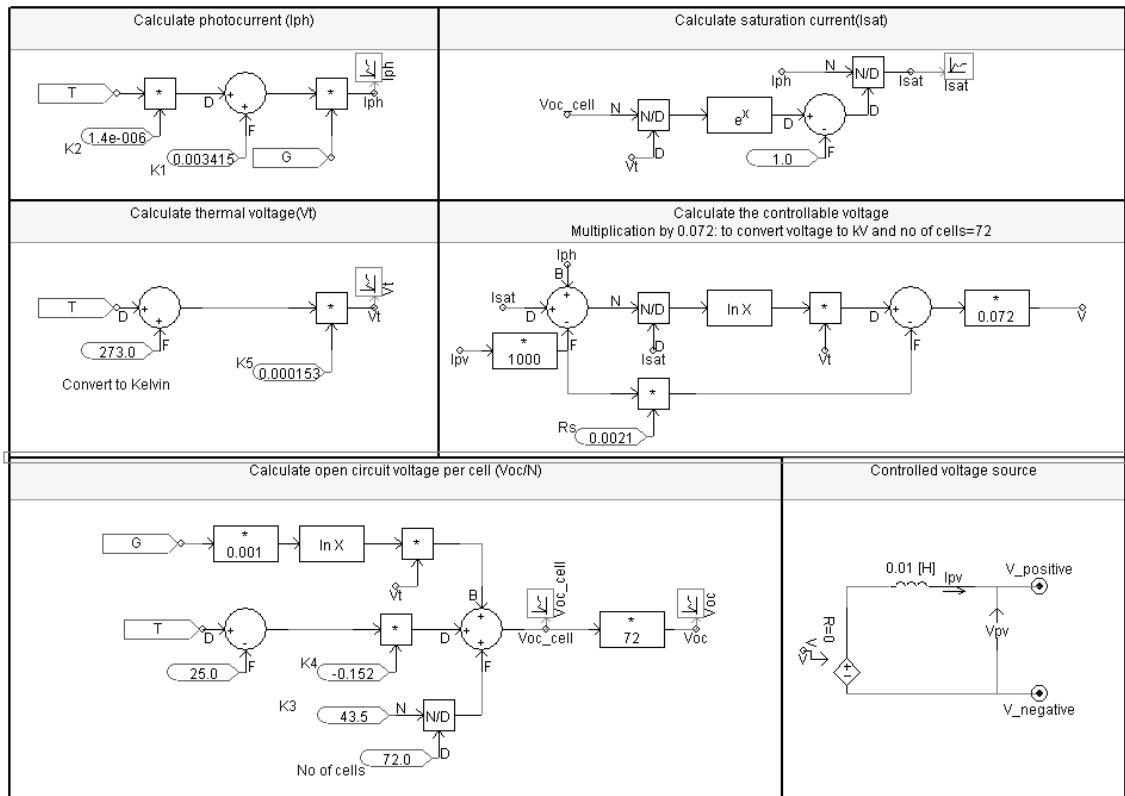
Figure B-4: Screen capture of the simulation model of the photovoltaic panel with inductor in series with voltage source

APPENDIX C

DETAILED RESULTS OF OPEN LOOP TESTING OF POWER ELECTRONIC CONVERTERS

C.1 INTRODUCTION

This appendix presents the detailed results of the power electronic converters used in the proposed when tested under open loop condition. The results presented in Chapter 6 are omitted.

C.2 DC-DC CONVERTER

Figure C-1 shows the schematic diagram of the modified forward dc-dc converter topology. The switches (Q_1 and Q_2) are turned on simultaneously and the energy is transferred to the secondary winding of the transformer during the on-state of the switches. Stored energy in the inductor is released to the load during the turn-off period though the diode D_4.
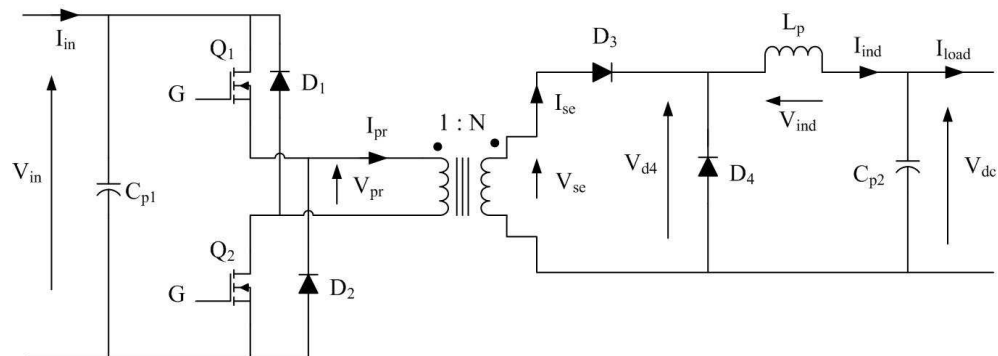

Figure C-1: Schematic diagram of the modified forward dc-dc converter

A screen capture of the simulation model of the modified forward dc-dc converter is shown in Figure C-2. The Pulse Width Modulation (PWM) signal is generated by comparing a triangular signal with a dc reference signal.
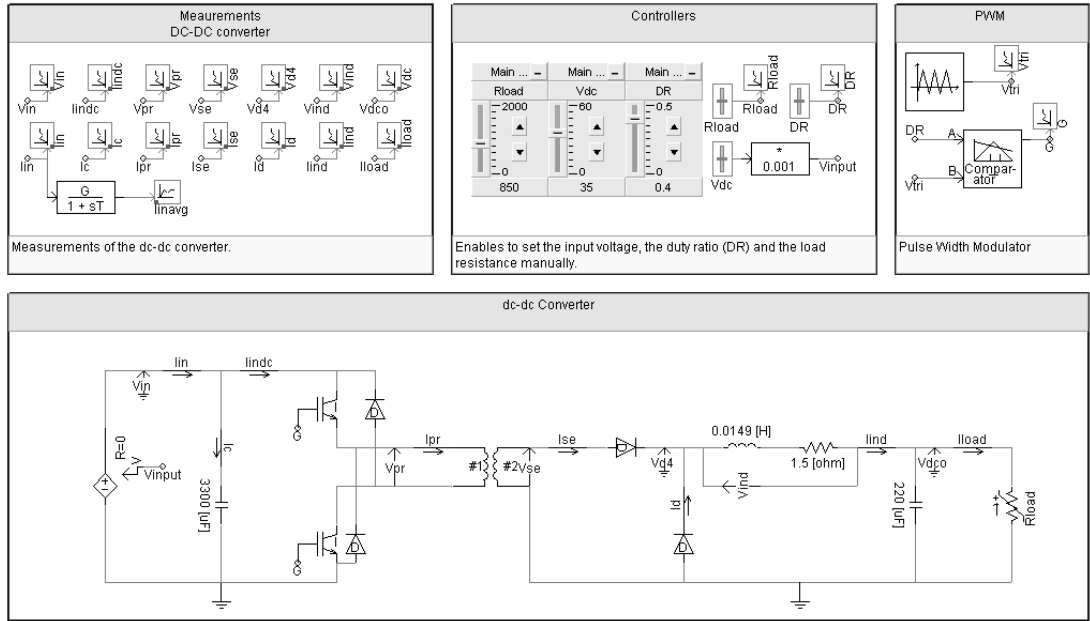
Figure C-2: Screen capture of the simulation model of the modified forward dc-dc converter

C.2.1 Detailed results of open loop testing

The voltage across the primary and the secondary winding of the transformer are shown in Figure C-3. As a result of the stray inductance and capacitance of transformer, high frequency oscillations are visible in voltages at the turn on transient. The magnetising current is fed into the supply through the diodes during the turn off period. Thus the voltage across the primary and secondary becomes negative.

(a) Simulation   (b) Experiment
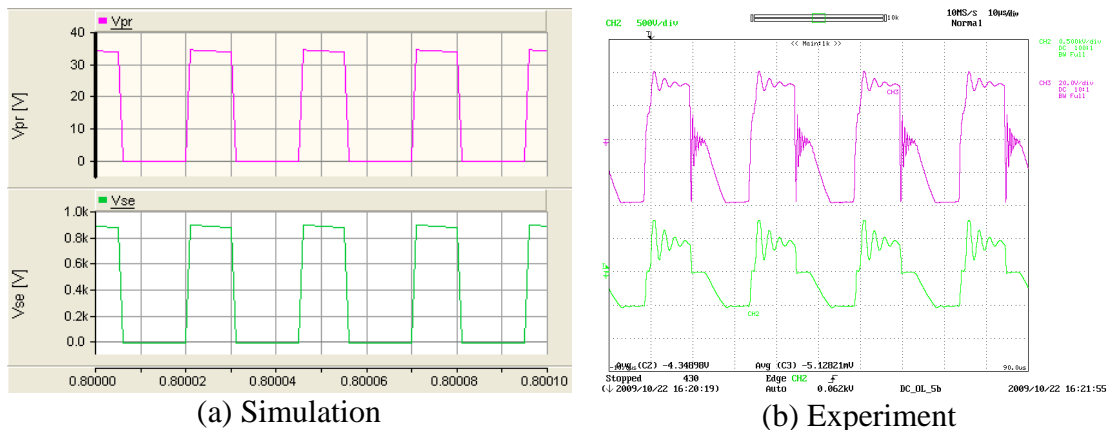
Y axis :V_{pr} – Pink (10V/div-simulation, 20V/div-Experimental), V_{se} – Light green (200V/div-Simulation, 500V/div-Experimental) ; X axis: Time (10µs/div)

Figure C-3: Voltage across the primary and the secondary of the transformer of the modified forward dc-dc converter

Figure C-4 shows the voltage across the diode D_4 and the current flowing through the inductor. Diode D_4 acts as a freewheeling path for the inductor current during off state of the switches. Thus the voltage across the diode becomes zero and the inductor current starts to decay.

(a) Simulation	(b) Experiment
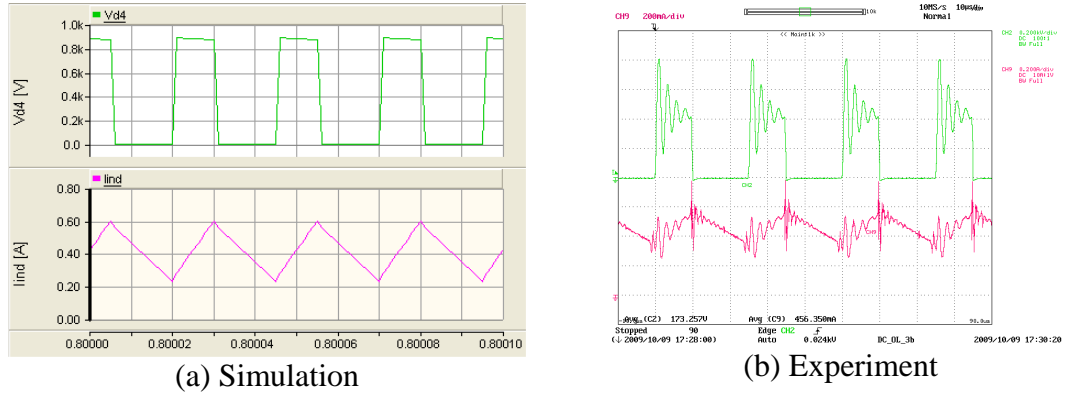
Y axis : V_{D4} - Green (200V/div-simulation, 400V/div-Experiment), I_{ind} - Pink (0.2A/div) ; X axis: Time (10µs/div)

Figure C-4: Voltage across the diode D_4 and the current flowing through the inductor of the modified forward dc-dc converter

C.3 BI-DIRECTIONAL DC-DC CONVERTER

C.3.1 Open loop testing of bi-directional dc-dc converter

C.3.1.1 Step-up mode

The test set-up for the bi-directional dc-dc converter is presented in Figure C-5. A voltage source was connected to the low-voltage end of the converter while a resistive load was connected to the high voltage end of the converter.
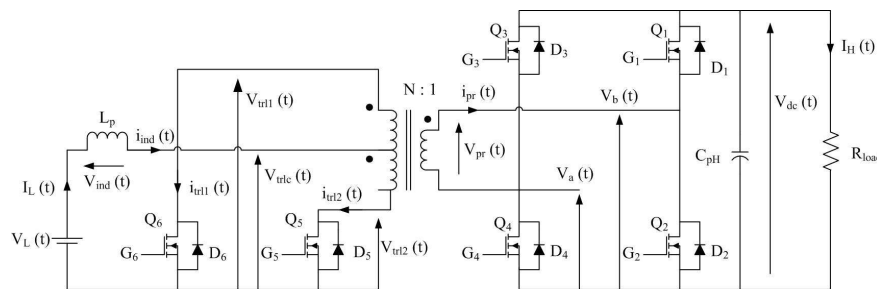

Figure C-5: Test set-up used to the operation of the step-up mode of the bi-directional converter

Figure C-6 presents the screen capture of the simulation model of the bi-directional dc-dc converter used for step-up mode testing. Further the Pulse Width Modulator (PWM) and signal extractor is presented in Figure C-7.
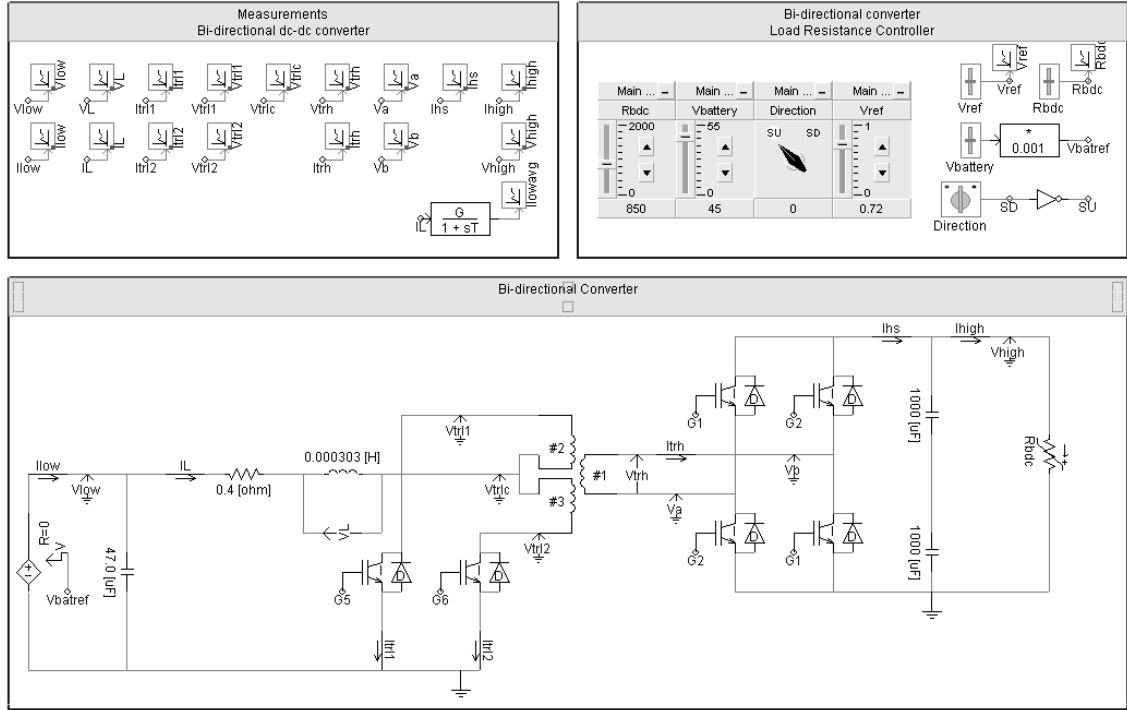

Figure C-6: Screen capture of the simulation model of the bi-directional dc-dc converter in step-up mode
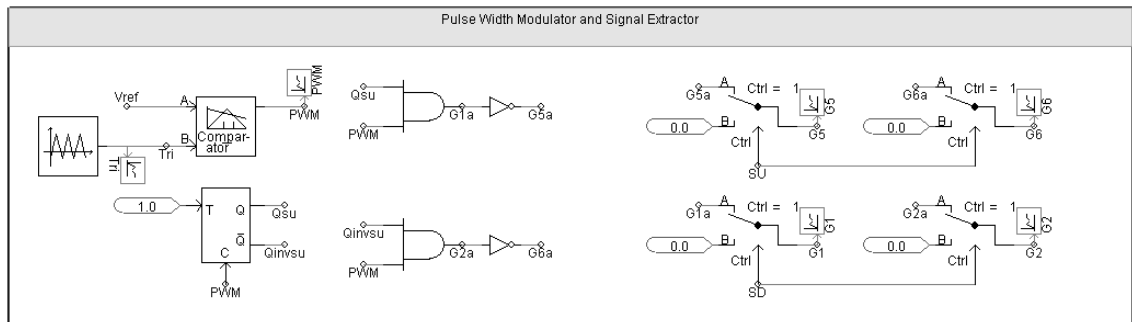

Figure C-7: PWM generator and signal extractor used to test the step-up mode

The voltage at the centre of the low voltage side windings of the transformer and the current flowing through the inductor are shown in Figure C-8. The voltage at the centre of the low voltage side windings becomes zero when both switches are turned off. Thus the current flowing through the inductor linearly increases.

<table>
<tr><td>(a) Simulation</td><td>(b) Experiment</td></tr>
</table>
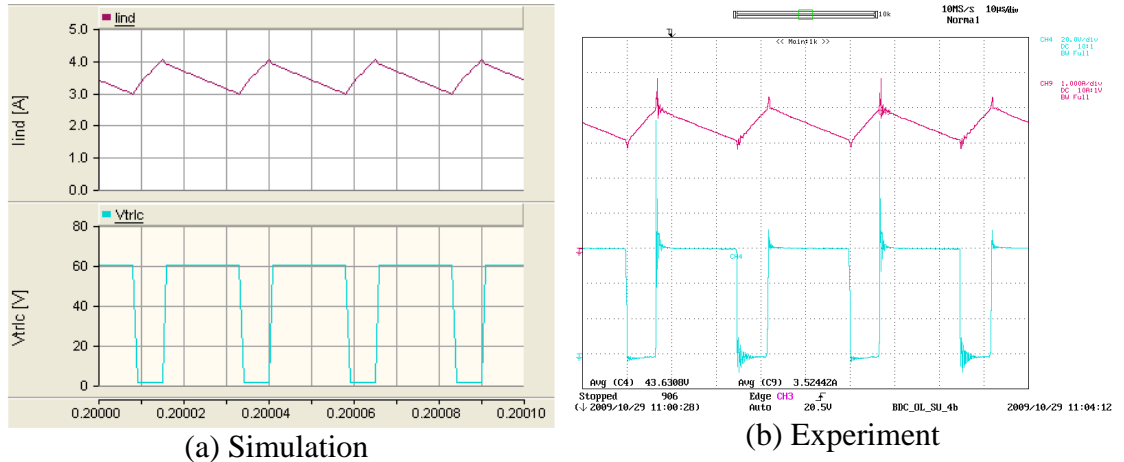
Y axis :I_L – Light brown (1A/div), V_{trlc} – Light blue (20V/div) ; X axis: Time (10µs/div)

Figure C-8: Voltage at the centre of the transformer and current flowing through the inductor of the bi-directional converter (step-up mode)

The currents flowing through the low voltage side windings and the high voltage side winding are presented in Figure C-9. Energy is stored in the inductor when both the switches are turned on and during this period the low voltage side windings share the inductor current. The high voltage side winding conducts only when a switch is turned off. The direction of the current flowing through the high voltage side winding alternates in adjacent switching cycles.


<table>
<tr><td>(a) Simulation</td><td>(b) Experiment</td></tr>
</table>
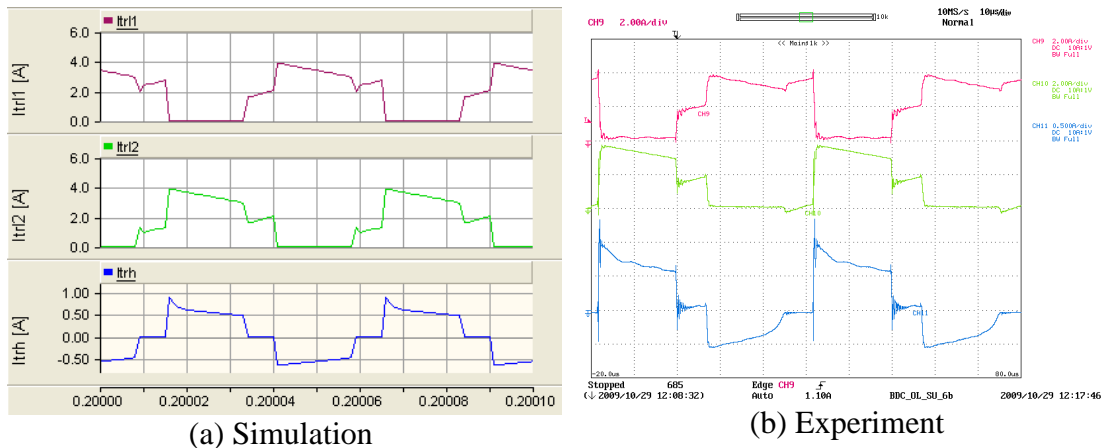
Y axis :I_{trl1} – Light brown (2A/div), I_{trl2} – Light green (2A/div), I_{trh}– Light blue (0.5A/div) ; X axis: Time (10µs/div)

Figure C-9: Current flowing through the windings of the transformer of the bi-directional converter (step-up mode)

The drain to source voltage (V_{ds}) across the switches Q_2, Q_4, Q_5 and Q_6 are presented in Figure C-10. V_{ds} of switches Q_5 and Q_6 becomes zero when they are turned on. Since

248

energy is not transferred both switches are turned on, and V_{ds} of Q_2 and Q_4 would be half the high voltage side voltage. V_{ds} of Q_2 and Q_4 becomes either zero or output voltage when either Q_5 or Q_6 turn off.

| (a) Simulation | (b) Experiment |
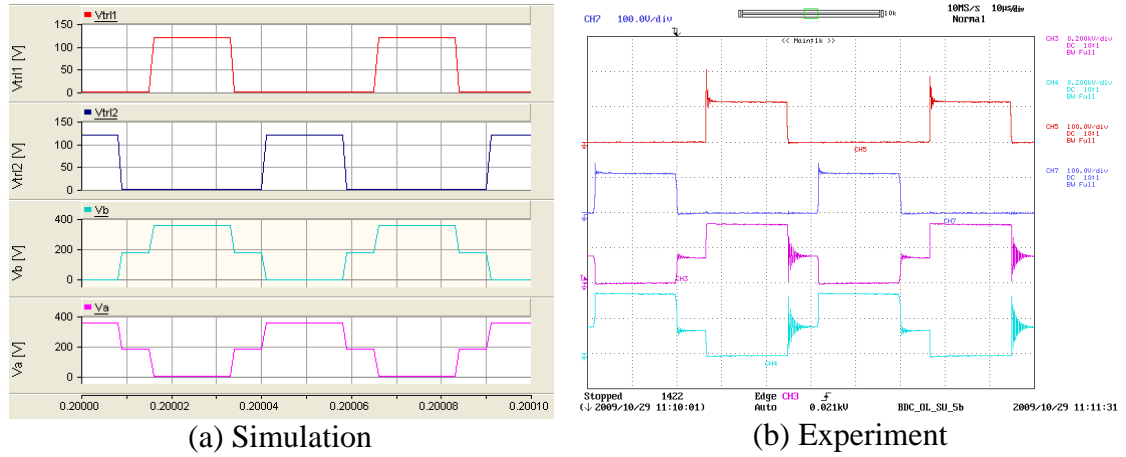
Y axis : V_{trl1} – Light brown (50V/div-Simulations, 100V/div-Experiment), V_{trl2} – Dark blue (50V/div-Simulations, 100V/div-Experiment), V_a – Pink (200V/div), V_b – Light blue (200V/div); X axis: Time (10µs/div)

Figure C-10: Voltage across switches Q_2, Q_4, Q_5 and Q_6 of the bi-directional converter (step-up mode)

C.3.1.2 Step-down mode

The test set-up for the step-down mode testing of the bi-directional dc-dc converter is presented in Figure C-11. Figure C-12 presents the screen capture of the simulation model of the bi-directional dc-dc converter used to test the step-down mode. Figure C-13 shows the PWM generator and the signal extractor.
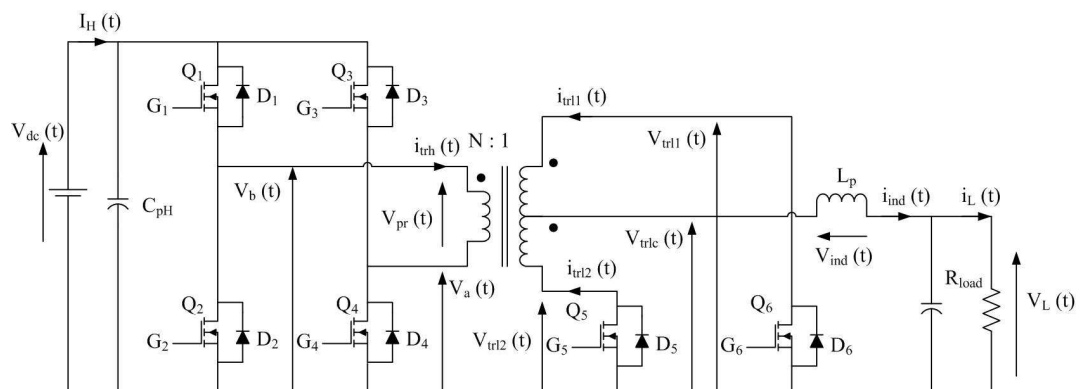

Figure C-11: Test set-up used to test the operation of the step-down mode of the bi-directional dc-dc converter

249
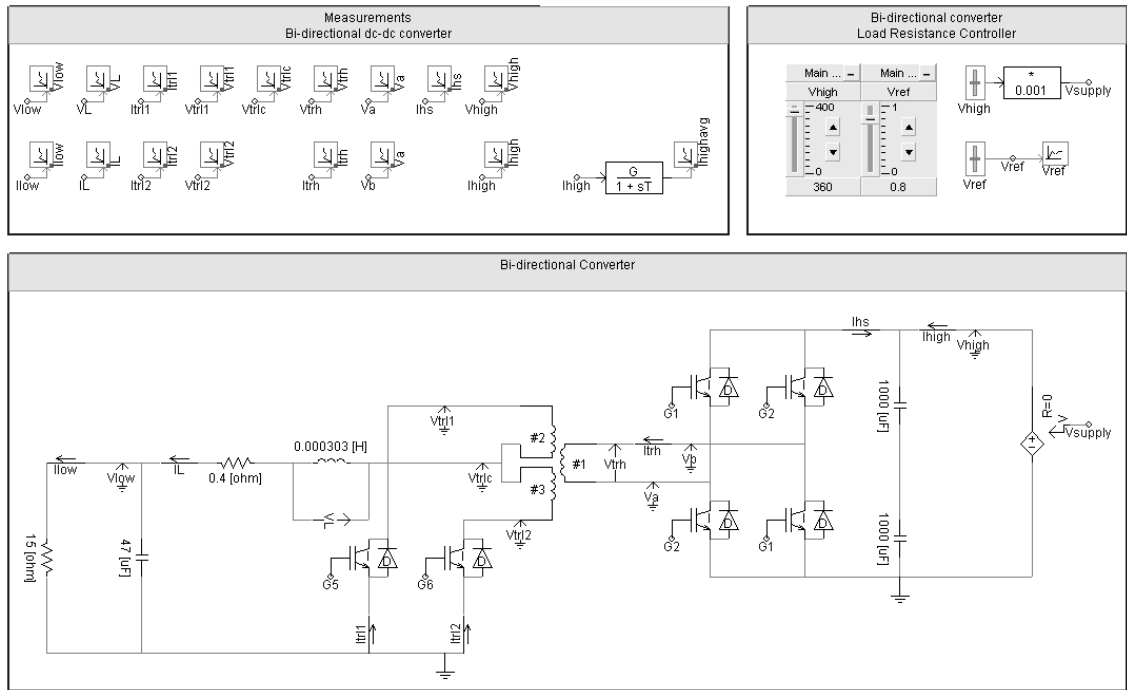
Figure C-12: Screen capture of the simulation model of the bi-directional dc-dc converter operating in step-down mode
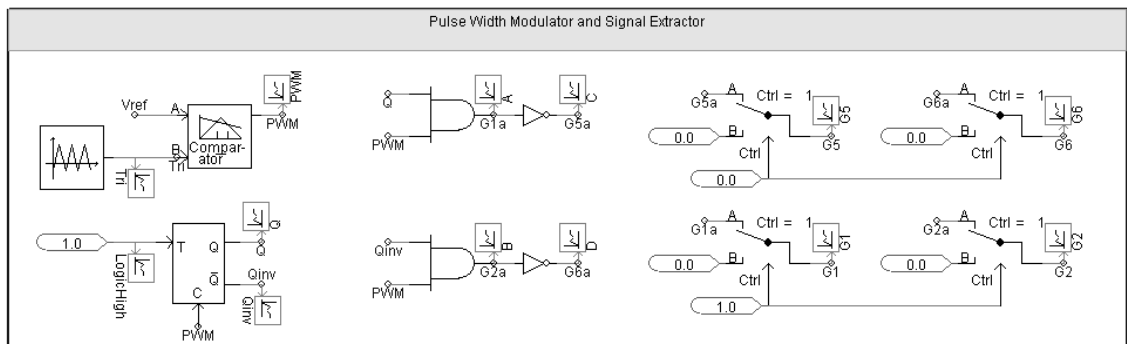

Figure C-13: PWM generator and signal extractor used in the step-down mode of the bi-directional dc-dc converter

The drain to source voltage (V_{ds}) of switches Q_2, Q_4, Q_5 and Q_6 are presented in Figure C-14. When all the switches are turned off, V_{ds} of switches Q_2 and Q_4 are equal to the half of the supply voltage. Energy is only transferred when switches are turned on.

(a) Simulation   (b) Experiment
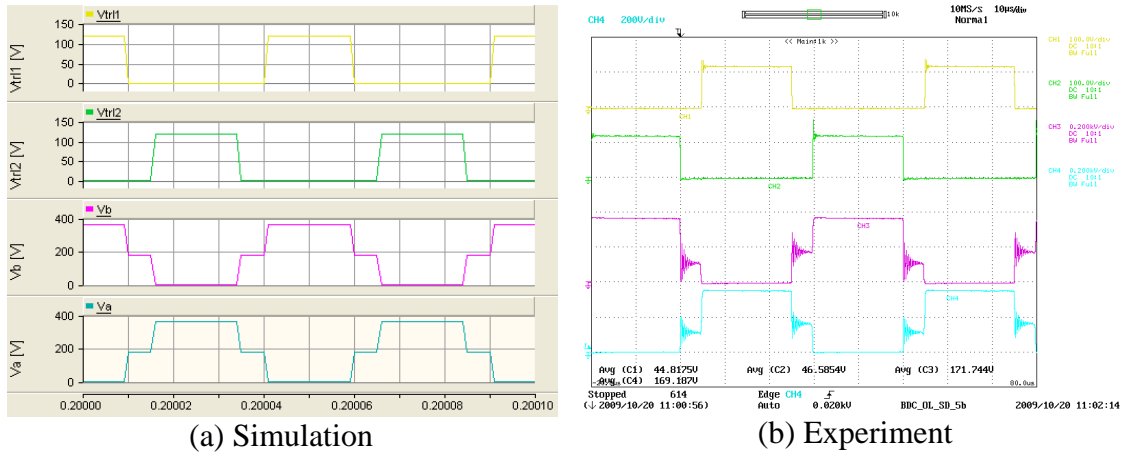
Y axis :V$_{trl1}$ – Light yellow (50V/div-simulations, 100V/div-Experiment), V$_{trl2}$ – Green (50V/div-simulations, 100V/div-Experiment), V$_a$ – Pink (200V/div), V$_b$ – Light blue (200V/div); X axis: Time (10µs/div)

Figure C-14: Voltage across the primary and secondary windings of the bi-directional dc-dc converter (step-down mode)

Currents flowing through the low-voltage and high-voltage side windings are shown in Figure C-15. The high voltage side winding conducts during every on-state of the switches however the direction of current flow changes in adjacent on-states. Low-voltage side windings conduct alternately during on states. During the off-state the low-voltage side windings share the currents.

(a) Simulation   (b) Experiment
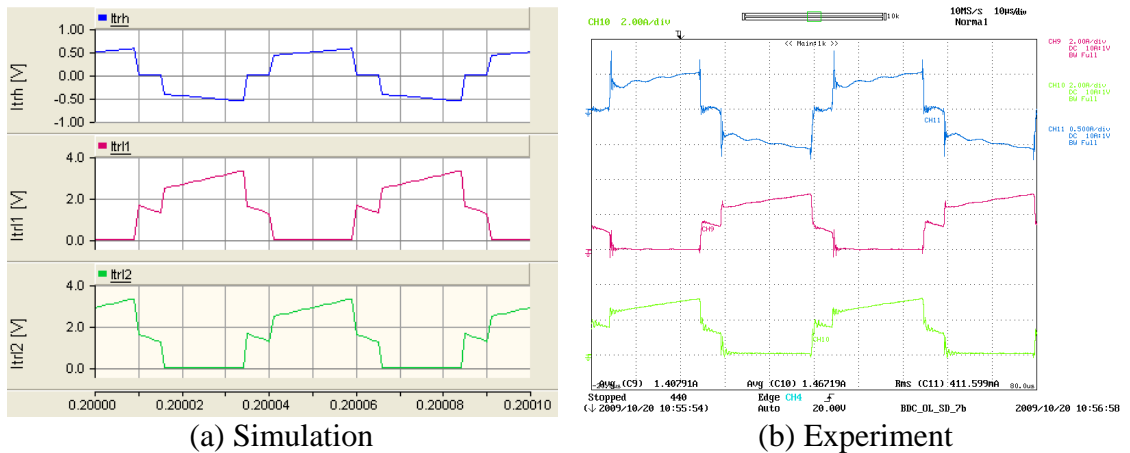
Y axis :I$_{trh}$ – Blue (0.5A/div), I$_{trl1}$ – Brown (2A/div), I$_{trl2}$ – Green (2A/div); X axis: Time (10µs/div)

Figure C-15: Currents flowing through the windings of the transformer of the bi-directional dc-dc converter (step-down mode)

The voltage at the centre of the low-voltage side winding and the current flowing through the inductor are shown in Figure C-16. Inductor current increases when the

voltage at the centre of winding is positive. The inductor current decreases when the voltage at the centre of the windings is zero.

<div style="text-align:center">(a) Simulation   (b) Experiment</div>
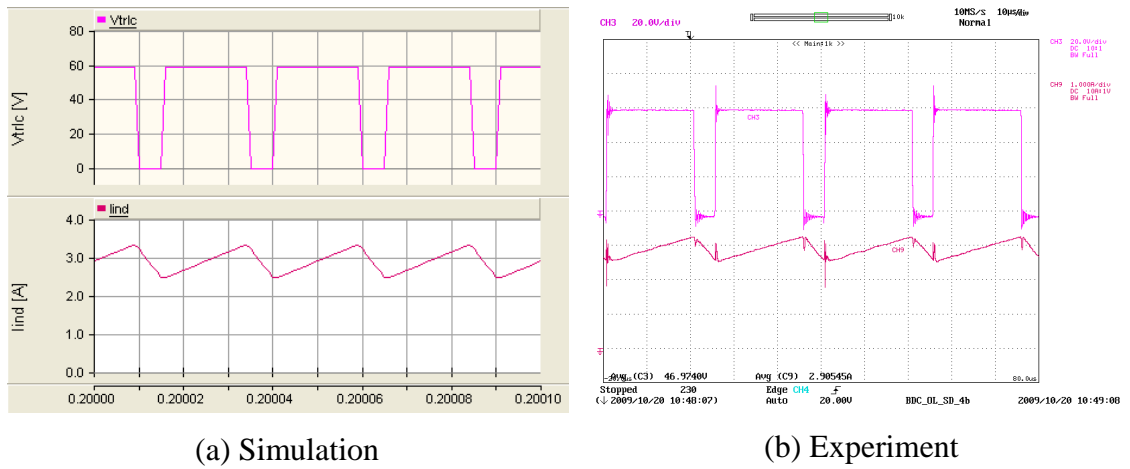
Y axis : V_{trlc} – Pink (20V/div), I_{ind} – Light brown (1A/div); X axis: Time (10μs/div)

Figure C-16: Voltage across the centre of the secondary windings and current flowing through the inductor of the bi-directional dc-dc converter (step-down mode)

C.4 SINGLE-PHASE INVERTER

Figure C-17 shows the typical application diagram of the three-phase inverter module [C1]. Gate driver circuits are inbuilt. Therefore only the logic signals needs to be provided to operate the inverter module. The currents flowing through each phases and temperature of the module can be measured with some external circuitries.
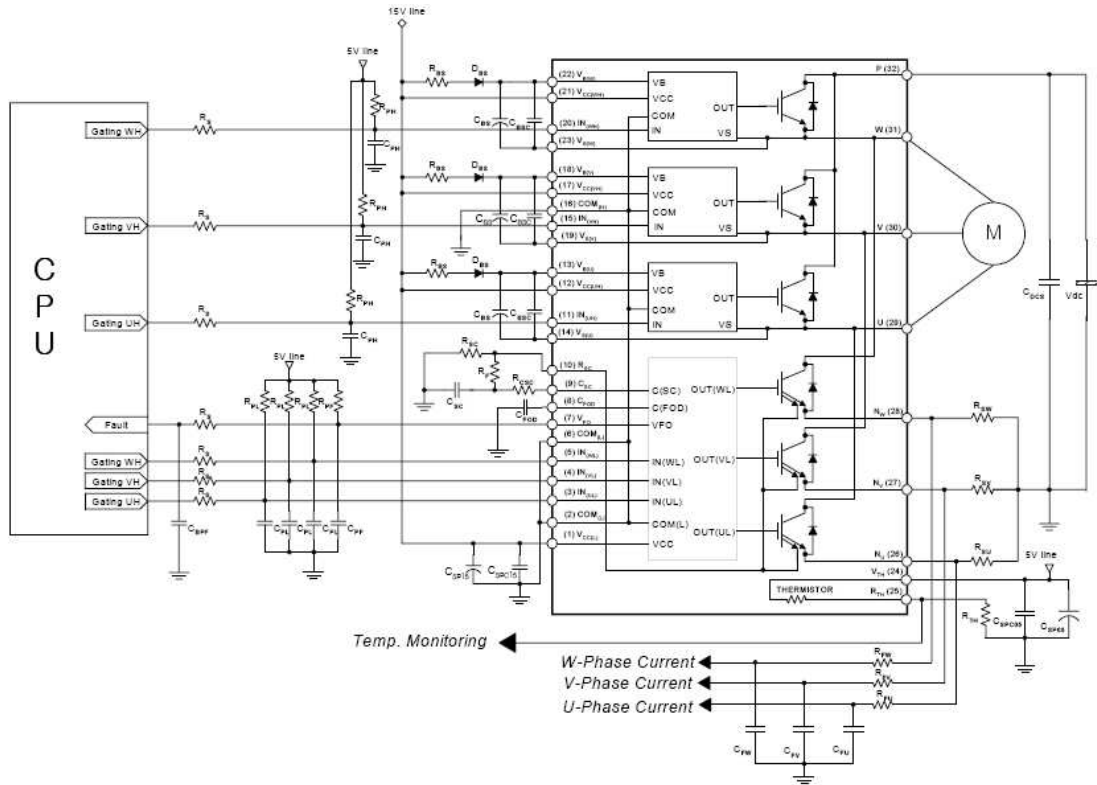
Figure C-17: Typical application diagram of the three-phase inverter module

C.4.1 Open loop and open circuit behaviour of the single-phase inverter

The single-phase inverter under open circuit test is presented in Figure C-18. The dc-link voltage was set to 360 V which is the rated voltage for this application and the amplitude modulation ratio was set to one. Figure C-19 shows the screen capture of the simulation model used to test the single-phase inverter under no-load condition.
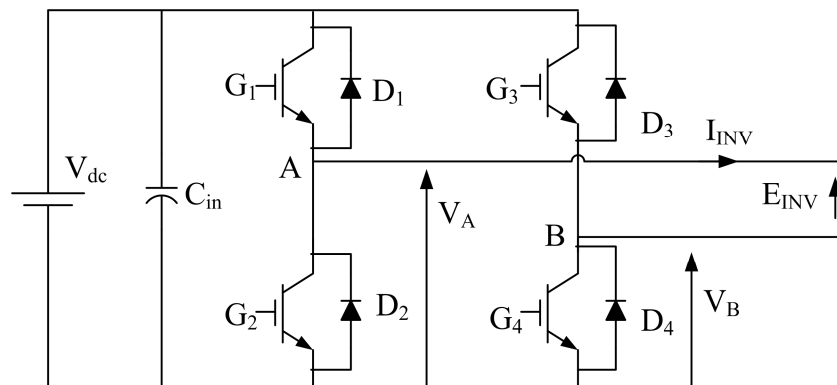

Figure C-18: Single-phase inverter under open circuit test
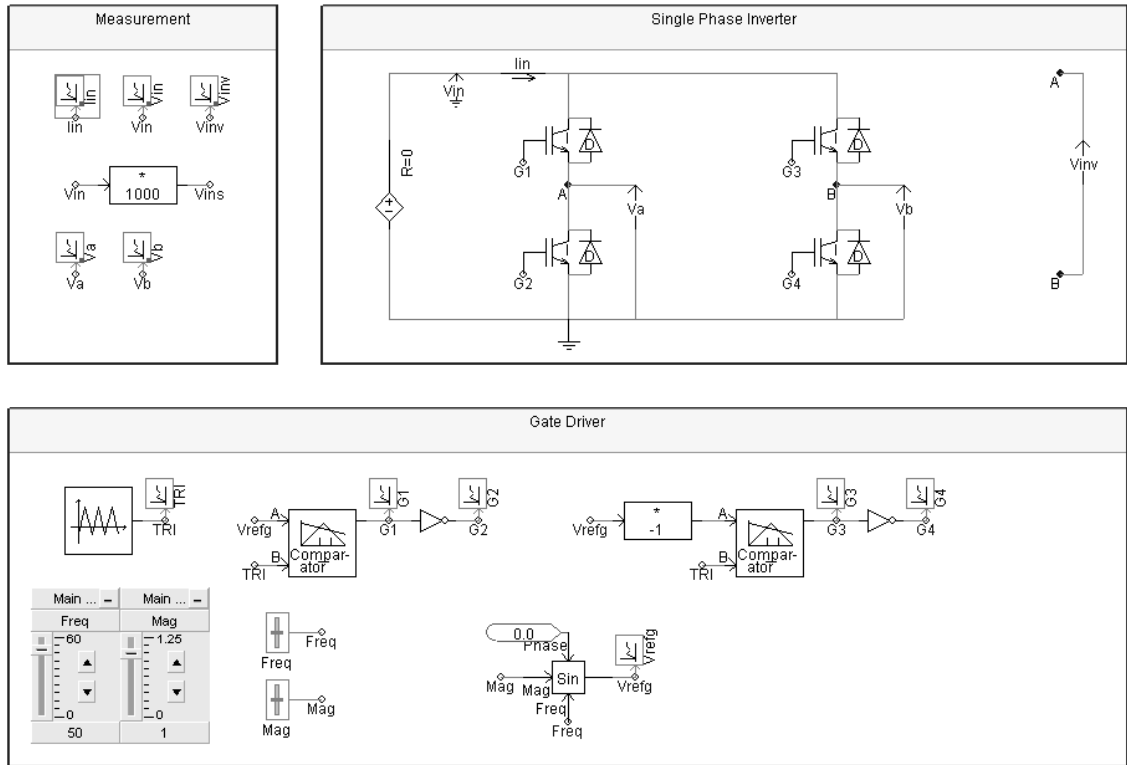
Figure C-19: Screen capture of the single-phase inverter operated in no-load condition

Figure C-20 to Figure C-22 present the no load testing results of the inverter. The voltage at point A and the gate signals G_1 and G_2 are presented in Figure C-20. Figure C-21 shows the voltage at point B and gates G_3 and G_4.

(a) Simulation
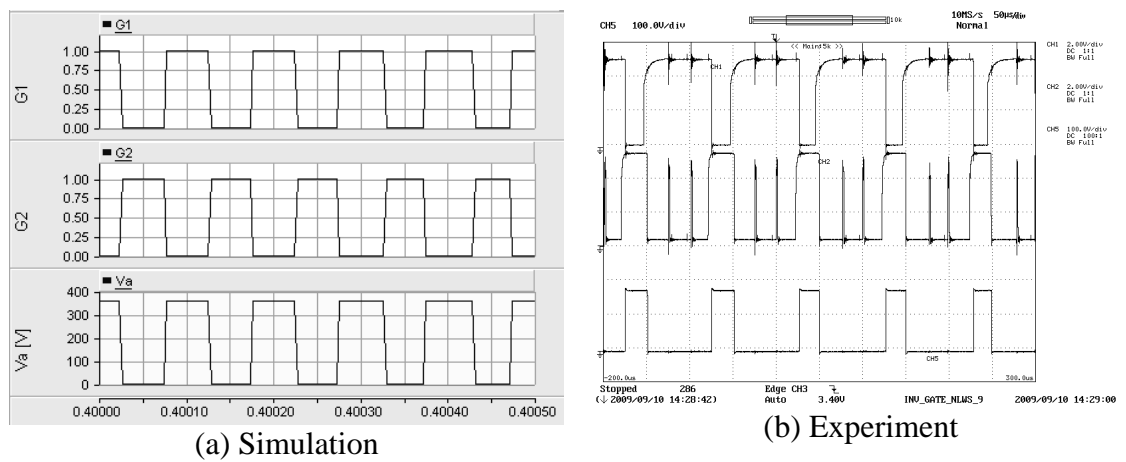
(b) Experiment

Y axis :Top – G_1 (2V/div-Experiment), Middle – G_2 (2V/div- Experiment), Bottom – V_A (100V/div-Simulation, 200V/div-Experiment); X axis: Time (50μs/div)

Figure C-20: G_1 and G_2 and voltage at node-A
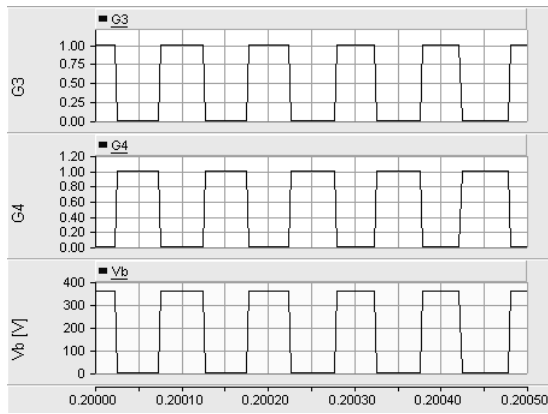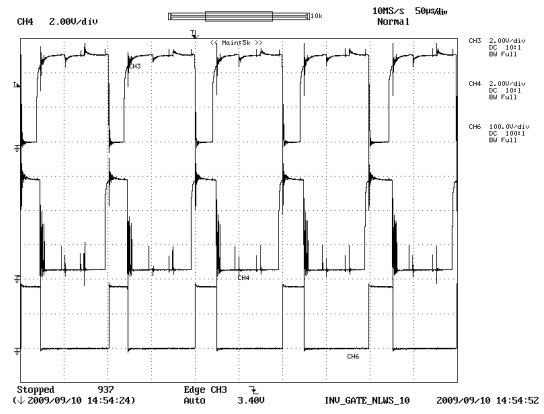
(a) Simulation   (b) Experiment

Y axis :Top – G_3 (2V/div-Experiment), Middle – G_4 (2V/div-Experiment), Bottom – V_B (100V/div-Simulation, 200V/div-Experiment); X axis: Time (50μs/div)

Figure C-21: G_3 and G_4 gate signals and voltage at node-B

The voltage at the centre of each 'leg' and the output voltage of the inverter are presented in Figure C-22. A flat top is visible at the middle of the positive and the negative half cycles in the experimental results, which is due to the introduction of dead time.
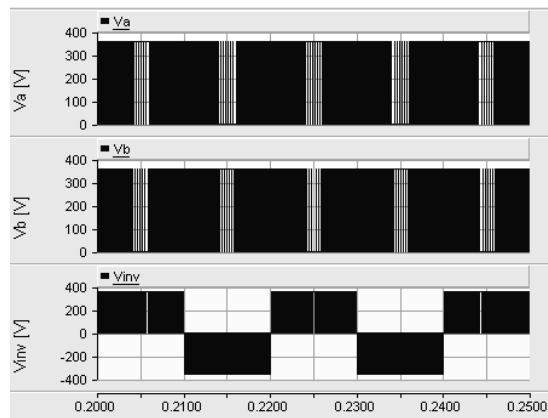
(a) Simulation   (b) Experiment
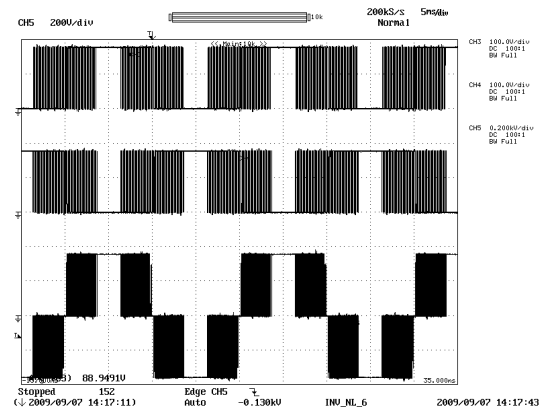
Y axis :Top – V_A (100V/div-Simulation, 200V/div-Experiment), Middle – V_B (100V/div, 200V/div-Experiment), Bottom – V_{INV} (200V/div); X axis: Time (5ms/div)

Figure C-22: Single-phase inverter under no load test

C.4.2 Single-phase inverter connected to a resistive load

The single-phase inverter was connected to a resistive load as in Figure C-23. The input voltage was set to 360V and a load resistor with 800Ω resistance was connected. The

amplitude modulation ratio was set to one. Figure C-24 presents the screen capture of the simulation model of the single-phase inverter connected to a resistive load.
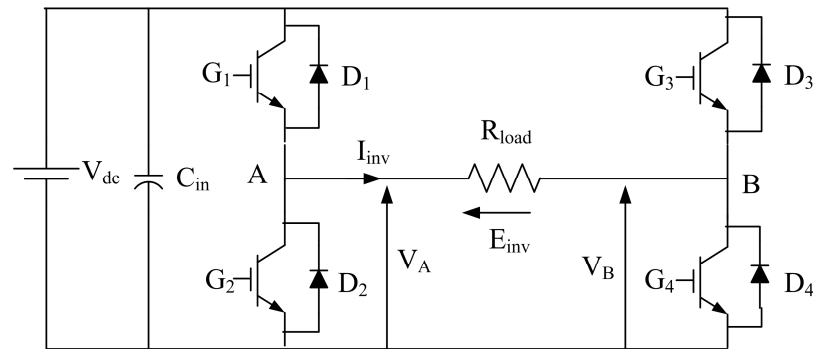

Figure C-23: Single-phase inverter connected to a resistive load
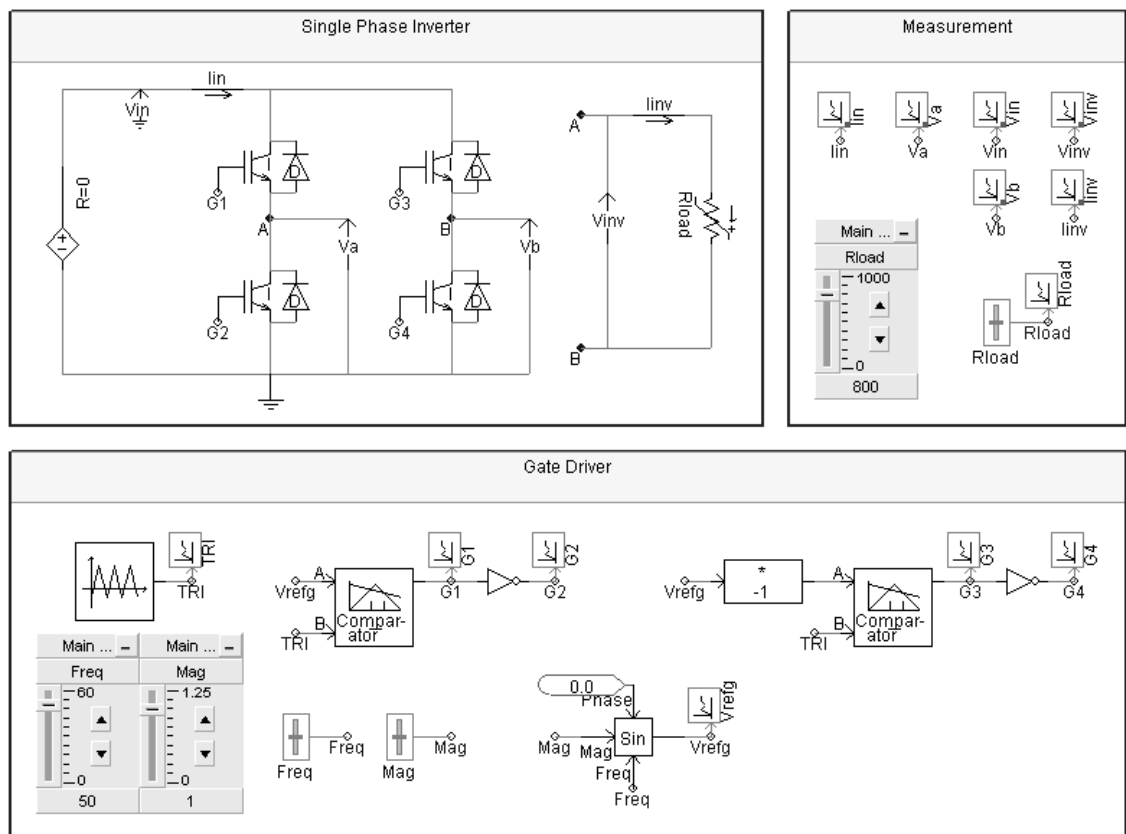

Figure C-24: Screen capture of the simulation model of the single-phase inverter connected to a resistive load

Figure C-25 to Figure C-28 present the results of the single-phase inverter connected to a resistive load. Figure C-25 shows the voltage at the centre of each 'leg'.

(a) Simulation	(b) Experiment
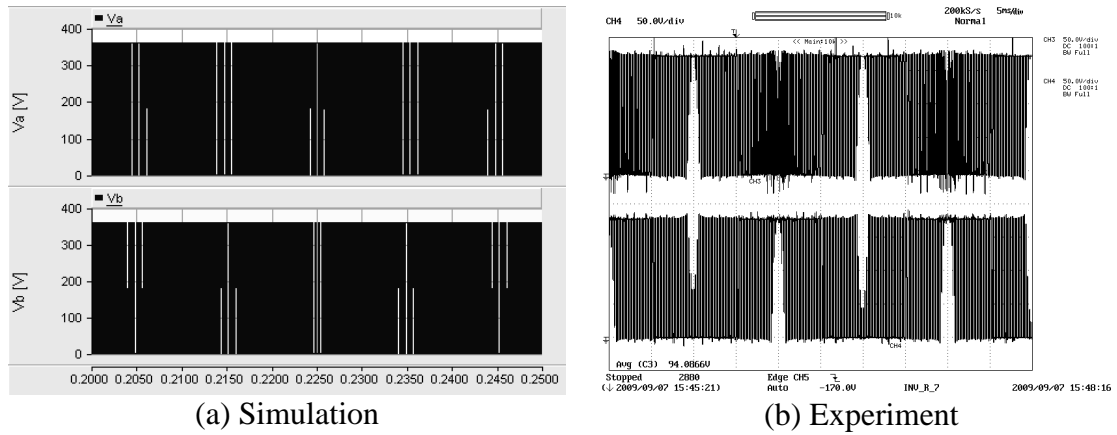
Y axis :Top – V_A (100V/div), Bottom – V_B (100V/div); X axis: Time (5ms/div)

Figure C-25: Voltage at the centre of a one arm

The load current and the inverter output voltage are presented in Figure C-26 and results are magnified over several switching cycles in Figure C-27. The load current is proportional to the inverter output voltage when considering the simulation results. The load connected to the prototype has parasitic inductance and capacitance. Thus the load current is not proportional to the inverter output voltage. The input current and the input voltage are presented in Figure C-28. The input current is partially filtered by the input capacitor in the prototype. Figure C-29 shows the screen capture of measured waveforms plotted in dSPACE. All the measurements were fed through a low pass analogue hardware filter with 5kHz bandwidth before feeding them into the dSPACE system.

|	
(a) Simulation	(b) Experiment
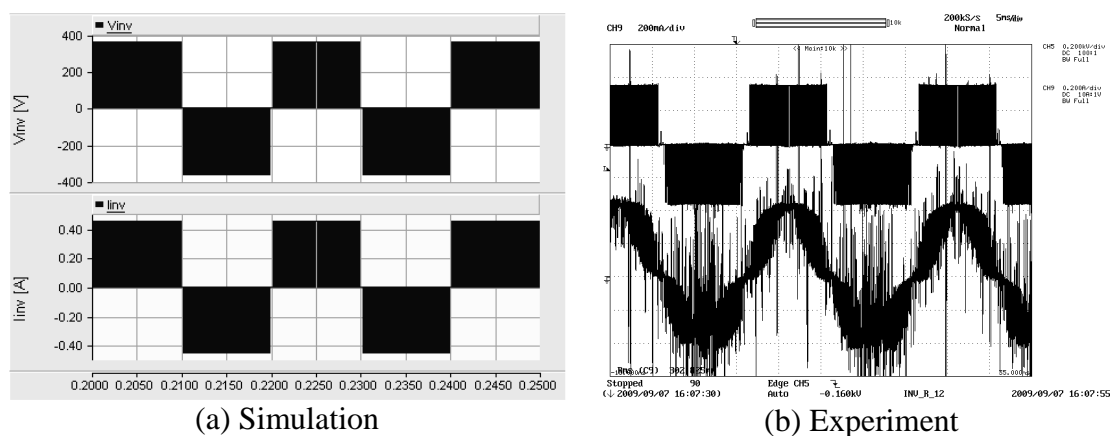
Y axis :Top – E_{INV} (200V/div), Bottom – I_{INV} (0.2A/div); X axis: Time (5ms/div)

Figure C-26: Voltage across the load and current flowing through the load

(a) Simulation   (b) Experiment
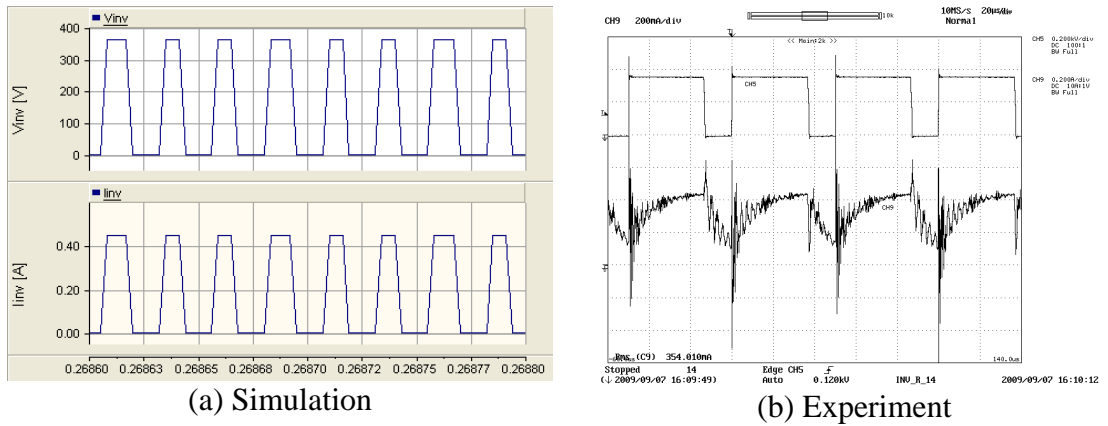
Y axis :Top – E_{INV} (100V/div-simulation, 200V/div-experiment), Bottom – I_{INV} (0.2A/div); X axis:
Time (20µs/div)

Figure C-27: The output voltage and output current over few switching cycles

(a) Simulation   (b) Experiment
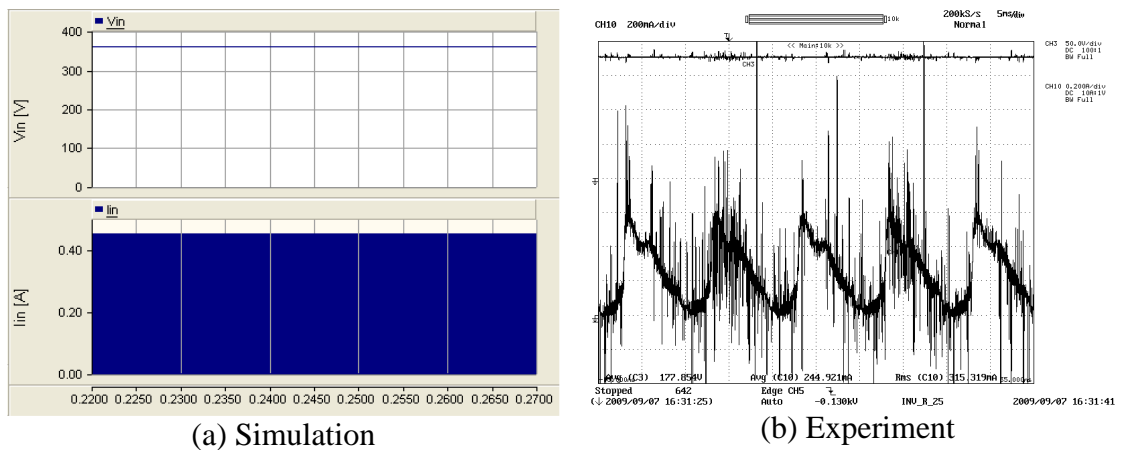
Y axis :Top - V_{dc} (100V/div), Bottom – I_{dc} (0.2A/div); X axis: Time (5ms/div)

Figure C-28: Input voltage and input current flowing through the inverter
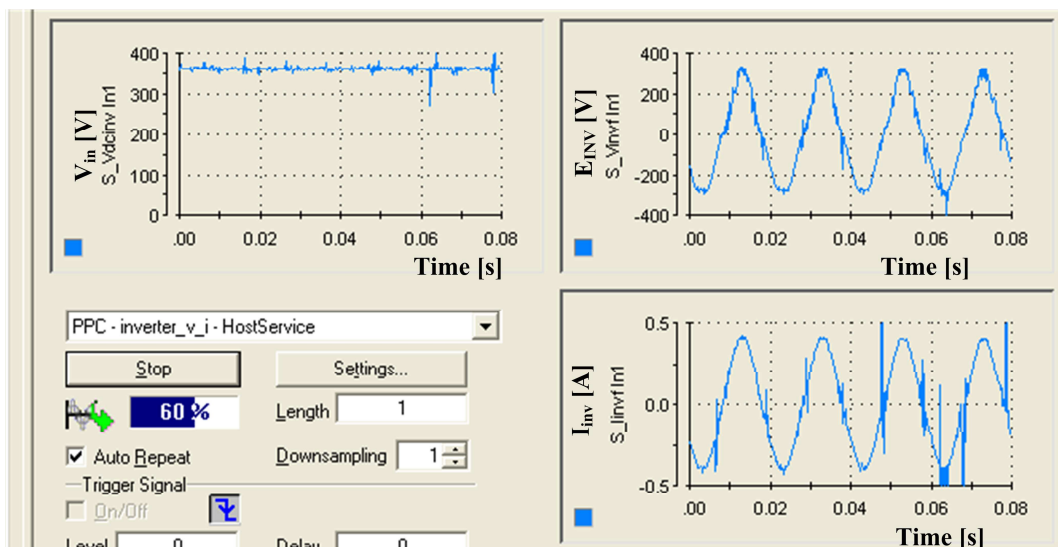

Figure C-29: Screen capture of measured quantities plotted in dSPACE

C.4.3 Single-phase inverter connected to a RL load

A screen capture of the simulation model of the single-phase inverter connected to a RL load is shown in Figure C-30.
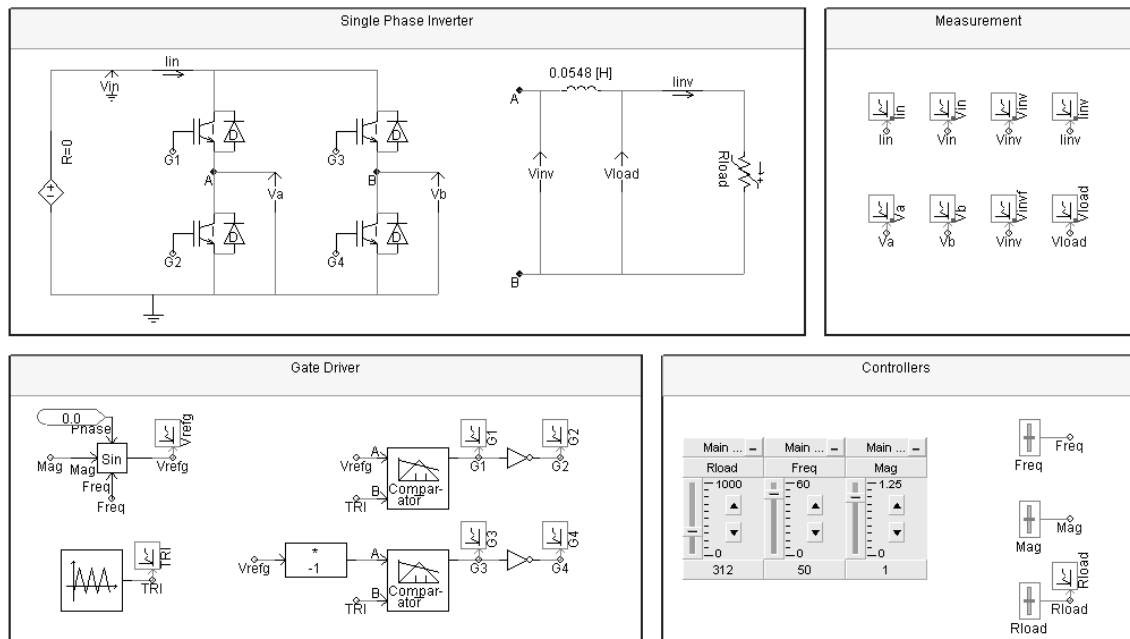

Figure C-30: Screen capture of the simulation model of the single-phase inverter connected to a RL load

C.5 REFERENCE

[C1]   Fairchild Semiconductor, "FSAM20SH60A Smart Power Module datasheet," Fairchild   Semiconductor,   2003,   pp.   16, http://www.fairchildsemi.com/ds/FS/FSAM20SH60A.pdf   last   accessed   on 2010.04.22.

APPENDIX D

DEVELOPMENT OF CONTROLLERS FOR DC-DC CONVERTERS

D.1 INTRODUCTION

For analysis purposes, the proposed microsource interface is divided into two sections as presented in Figure D-1. Section-A comprises the photovoltaic panel, modified forward dc-dc converter, battery storage and bi-directional dc-dc converter. The single-phase inverter connected to the MicroGrid represents Section-B. Section-A should appear to the Section-B as a stiff dc voltage source.

This appendix focuses on the design of controllers for the modified forward dc-dc converter and the bi-directional dc-dc converter. In the case of the bi-directional dc-dc converter, the controller is designed for two operating modes. The controllers are designed based on dynamic stiffness properties of the system. Then the designed controllers are implemented in the simulation model and in the hardware prototype. Finally simulation and experimental results are compared.
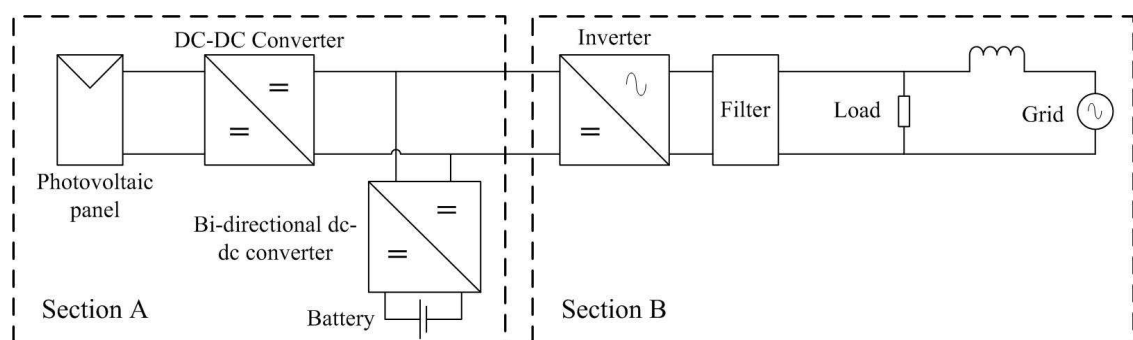

Figure D-1: Proposed microsource interface

D.2 DEVELOPMENT OF A CLOSE LOOP CONTROLLER FOR THE MODIFIED FORWARD DC-DC CONVERTER

The controller of the modified forward dc-dc converter makes sure that the photovoltaic panel operates at the maximum power point. The controller consists of two control loops as shown in Figure D-2. The inner voltage loop ensures that PV panel is operating at the reference voltage generated by the outer loop. The reference voltage is generated by the MPPT which is the outer loop of the controller.
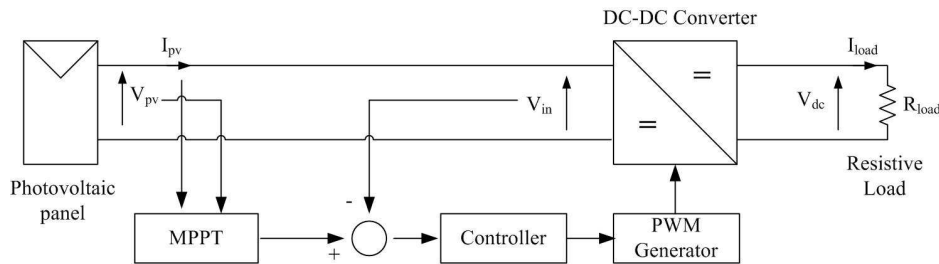

Figure D-2: Structure of the controller used for the modified forward dc-dc converter

D.2.1 Inner voltage loop for the modified forward dc-dc converter

The inner voltage loop was designed based on the operating point model of the modified forward dc-dc converter. Figure D-3 presents the operating point model of the converter which is derived in Chapter 4. A controller based on a PI controller is implemented as shown in Figure D-4. The voltage measurement was passed through a first order low pass filter before applying it to the controller. Input current $\Delta I_{in}(s)$ and inductor current $\Delta I_L(s)$ are considered as disturbances. A simplified block diagram of the controller is presented in Figure D-5 assuming the transformer turns-ratio and operating point inductor current are estimated accurately. The effect of disturbances is combined and represented as a single variable $\Delta I_D(s)$.
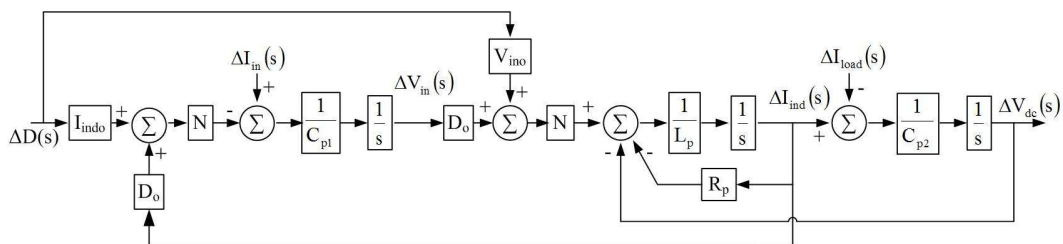

Figure D-3: Operating point state feedback block diagram of the modified forward dc-dc converter

Dynamic stiffness, which is the amount of disturbance required per unit output, is used to design the controller. Equation D-1 and Equation D-2 presents the dynamic stiffness of the controller with proportional controller (G_a) and a PI controller (G_a and K_{sa}) respectively. Further Equation D-3 gives the transfer function of command tracking for the controller. Table D-1 presents the gains selected for the controller. The eigenvalues of the system placed at 4.82 kHz, 8.62 Hz and 2.45 Hz respectively. The gains were selected such a way that fast response is achieved. In order to achieve well-defined and smooth response, real roots for the characteristic equation were selected. The poles corresponding to gains were separated by approximately a factor of four.
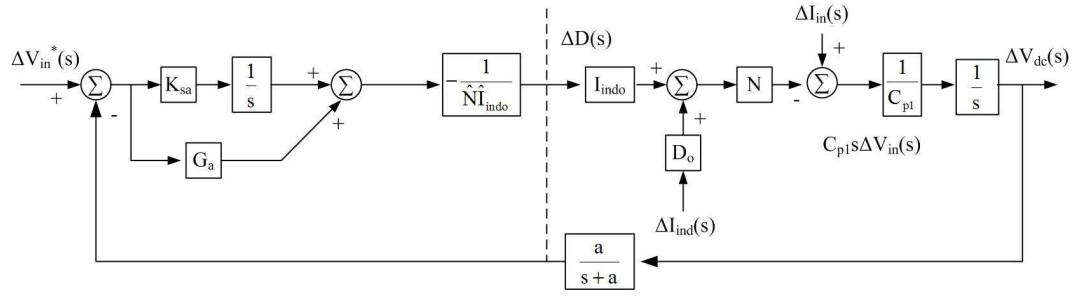
Figure D-4: State feedback block diagram of the controller of the modified forward dc-dc converter
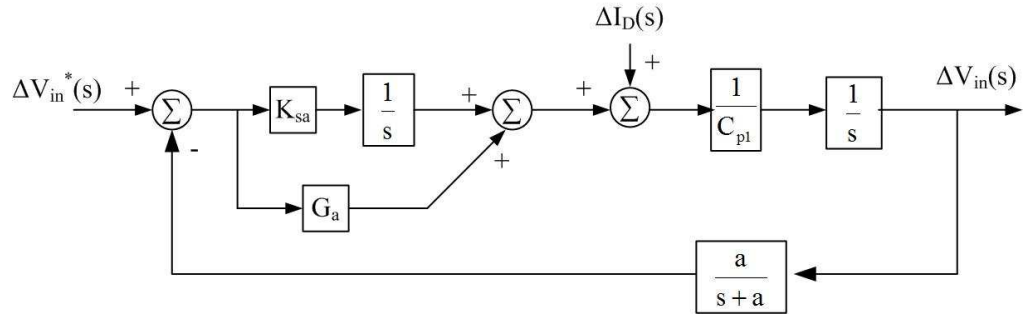
Figure D-5: Simplified block diagram of the controller of the modified forward dc-dc converter

$$\frac{\Delta I_D(s)}{\Delta V_{in}(s)} = \left(C_{p1}s + \frac{aG_a}{s+a} \right)$$
       Equation D-1

$$\frac{\Delta I_D(s)}{\Delta V_{in}(s)} = C_{p1}s + \frac{a(G_a s + K_{sa})}{s(s+a)}$$
       Equation D-2

$$\frac{\Delta V_{in}(s)}{\Delta V_{in}^*(s)} = \frac{G_a s^2 + (aG_a + K_{sa})s + aK_{sa}}{C_{p1}s^3 + aC_{p1}s^2 + aG_a + aK_{sa}}$$
       Equation D-3

Table D-1: Gains selected for the PI controller of the modified forward dc-dc converter

Parameter	Value
G_a	0.25
K_{sa}	3.00

Dynamic stiffness properties of the system are presented in Figure D-6. High frequency dynamic stiffness is determined by the input capacitance. A PI controller provides better dynamic stiffness when compared with a proportional controller. With a PI controller, infinite dynamic stiffness could be achieved at steady state. Figure D-7 shows the frequency response of command tracking.
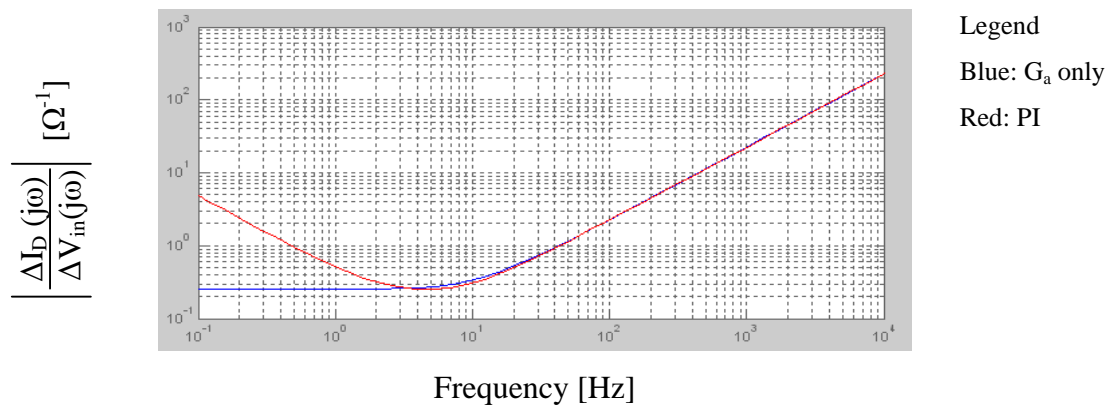
Figure D-6: Dynamic stiffness response of the controller
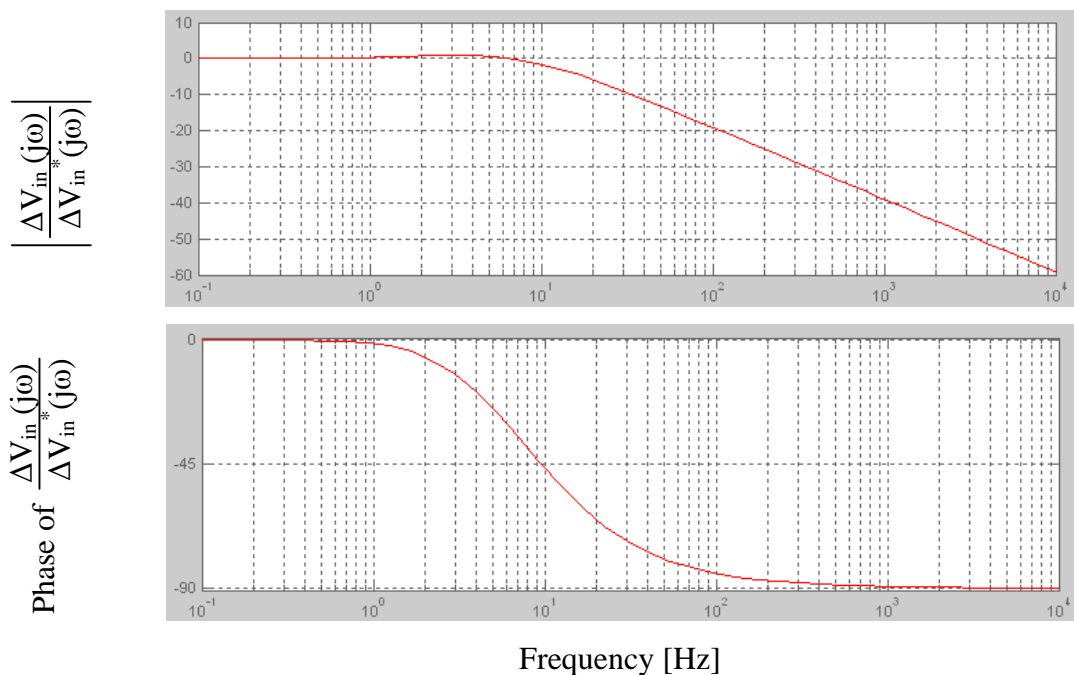
Figure D-7: Command tracking response of the controller

Figure D-8 presents the controller of the modified forward dc-dc converter with an integrator anti-wind up controller which ensures that the integrator always varies within limits.
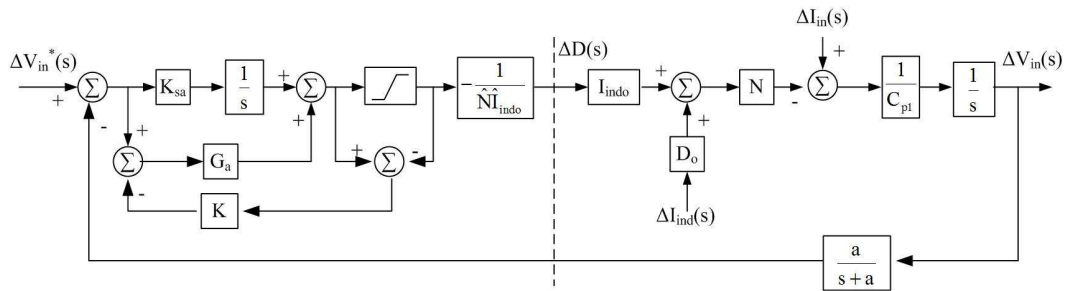

Figure D-8: Controller of the modified forward dc-dc converter with an integrator anti-wind up block

A resistive load with 1352Ω resistance was connected at the output of the modified forward dc-dc converter. The photovoltaic panel output corresponds to 1000W/m^2 irradiance at 25°C. Duration, solution time step and channel plot step of the simulation were set to 1.5s, 0.5μs, and 11μs respectively. Figure D-9 and Figure D-10 show the results of the controller of the modified forward dc-dc converter. The output voltage and the current of the photovoltaic panel are presented in Figure D-9. The photovoltaic panel reaches the reference voltage within 200ms.

    (a) Simulation   (b) Experiment
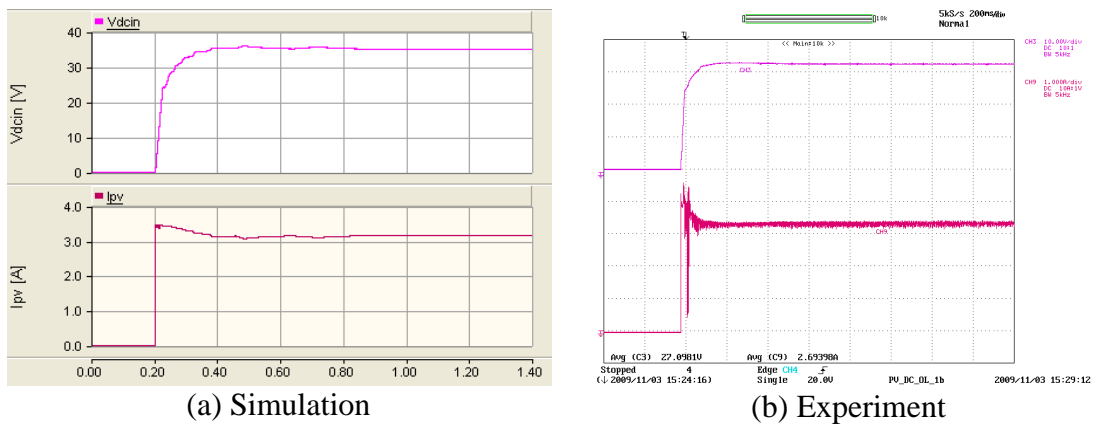
Y axis: V_{in} – Pink (10V/div), I_{pv} – Maroon (1A/div), Experimental results oscilloscope channel bandwidth = 5kHz; X axis: Time (200ms/div)

Figure D-9: Variation of V_{in} and I_{pv} with time of modified forward dc-dc converter

Similarly Figure D-10 presents the output quantities of the modified forward dc-dc converter. The output voltage and current of the converter reach the steady state by 800ms. The response of the controller during the transient is presented in Figure D-11.

The steady state duty ratio is slightly higher for the prototype which is due to the turn on delay of the switches of the converter. As a result the integrator of the controller settles at a lower value compared to that simulation model.

(a) Simulation   (b) Experiment
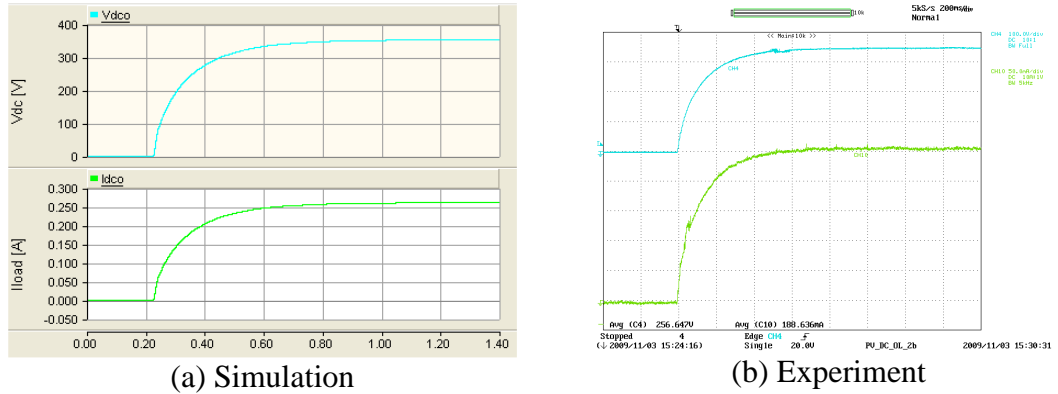
Y axis: V_{dc} – Light blue (100V/div), I_{load} – Light green (50mA/div) Experimental oscilloscope channel bandwidth = 5kHz; X axis: Time (200ms/div)

Figure D-10: Variation of V_{dc} and I_{load} of the modified forward dc-dc converter

Red: Reference; Green: V_{in} Red: Reference; Green: V_{in}

Blue: Proportional, Green: Integrator; Red: PI   Blue: Proportional, Green: Integrator; Red: PI

Time [s]   Time [s]

(a) Simulation   (b) Experimental
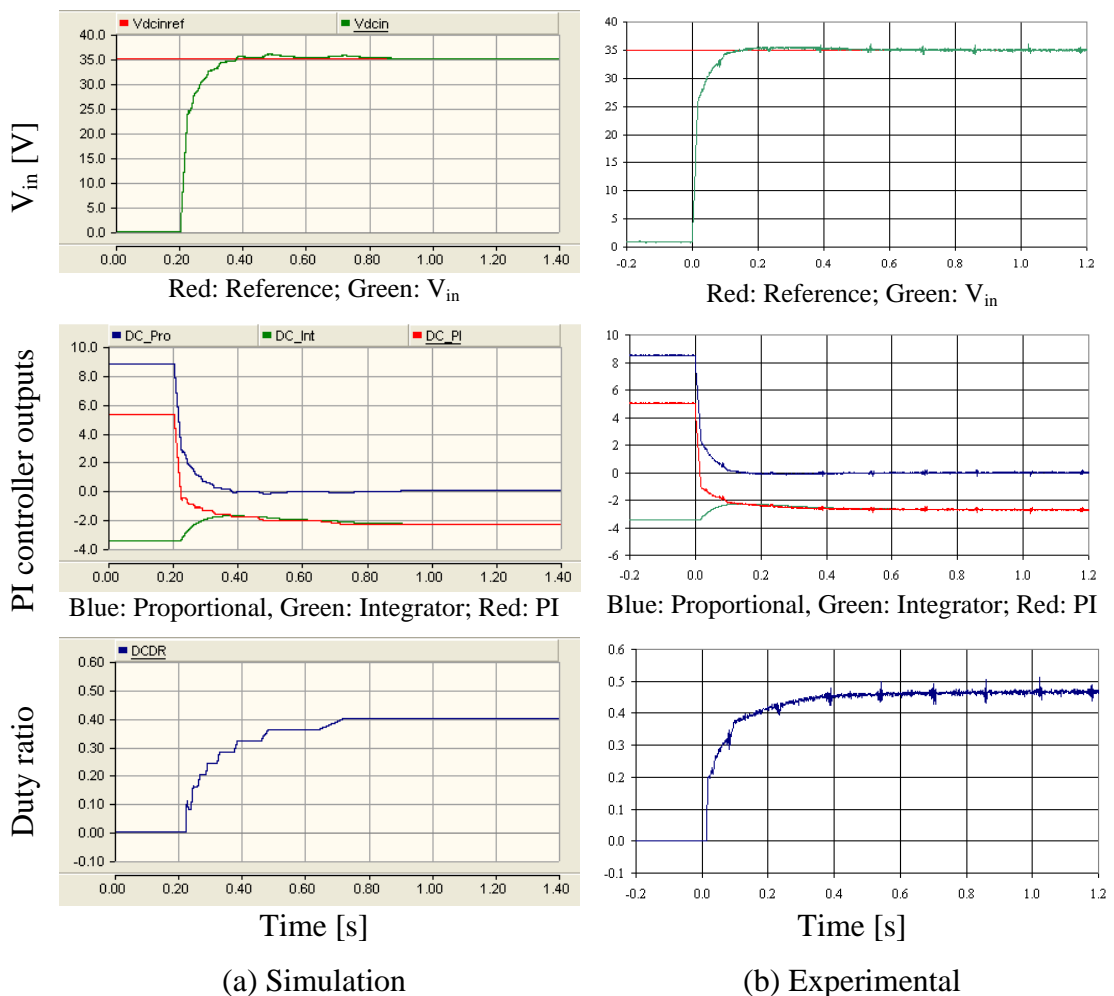
Figure D-11: Response of the controller of the modified forward dc-dc converter

## D.3 CONTROL OF BI-DIRECTIONAL DC-DC CONVERTER

The function of the controller of the bi-directional dc-dc converter is to keep the dc-link voltage constant irrespective of variations in either load or PV panel output power. The controller should be operated during step-up and step-down modes. Initially the controllers are tested for each mode separately and finally the modes are combined together.

D.3.1 Design of controller for the step-up mode

The operating point model of the bi-directional dc-dc converter during step-up mode is presented in Figure D-12. The controller of the bi-directional dc-dc converter comprises two loops. The inner current loop controls the average inductor current and the outer voltage loop controls the voltage at the high-voltage side of the converter.
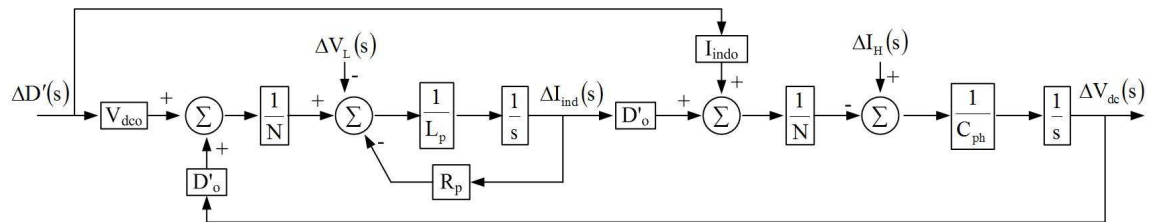
Figure D-12: Operating point model of the bi-directional dc-dc converter during step-up mode

Figure D-13 shows the state feedback block diagram of the inner current loop controller which is based on a PI controller. A simplified controller for the inner current loop is presented in Figure D-14. $\Delta V_L(s)$ and $\Delta V_{dc}(s)$ are considered as disturbances and represented in a single variable. Further it is assumed the estimated values of system variables used to design the controller are equal to the operating point values.
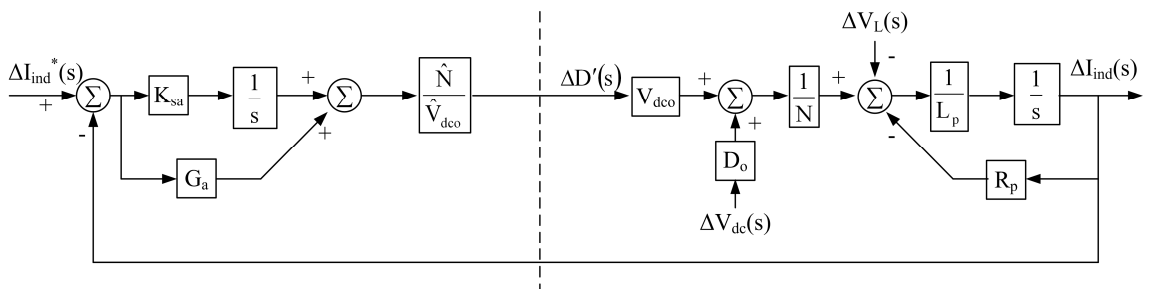

Figure D-13: Inner current loop for the bi-directional dc-dc converter
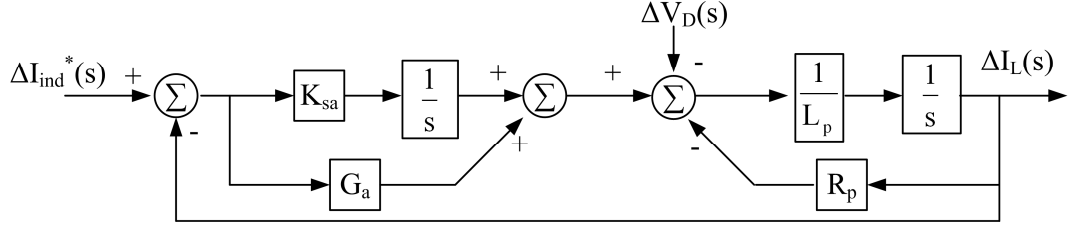
Figure D-14: Simplified block diagram of the controller with inner current loop

Similar to the design of controller for the modified forward dc-dc converter, the controller for the bi-directional dc-dc converter is designed based on the dynamic stiffness performance. Equation D-4 and Equation D-5 give the dynamic stiffness of the controller with only proportional controller and PI controller respectively. Further the transfer function of the command tracking is given in Equation D-6. Table D-2 presents the gains selected for the PI controller based on these equations. The eigenvalues of the system are placed at 471 Hz and 133Hz. The gains were selected such a way that fast response is achieved. In order to achieve well-defined and smooth response, real roots for the characteristic equation were selected. The poles corresponding to gains were separated by approximately a factor of four. The frequency response of the analytical model of dynamic stiffness is plotted and presented in Figure D-15 while the frequency response of the command tracking is presented in Figure D-16 based on Equation D-6.

$$\frac{\Delta V_D(s)}{\Delta I_{ind}(s)} = \left(L_p s + R_p + G_a \right) \qquad \text{Equation D-4}$$

$$\frac{\Delta V_D(s)}{\Delta I_{ind}(s)} = \left[L_p s + R_p + G_a + \frac{K_{sa}}{s} \right] \qquad \text{Equation D-5}$$

$$\frac{\Delta I_{ind}(s)}{\Delta I_{ind}^*(s)} = \frac{G_a s + K_{sa}}{L_p s^2 + \left(R_p + G_a \right) s + K_{sa}} \qquad \text{Equation D-6}$$

Table D-2: Gains selected for the PI controller of the inner current loop of the bi-directional dc-dc converter (step-up mode)

Parameter	Value
G_a	0.75
K_{sa}	750

For the testing of the inner current loop, a 1410Ω resistor was connected to the high-voltage side of the bi-directional dc-dc converter as the load resistor. Further a voltage source was connected to the low-voltage side of the converter and the voltage was set to 48V. Initially average inductor current was allowed to settle at 2A. Then a step of 0.5A was give to the reference current.
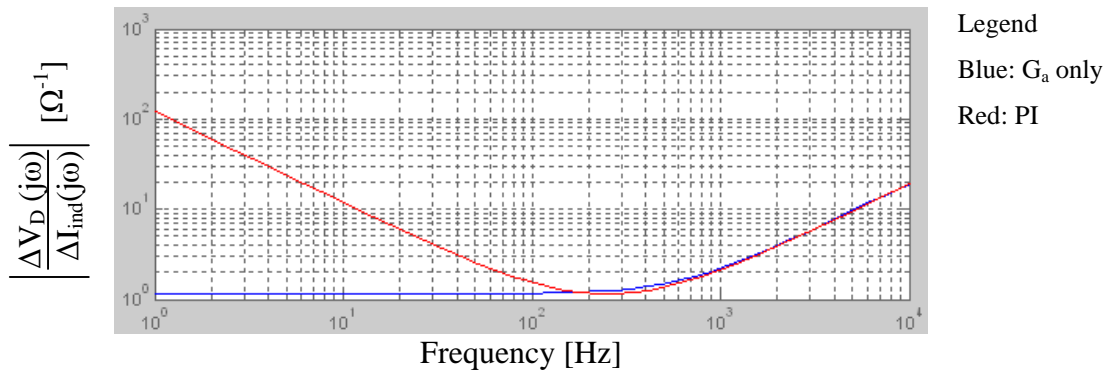
Figure D-15: Dynamic stiffness response of the inner current controller
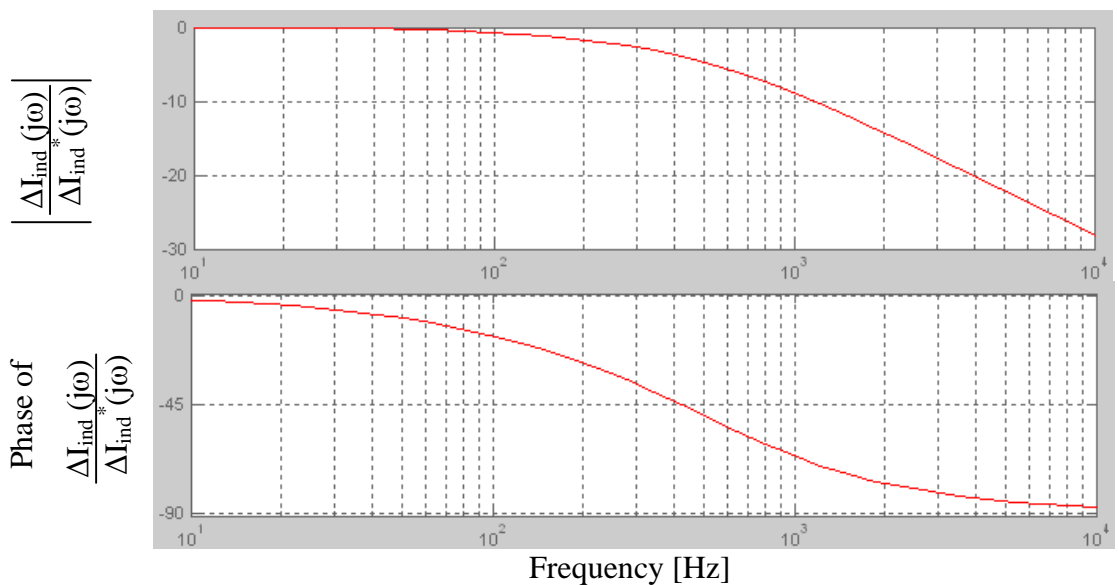
Figure D-16: Command tracking response of the inner current loop

The behaviour of the PI controller of the inner current loop is presented in Figure D-17. According to the controller results, average inductor current reaches the reference virtually instantaneously. The actual current is less than the reference which is due an error in the current measurement device. The duty ratio of the prototype has a response similar to first order while in the simulation model duty ratio changes in a step. In the simulation model, the integrator value changes when an error occurs at around 2.2s.

The voltage at the low-voltage end of the converter is slightly different in the simulation model and prototype - thus the steady state duty ratio before and after the step change is slightly different for the simulation model and the prototype. Figure D-18 shows the average inductor current and the voltage at the low-voltage end of the converter.

Red: Reference, Green: Measured

Red: Reference, Green: Measured

Blue: Proportional, Green: Integrator, Red: PI

Blue: Proportional, Green: Integrator, Red: PI

Time [s]

Time [s]

(a) Simulation

(b) Experimental
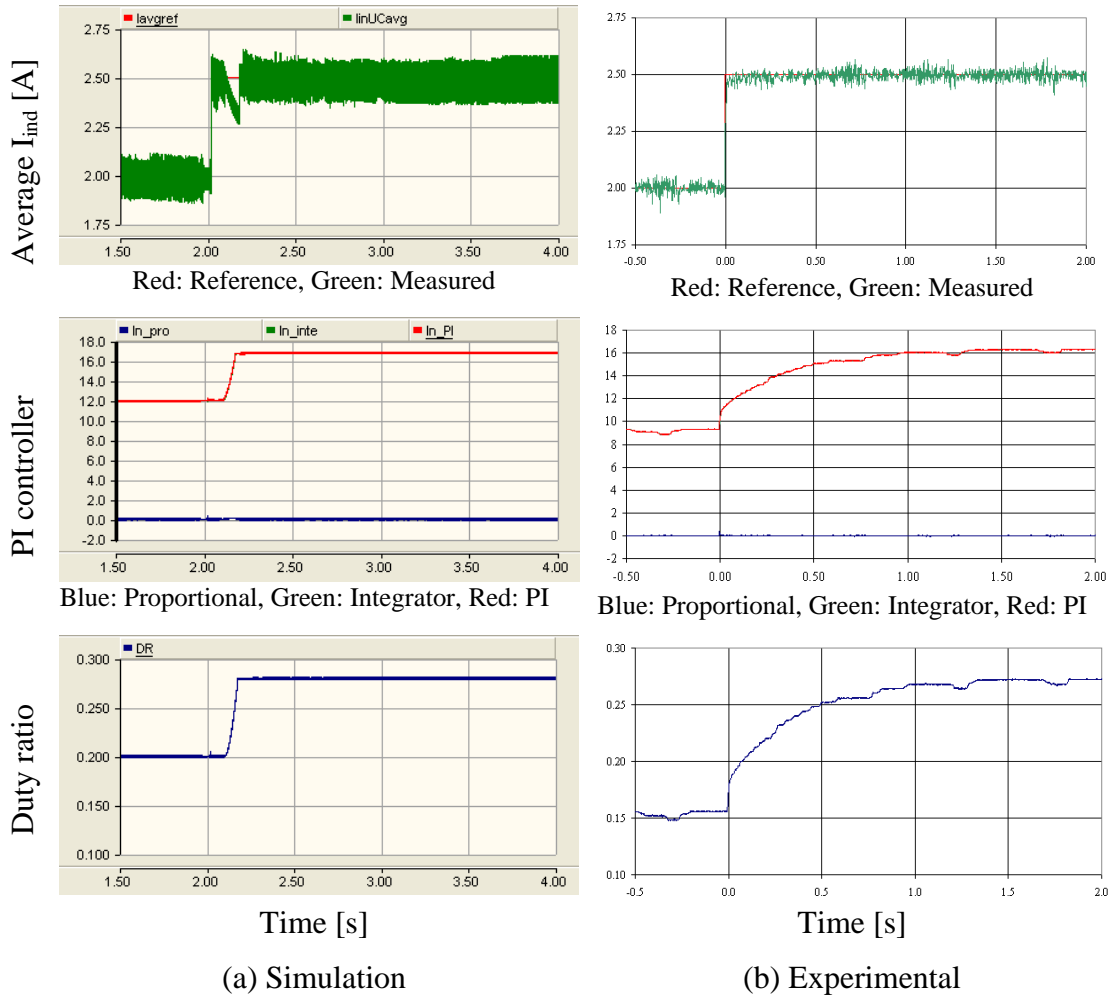
Figure D-17: Behaviour of the inner current controller of the bi-directional dc-dc converter at step-up mode

The outer voltage loop of the bi-directional dc-dc converter controls the voltage at the high-voltage side. The outer control loop is presented in Figure D-19. It is assumed that the inner current loop is faster than the outer voltage loop. $\Delta I_o(s)$ and $\Delta D(s)$ are assumed as disturbances. Disturbances are lumped together as a single variable in the simplified model shown in Figure D-20. Further it is assumed that the estimated values are equal to the actual values. Equation D-7 and Equation D-8 give the dynamic stiffness transfer functions for the outer control loop while Equation D-9 gives the transfer function of the command tracking.

(a) Simulation   (b) Experiment
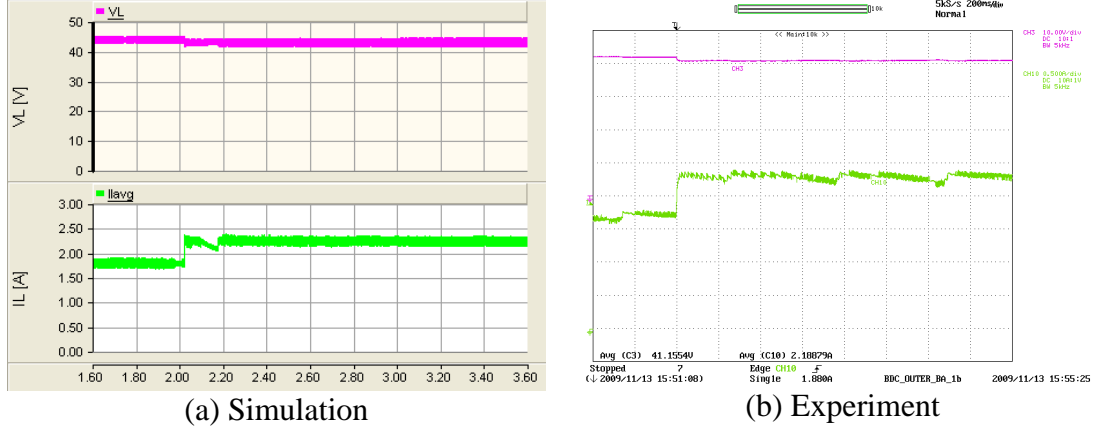
Y axis: V_L – Pink (10V/div), I_L – Light green (0.5A/div), Oscilloscope channels bandwidth = 5kHz; X axis: Time (200ms/div)

Figure D-18: Average inductor current and voltage at the low-voltage end of the bi-directional dc-dc converter (step-up mode)
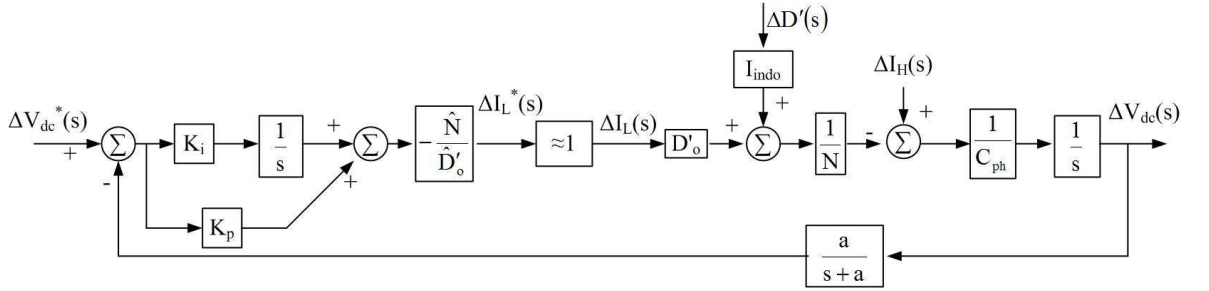
Figure D-19: Outer control loop of the bi-directional dc-dc converter at step-up mode
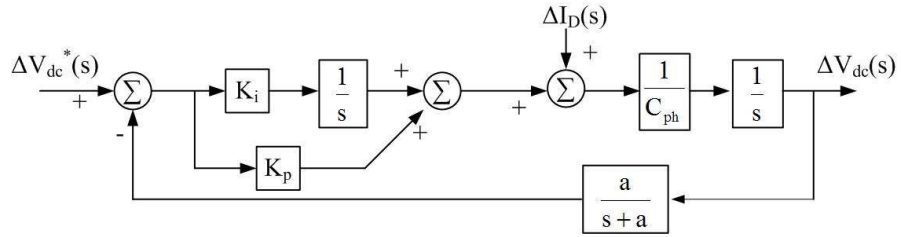
Figure D-20: Simplified block diagram of the outer control loop

$$\frac{\Delta I_D(s)}{\Delta V_{dc}(s)} = \left[C_{po}s + \frac{aK_p}{s+a} \right] \qquad \text{Equation D-7}$$

$$\frac{\Delta I_D(s)}{\Delta V_{dc}(s)} = \left[C_{po}s + \frac{a(K_p s + K_i)}{s(s+a)} \right] \qquad \text{Equation D-8}$$

$$\frac{\Delta V_{dc}(s)}{\Delta V_{dc}^*(s)} = \frac{(K_p s + K_i)(s+a)}{C_{po}s^3 + aC_{po}s^2 + aK_p s + aK_i} \qquad \text{Equation D-9}$$

Based on these equations, gains presented in Table D-3 are selected for the controller. The eigenvalues of the controller are 4.72 kHz, 64.8 Hz and 16.9 Hz respectively. The gains were selected such a way that fast response is achieved. In order to achieve well-defined and smooth response, real roots for the characteristic equation were selected. The poles corresponding to gains were separated by approximately a factor of four. The frequency response of the dynamic stiffness is plotted in Figure D-21 while the frequency response of command tracking is presented in Figure D-22.

Table D-3: Gains selected for the PI controller of the outer voltage loop of the bi-directional dc-dc converter (step-up mode)

| Parameter	Value
G_a	0.01
K_{sa}	0.03
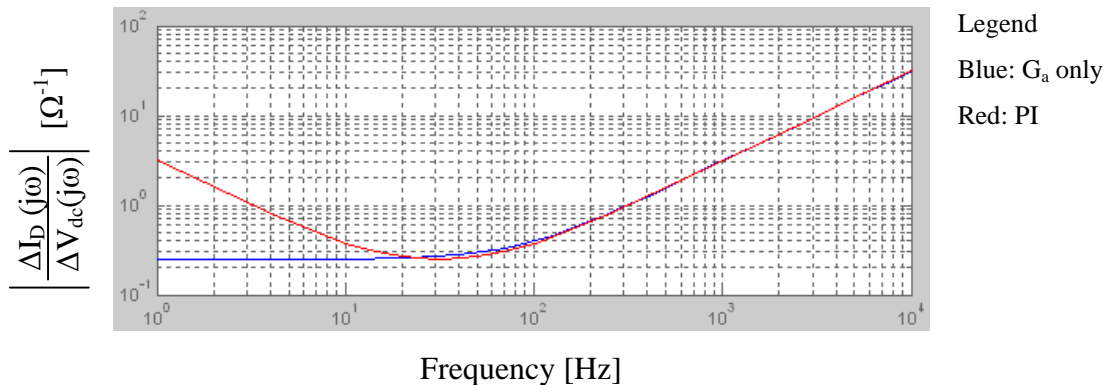
Figure D-21: Dynamic stiffness response of the outer control loop

In order to test the outer control loop performance, a 1410Ω resistive load was connected to the high-voltage side while a 48V battery was connected to the low-voltage side of the converter. Initially the bi-directional dc-dc converter allowed settle at 320V and then a step of 40V is given.

Figure D-23 shows the dc-link voltage and load current. The average current flown through the inductor and the voltage at the low-voltage end of the converter is presented in Figure D-25. The behaviour of the inner and the outer loops of the controller are presented in Figure D-24. Approximately within one second the dc-link voltage reaches its new steady state. The transient behaviour of the duty ratio is different in the

simulation and prototype due the difference in the integrator action. The steady state duty ratio difference is due the voltage at the low-voltage side in the simulation model and prototype. Simulation and experimental results nevertheless show reasonable agreement.

Frequency [Hz]
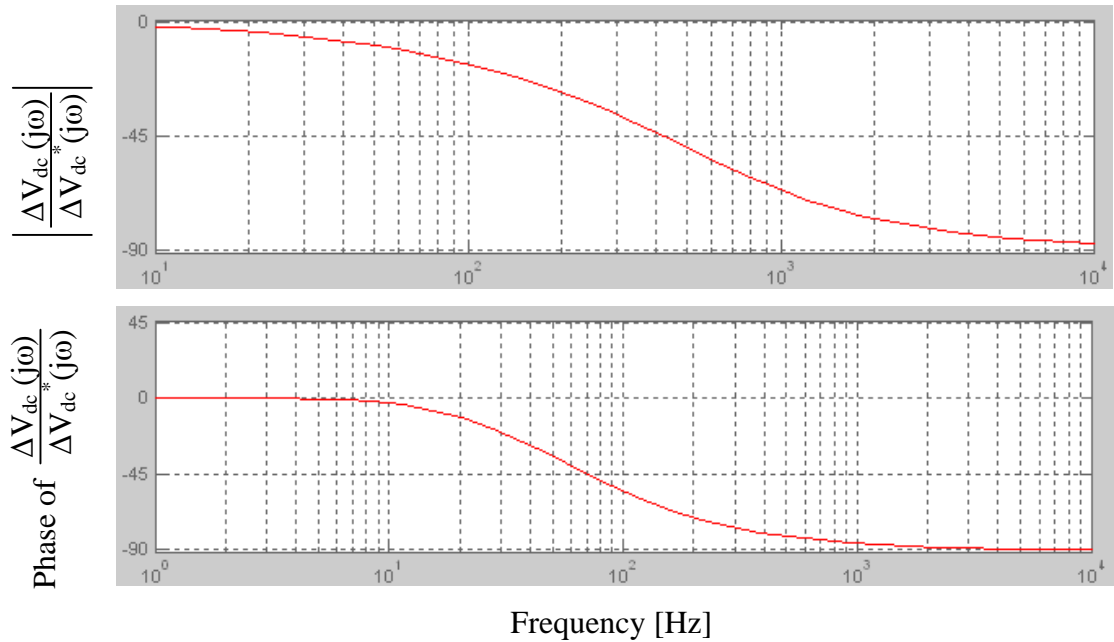
Figure D-22: Command tracking response of the outer voltage loop
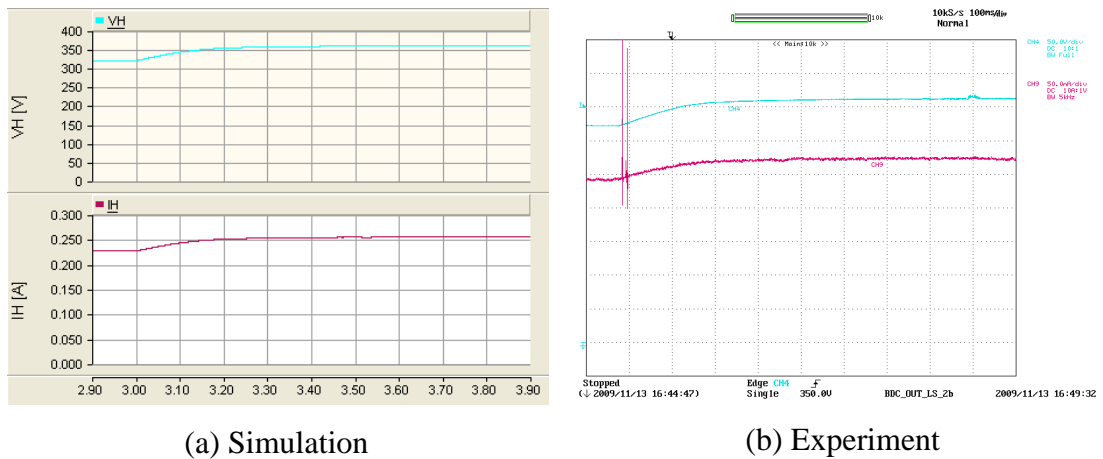
(a) Simulation   (b) Experiment

Y axis: V_{dc} – Light blue (50V/div), I_{load} – Maroon (50mA/div) Experimental oscilloscope channel

bandwidth = 5kHz;   X axis: Time (100ms/div)

Figure D-23: DC-link voltage and load current

Red: Reference, Green: Measured   Red: Reference, Green: Measured

Blue: Proportional, Green: Integrator, Red: PI   Blue: Proportional, Green: Integrator, Red: PI

Blue: Reference, Green: Measured   Blue: Reference, Green: Measured

Blue: Proportional, Green: Integrator, Red: PI   Blue: Proportional, Green: Integrator, Red: PI

Time [s]   Time [s]

(a) Simulation   (b) Experimental
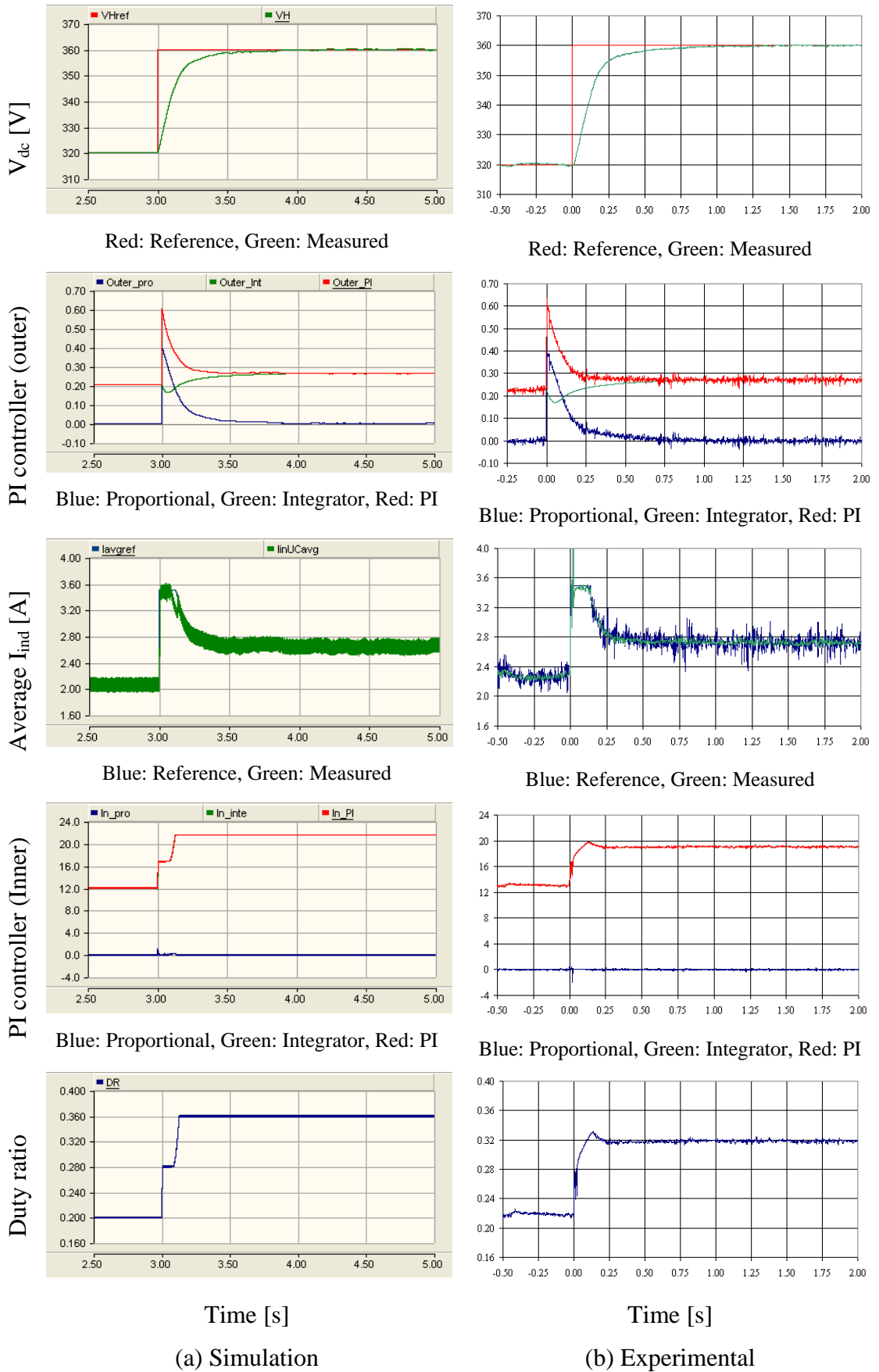
Figure D-24: Behaviour of the controller of the bi-directional dc-dc converter (step-up mode)
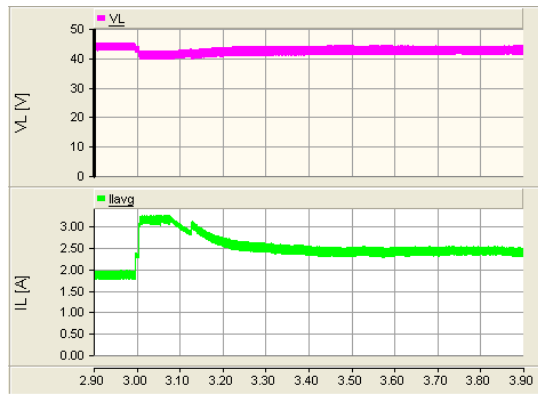
(a) Simulation   (b) Experiment
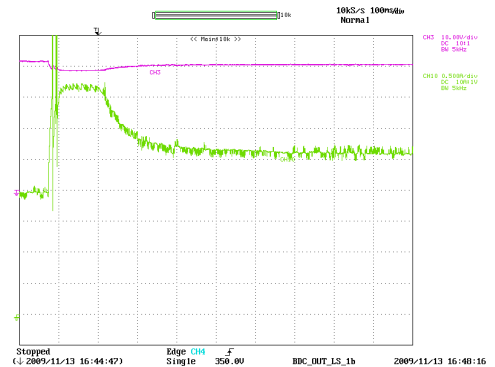
Y axis: V_L – Pink (10V/div), I_L – Green (500mA/div) Experimental oscilloscope channel bandwidth = 5kHz;   X axis: Time (100ms/div)

Figure D-25: Voltage at the low-voltage end of the bi-directional dc-dc converter and battery current

The photovoltaic panel, modified forward dc-dc converter and bi-directional dc-dc converter were integrated as shown in Figure D-26. The bi-directional dc-dc converter step-up mode operation with the PV panel emulator providing power to a load is analysed with this set-up. A load resistor with 1178Ω resistance was connected to the dc-link. The PV panel output corresponds to an irradiance of 1000W/m^2 and 25°C. The load was initially powered by the PV panel completely. The bi-directional dc-dc converter was turned on manually to step-up mode. The dc-link reference voltage was set to 340V. Once the dc-link stabilises at 340V, a 20V step change in reference dc-link voltage was given. The duration, the solution time step and the channel plot step of the simulation were set to 10s, 1μs and 23μs respectively.
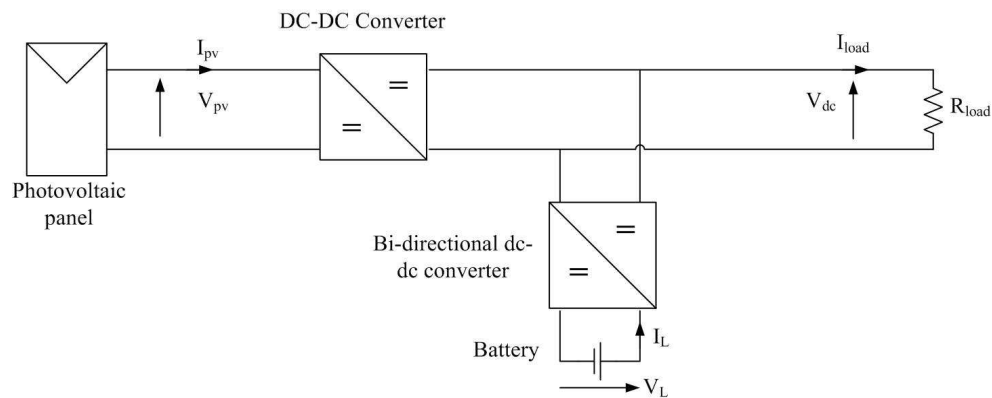

Figure D-26: Integrated test set-up used to test the operation of step-up mode of the bi-directional dc-dc converter

As shown in Figure D-27, dc-link voltage smoothly reaches the new reference. The average current through the inductor of the bi-directional dc-dc converter, Figure D-28, experiences a current surge at the transient before reaching the steady state. The behaviour of the controller of the bi-directional converter is shown in Figure D-29. The dc-link voltage reaches its new reference approximately within 500ms. The duty ratio applied to bi-directional dc-dc converter differs in the simulation and experimental results. The voltage at the low-voltage end of the bi-directional dc-dc converter is different due to slight variations between the model and the reality which is the reason for the duty ratio difference. According to Figure D-30, the dynamics of the dc-link has not affected the photovoltaic panel output voltage or current.
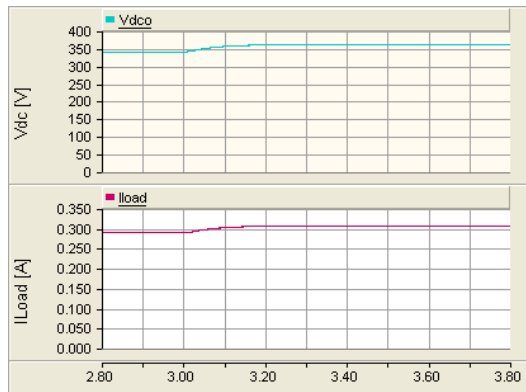
(a) Simulation
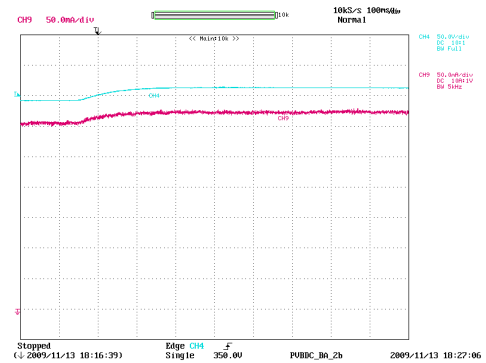
(b) Experiment

Y axis: V_{dc} – Light blue (50V/div), I_{load} – Brown (50mA/div) Experimental oscilloscope channel bandwidth = 5kHz; Ground level of CH4 and CH9 are same in experimental results; X axis: Time (100ms/div)

Figure D-27: Load current and dc-link voltage during the transient
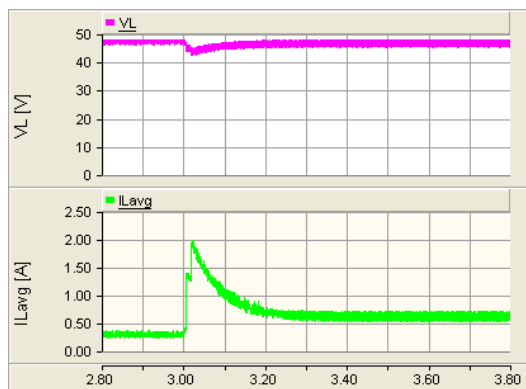
(a) Simulation
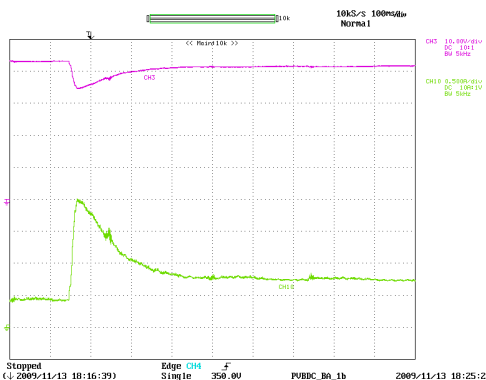
(b) Experiment

Y axis: V_L – Pink (10V/div), I_L – Light green (0.5A/div), Experimental results oscilloscope channel bandwidth = 5kHz; X axis: Time (100ms/div)

Figure D-28: Voltage at the low-voltage end of the bi-directional dc-dc converter and battery current

Red: Reference, Green: Measured

Red: Reference, Green: Measured

Blue: Proportional, Green: Integrator, Red: PI

Blue: Proportional, Green: Integrator, Red: PI

Blue: Reference, Green: Measured

Blue: Reference, Green: Measured

Blue: Proportional, Green: Integrator, Red: PI

Blue: Proportional, Green: Integrator, Red: PI

Time [s]

Time [s]
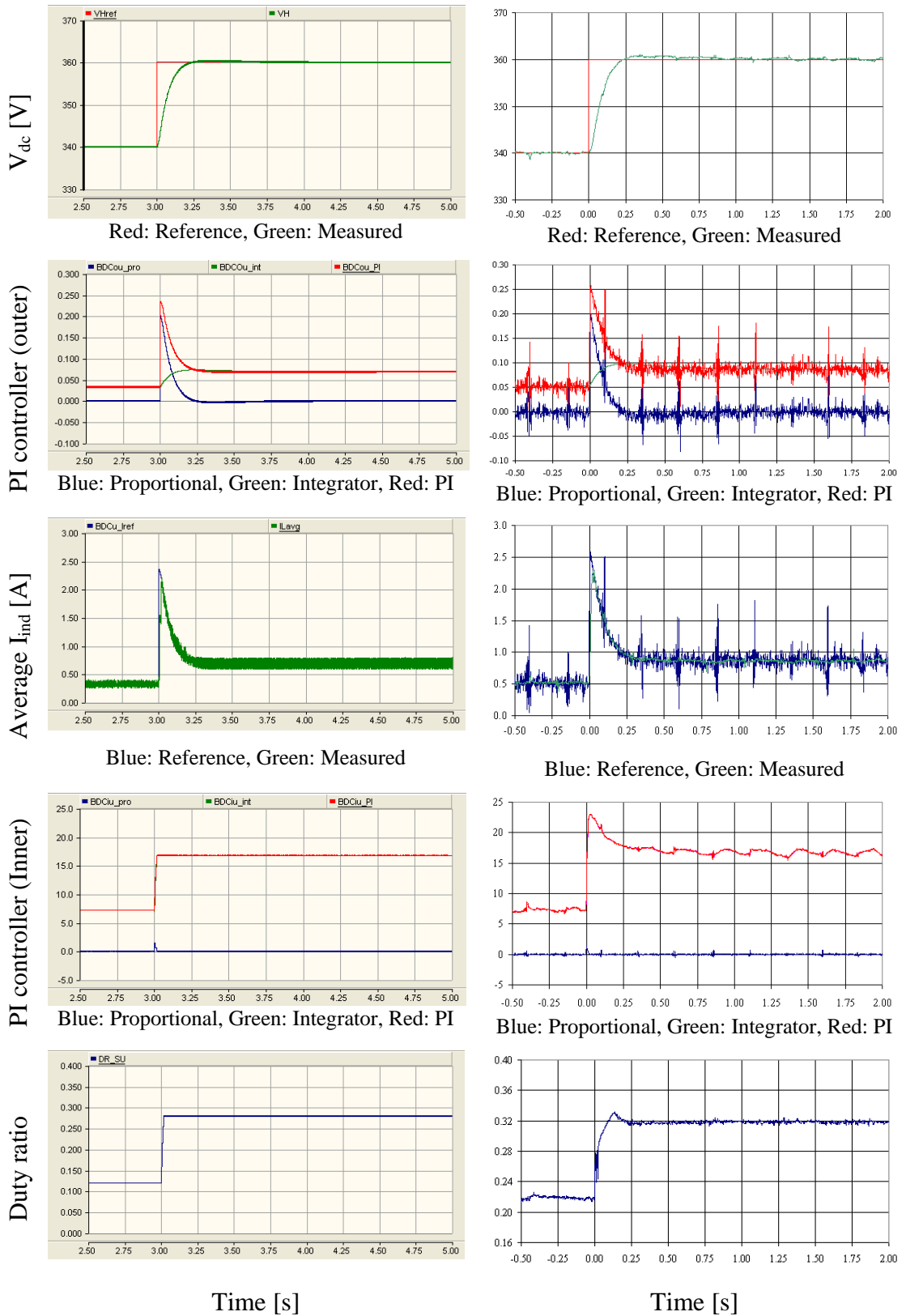
(a) Simulation

(b) Experimental

Figure D-29: Behaviour of the bi-directional dc-dc converter controller during the step-up mode

276
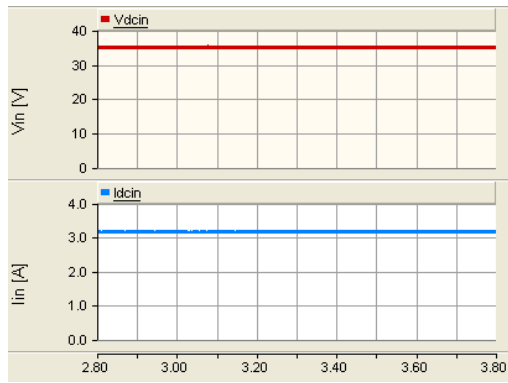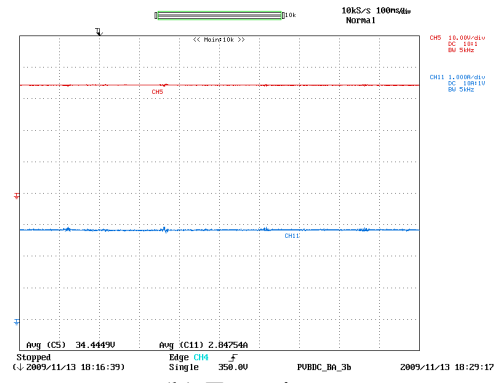
(a) Simulation   (b) Experiment

Y axis: V_{dcin} – Brown (10V/div), I_{pv} – Blue (1.0A/div), Experimental results oscilloscope channel bandwidth = 5kHz; X axis: Time (100ms/div)

Figure D-30: Photovoltaic panel voltage and current

Figure D-31 presents the modified forward dc-dc converter behaviour. The duty ratio of the modified forward dc-dc converter is slightly adjusted to accommodate the voltage increase in the dc-link.


Red: Reference; Green: V_{in} Red: Reference; Green: V_{in}

Blue: Proportional, Green: Integrator; Red: PI   Blue: Proportional, Green: Integrator; Red: PI

Time [s]   Time [s]
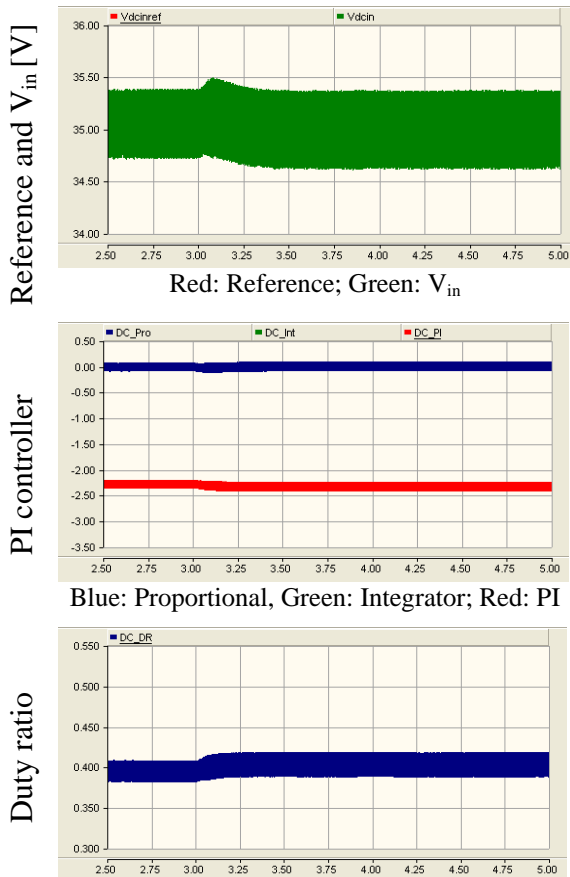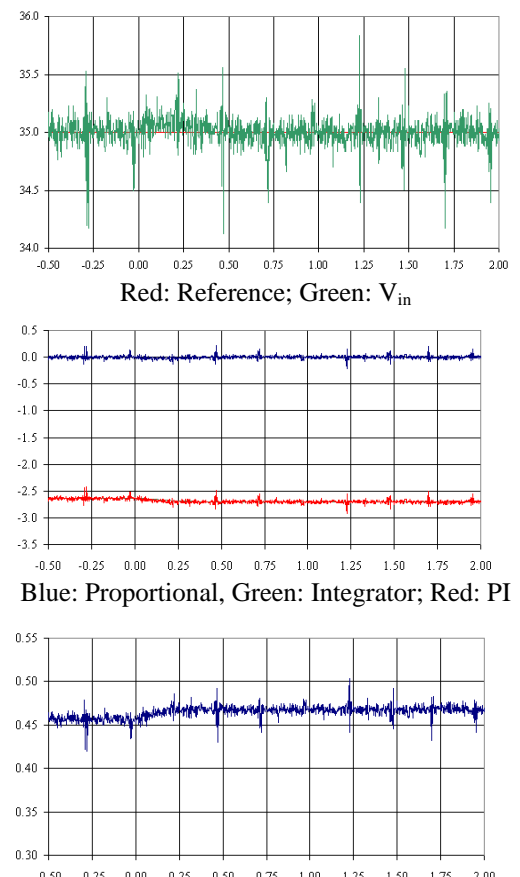
(a) Simulation   (b) Experimental

Figure D-31: Behaviour of the controller of the modified forward dc-dc converter

D.3.2 Design of Controller for the step-down mode

The operating point model of the bi-directional dc-dc converter for the step-down mode is presented in Figure D-32. Similar to the controller of the step up mode, the controller for the step-down mode consists of two loops. The inner loop controls the average inductor current while the outer loop controls the dc-link voltage.
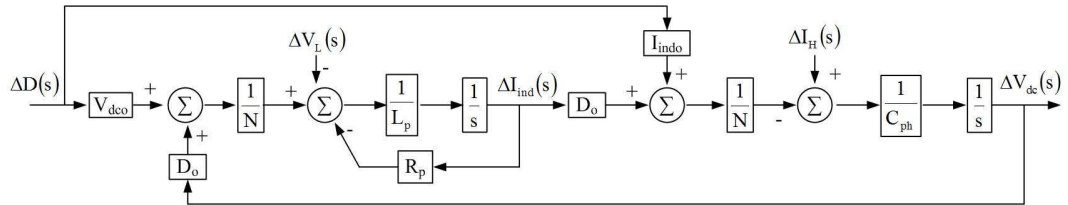

Figure D-32: Operating point block diagram of the bi-directional dc-dc converter at step-down mode

Figure D-33 shows the detailed inner current loop for the step-down mode. The voltage at the low-voltage side and the high-voltage side are treated as disturbances. The simplified block diagram of the system with inner current loop is presented in Figure D-34 assuming estimates are equal to actual values. Furthermore the disturbances are represented by a single variable. The simplified block diagram of the inner current loop is similar to the inner current loop of the step-up mode. Thus the controller gains used in the step-up mode are used for the step-down mode as well.
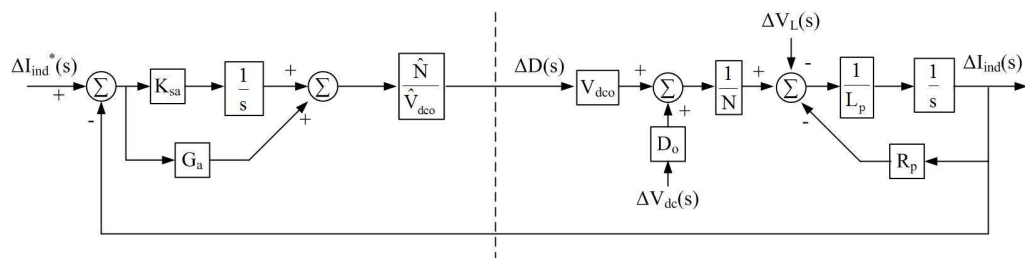

Figure D-33: Block diagram of the inner current control loop of the bi-directional dc-dc converter (step-down mode)
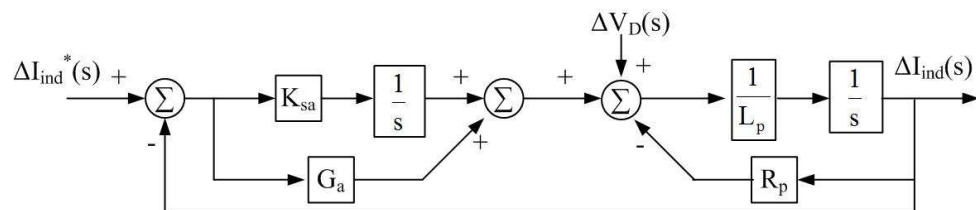

Figure D-34: Simplified block diagram of the inner current control loop

In order to test the inner current loop, a voltage source was connected to the high-voltage side of the bi-directional dc-dc converter and its voltage was set to 360V. An XHR 600-1.7 laboratory power supply was used to test the prototype. A 48V lead acid battery bank was connected to the low-voltage side of the bi-directional dc-dc converter. The duration, the solution time step and the channel plot step were set to 2s, 1μs and 7μs respectively. Initially the converter was allowed to settle to 1.5A and then a step change of 0.5A was introduced.

Figure D-35 shows the behaviour of the controller for the inner current loop. The controller reaches the reference virtually instantly. However the duty ratio applied to the converter in the simulation model and the prototype are different. This is due to the voltage differences in the low-voltage end of the converter, due to slight variations between the model and reality.

(a) Simulation   (b) Experimental
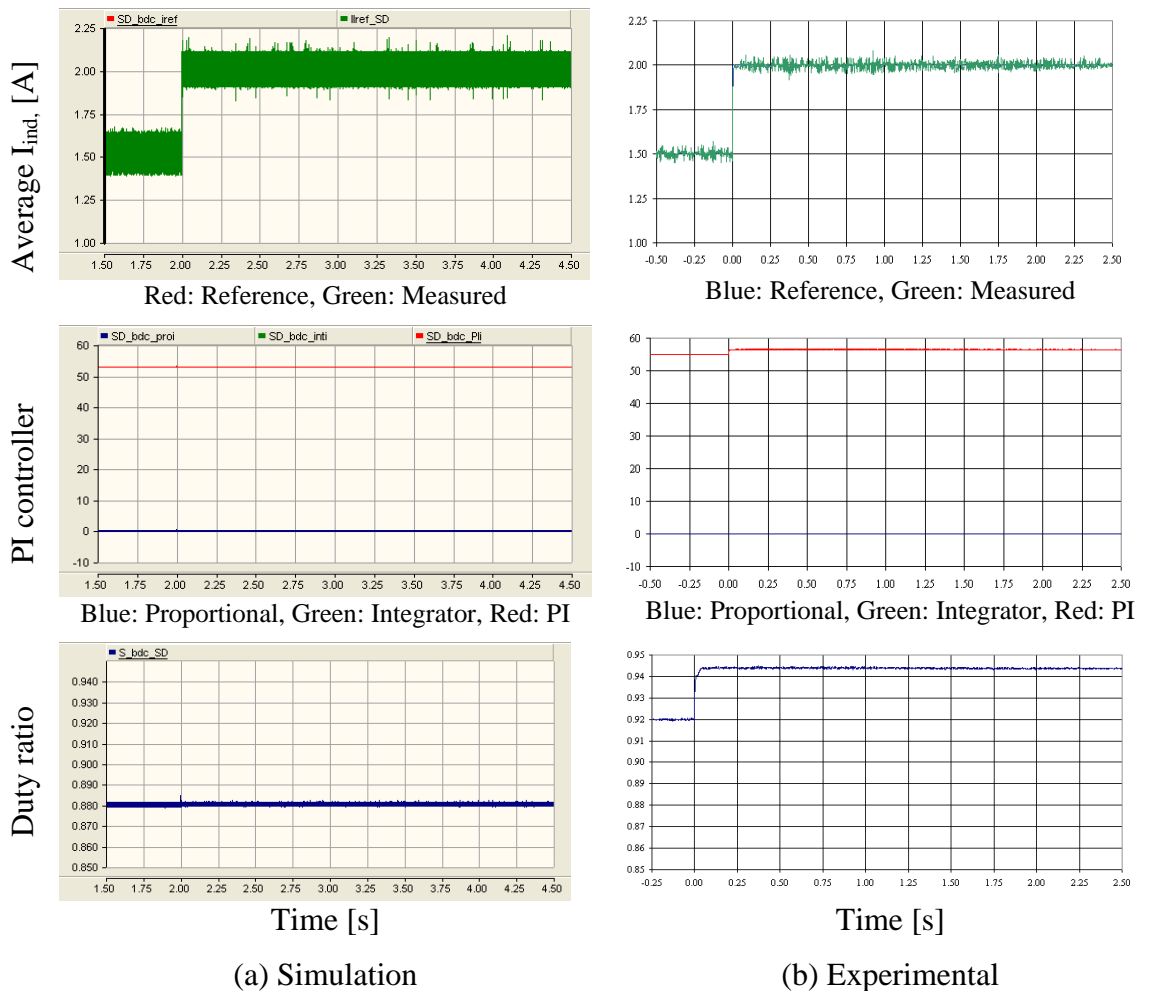
Figure D-35: Behaviour of the inner current control loop of the bi-directional dc-dc converter during step-down mode

Figure D-36 presents the voltage at the low-voltage end of the bi-directional dc-dc converter and the current into the battery. Due a measurement error, the current is slightly lower than the current reference.

<div align="center">(a) Simulation   (b) Experiment</div>
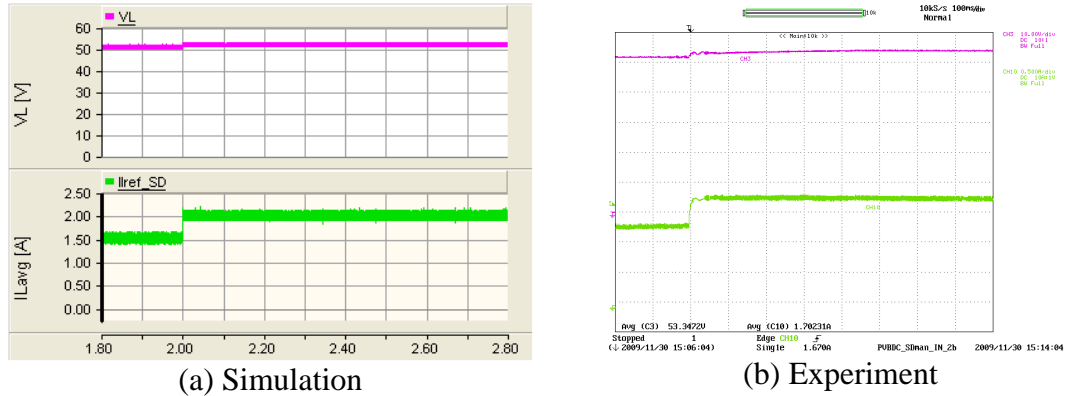
<div align="center">Y axis: V_L – Pink (10V/div), I_L – Light green (0.5A/div); X axis: Time (100ms/div)</div>

<div align="center">Figure D-36: Voltage at the low-voltage end of the bi-directional dc-dc converter and the battery current</div>

The outer voltage loop of the bi-directional dc-dc converter controls the voltage at the high-voltage side. Detailed and simplified outer control loops are presented in Figure D-37 and Figure D-38 respectively. The duty ratio and the input current are treated as disturbances and assumed to be perfect estimations. In the simplified model, disturbances are represented by a single variable. The simplified block diagram of the outer voltage loop is similar to the outer voltage loop used for the step-up mode. Therefore the same values for gains are used in the step-down mode outer voltage loop as well.
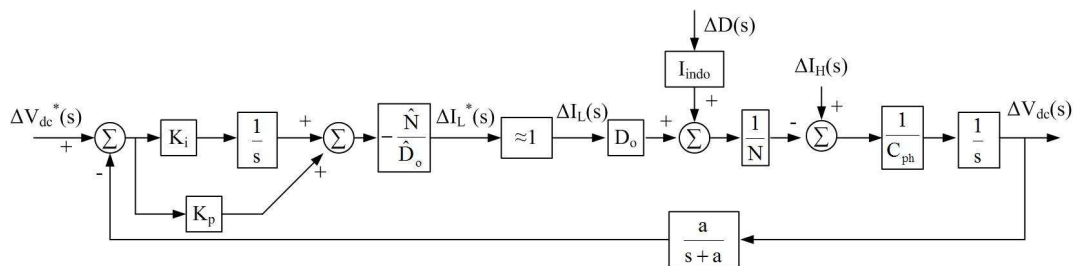

<div align="center">Figure D-37: Outer voltage control loop of the bi-directional dc-dc converter during step-down mode</div>

The test set-up presented in Figure D-39 is used to test the step-down mode outer voltage loop. A resistive load of 1642Ω was connected across the dc-link. Initially the

load was fully powered by the PV panel. The bi-directional dc-dc converter was set to step-down mode with dc-link voltage reference set to 360V. Once the system reached steady state, the dc-link voltage was reduced to 340V in a step.
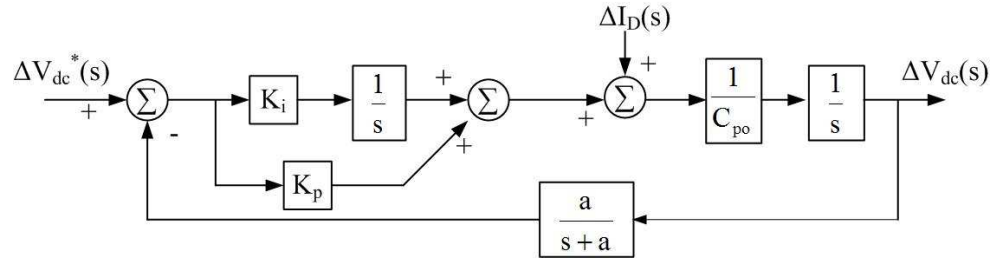

Figure D-38: Simplified outer voltage control loop
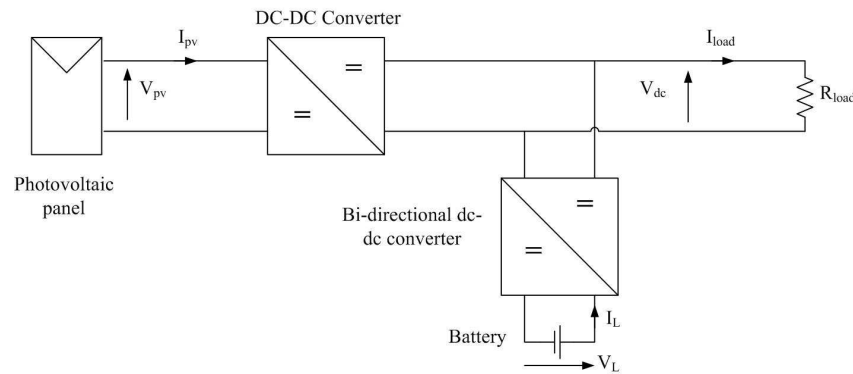
Figure D-39: Test set-up for outer voltage loop of bi-directional dc-dc converter during step-down mode

Figure D-40 presents the dc-link voltage and the load current. The dc-link voltage smoothly reaches its new reference. The voltage at the low-voltage end of the bi-directional dc-dc converter and the current flown into the battery are shown in Figure D-41. The current probe used to measure the inductor current was placed in opposite direction thus the average inductor current measured within the experimental set-up is positive. The output voltage and current were not affected as shown in Figure D-42.

The controller behaviour of the bi-directional dc-dc converter is shown in Figure D-43. The dc-link voltage reaches the new steady state approximately within one second. Figure D-44 presents the behaviour of the controller of the photovoltaic panel. The output voltage and the output current of the photovoltaic panels were not affected by the operation of the bi-directional dc-dc converter. The output duty ratio is adjusted to accommodate the output voltage of the modified forward dc-dc converter.
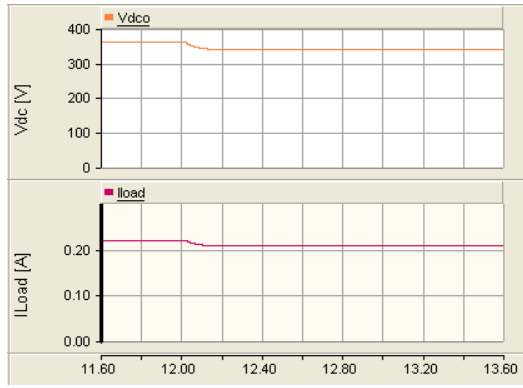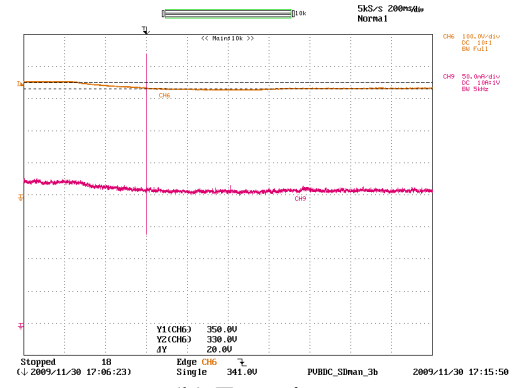
(a) Simulation   (b) Experiment

Y axis: V_{dc} – Orange (100V/div), I_{load} – Maroon (100mA/div – Simulation, 50mA/div-Experimental) Experimental

oscilloscope channel bandwidth = 5kHz; X axis: Time (200ms/div)

Figure D-40: DC-link voltage and load current
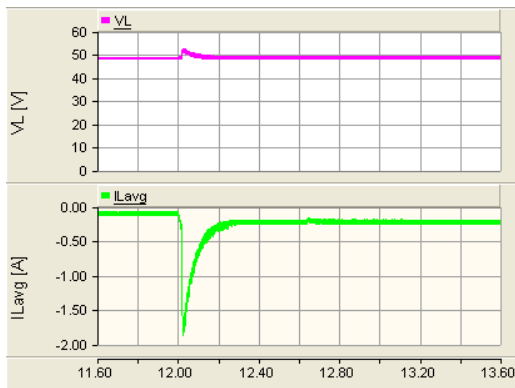
(a) Simulation   (b) Experiment
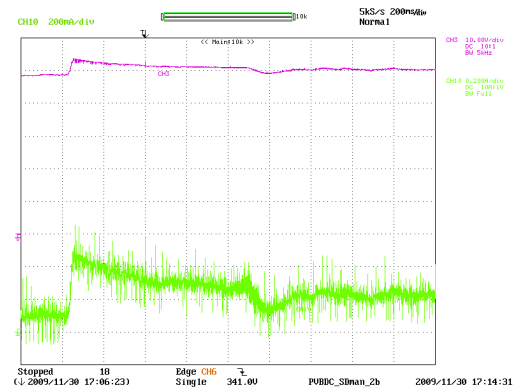
Y axis: V_L – Pink (10V/div) Experimental oscilloscope channel bandwidth = 5kHz, I_L – Green (0.5A/div –

Simulation, 0.2A/div – Experimental); X axis: Time (200ms/div)

Figure D-41: Voltage at the low-voltage end of the bi-directional dc-dc converter and

the battery current
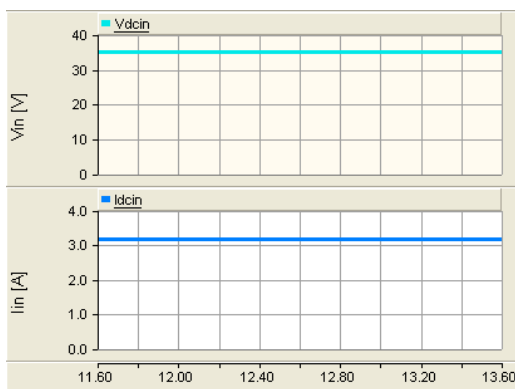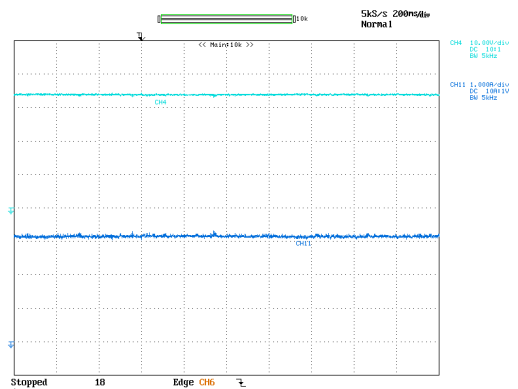
(a) Simulation   (b) Experiment

Y axis: V_{dcin} – Light blue (10V/div), I_{pv} – Dark blue (1A/div), Experimental results oscilloscope channel bandwidth

= 5kHz; X axis: Time (200ms/div)

Figure D-42: Photovoltaic panel voltage and current
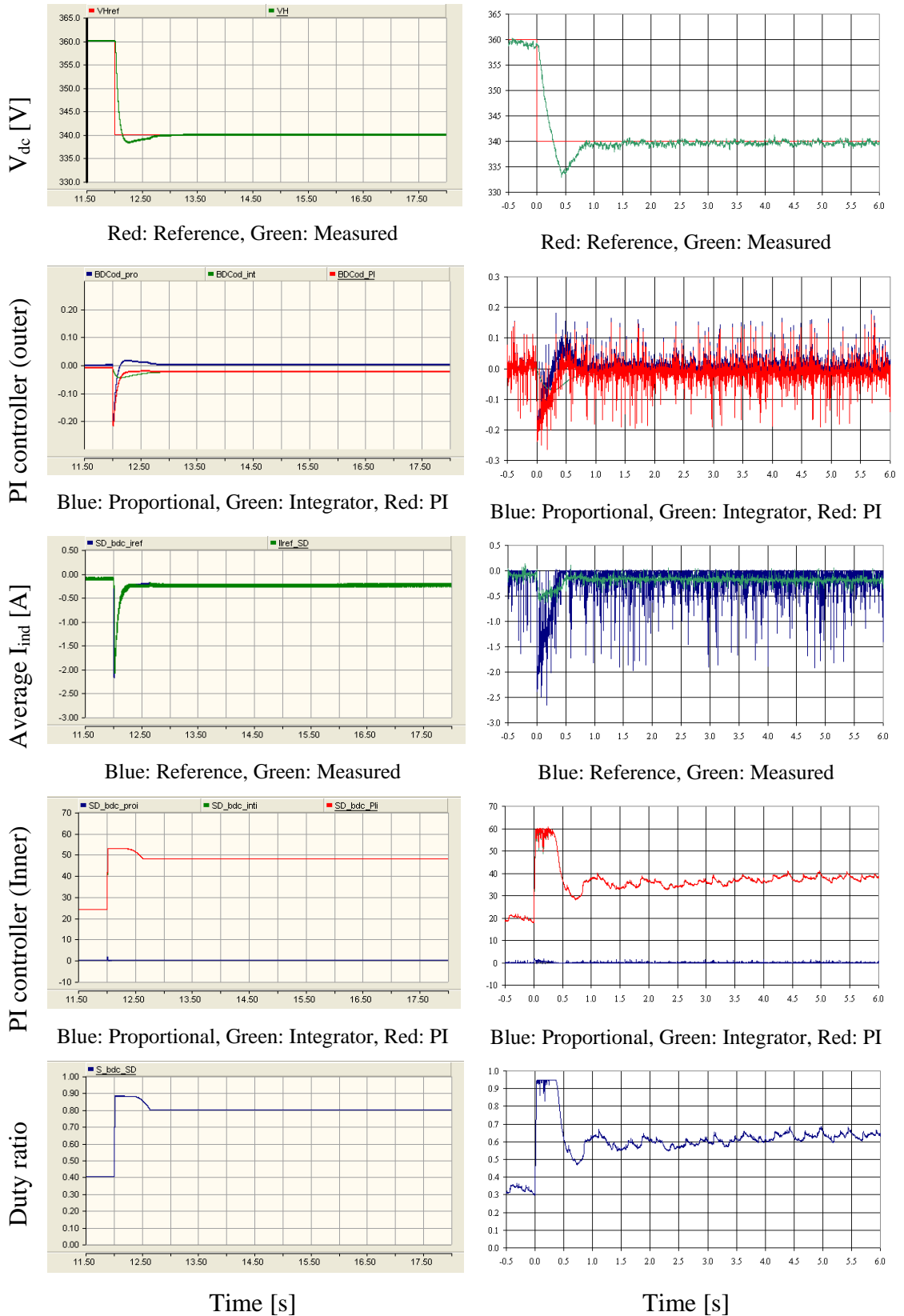
Figure D-43: Behaviour of the controller of the bi-directional converter (step-down mode)

(a) Simulation   (b) Experimental
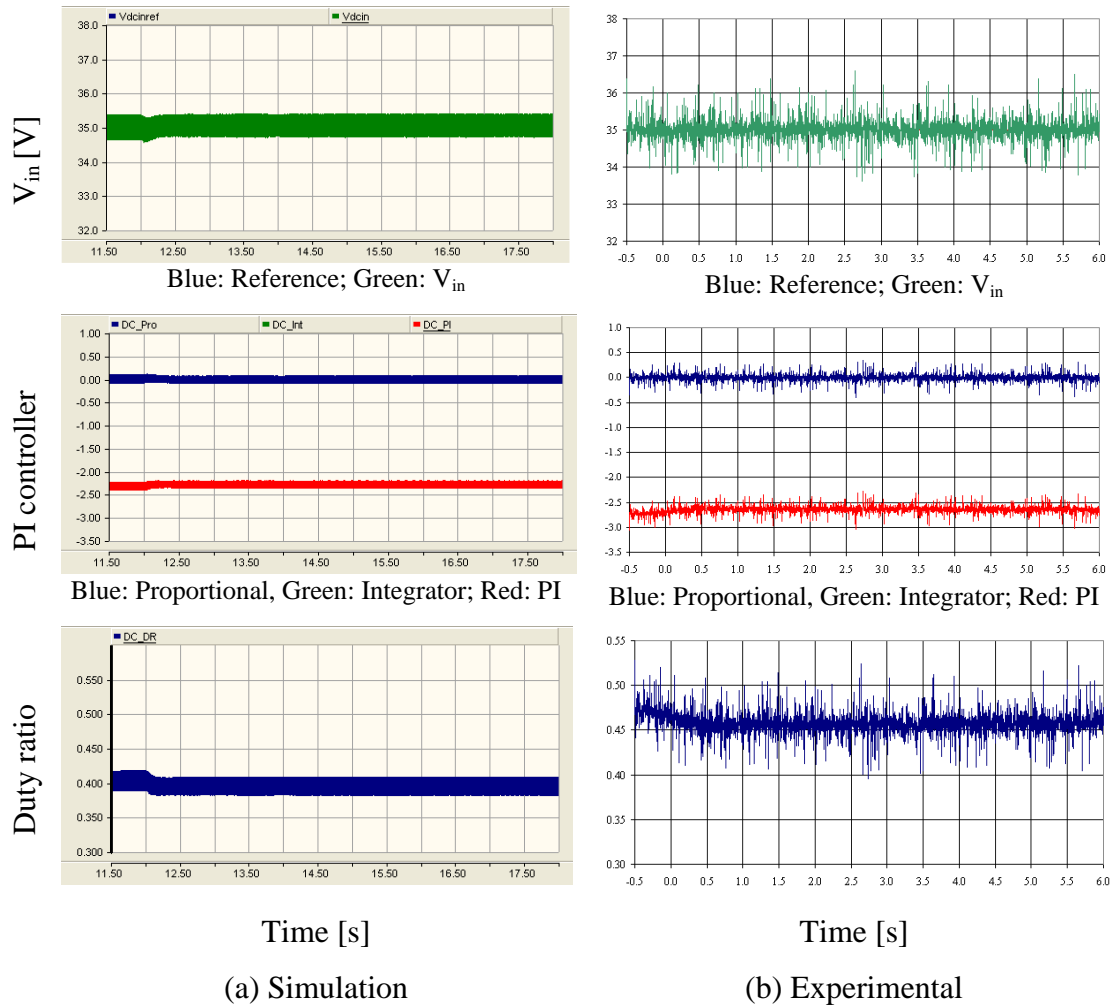
Figure D-44: Behaviour of the controller of the modified forward dc-dc converter

D.4 SUMMARY

This appendix presented the design of controllers for the modified forward dc-dc converter and the bi-directional dc-dc converter. The operating point model developed in earlier chapters was used for the controller design. All the controllers were based on PI controllers. The gains for PI controllers were selected based on the dynamic stiffness properties of individual system. The designed controllers were added to the EMTDC/PSCAD simulation models. The closed loop controllers were also implemented on the hardware prototype.

The controllers were initially tested for the corresponding converter. The modified forward dc-dc converter simulation and experimental results matched each other. For the bi-directional dc-dc converter two modes were tested separately with a laboratory power supply and battery storage except for the outer voltage loop control for step-

down mode as it was not possible to control with a laboratory power supply. The results of the bi-directional dc-dc converter controllers were as expected and results obtained from the simulation model and prototype matched each other. In order to test the outer control loop of the bi-directional dc-dc converter in step-down mode, both the modified forward dc-dc converter and bi-directional dc-dc converter were connected. The simulation and experimental results of the outer voltage loop in step-down mode were compatible.

From the results in the appendix it is possible to state that the controllers of each converter operate according to the requirement of each converter. Section-A of the proposed microsource interface was able to keep the dc-link voltage constant when the bi-directional dc-dc converter modes were selected manually.